Multimode optomechanics in the strong cooperativity regime - Towards optomechanical entanglement with micromechanical membranes

Von der

Fakultät für Mathematik und Physik
der Gottfried Wilhelm Leibniz Universität Hannover

und der

Fakultät für Physik der Universität Wien

zur Erlangung des akademischen Grades

Doktor der Naturwissenschaften Dr. rer. nat.

genehmigte Dissertation
von

M.Sc., Ramon Moghadas Nia

2018

Betreuer und Referent: Prof. Klemens Hammerer (Leibniz Universität Hannover)

Betreuer: Prof. Markus Aspelmeyer (Universität Wien, Österreich)

Korreferent: Prof. Roman Schnabel (Universität Hamburg)

Korreferent: Prof. Francesco Marin (Universität Florenz, Italien)

Tag der Promotion: 09. November 2018

MULTIMODE OPTOMECHANICS IN THE STRONG COOPERATIVITY REGIME

TOWARDS OPTOMECHANICAL ENTANGLEMENT WITH MICROMECHANICAL MEMBRANES

RAMON MOGHADAS NIA

Master of Science (M.Sc.)
University of Vienna
Faculty of Physics
Quantum Group

To my family.

ABSTRACT

Quantum entanglement is an essential feature of quantum physics and an important resource for applications in quantum information processing and quantum communication, including prominent examples such as quantum teleportation and quantum cryptography, as well as for fundamental tests of quantum theory. This thesis explores the generation and verification of continuous wave optomechanical entanglement between a light mode and a multimode mechanical oscillator.

The optomechanical system consists of a thin silicon nitride membrane placed within a high finesse Fabry-Pérot cavity. It is successively improved and verified to operate in the strong cooperativity regime, a necessary condition for the generation of entanglement.

A pulsed-continuous verification protocol is applied to correlation measurements with strong cooperativity. The results demonstrate that the naive approach of filtering a single high-Q mode to obtain a witness for entanglement is not viable. The multimode nature of the mechanics has to be, and is, explicitly considered in the evaluations as well as spectral features of the detection scheme, thereby paving the way towards multimode optomechanical entanglement.

ZUSAMMENFASSUNG

Quantenverschränkung ist ein wesentliches Merkmal der Quantenphysik und sie findet Anwendung in der Quanteninformationsverarbeitung und Quantenkommunikation. Prominente Beispiele hierfür sind Quantenteleportation, Quantenkryptographie sowie fundamentale Tests der Quantentheorie. Diese Arbeit befasst sich mit der Erzeugung und dem Nachweis von optomechanischer Verschränkung kontinuierlicher Variablen zwischen einer Licht-Mode und einem mechanischen Multimoden-Oszillator.

Das optomechanische System besteht aus einer Siliziumnitrid-Membran, die sich in einem Fabry-Pérot Resonator mit einer hohen Finesse befindet. Das System wurde optimiert und operiert nachweislich im Bereich starker Kooperativität, einer notwendigen Bedingung für die Erzeugung von Verschränkung.

Ein gepulst-kontinuierliches Protokoll zum Nachweis von Verschränkung ist auf Korrelationsmessungen im Bereich starker Kooperativität angewendet worden. Die Ergebnisse demonstrieren, dass der übliche Ansatz, bei dem eine mechanische Mode hoher Güte isoliert wird um Verschränkung nachzuweisen, nicht anwendbar ist. Der Multimodenaspekt der Membran muss und wird in der Auswer-

tung explizit berücksichtigt, genauso wie spektrale Eigenschaften der Detektion, wodurch der Weg zu optomechanischer Multimodenver-schränkung geebnet wird.

Keywords: Optomechanics, Quantum optics, Quantum entanglement

Schlüsselwörter: Optomechanik, Quantenoptik, Quantenverschränkung

Physics isn't the most important thing.
Love is.

— Richard Feynman, *Feynman Lectures on Physics, Volume 2: Mainly Electromagnetism and Matter by Richard Phillips Feynman (1964-06-05)*

ACKNOWLEDGMENTS

What has defined my life during the last years?

Someone who spent the last five years pursuing a Ph.D. in experimental physics might be tempted to answer this question with the work as a Ph.D. student itself. When I give myself some time to think about this question again, I am now firmly convinced that the answer is *the people I spent my time with*: Colleagues and friends, the people that are there for each other at intense and tough times.

Therefore, first and foremost, I want to thank Markus Aspelmeyer. Markus gave me the opportunity to join his group at the University of Vienna, a group filled with lovely, motivated and fun people. You always found the right words when I faced setbacks at work or in my personal life. You keep on surprising me with your commitment and support for your group members. I do not take this for granted and I am very thankful for that, as it is one of the most distinguishing aspects of work and life within your group.

I took my first lectures in optomechanics around 2010. It was a course given by Klemens Hammerer, who had just started his professorship at the University of Hanover. At that time, I couldn't have pictured myself going to Vienna for a Ph.D. and to partly come back to Hanover for our joint collaboration. Thank you for making it possible to extend my studies and life from my new home Vienna back to my hometown Hanover. Pursuing the Cotutelle wasn't as easy as assumed, but I would like to thank you for making it possible.

Roman Schnabel, who welcomed me into his group as a Bachelor student (it's been eight years!) in nonlinear optics. After several lectures and seminars I had the chance to work with silicon nitride membranes and finally you introduced me to Markus. No one else supported and accompanied me over such a long period as you did and I am deeply thankful for that. I am looking forward to visit you and your new labs very soon!

I had the chance to work on a very challenging project, which over the course of the years, attracted a lot of people with whom I enjoyed spending time with in the laboratory and in the office. Jason was the very first member of the membrane team that I met[1] and probably the one I spend the most time with. I will miss your positive attitude and

1 Not true. I met Sebastian earlier in Hanover, but we weren't working together.

(to some extent) the long days and nights we spent in the lab during long measurement runs. Witlef, who I will always keep in my memories as the frenzy troubleshooter who fixed every problem before others could phrase it with words. Sebastian, the grumpy theorist in the midst of a bunch of wishy-washy experimentalists and Corentin, the new and not-so-grumpy theorist in the midst of a bunch of wishy-washy experimentalists. And finally Josh, the person who always put me back on track, when I was losing my way, and also my closest friend during the last years. Many other people were involved and contributed to the project. I want to also thank Tobias Wenzl for good times in the lab, Tobias Westphal for following me from town to town (?), Claus for partying like it's 2013 (and membranes), Klemens W. for good times in the office and Manuel for pulling me over the finishing line.

I want to thank all editors who spent their valuable time on giving me suggestions to improve the manuscript: Josh, who spent a huge amount of his time working through the whole manuscript, making sure the story is presented in a coherent way and providing a large amount of possible improvements. He clearly knows all the words. Markus, who thoroughly worked through my final draft and contributed many comments, especially regarding the presentation of results. Corentin for readily providing me a large amount of data for plotting nice figures, at a point when time became short. Nick, Lisa T., Amrit and Sacha for helpful comments on several parts of the early and intermediate state of the manuscript.

During my time in the Aspelmeyer group I became close friends with a number of people. We had a great time and produced so many good memories that we won't fall short of good anecdotes in the future. Among many others, I want to mention the following people that clearly earned a special spot in my heart: Uros, the timeless long runner in the group. David, everybody's favorite Saarländer. Ralf, the always-smiling, never-tiring Cylon! Sebastian, my favorite brawl-partner. Lorenzo, my lab-music (LotR) and vegetable market buddy. Jonas, who is tearing me apart! (Sorry!) Corentin, my favorite Swiss. Josh, my best chummer. And many many many others! Did I mention Josh already?[2]

Since I studied physics in Hanover and because I had the chance to spend some of my time as a Ph.D. student in Hanover, I want to also thank some people in Germany. Amrit, Steffen, Lisa K. and Axel, we started studying physics almost eleven years ago, we managed to keep in touch even though we moved to different places and I hope we maintain our connection in the future. Sacha, Paolo and Mikhail, the optoboys, we had a great time and I am still counting down the days until we gather all together again. Henning and Stefan, you primed me as an experimental physicist and taught me most of

2 He didn't pay me to mention him over and over again.

the tools in my early years and I am grateful for the time we were working together.

Apart from my life at the university, I can be grateful to have a very outstanding circle of friends. You kept your eyes on me and my sanity, even when I was out of sight. I am thankful to call you my friends: Fabian, Lisa T., Yassin, T. Yassin, Nick, Johannes, Robert, Jan Patrick, Emanuel, Fares and Greta.

My family, who always put my well being and success before their own. Without you it wouldn't have been possible for me to get to the point I am at right now. I am looking forward to be around more often and keep an eye on you guys.

And finally, Greta. We met shortly after I started my Ph.D. and over the course of years, you were my source of positive energy and I am grateful for your support, warmth and love. We experienced some difficult and complicated times, since our relationship took place in a superposition of four cities: Vienna, Bayreuth, Hanover and Lüneburg. We don't know for sure (yet) where we will end up, but fortunately we know that the next chapter of our life will be written at a common place.

Despite all these wonderful experiences and memories, it is certain that the next weeks will be my last in the Aspelmeyer group and in Vienna[3]. Let's enjoy the remaining time that is given us.

All we have to decide is what to do with the time that is given us.

— J.R.R. Tolkien, *The Fellowship of the Ring*

3 This does also apply to at least David and Ralf

CONTENTS

LIST OF FIGURES

LIST OF TABLES

LISTINGS

ACRONYMS

FWHM full width half maximum

SiN silicon nitride

LPCVD low pressure chemical vapour deposition

NPS noise power spectral density

FT Fourier transform

FDT	fluctuation-dissipation theorem
LO	local oscillator
BS	beam-splitter
TMS	two-mode squeezing
EoM	equation of motion
ZPF	zero-point fluctuations
FSR	free spectral range
CW	continuous-wave
FC	filter cavity
OMIT	optomechanically induced transparency
PD	photodiode
CM	covariance matrix
FCL	feedback control loop
DAQ	data aquisition card
OMC	optomechanical cavity
MIM	membrane-in-the-middle
KOH	Potassium hydroxide
RWA	rotating-wave approximation

Part I

INTRODUCTION

1 INTRODUCTION

Quantum entanglement is the most distinctive feature exhibited by quantum mechanics. It is the manifestation of inseparable quantum correlations between two or more physical systems, and an important resource that allows for tests of fundamental aspects of quantum physics as well as applications in quantum communication, computation and information, such as quantum networks [79] and potentially unbreakable quantum key distribution, in a regime inaccessible by classical physics.

Recently, solid-state mechanical devices have become available in the quantum regime. They show significant potential to be an engineerable interface to other quantum systems, essentially by entangling mechanical motion with other degrees of freedom.

The ultimate goal of the presented experiment is the generation and verification of steady-state continuous variable entanglement between an optical field and a mechanical system. This is done by using the tools of cavity quantum optomechanics (CQOM) as described in the following section. A brief history of the concept of entanglement as well as its verification and impact on modern physics is given, before presenting the key features addressed within the presented work and how it distinguishes itself from past works.

Cavity quantum optomechanics

The optomechanical interaction between mechanical and electromagnetic degrees of freedom arises from the radiation pressure coupling due to momentum transfer of photons from the light field to the mechanical oscillator. Oftentimes, that is by photons being reflected off a micromechanical mirror.

Cavity quantum optomechanics is the field of resonantly enhanced optomechanical interaction by means of a cavity, which can enable the preparation and control of macroscopic oscillators into quantum states of motion. This paves the way towards fundamental tests of quantum physics with unprecedentedly large masses, as well as towards applications in sensing and quantum information processing.

First experimental demonstrations of radiation pressure forces on a mechanical system, as described by Maxwell's equations, were by means of the light mill configuration in 1901 [95]. In 1909 Einstein studied the statistics of radiation pressure forces onto a movable mirror [51]. But it wasn't until 1967, in the era of modern physics, that Braginsky studied ponderomotive effects of microwave and optical ra-

diation fields onto a mirror [34], followed by the first demonstration of damping of the motion of a mirror by radiation in 1970 [129].

Recent advances in microfabrication produced mechanical oscillators with a wide range of sizes, featuring exceptionally low mechanical decoherence (losses) and sufficiently large susceptibility towards radiation pressure forces. These micro- and mesoscopic mechanical oscillators revealed a new parameter regime between kilogram scale mirrors in advanced gravitational wave interferometers like advanced LIGO on the one hand, and picogram-scale nanophotonic devices on the other hand, opening the field of cavity enhanced quantum optomechanics [27]. By now, a wide range of optomechanical systems has entered the quantum regime, allowing for fundamental tests of quantum theory on unprecedented large scales and pioneering work towards applications in quantum information processing.

Recent experimental efforts include the ground state cooling of micromechanical membranes and silicon nanobeams coupled to radiation fields by Teufel *et al.* [126] and Chan *et al.* [39]. These experiments demonstrated the preparation of a mesoscopic mechanical system into a state with on average less than one quantum excitation of motion.

The strong cooperativity regime for a micromechanical oscillator has been entered by Gröblacher *et al.* in [63] and quantum coherent coupling, which is the coherent coupling between light and mechanics exceeding the optical decay of the cavity and the dissipation to the thermal bath of the oscillator, has been realized in toroidal optical microcavities by Verhagen *et al.* [134], in principle allowing the coherent exchange of quantum states between light fields and mechanical systems and vice versa. Concurrently, quantum coherent transfer has also been realized with microwave resonators coupled to drum modes of mechanical oscillators by Palomaki *et al.* [100] and O'Connell *et al.* [97].

Ponderomotive squeezing of light has been demonstrated by Purdy *et al.* [110], Safavi-Naeini *et al.* [116] and Brooks *et al.* [35], enabling the generation of squeezing within the interferometric device itself to surpass the shot noise limit of displacement sensing. These results are particularly interesting for the improvement of gravitational wave detectors, without relying on external sources of squeezing by nonlinear crystals and parametric down conversion [89]. Recently, mechanical squeezing of motion has been demonstrated by Wollman *et al.* [146], Clark *et al.* [43] and Palomaki *et al.* [101].

Position measurements solely limited in precision by the back action of quantum noise onto the mirror have been achieved with micromechanical membranes by Purdy *et al.* [109] and recently in the audio band frequency regime by Cripe *et al.* [45], enabling the demonstration of quantum non-demolition position measurements.

Feedback control at the thermal dissipation timescale by Wilson *et al.* [143] has been realized, enabling the stable control of a mechanical system in a desired (prepared) quantum state. Recently, feedback cooling into the quantum ground state has been reported by Rossi *et al.* [115].

All these remarkable experiments rely on one or more of the following requirements, such as sideband resolution (i.e. the cavity line width is much smaller than the mechanical frequency) or the strong coupling regime (i.e. the optomechanical coupling strength surpassing the cavity line width). But the single most important figure of merit for enabling true quantum mechanical features in an optomechanical system is the quantum cooperativity. It is defined as the ratio of the coherent optomechanical coupling strength due to radiation pressure forces, to the product of all decoherence mechanisms present in the system, usually the decay rate of the optical cavity, the mechanical decoherence and the coupling to the thermal bath at a given temperature (see chapter 4.2.2).

The necessary condition for carrying out optomechanical experiments at the quantum level, such as the generation of entanglement, is the so called strong cooperativity regime, where the optomechanical coupling strength surpasses all decoherence rates in the system.

Quantum entanglement

Quantum entanglement is likely the most defining phenomenon of quantum physics. It has become famous through the *Gedankenexperiment* by A. Einstein, B. Podolsky and N. Rosen from 1935 [50] (EPR paradox), in which they show that entanglement is inconsistent with a complete description of physical reality through quantum theory. The term *entanglement* was first introduced by E. Schrödinger who considered it not *one but rather the characteristic trait of quantum mechanics*, in [118]. Over the course of the last decades, quantum entanglement has been found to be a rich source for applications such as in quantum teleportation and quantum cryptography. In principle allowing the implementation of secure communication protocols and more efficient computational algorithms that are not achievable by classical physics.

J. S. Bell's no-go theorem from 1964 [30] gave experimentalists a strong tool at hand to solve the dispute among physicists about the EPR experiment. The first experimental test on a variant of Bell's theorem has been conducted in 1972 by Freedman and Clauser [53]. It wasn't before the early 80's that experimental Bell tests were conducted on calcium cascade sources by A. Aspect, P. Grangier, J. Dalibardand and G. Roger [23, 24], that violated the Bell's theorem and ruled out theories of local hidden variables, which were claimed to be needed by the EPR publication. A wide range of Bell tests has been

conducted over the course of the following decades, while another milestone has been reached by Weihs *et al.* in Innsbruck (1998) [139], which closed the locality loophole. Another breakthrough has been reached by the realization of the so called loophole-free Bell tests in 2015. Three different realizations have been presented, with the first using entangled pairs of electron spins in diamond, spatially separated by more than one kilometer and the other two using entangled pairs of photons [60, 121]. Rosenfeld *et al.* [114] added a Bell test by measuring atomic spin states of entangled atoms separated by 398 m.

In contrast to these experiments involving pairs of entangled particles, steady-state continuous variable entanglement is needed for the efficient implementation of a vast number of protocols. Prominent examples are the generation of large keys for quantum key distribution and quantum computing. Light-mechanics entanglement is particularly interesting for quantum nodes in quantum networks, by sending the light from node to node and storing information locally in the mechanics. Optomechanical systems are especially intriguing as they are inherently constituting a light-mechanics interface for quantum information networks has been shown by [91, 106, 107].

A protocol for the generation of steady-state continuous variable optomechanical entanglement between an electromagnetic radiation field and a massive mechanical oscillator has been proposed by Vitali *et al.* in 2007 [136]. The authors consider a movable mirror as part of a Fabry-Pérot resonator being pumped by a laser drive, that is the laser frequency to be the sum of the cavity resonance and the mechanical resonant frequency. Stokes scattering towards lower frequencies creates an entangled pair consisting of a photon and a phonon at the mechanical resonant frequency of the mirror. This is the optomechanical analog to parametric down-conversion when generating squeezing of light in nonlinear crystals.

Genes *et al.* [58] expanded this approach by analyzing the mediation of the inaccessible intra-cavity light-mechanics entanglement onto the output modes of the cavity, which can be measured with photodetectors to prove the intra-cavity entanglement.

These entanglement schemes rely on a break-down of the rotating wave approximation (RWA) and are therefore always operated close to instability. An alternative approach proposed by Hofer *et al.* [69] suggests a pulsed scheme to circumvent instabilities. The proposal presents a pump-probe scheme consisting of two steps. In the first step, a blue-detuned pulse is sent into the cavity, generating entangled photon-phonon pairs by Stokes scattering towards the cavity resonance. In the second step, a red-detuned pulse is sent into the cavity, these lower energy photons will preferably be scattered onto cavity resonance (anti-Stokes scattering) by absorbing the energy from a phonon and therefore swap the mechanical state onto the light field. Effectively, the entanglement between the first pulse

and the mechanics is transferred onto entanglement between the two light pulses. The verification takes place by carefully analyzing the correlations between these pulses after leaving the optomechanical cavity. This protocol has been successfully used to entangle the motion of a micromechanical disc to a microwave radiation field in an inductor-capacitor (LC) resonator [99].

Towards multimode optomechanical entanglement

Here, we will detail experimental efforts towards the generation of continuous variable steady-state optomechanical entanglement of a silicon nitride membrane incorporated into a high finesse Fabry-Pérot cavity. We will put particular emphasize on unique experimental challenges of this inherently multimode physical system, which has not been considered in previous works.

The presented optomechanical system is simpler than many other systems and solely relies on a single laser beam pumping the optomechanical cavity close to its resonance. Neither non-classical light sources nor ground state cooling of the mechanical oscillator are necessary to begin with. Two-mode squeezing (anti-Stokes) and beam splitter (Stokes) interaction will simultaneously scatter photons into red- and blue-detuned sidebands. These sidebands are recorded in reflection of the optomechanical cavity and the entanglement verification step is solely applied in post-processing, which allows for flexibility.

The multimode aspect of SiN membranes will be considered while designing and implementing the experiment towards reaching the strong cooperativity regime, which is the single most important figure of merit for the generation of optomechanical entanglement.

The setup leads to unique experimental challenges which we address experimentally and also in our analysis in post-processing, e.g. low frequency laser noise and detector characteristics.

1.1 OUTLINE OF THIS THESIS

The remainder of this thesis is divided into the following parts:

Part two presents the theoretical tools that are necessary for the understanding of the remainder of this thesis. Chapter 2 deals with the basics of the quantum description of light and mechanics. Chapter 3 discusses the theory of different detection methods to characterize the state of a light field. Chapter 4 introduces the optomechanical interaction and the linearization of the optomechanical Hamiltonian, the core elements to describe the physics of the coupled light-mechanics systems, as well as the two-mode squeezing and beam splitter interactions, which are the fundamental processes for the generation and

verification of optomechanical entanglement. We conclude with defining the quantum cooperativity.

Part three, is composed of chapters 5 to 7. It focuses on the experimental techniques to building up the backbone of the experimental efforts. Chapter 5 starts with the description of the main laser source, the description of laser noise in the sideband picture and the introduction of the high finesse filter cavity, which is used to filter classical noise on the laser to achieve a shot noise limited laser drive for the optomechanical system. We will see that this is an important detail not addressed by the quantum cooperativity. The chapter concludes with the generation of a second laser beam that can be independently manipulated and is often used to characterize the optomechanical coupling strength. Chapter 6 deals with the dual-rail homodyne setup used in this experiment to simultaneously measure the amplitude and phase quadrature of the light exiting the optomechanical cavity, which is then used to reconstruct the full state of the optomechanical system and to retrieve quantum correlations between the light and mechanics. Chapter 7 describes the techniques used to stabilize the distinctive optical cavities and interferometers necessary to run the full experiment.

Part four focuses on the optomechanical system and stable operation in the strong cooperativity regime for the generation of optomechanical entanglement. The mechanical resonator is introduced in chapter 8, with special emphasis on the effective mass of the membrane. We introduce the mechanical quality factor, its measurement and efforts towards increasing the quantum cooperativity by reducing dissipation of the mechanical oscillator to its environment. Special emphasis is given on the multimode nature of silicon nitride membranes. Chapter 9 features the optomechanical cavity, its alignment procedure and its modification over time to increase stability, thermalization and optomechanical coupling strength. A method to incorporate membranes into the optomechanical cavity is given, which reliably results in high mechanical quality factors and low optical losses. The remainder of the chapter focuses on the characterization of the experimental parameters entering the quantum cooperativity, showing that the experiment reaches the strong cooperativity regime necessary for the generation of optomechanical entanglement.

Part five starts with chapter 10 and a brief discussion of optomechanical entanglement protocols, which is followed by the introduction of the pulsed-continuous entanglement protocol used in this work. The pulsed-continuous protocol is a two step generation-verification scheme, that can be applied entirely in post-processing. The data acquisition procedure by means of a dual-rail homodyne detector scheme and the calibration of the data is described with emphasis on the detector frequency response. Chapter 11 presents a number of evaluations of simulated data sets with realistic laser

noise and detector frequency response models. The focus lies on simulations with realistic parameters and comparisons of genuine single mode systems with real, inherently multimode micromechanical membranes. The simulations are followed by evaluations of experimental data taken while the experiment was operated in the strong cooperativity regime. We find that our results indicate the presence of multimode optomechanical entanglement. However, an unquestionable statement about entanglement can not be made at this point. Chapter 12 discusses two roads towards the verification of entanglement with the presented system: The first way is by means of low frequency laser noise reduction, as it is believed to corrupt the measurements presented in chapter 11; and the second way is by further improvements of the quantum cooperativity.

The thesis ends with chapter 13 by providing a short summary of the presented manuscript.

Part II

THEORY

The following chapters are meant to set the theoretical background for the remainder of this thesis. Most of the topics presented here are well known and for further reading I want to refer to the overview articles in quantum optomechanics that have been published over the years [25, 64, 93] and the more comprehensive review articles by Aspelmeyer *et al.* [27] and Y. Chen [42]. More sources are referenced when needed.

Chapter 2 introduces the basic quantum mechanical descriptions of mechanical systems and of light. Most of these aspects introduced here are used throughout the rest of this thesis.

Chapter 3 discusses the different methods for the detection of light. Starting from a simple power measurement over balanced homodyne detection to a the dual-rail detection scheme, a setup that allows the full characterization of the quantum state. Dual-rail detection is applied in the experiment to derive the covariance matrix of a generated entangled state and to deduce the verification and amount of entanglement.

Chapter 4 deals with the basics of the optomechanical interaction. We will derive the interaction Hamiltonian in the linearized regime and discuss the two main interaction types, namely the two-mode squeezing that can generate entanglement between photons and phonons and the beam splitter interaction which can swap a mechanical phonon onto a detectable photon.

We close by giving a brief summary and discussing the quantum cooperativity, the ratio of the optomechanical coupling strength to all decoherence channels available in the system. We will see that the so called strong cooperativity regime, the regime where the coupling strength surpasses all decoherence channels, is a necessary condition for the generation of entanglement. This statement will in turn set the benchmark for the experimental efforts presented in the remainder of this thesis.

2

THEORY OF LIGHT AND MECHANICS

In this chapter, I will introduce the theory of mechanical oscillators and their quantum nature to a level that is important to describe the experiments I am going to present. These concepts will be picked up in chapter 8 and further explored, with a focus on our particular implementation.

This description of the quantum nature of light, coherent states and optical cavities, is by no means exhaustive. The intention is to give the reader the most important expressions that will be needed routinely when introducing the optomechanical coupling, treating our laser source (chapter 5) and detection schemes (chapter 3) used in our experiment and our specific optomechanical system (chapter 9).

2.1 A REVIEW OF MECHANICAL OSCILLATORS

Cavity optomechanics is the research field that studies mechanical systems, e.g. mechanical oscillators, that are coupled to optical degrees of freedom, i.e. an optical cavity mode. We will start the description and brief overview of mechanical resonators in this section. Many of the concepts presented here will be further discussed in great detail over the course of this thesis, mainly in chapter 8, when we will see our specific mechanical oscillator.

At this point we want to restrict ourselves to the simple example of a one dimensional (1D) harmonic oscillator featuring a single mode of vibration at an angular frequency ω_m. We will always deal with mechanical systems suffering from mechanical losses γ and experiencing external forces F_{ext}. The equation of motion (EoM) for the position coordinate $x(t)$ of such an oscillator is given by

$$m\ddot{x}(t) + m\gamma\dot{x}(t) + kx(t) = F_{\text{ext}}(t), \tag{2.1}$$

in which m is the mass of the resonator and $k = m\omega_m^2$ the spring constant of the system. Note that in chapter 8 we will extend this equation and look into a more general and detailed approach of the concept of mass, damping and spring constant. There we will also look into the normal modes of the mechanical resonators used in this thesis, namely silicon nitride membranes, because their multimode nature will play a significant role in our experiment.

Quantum harmonic oscillator

For the moment we will stay with the 1D harmonic oscillator, as depicted in figure 2.1 a), and look at its quantum mechanical description. We consider a mechanical resonator with a pair of canonical coordinates with $x(t)$ being the position coordinate and $p(t) = m\dot{x}(t)$ the resonator's momentum. The total energy is the sum of kinetic and potential energy and is given by the Hamiltonian $H = E_{\text{kin}} + E_{\text{pot}}$.

We quantize the Hamiltonian by replacing the canonical variables x and p by their equivalent quantum operators $\hat{x}$ and $\hat{p}$, which must fulfill the canocial commutation relation

$$[\hat{x}, \hat{p}] = i\hbar. \tag{2.2}$$

The Hamilton operator is then given by the equation

$$\hat{H} = \frac{1}{2}\left(\hat{p}^2/m + m\omega_m^2\hat{x}^2\right). \tag{2.3}$$

At this point we will introduce the phonon creation, $\hat{b}^\dagger$, and annihilation, $\hat{b}$, operators defined by the relations

$$\hat{x} = x_{\text{ZPF}}\left(\hat{b} + \hat{b}^\dagger\right), \tag{2.4}$$

$$\hat{p} = -im\omega_m x_{\text{ZPF}}\left(\hat{b} - \hat{b}^\dagger\right), \tag{2.5}$$

while $x_{\text{ZPF}} = \sqrt{\hbar/2m\omega_m}$ denotes the zero-point fluctuations (ZPF) and $\hat{b}$, $\hat{b}^\dagger$ fulfill the commutation relation

$$\left[\hat{b}, \hat{b}^\dagger\right] = 1. \tag{2.6}$$

Inserting equations 2.4 and 2.5 into equation 2.3 yields the second form of the Hamilton operator as a function of creation and annihilation operators

$$\hat{H} = \hbar\omega_m\left(\hat{b}^\dagger\hat{b} + \frac{1}{2}\right). \tag{2.7}$$

To find solutions for $\hat{b}$ and $\hat{b}^\dagger$ we apply the Heisenberg formalism. The Heisenberg equation for the mechanical annihilation operator reads

$$\frac{d\hat{b}}{dt} = \frac{i}{\hbar}\left[\hat{H}, \hat{b}\right]. \tag{2.8}$$

Applying the commutator and using equation 2.6 the equation reads

$$\frac{d\hat{b}}{dt} = -i\omega_m\hat{b} \tag{2.9}$$

with the solutions

$$\hat{b}(t) = \hat{b}_0\, e^{-i\omega_m t}, \tag{2.10}$$

$$\hat{b}^\dagger(t) = \hat{b}_0^\dagger\, e^{i\omega_m t}, \tag{2.11}$$

in which the zero index in $\hat{b}_0$ and $\hat{b}_0^\dagger$ denotes the operators at time $t = 0$ and simply taking the Hermitian conjugate of $\hat{b}$ to get the solution for $\hat{b}^\dagger$. These solutions can be seen as a rotation in the complex plane with the frequency ω_m or as an angle $\omega_m t$.

We will also introduce the phonon number operator

$$\hat{n} = \hat{b}^\dagger \hat{b}, \tag{2.12}$$

which is defined via the eigenvalue equation

$$\hat{n} \left|n\right\rangle = n \left|n\right\rangle, n \in \mathbb{N}^0. \tag{2.13}$$

Here the eigenvalue n is the phonon number and the eigenstate $\left|n\right\rangle$ the n-phonon state of the system, i.e. n excitations within the oscillator. In the vacuum state $\left|0\right\rangle$ (zero-phonon state) the so called zero-point energy $\frac{1}{2}\hbar\omega_m$ remains in the Hamiltonian 2.7. Generally, the energy eigenvalues are given by the equation

$$\hat{H} \left|n\right\rangle = E_n \left|n\right\rangle, \tag{2.14}$$

and the equidistant energy eigenvalues are

$$E_n = \hbar\omega_m \left(n + \frac{1}{2}\right), n \in \mathbb{N}^0. \tag{2.15}$$

As an example, figure 2.1 b) shows the ground state and the first two excitations of the mechanical mode.

The expectation value of the position operator in the vacuum state yields the zero-point fluctuations $(\left\langle 0 \right| \hat{x}^2 \left| 0 \right\rangle)^{1/2} = x_{\mathrm{ZPF}}$ and the expectation value of the phonon number operator $\hat{n}$ yields the average number of phonons $\bar{n} = \langle \hat{n} \rangle$.

The mechanical noise spectrum

In the laboratory we will usually not only face a single oscillation $x(t)$ at frequency ω_m but a large number of different mechanical modes, each oscillating at its own frequency ω_{m_i}, suffering some amount of loss γ_i and experiencing fluctuating forces. Therefore, for convenience in an experimental investigation, we will instead frequently look at the noise spectrum of the mechanical system, which will allow us to easily select signals and assign them to the respective mechanical mode and also to read off noise levels, scaling and frequency dependencies of different noise sources.

We get the description of $x(t)$ in frequency space by means of the Fourier transform (FT) over the time scale τ of a realization of a measurement (here, I am closely following [27] and will make clear when I differ with my notation)

$$\tilde{x}(\omega) = \mathrm{FT}(x(t)) = \frac{1}{\sqrt{\tau}} \int_0^\tau dt\, x(t) e^{-i\omega t}. \tag{2.16}$$

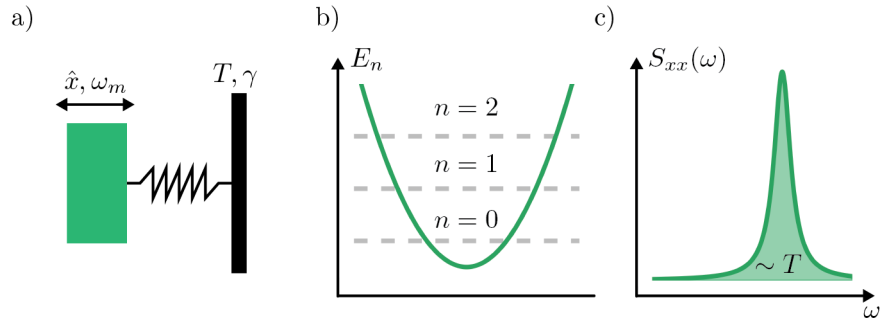

Figure 2.1: Quantum harmonic oscillator. a) schematic of a harmonic oscillator with its position operator $\hat{x} = x_{\mathrm{ZPF}}\left(\hat{b} + \hat{b}^{\dagger}\right)$ and resonant frequency ω_m and coupled to a bath with temperature T at a rate γ. b) Harmonic potential and quantized energy levels $E_n = \hbar\omega_m\,(n + 1/2)$ (dashed grey lines). c) The noise power spectral density of a mechanical oscillator with a peak at its resonant frequency ω_m. The area below the spectral density (light green area) yields the energy of the mechanical mode.

The spectral density is obtained by averaging over individual measurements $\left\langle \left| \tilde{x}(\omega) \right|^2 \right\rangle$. For a stationary process the Wiener-Khinchin theorem relates the spectral density of $x(t)$ with the Fourier transform of the autocorrelation function of it via

$$\lim_{\tau\to\infty} \left\langle \left| \tilde{x}(\omega) \right|^2 \right\rangle = \int_{-\infty}^{\infty} dt\ \langle x(t)x(0)\rangle\, e^{i\omega t} \equiv S_{xx}(\omega), \tag{2.17}$$

while the latter is the definition of the noise power spectral density (NPS) $S_{xx}(\omega)$ (The single-sided NPS is defined by $S_x(\omega) \equiv 2 \times S_{xx}(\omega)$). The noise power spectral density is an easily measurable quantity in the laboratory and the Wiener-Khinchin theorem (equation 2.17) allows us to calculate the variance of x

$$\int_{-\infty}^{\infty} d\omega\, \frac{S_{xx}(\omega)}{2\pi} = \langle x^2 \rangle \propto \langle E \rangle\,, \tag{2.18}$$

which is directly a measure for the temperature T of the oscillator when we apply the equipartition theorem $\langle E \rangle = k_B T/2$. We will frequently make use of this relation experimentally, to obtain quantities like the optical cooling power and from that the optomechanical coupling strength in our experiment, see chapter 9.

We have introduced several basic aspects of mechanical resonators in this section, they will all be either used or further explored over the course of this thesis.

2.2 AN OVERVIEW OF THE DESCRIPTION OF LIGHT

We want to continue with the second building block of an optomechanical system, namely the optical cavity. We will start with the quantization of the electromagnetic field, which is well described in

quantum optics textbooks like Gerry and Knight [59], Walls and Milburn [138] and Loudon [88]. Then, we will briefly discuss the quantum fluctuations of light fields and close with a short description of optical cavities.

The quantum description of light

Let us consider a linear cavity with perfectly conducting walls at $z = 0$ and $z = L$ along the z direction. Solutions of the electromagnetic wave equation derived by Maxwell's equations can be found to have solutions of the form

$$E_x(z,t) = E_0 \times x(t)\sin(kz), \tag{2.19}$$

$$B_y(z,t) = B_0 \times p(t)\cos(kz), \tag{2.20}$$

while $k = \omega/c$ is the wave vector of the fields, c is the speed of light and ω is one of the longitudinal resonant frequencies $\omega_i = i\pi c/L, i \in \mathbb{N}^+$ of the fields.

The classical field energy of an electromagnetic field is given by the Hamiltonian

$$H = \frac{1}{2}\int_0^L dz\, \left(\epsilon_0 E^2(z,t) + \frac{1}{\mu_0}B^2(z,t)\right), \tag{2.21}$$

while ϵ_0 and μ_0 are the vacuum permittivity and permeability.

Inserting the solutions 2.19 and 2.20 into equation 2.21 leads to

$$H = \frac{1}{2}\left(p^2 + \omega^2 x^2\right). \tag{2.22}$$

In this form the Hamiltonian is formally equivalent to the one of a harmonic oscillator (see equation 2.3) with unity mass. Dropping scaling factors, we can now identify x and $p = \dot{x}$ as canonical variables of position and momentum.

Once again we quantize the harmonic oscillator for the light field by replacing the canonical variables q and p by their equivalent quantum operators $\hat{x}$ and $\hat{p}$.

Again, it will be useful for later discussions (which incidentally also avoids the introduction of labels for $\hat{x}$ and $\hat{p}$ to differentiate between light and mechanics) to introduce creation and annihilation operators for the light mode

$$\hat{a} = \frac{\omega\hat{x} + i\hat{p}}{\sqrt{2\hbar\omega}}, \qquad \hat{a}^\dagger = \frac{\omega\hat{x} - i\hat{p}}{\sqrt{2\hbar\omega}}, \text{ and vice versa} \tag{2.23}$$

$$\hat{x} = \sqrt{\frac{\hbar}{2\omega}}\left(\hat{a} + \hat{a}^\dagger\right), \qquad \hat{p} = i\sqrt{\frac{\hbar\omega}{2}}\left(\hat{a} - \hat{a}^\dagger\right), \tag{2.24}$$

which, just like the mechanical creation and annihilation operators, fulfill the commutation relation $\left[\hat{a}, \hat{a}^\dagger\right] = 1$. Similarly to equation 2.7, we can rewrite the Hamiltonian 2.22 as

$$H = \hbar\omega\left(\hat{a}^\dagger\hat{a} + \frac{1}{2}\right). \tag{2.25}$$

Applying the Heisenberg equation we get formally equivalent solutions to equations 2.10 and 2.11, reading

$$\hat{a}(t) = \hat{a}_0\, e^{-i\omega t}, \tag{2.26}$$

$$\hat{a}^\dagger(t) = \hat{a}_0^\dagger\, e^{i\omega t}. \tag{2.27}$$

$$\tag{2.28}$$

Similarly, the average number of photons $\bar{n}_{\mathrm{ph}} = \langle \hat{n}_{\mathrm{ph}} \rangle$ is given by the average of the photon number operator $\hat{n}_{\mathrm{ph}} = \hat{a}^\dagger \hat{a}$. And the energy eigenvalues (figure 2.2 b)) are

$$E_{n_{\mathrm{ph}}} = \hbar\omega \left(n_{\mathrm{ph}} + \frac{1}{2} \right), \; n_{\mathrm{ph}} \in \mathbb{N}^0. \tag{2.29}$$

The corresponding eigenstates $|\hat{n}\rangle$ are the so called Fock or number states, which form a complete set of an orthonormal basis, i.e. they fulfill the relations

$$\langle n \,|\, n' \rangle = \delta_{n,n'}, \tag{2.30}$$

$$\sum_{n=0}^{\infty} |n\rangle \langle n| = 1, \tag{2.31}$$

with $\delta_{n,n'}$ being the Kronecker delta symbol. Therefore, any state can be written as a linear combination of Fock states and we will make use of that relation in the next section when we discuss coherent states.

We have seen that the quantum description of both the mechanical resonator as well as the cavity light fields, are identical to that of the quantum harmonic oscillator. We will make use of this when discussing the optomechanical interaction of the two systems. A notable difference when comparing the Hamiltonians of the two systems, is the frequency of oscillations. For cavity photons in the optical domain ($\omega \approx 2\pi \times 10^{15}$) we obtain $\omega_m/\omega \approx 10^{-9}$.

Coherent states

At this point we want to briefly discuss the quantum mechanical description of some specific light fields and their statistics and noise properties. The starting point is given by the eigenvalue equation of the annihilation operator

$$\hat{a}\,|\alpha\rangle = \alpha\,|\alpha\rangle\,, \; \alpha \in \mathbb{C}, \tag{2.32}$$

with complex eigenvalue α and eigenstate $|\alpha\rangle$. Clearly the eigenstate can be written as a linear combination of Fock states $|\alpha\rangle = \sum_{n=0}^{\infty} c_n\,|n\rangle$, with complex coefficients c_n. By applying the number operator $\hat{n}$ onto the linear combination of number states and forcing the resulting

state $|\alpha\rangle$ to be normalized, that is $|\langle\alpha|\alpha\rangle|^2 = 1$, it can be shown that the coefficients are given by the following expression

$$|\alpha\rangle = e^{-|\alpha|^2} \sum_{n=0}^{\infty} \frac{\alpha^n}{\sqrt{n!}} |n\rangle . \tag{2.33}$$

This is the so called coherent state represented in the Fock basis. To understand the physical meaning of α, we calculate the expectation value of the photon number operator, which we already know to be $\bar{n}_{\mathrm{ph}} = \langle \hat{n}_{\mathrm{ph}} \rangle$, with respect to the coherent state $|\alpha\rangle$ and find:

$$\bar{n}_{\mathrm{ph}} = \langle \alpha | \hat{n} | \alpha \rangle = \left\langle \alpha \middle| \hat{a}^\dagger \hat{a} \middle| \alpha \right\rangle = |\alpha|^2, \tag{2.34}$$

therefore $|\alpha|^2$ is simply the average number of photons $\bar{n}_{\mathrm{ph}}$ and α can be seen as the complex amplitude of the light field. Moreover, the product of the uncertainty,

$$\Delta\hat{O} = \sqrt{\left\langle \hat{O}^2 - \langle \hat{O} \rangle^2 \right\rangle}, \tag{2.35}$$

for a given operator $\hat{O}$, of position and momentum operator (see equation 2.24 for $\hat{x}$ and $\hat{p}$ in terms of creation and annihilation operators), with respect to a coherent state yields

$$\Delta\hat{x} \cdot \Delta\hat{p} = \sqrt{\frac{\hbar}{2\omega}} \times \sqrt{\frac{\hbar\omega}{2}} = \frac{\hbar}{2}, \tag{2.36}$$

hence, coherent states are states of minimum uncertainty, just like the vacuum state.

One common way to visualize a coherent state is by means of polar coordinates for the amplitude $\alpha = |\alpha| e^{-i\phi}$. Therefore a coherent state equals a vacuum state displaced by its amplitude $|\alpha|$ and rotating with frequency $\omega = \dot{\phi}$.

A similar way to visualize a coherent state is by means of the so called amplitude and phase quadratures, $\hat{X}$ and $\hat{Y}$, which are defined as the real and imaginary part of the annihilation operator

$$\hat{X} = \frac{1}{2}\left(\hat{a} + \hat{a}^\dagger\right) \tag{2.37}$$

$$\hat{Y} = \frac{1}{2i}\left(\hat{a} - \hat{a}^\dagger\right), \tag{2.38}$$

$$\tag{2.39}$$

while $\hat{X}$ is the so called amplitude and $\hat{Y}$ the phase quadrature, fulfilling the Heisenberg uncertainty relation

$$\Delta\hat{X} \cdot \Delta\hat{Y} \geq 1 \tag{2.40}$$

and equality reached for coherent states $|\alpha\rangle$. This notation is illustrated in the so called ball-on-stick graphs (figure 2.2 c)). The description of light modes via its quadratures is commonly used when speaking of the detection of light and the reconstruction of the covariance matrix and will be regularly used throughout this thesis (e.g. chapter 3).

Quantum fluctuations and statistics

So far, we know that the average number of photons $\bar{n}_{\mathrm{ph}}$ equals the squared amplitude $|\alpha|^2$ of the light field. At this point, we want to extend our analysis and study the fluctuations of the photon number. Successive use of the eigenvalue equation 2.32 yields the following expression for the uncertainty of the photon number

$$\Delta n = \sqrt{\left\langle \hat{n}^2 - \langle \hat{n} \rangle^2 \right\rangle} = \bar{n}_{\mathrm{ph}}^{1/2}, \tag{2.41}$$

in which $\Delta n = \sqrt{\mathrm{Var}(n)}$ is the standard deviation of n and $\langle \cdots \rangle$ denotes the expectation value. Using equations 2.33 and 2.34 yields

$$P(n) = |\langle n \,|\, \alpha \rangle|^2 = e^{-\bar{n}_{\mathrm{ph}}} \frac{\bar{n}_{\mathrm{ph}}^n}{n!} \tag{2.42}$$

as the probability to detect n photons in the state $|\alpha\rangle$. This is a Poissonian distribution and the source for the quantum fluctuations of the laser light, also known as the quantum shot noise. Note, that the relative fluctuation is decreasing with n

$$\frac{\Delta n}{\bar{n}_{\mathrm{ph}}} = \frac{1}{\bar{n}_{\mathrm{ph}}^{1/2}} \tag{2.43}$$

and therefore, the relative photon number becomes more defined with larger n, that is the classical limit. This is just another reason why coherent states are said to be the quantum counterpart of classical fields.

There are two main manifestations of the quantum shot noise that we will encounter in a typical optomechanical experiment: The first is the fluctuating number of photons reflected off and therefore coupling to the mechanical oscillator. This causes a random motion of the oscillator; the so called quantum back-action noise. The second manifestation is the fluctuating number of photons at the detection apparatus which causes the so called read-out noise. Quantum noise, however, is only observed once the laser beam is sufficiently cleansed from classical noise sources.

2.3 THE OPTICAL CAVITY

Next, we will continue with the optical degree of freedom of n optomechanical system: The optical cavity or resonator, see figure 2.2 a). In this chapter, we will studdy the empty cavity, before we introduce the mechanical resonator and study the optomechanical interaction.

Two mirrors separated by a distance L will exhibit an interference condition that builds up standing waves inside the cavity. This configuration is called the Fabry-Pérot resonator (cavity). Multiples of half

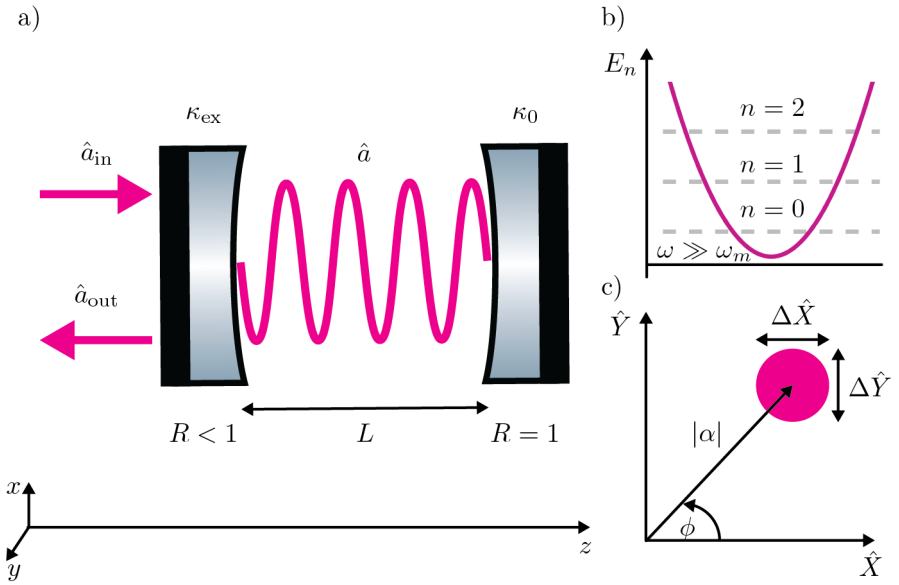

Figure 2.2: Quantum physical description of light. a) Illustration of an optical cavity of length L with input coupler decay rate κ_{ex} and all other loss contributions summed up in κ_0. Input laser drive towards the z-direction and intra cavity field $\hat{a}$, building up a standing wave. b) Energy levels of the electromagnetic field at frequency $\omega \gg \omega_m$. Note, that while the mathematical description is identical to the description of the mechanical harmonic oscillator, optical frequencies are so high (terahertz), that for all practical purposes, it is a valid assumption, that the light is considered to be coupled to a zero temperature bath. c) Ball-on-stick diagram, illustrating a coherent state of amplitude $|\alpha|$ and angle ϕ ($\dot{\phi} = \omega$) in the basis of the quadrature operators $\hat{X}$ and $\hat{Y}$. The fluctuations around the mean amplitude, the standard deviations $\Delta\hat{X}$ and $\Delta\hat{Y}$ equal unity for a coherent state $|\alpha\rangle$.

the optical wavelength λ will fit into the cavity such that the interference condition reads

$$n \times \frac{\lambda}{2} = L,\ n \in \mathbb{N}^+. \tag{2.44}$$

The distance of two successive longitudinal resonances in frequency, the so called free spectral range (FSR), is given by

$$\omega_{FSR} = \pi \frac{c}{L}, \tag{2.45}$$

in which c is the speed of light inside the resonator.

A photon inside the cavity will have a finite life time τ due to imperfect reflectivity of the mirrors and additional losses within the cavity. The attributed cavity decay rate for intensity within the cavity is given by $\kappa = \tau^{-1}$ and is the full width at half maximum of the cavity spectrum.

Another frequently used parameter is the finesse

$$\mathcal{F} \equiv \frac{\omega_{FSR}}{\kappa}, \tag{2.46}$$

a parameter that is giving the average number of round trips for a photon inside the cavity.

For us it is important to distinguish between losses attributed to the residual transmission of the input mirror that will let photons couple into and out of the cavity at a rate κ_{ex}, and all other loss channels within the cavity such as absorption and scattering of photons out of the light mode and residual transmission losses through the end mirror denoted by κ_0.

Typically, we will send some input power

$$P = \hbar\omega_l \left\langle \hat{a}_{in}^{\dagger}\hat{a}_{in} \right\rangle \tag{2.47}$$

at laser frequency ω_l, described by the annihilation operator $\hat{a}_{in}$, onto the cavity. The amount of light coupled into the cavity is determined by the transmission of the input mirror and is $\sqrt{\kappa_{ex}}\hat{a}_{in}$. The input-output theory specifies the field reflected off the Fabry-Pérot cavity to follow

$$\hat{a}_{out} = \hat{a}_{in} - \sqrt{\kappa_{ex}}\hat{a}, \tag{2.48}$$

while $\hat{a}$ denotes the intra-cavity field amplitude and $\sqrt{\kappa_{ex}}\hat{a}$ the amount of it that leaks out of the cavity through the input mirror.

The Heisenberg equation for the time evolution of the intra-cavity field is given by [26]

$$\dot{\hat{a}} = -\frac{\kappa}{2}\hat{a} + \sqrt{\kappa_{ex}}\hat{a}_{in} + i\Delta\hat{a}. \tag{2.49}$$

On the right hand side, the first term is the loss rate of the intra-cavity field, the second term denotes the input field coupling into the cavity and the third term is the evolution of the intra-cavity field, where we used the commonly chosen rotating frame at laser frequency ω_l with the transformation $\hat{a}^{old} = e^{-i\omega_l t}\hat{a}^{new}$. And $\Delta = \omega_l - \omega_{cav}$ the detuning of the laser with respect to the cavity resonance.

The classical field amplitudes can be obtained by taking the expectation value, as we have seen in the last section. For that case the steady-state solution reads

$$\langle\hat{a}\rangle = \frac{\sqrt{\kappa_{ex}}}{\kappa/2 - i\Delta}\langle\hat{a}_{in}\rangle. \tag{2.50}$$

The prefactor is the so called optical transfer function or optical susceptibility

$$\chi_{opt}(\omega) = \frac{\sqrt{\kappa_{ex}}}{\kappa/2 - i(\omega - \omega_{cav})}. \tag{2.51}$$

We will frequently make use of the last two expressions as for determining the optomechanical coupling strength for a given detuning Δ of the laser light with respect to the cavity resonance.

3 DETECTION SCHEMES

Throughout the experimental setup, the detection of light fields by means of photodetectors play a crucial role. The applications of photodetectors range from DC coupled detectors for alignment purposes and laser power monitoring to two channelled DC and/or AC coupled detectors that simultaneously provide laser power monitoring as well as AC signals that can be used for cavity length and laser frequency stabilization. We also use balanced homodyne detection for quantum shot noise limited detection of the mechanical oscillators motion and dual-rail homodyne detection for the state reconstruction of the optomechanical system. For early work on homodyne detection I refer to Yuen and Shapiro [151], for further reading and detailed descriptions I want to recommend Bachor and Ralph's textbook [28] (chapter 7 and 8) and the theses by Mehmet [94] and Vahlbruch [130].

We will break down the optical field operators into the sum of a strong DC component α chosen to be real and a fluctuating term $\hat{a}$, while dismissing second order fluctuations. We choose to express the number operator in terms of the fluctuations δ of amplitude and phase quadratures instead of the fluctuations of the annihilation and creation operators:

$$\hat{n} = (\alpha^* + \delta\hat{a}^\dagger)(\alpha + \delta\hat{a}) \tag{3.1}$$
$$\approx \alpha^2 + \alpha(\delta\hat{a}^\dagger + \delta\hat{a}) \tag{3.2}$$
$$\approx \alpha^2 + \alpha\delta\hat{X} \tag{3.3}$$

and similarly

$$\Delta^2\hat{n} = \alpha^2\Delta^2\hat{X}. \tag{3.4}$$

3.1 DIRECT DETECTION

First of all, I want to consider the case of a light field impinging on a single detector, figure 3.1 a). The most important part of a photodetector is the photodiode (PD), a semi-conductor that converts photons (light) to electrons. The photocurrent generated by a light field is proportional to the number of photons impinging on the diode

$$i(t) \propto \hat{n}(t) \approx \alpha^2 + \alpha\delta\hat{X}(t). \tag{3.5}$$

Oftentimes the photocurrent is amplified and transformed into a voltage by means of a transimpedance amplifier. In case of the detection of mechanical motion at a sideband frequency ω_m, this voltage is high

pass filtered and then can be Fourier transformed, e.g. by a spectrum analyzer, to display the variance of the signal [94]. Mathematically the Fourier transform of the photocurrent reads

$$i(\omega) \propto \alpha^2 + \alpha\delta\hat{X}(\omega), \tag{3.6}$$

omitting the high pass filtered DC contribution ($i(\omega = 0) \propto \alpha^2$), the variance reads

$$\mathrm{Var}_i(\omega) \propto \alpha^2 \left\langle (\delta\hat{X}(\omega))^2 \right\rangle \equiv \alpha^2 \mathrm{Var}(X), \tag{3.7}$$

in which the equivalent symbol defines the variance of the amplitude quadrature of the light field.

To summarize, the direct measurement of a light field by means of a single photodetector is a measurement of the amplitude quadrature $\hat{X}$ amplified by the amplitude α. No other quadrature, i.e. no phase information, is accessible by a single detector measurement. Also, for a real laser beam, the fluctuations (variance) on the light field might be spoiled by classical laser noise making it more difficult to perform shot noise limited measurements. Though, for many applications, such as monitoring laser power, generating error signals and classical amplitude noise measurements, the detection by means of a single detector is sufficient.

3.2 BALANCED HOMODYNE DETECTION

Next, we want to consider a slightly more delicate but much more powerful detection scheme; the balanced homodyne detection. For the moment we look at a beam splitter with two input and two output ports, figure 3.1 b). We consider the optical fields $\hat{a}$ and $\hat{b}$ being coherent and both impinging at the two input ports of the beam splitter with amplitude (power) reflectivity r ($R = r^2$) and amplitude (power) transmission t ($T = t^2$). Using matrix formalism, the output fields are connected to the input fields by the relation [152]

$$\begin{pmatrix} \hat{c} \\ \hat{d} \end{pmatrix} = \begin{pmatrix} t & r \\ -r & t \end{pmatrix} \begin{pmatrix} \hat{a} \\ \hat{b} \end{pmatrix}. \tag{3.8}$$

The beam splitter is assumed to be lossless and perfectly balanced, such that $R = T = 0.5$. Under these circumstances the output fields are defined by

$$\hat{c} = +t\hat{a} + r\hat{b} = \frac{1}{\sqrt{2}}\left(+\hat{a} + \hat{b}\right), \tag{3.9}$$

$$\hat{d} = -r\hat{a} + t\hat{b} = \frac{1}{\sqrt{2}}\left(-\hat{a} + \hat{b}\right). \tag{3.10}$$

As we do not want to lose any information, we will use two photodetectors, one measuring the output field $\hat{c}$ and the other the field $\hat{d}$. The photocurrent of the first detector is calculated as

$$
\begin{aligned}
i_c(t) \propto \hat{c}^\dagger \hat{c} &= \frac{1}{2}(\hat{a}^\dagger + \hat{b}^\dagger)(\hat{a} + \hat{b}), \\
&= \frac{1}{2}(\hat{a}^\dagger \hat{a} + (\hat{a}^\dagger \hat{b} + \hat{b}^\dagger \hat{a}) + \hat{b}^\dagger \hat{b}), \\
&\approx \frac{1}{2}(\alpha^2 + \alpha(\delta\hat{a}^\dagger + \delta\hat{a})) \cdots \\
&\quad + \frac{1}{2}(\alpha\beta e^{i\Theta} + \alpha\delta\hat{b}e^{-i\Theta} + \delta\hat{a}^\dagger \beta e^{i\Theta} + \delta\hat{a}^\dagger \delta\hat{b}e^{i\Theta}) \cdots \\
&\quad + \frac{1}{2}(\alpha\beta e^{-i\Theta} + \alpha\delta\hat{b}^\dagger e^{i\Theta} + \delta\hat{a}\beta e^{-i\Theta} + \delta\hat{a}^\dagger \delta\hat{b}e^{-i\Theta}) \cdots \\
&\quad + \frac{1}{2}e^{-i\Theta}e^{i\Theta}(\beta^2 + \beta(\delta\hat{b}^\dagger + \delta\hat{b})), \\
&\approx \frac{1}{2}(\alpha^2 + \beta^2 + 2\alpha\delta\hat{X}_a + 2\beta\delta\hat{X}_b + 2\alpha\beta\cos\Theta) \cdots \\
&\quad + \frac{1}{2}(\alpha(\delta\hat{b}e^{-i\Theta} + \delta\hat{b}^\dagger e^{i\Theta}) + \beta(\delta\hat{a}e^{-i\Theta} + \delta\hat{a}^\dagger e^{i\Theta}))
\end{aligned}
$$

in which both fields have been linearized and the amplitude α has been chosen to be real and a relative phase $e^{i\Theta}$ (between signal and local oscillator) has been introduced for $\hat{b}$. We introduce generalized quadratures of the fluctuation for an arbitrary phase angle Θ; they read $\delta\hat{X}_a^\Theta = 1/2(\delta\hat{a}e^{-i\Theta} + \delta\hat{a}^\dagger e^{i\Theta})$ and $\delta\hat{X}_b^\Theta = 1/2(\delta\hat{b}e^{-i\Theta} + \delta\hat{b}^\dagger e^{i\Theta})$, respectively.

Finally, we consider the field α to be the weak signal field we want information for and β the strong local oscillator, i.e. $\beta \gg \alpha$. The photocurrent simplifies to

$$
i_c(t) \propto \hat{c}^\dagger \hat{c} \approx \frac{\beta^2}{2} + \beta\delta\hat{X}_b + \beta\delta\hat{X}_a^\Theta \tag{3.11}
$$

and a similar calculation for the output port $\hat{d}$ at the second detector yields

$$
i_d(t) \propto \hat{d}^\dagger \hat{d} \approx \frac{\beta^2}{2} + \beta\delta\hat{X}_b - \beta\delta\hat{X}_a^\Theta. \tag{3.12}
$$

Looking at the last two equations strongly suggests one should calculate the difference current of the two detectors

$$
i_-(t) = i_c(t) - i_d(t) \propto 2\beta\delta\hat{X}_a^\Theta. \tag{3.13}
$$

This result clearly demonstrates the full power of balanced homodyne detection; the resulting difference current is proportional to the generalized fluctuations $\delta\hat{X}_a^\Theta$ of the weak signal beam and amplified by the strong amplitude of the local oscillator. Any quadrature of the weak signal can be measured by carefully choosing the phase Θ. Note, that $\delta\hat{X}_a^{\Theta=0\,\mathrm{deg}} = 1/2(\delta\hat{a} + \delta\hat{a}^\dagger) = \delta\hat{X}_a$ equals the amplitude quadrature and $\delta\hat{X}_a^{\Theta=90\,\mathrm{deg}} = 1/2(\delta\hat{a} + \delta\hat{a}^\dagger) = \delta\hat{Y}_a$ equals the phase quadrature

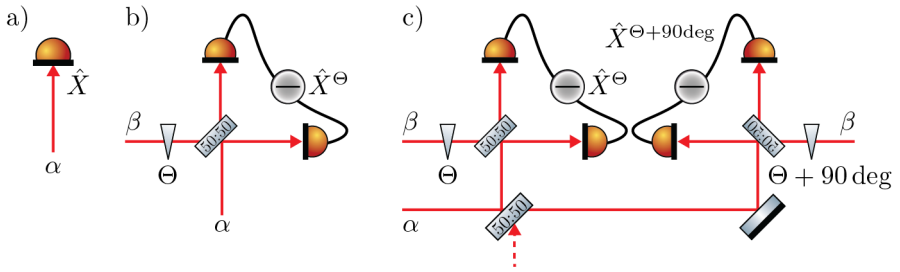

Figure 3.1: Illustration of detection schemes. The classical mean amplitude is given by α and $\beta \gg \alpha$ in case of the strong local oscillator. a) Direct detection: The signal is simply detected by a single photodiode, which produces a current proportional to the light impinging on the detector and therefore measuring the amplitude quadrature $\hat{X}$ of the signal. b) Balanced homodyne detection: The signal and local oscillator are combined on a balanced beam splitter, they interfere and after equal path lengths hit two detectors. The difference of the two currents can be proportional to any quadrature $\hat{X}^{\Theta}$ of the signal by tuning the relative phase between signal and local oscillator via a phase shifter Θ. c) Dual-rail homodyne detection: The signal is first split into two beams that are each detected by means of balanced homodyne detection. The local oscillators of each detector can be set to two orthogonal quadratures, such that simultaneous measurements of two orthogonal quadratures $\hat{X}^{\Theta}$ and $\hat{X}^{\Theta+90^{\circ}}$ is possible. In particular, it is possible to choose the amplitude and phase quadratures $\hat{X}$ and $\hat{Y}$ to reconstruct the full state of the measured light mode. Note, however, that the beam splitter used to split up the signal in the first place, introduces one unit of snot noise through its open port, which needs to be taken into account for proper characterizations.

of the weak signal. Moreover, the fluctuations of the strong local oscillator cancel out, such that their noise budgets do not contribute to the signal.

Measurements of the variance of the difference current, e.g. by means of a spectrum analyzer, yields

$$\text{Var}_{i\_}(\omega) \propto \beta^2 \text{Var}(\delta \hat{X}_a^{\Theta}), \tag{3.14}$$

which is a convenient result, as blocking the weak signal input port and replacing it with vacuum fluctuations with a variance of $\text{Var}(\delta \hat{X}_{\text{vacuum}}) = 1$, is an easy way to calibrate the signal $\text{Var}(\delta \hat{X}_a^{\Theta})$ in units of shot noise.

3.3 DUAL-RAIL HOMODYNING AND COVARIANCE MATRIX

All states we are dealing with, such as coherent and thermal states and also squeezed states, fall under the category of Gaussian states. An important trait of Gaussian states is that they remain Gaussian if only linear operations are applied, which will be the case in all our experiments.

Consider a Gaussian state ρ with n-modes and the column vector

$$\mathbf{R} = \left(\hat{X}_1, \hat{Y}_1, \cdots, \hat{X}_n, \hat{Y}_n\right)^\top \tag{3.15}$$

in which the entries R_i consist of the n pairs of amplitude $\hat{X}_i$ and phase $\hat{Y}_i$ quadrature operators. This description fully characterizes all n modes of the Gaussian state ρ. The state ρ is then fully characterized by its second moments (the first order moments are a displacement in phase space and can be neglected after applying a proper transformation [18], see figure 2.2 c)). The first moments are given by the expectation values of the vector

$$\bar{\mathbf{R}} = \left(\left\langle \hat{X}_1 \right\rangle, \left\langle \hat{Y}_1 \right\rangle, \cdots, \left\langle \hat{X}_n \right\rangle, \left\langle \hat{Y}_n \right\rangle\right)^\top, \tag{3.16}$$

and the covariance matrix (CM) σ with the matrix elements

$$\sigma_{ij} = \frac{1}{2}\left\langle R_i R_j + R_j R_i \right\rangle - \left\langle R_i \right\rangle \left\langle R_j \right\rangle. \tag{3.17}$$

In section 3.2 we saw that we can measure any quadrature by means of homodyne detection. This approach can be expanded by means of dual-rail (or 8-port) homodyne detection [137], where the signal is split up by a balanced beam splitter and sent to two homodyne detectors, one measuring the amplitude quadrature and one measuring the phase quadrature (see figure 3.1 c) for an illustration). Note that by introducing a balanced beam splitter to split the signal, one unit of vacuum noise is added through the unused beam splitter port.

This detection scheme allows us to characterize the Gaussian optical quantum states in all our experiments. It will be our main detection scheme after bringing the optomechanical system into the strong cooperativity regime and describing our entanglement protocol and present measurements towards multimode optomechanical entanglement in chapters 10 and 11.

4

INTRODUCTION TO CAVITY OPTOMECHANICS

The source of optomechanical interaction of an optical field with a mechanical oscillator in the simplest case, is due to the reflection of a photon and consequently the momentum change of $\Delta p_{\mathrm{ph}} = 2h/\lambda_{\mathrm{ph}}$ which applies a radiation force $F_{\mathrm{rad}} = \frac{d}{dt}(\Delta p_{\mathrm{ph}})$, depending on the total photon flux, onto the mechanical oscillator. We will make use of the Hamiltonian formulation of light and mechanics from the last chapter and for the remainder of this chapter we will stick to the standard model of optomechanics, a Fabry-Pérot cavity with a movable end-mirror, where the first being the optical and the latter the mechanical degree of freedom (see figure 4.1 for reference). We will expand this description at a later stage, when we introduce our optomechanical setup of choice, namely the membrane in the middle setup, a thin dielectric film placed inside a high finesse Fabry-Pérot cavity.

4.1 HAMILTON FORMALISM

The starting point of our discussions will be the Hamilton operator H_0 for the optical field and the mechanical oscillator as two uncoupled quantum harmonic oscillators. Note, that the theory presented here is not original and follows mainly the review of cavity optomechanics by Aspelmeyer *et al.* [27]. Deviations in the notations will be marked and other sources are cited when used.

The bare Hamiltonian reads

$$\hat{H}_0 = \hbar\omega_{\mathrm{cav}}\hat{a}^\dagger\hat{a} + \hbar\omega_m\hat{b}^\dagger\hat{b}, \tag{4.1}$$

here we used the creation and annihilation operator description and restricted ourselves to a single mechanical mode with frequency ω_m and a single optical mode, that is the cavity resonance ω_{cav} closest to the driving laser frequency ω_l. The optomechanical coupling arises from the fact that the movable mirror changes its position due to radiation pressure forces and vice versa the moving mirror changes the cavity resonance frequency depending on its position x. A Taylor expansion yields

$$\omega_{\mathrm{cav}}(x) \approx \omega_{\mathrm{cav}} + x\frac{\partial\omega_{\mathrm{cav}}}{\partial x} + \mathcal{O}(x)^2 + \cdots, \tag{4.2}$$

where for the purposes of this thesis the linear term is sufficient, such that we neglect quadratic and higher order terms $\mathcal{O}(x)^{\geq 2}$. A detailed

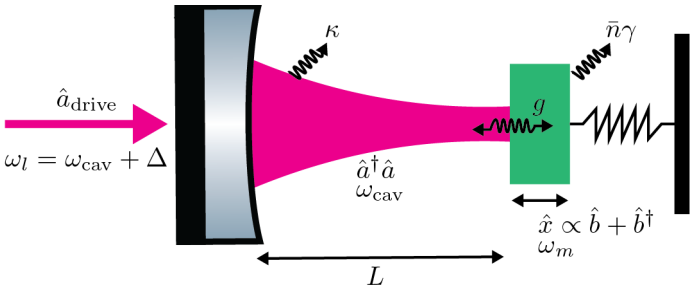

Figure 4.1: Prototype optomechanical system. The so called end mirror configuration, a Fabry-Pérot cavity of length L featuring a light end mirror with a mechanical degree of freedom $\hat{x}$ coupled to the cavity photons $\hat{a}^\dagger\hat{a}$ via radiation pressure at a rate g. The mechanical oscillator is coupled to a heat bath at temperature T at a rate $\bar{n}\gamma$ and the optical cavity mode with decay rate κ and pumped via a driving field $\hat{a}_{\mathrm{drive}}$ detuned by Δ with respect to the cavity.

derivation can be found in the literature [85]. We follow the notation from [27] and introduce the optical frequency shift per displacement $G = -\partial\omega_{\mathrm{cav}}/\partial x$ and insert 4.2 into equation 4.1, which gives rise to a coupling term

$$\hbar\omega_{\mathrm{cav}}(x)\hat{a}^\dagger\hat{a} \approx \hbar(\omega_{\mathrm{cav}} - G\hat{x})\hat{a}^\dagger\hat{a} \tag{4.3}$$

and the interaction part of the Hamiltonian using equation 2.4 reads

$$\hat{H}_{\mathrm{int}} = -\hbar g_0 \hat{a}^\dagger\hat{a}(\hat{b} + \hat{b}^\dagger). \tag{4.4}$$

Here we introduced the optomechanical single photon coupling strength

$$g_0 = G x_{\mathrm{ZPF}}, \tag{4.5}$$

while $G = \omega_{\mathrm{cav}}/L$ for a Fabry-Pérot cavity of length L. The negative sign in equation 4.4 corresponds to a reduction of both the cavity frequency and the energy for positive displacements $x > 0$. The radiation pressure force associated with the optomechanical interaction is then given by

$$\hat{F}_{\mathrm{rad}} = -\frac{d\hat{H}_{\mathrm{int}}}{d\hat{x}} = \hbar G\hat{a}^\dagger\hat{a}. \tag{4.6}$$

Note that we restricted ourselves to the case of the so called dispersive coupling, where the cavity frequency is depending on the mirror position. There are of course other systems where different kinds of optomechanical coupling can arise. For instance, the so called dissipative coupling for a thin dielectric membrane inside a Sagnac interferometer [78, 149], where the cavity decay rate $\kappa(x)$ is depending on the mirror position.

4.2 LINEARIZED OPTOMECHANICS

The optomechanical interaction (equation 4.4) is a three-wave mixing process and inherently nonlinear. For most optomechanical systems and also in the context of this thesis, it is legitimate to apply the so-called linear approximation by rewriting the annihilation operator as the sum of small fluctuations $\delta\hat{a}$ around the (real) coherent mean field cavity amplitude $\alpha = \alpha^\dagger = \sqrt{\bar{n}_{\mathrm{cav}}}$ (subsection 2.2), such that

$$\hat{a} = \alpha + \delta\hat{a}. \tag{4.7}$$

Using this approximation, the photon number operator becomes

$$\begin{aligned} \hat{a}^\dagger\hat{a} &= (\alpha + \delta\hat{a})^\dagger \times (\alpha + \delta\hat{a}) && (4.8)\\ &= \underbrace{\alpha^2}_{\mathcal{O}(\alpha^2)} + \underbrace{\alpha\delta\hat{a} + \alpha\delta\hat{a}^\dagger}_{\mathcal{O}(\alpha^1)} + \underbrace{\delta\hat{a}\delta\hat{a}^\dagger}_{\mathcal{O}(\alpha^0)}. && (4.9) \end{aligned}$$

The first term applies a DC radiation pressure force onto the mirror, shifting it into a new equilibrium position. We introduce a new position operator $\hat{x}_{\mathrm{new}} = \hat{x}_{\mathrm{old}} + \Delta\hat{x} \equiv \hat{x}$ that takes this shift into account.

The second term is linear in α and the one we keep, while the third term is smaller by at least one order of the field amplitude $\mathcal{O}(\alpha^1)$. The linearized interaction Hamiltonian becomes

$$\hat{H}_{\mathrm{int}}^{(\mathrm{lin})} = -\hbar g_0 \alpha (\delta\hat{a} + \delta\hat{a}^\dagger)(\hat{b} + \hat{b}^\dagger). \tag{4.10}$$

The full Hamiltonian of the optomechanical system is then given by

$$\hat{H}_{\mathrm{lin}} = -\hbar\Delta\delta\hat{a}^\dagger\delta\hat{a} + \hbar\omega_m\hat{b}^\dagger\hat{b} - \hbar g(\delta\hat{a} + \delta\hat{a}^\dagger)(\hat{b} + \hat{b}^\dagger), \tag{4.11}$$

where we introduced the laser drive and switched to the rotating frame with a unitary transformation at laser frequency ω_l. In this frame the optical field is now oscillating at a frequency given by the detuning $\Delta = \omega_l - \omega_{\mathrm{cav}}$ between laser drive and cavity resonance. Note, that we already took care of the shift by the average radiation pressure force. We also introduced the so called optomechanical coupling strength

$$g = g_0\alpha = g_0\sqrt{\bar{n}_{\mathrm{cav}}}, \tag{4.12}$$

which is the single photon coupling strength amplified by the total number of cavity photons.

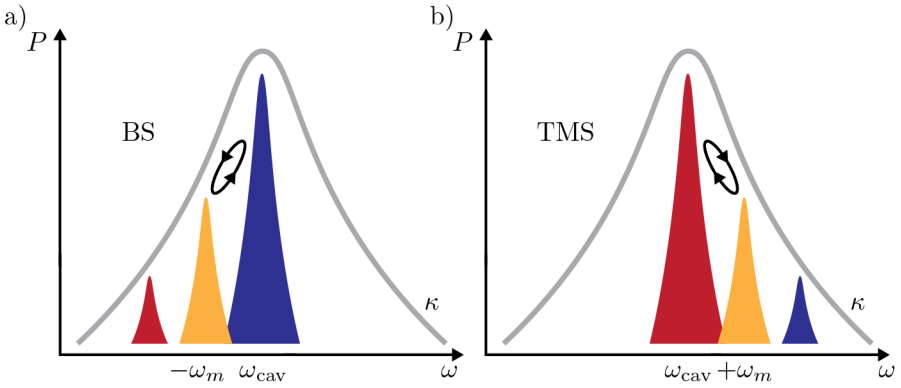

Figure 4.2: Red- and blue detuned drive of an optomechanical cavity with line width κ (grey line). Yellow modes depict the driving laser, red-detuned ($\Delta = -\omega_m$) in figure a) and blue-detuned ($\Delta = +\omega_m$) in figure b). In case of red-detuning. Stokes scattering creates a lower energy sideband (red modes) and anti Stokes scattering creates a higher energy sideband (blue modes). a) In case of a red-detuned drive, the up-scattering resonates in the cavity, while the lower energy sideband is reduced, effectively cooling the mechanical oscillator. The Hamiltonian (eq. 4.13) reduces to the beam splitter interaction, which swaps the mechanical state onto the light and vice verse. b) In case of a blue-detuned drive, the down-scattered sideband is resonant and the higher energy sideband is decreased, effectively heating, or amplifying, the oscillators motion. The Hamiltonian (eq. 4.14) reduces to the two mode squeezing interaction, where pairs of phonons and photons are created, that can lead to quantum correlations and ultimately entanglement between the mechanics and light.

Red-detuning

There are three different choices for the detuning of the laser drive with respect to the cavity and each case gives rise to different applications in optomechanics.

To start with, we assume the laser drive to be red-detuned by one mechanical resonance, e.g. $\Delta = -\omega_m$, as depicted in figure 4.2 a). The Hamiltonian (4.11) reduces to the optical and mechanical harmonic oscillators at frequency ω_m. The effective interaction Hamiltonian reduces to the so called beam-splitter (BS) interaction

$$\hat{H}_{\mathrm{bs}} = -\hbar g(\delta\hat{a}\hat{b}^\dagger + \delta\hat{a}^\dagger\hat{b}), \tag{4.13}$$

which describes the creation of a resonant photon at the cost of a mechanical phonon, or vice versa (figure 4.3 a)). Therefore, this interaction can be used to swap energy between the optical field and the mechanics, while the other two interaction terms are non-resonant. A red-detuned drive is used for sideband cooling [92, 117] of the mechanical oscillator.

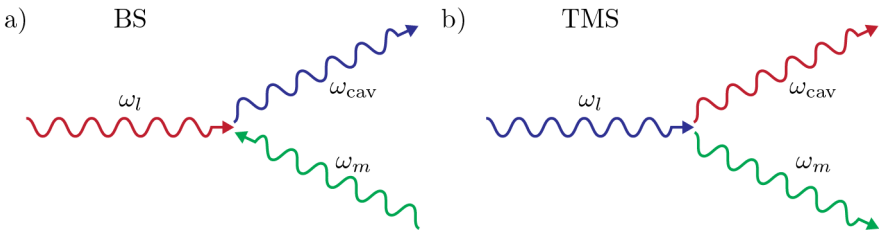

Figure 4.3: Photon-phonon illustration of the optomechanical interaction. a) Beam splitter interaction: Red-detuned drive at ω_l. The low frequency photon is scattered resonantly to ω_{cav}, taking the missing energy ω_m from the mechanical oscillator. b) Two mode squeezing: A blue-detuned photon is decaying into a correlated photon-phonon pair and thereby also amplifying the mechanical motion.

Blue-detuning

The second interesting case is the blue-detuned drive at $\Delta = +\omega_m$ (figure 4.2 b)), where the two resonant interactions being the simultaneous creation (annihilation) of a photon and phonon pair (figure 4.3 b)). The effective Hamiltonian in this case reduces to

$$\hat{H}_{\mathrm{tms}} = -\hbar g(\delta\hat{a}^\dagger\hat{b}^\dagger + \delta\hat{a}\hat{b}), \tag{4.14}$$

the so called two-mode squeezing (TMS) Hamiltonian, as it can create highly correlated and entangled photon-phonon pairs, being the optomechanical analogue to optical down-conversion. We will make use of this interaction in the remainder of this thesis as the source for the generation of optomechanical entanglement. In contrast to the red-detuned case, the creations of phonons is an effective heating of the mechanical mode and can yield to instabilities in the system.

Resonant drive

In case of a resonant drive ($\Delta = 0$) both interactions contribute equally as in equation 4.11. Note, that $\hat{b} + \hat{b}^\dagger \propto x$, which will induce phase shifts on the light field and in combination with a phase measurement, to position measurements with high sensitivity, as in gravitational wave detectors. Furthermore, this case can be used to generate ponderomotive squeezing [35, 116] or perform quantum non-demolition measurements (QND).

4.2.1 *Quantum Langevin equations*

To summarize the description of the optomechanical system, we want to treat the quantum operators of the mechanics and light in the Heisenberg picture and write down their equations of motion. We

choose the linearized operators and drop the δ since we are only interested in the fluctuations, e.g. $\delta\hat{a} \to \hat{a}$. Additionally, we will describe the mechanical part by the position and momentum operators $\hat{x}$ and $\hat{p}$. And the optical subsystem by the quadrature operators $\hat{X}$ and $\hat{Y}$.

The so called linearized quantum Langevin equations read

$$\dot{\hat{x}} = +\omega_m \hat{p}, \tag{4.15}$$

$$\dot{\hat{p}} = -\omega_m \hat{x} - \gamma\hat{p} - \sqrt{2}g(\hat{a} + \hat{a}^\dagger) - \sqrt{2\gamma}\hat{f}, \tag{4.16}$$

$$\dot{\hat{a}} = -(i\Delta + \kappa)\hat{a} - i\sqrt{2}g\hat{x} - \sqrt{2\kappa}\hat{a}_{\text{in}}, \tag{4.17}$$

while κ denotes the cavity decay rate, γ the mechanical decay rate and g the optomechanical coupling strength. The operator $\hat{f}$ is the stochastic Brownian noise term and $\hat{a}_{\text{in}}$ the quantum noise coupling into the system by the full cavity line width. Both are assumed to describe Markovian processes and therefore being delta-correlated, fulfilling $\left\langle \hat{a}_{\text{in}}(t)\hat{a}^\dagger_{\text{in}}(t') \right\rangle = \delta(t - t')$ and (in the limit of high temperatures) $\left\langle \hat{f}(t)\hat{f}(t') + \hat{f}(t')\hat{f}(t) \right\rangle /2 = (\bar{n} + 1/2)\delta(t - t')$, while δ denotes Kronecker delta function and $\bar{n}$ is the mean number of phonons in the mechanical system.

4.2.2 *Summary and quantum cooperativity*

The goal of the last three chapters was to provide an overview and explain the basic theory of mechanical oscillators and light, of optical resonators and the detection of output modes, and finally the foundations of optomechanics.

We studied the quantum mechanical description of mechanical resonators and used that to derive the zero point fluctuations and the energy levels and number of phonons of the harmonic oscillator. Then, after Fourier transforming the solution of its equation of motion, we connected the spectral noise density to the variance of the position coordinate and the temperature. Both quantities will be used frequently in the experiment, as measurements of the spectral noise density are being used to study the performance of the mechanical resonator in chapter 8 and for determining the optomechanical coupling strength via the evaluation of spectra taken while sideband cooling the mechanics.

Then, we continued with the description of quantum states of light and its statistics, ultimately giving rise to quantum noise. The description of optical cavities build the basis of main building blocks of the experiment, such as the optomechanical cavity 9 and the filter cavity in chapter 5.

The theory of the detection of light is crucial, not only for the daily work in the laboratory, but also for the verification of entanglement, as we will see in chapter 10, because ultimately, any type of entangle-

ment verification will rely on measurements of the output modes of the optomechanical cavity.

Finally, we brought the mechanical and optical subsystems together and introduced the optomechanical interaction mediated by radiation pressure forces. We linearized the dynamics and differentiated between different type of interactions, depending on the detuning of the input laser beam with respect to the cavity resonance, effectively choosing between the beam splitter interaction, which can give rise to swap the mechanical state onto the light field, and the two mode squeezing interaction, which produces pairs of photons and phonons which can give rise to quantum correlations and ultimately entanglement between the light and the mechanics.

The linearized Langevin equations including thermal and quantum noise sum up the foundations of the optomechanical interaction used within this thesis, from basic applications like sideband cooling up to the entanglement protocol used for the generation and verification of steady-state continuous variable multimode entanglement.

The figure of merit for the generation of optomechanical entanglement (and also other quantum effects in such systems) is the so called quantum cooperativity

$$C = \frac{4g^2}{\kappa\gamma(\bar{n}+1)}, \tag{4.18}$$

which is the ratio of the coherent optomechanical interaction strength g, to the different decoherence rates in the experiment, i.e. the optical decay rate κ, the mechanical dissipation at a rate $\gamma\bar{n}$.

The so called strong cooperativity regime, $C > 1$, is a necessary condition to reveal quantum effects such as the generation of entanglement. The ingredients of the cooperativity are important to understand to come up with a feasible set of parameters, which can push the system into the strong cooperativity regime.

It is useful to rephrase equation 4.18 in an experimentally more accessible way. By replacing $\gamma = \omega_m/Q$, the cavity line width κ and optomechanical coupling strength g by the cavity finesse $\mathcal{F}$, input power P_{in} and mass m, as well as $\bar{n}$ by the temperature T for $\bar{n} \gg 1$, we can obtain

$$C = \frac{32\hbar}{\pi} \times \frac{\mathcal{F}^2 P_{\text{in}}}{\lambda c} \times \frac{Q}{m\omega_m k_B T}, \tag{4.19}$$

with the reduced Planck constant $\hbar$, the speed of light c, the Boltzmann constant k_B. We use a laser with a wavelength of $\lambda = 1064\,\text{nm}$ and a cryogenic environment of $T = 8\,\text{K}$. We further aim for a short 5.5 mm cavity with a moderate finesse of $\mathcal{F} = 5000$. Moreover, we plan to use a thin silicon nitride membrane as our mechanical oscillator incorporated into the optical cavity. We aim at a resonance

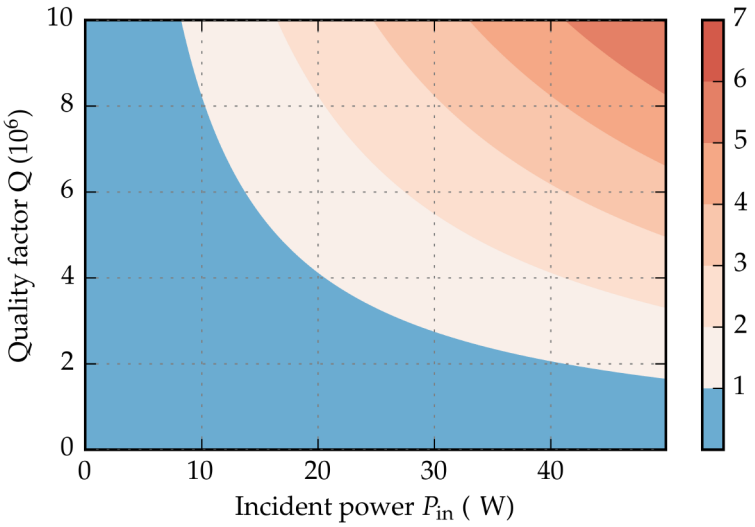

Figure 4.4: Quantum cooperativity as a function of experimental parameters, see main text. Depicted is the quantum cooperativity as a function of mechanical quality factor and cavity input power. The strong cooperativity regime is accessible for a wide range of input powers and mechanical quality factors (different shades of red).

frequency of $\omega_m = 2\pi \times 1\,\mathrm{MHz}$ and a mass of $m = 10\,\mathrm{ng}$. Figure 4.4 shows the cooperativity as a function of input power and mechanical quality factor for the mentioned parameters. For a wide range of feasible combinations of P_{in} and Q, strong cooperativity $C > 1$ is accessible.

The following chapters deal with the description and understanding of these parameters and their realization, paving the way to the strong cooperativity regime. Additionally, we will see that other external parameters are crucial too, if aiming for the generation and verification of optomechanical entanglement. The most prominent issues are classical laser noise, the characteristics of the photodetectors and a proper characterization of the experiment. Ultimately, the inherent multimode nature of our mechanical oscillators play a significant role towards entanglement, since it first seems to hinder entanglement, but if properly taken into account, is a source of richer physics.

Part III

EXPERIMENTAL SETUP

In this part of the thesis, we give an overview of the full experimental setup and focus on the main building blocks that do not enter the cooperativity directly, but can indirectly prevent the generation and verification of optomechanical entanglement.

Chapter 5 deals with the stable laser source and the reduction of classical laser noise by means of a high finesse filter cavity operated in double pass configuration to achieve a quantum noise limited laser drive for the optomechanical cavity. We will describe the generation of a second laser beam that is phase coherent with the signal beam, which can be individually controlled and is used for characterization of the optomechanical cavity and coupling strength.

Chapter 6 features the dual-rail homodyne detection scheme necessary for simultaneous measurements of the phase and amplitude quadratures of the light, which is needed for a full reconstruction of the generated entangled state. We will focus on the experimental realization of the shot noise limited detection, the alignment procedure and the characterization of the detectors.

Chapter 7 deals with the fact that every optical beam on the table needs to be stabilized with respect to a reference. This is not only important for stable operation of the experiment, but also to have a defined and fixed detuning between the input laser and optomechanical cavity, or between signal and local oscillator to measure a well defined quadrature of the signal. I will discuss the different experimental techniques used to stabilize the optomechanical cavity, the filter cavity, the cooling beam filter cavity and the (in total) four homodyne detectors.

A full overview of the experimental setup is given by figure 4.5, which also includes the optomechanical cavity in a cryogenic environment.

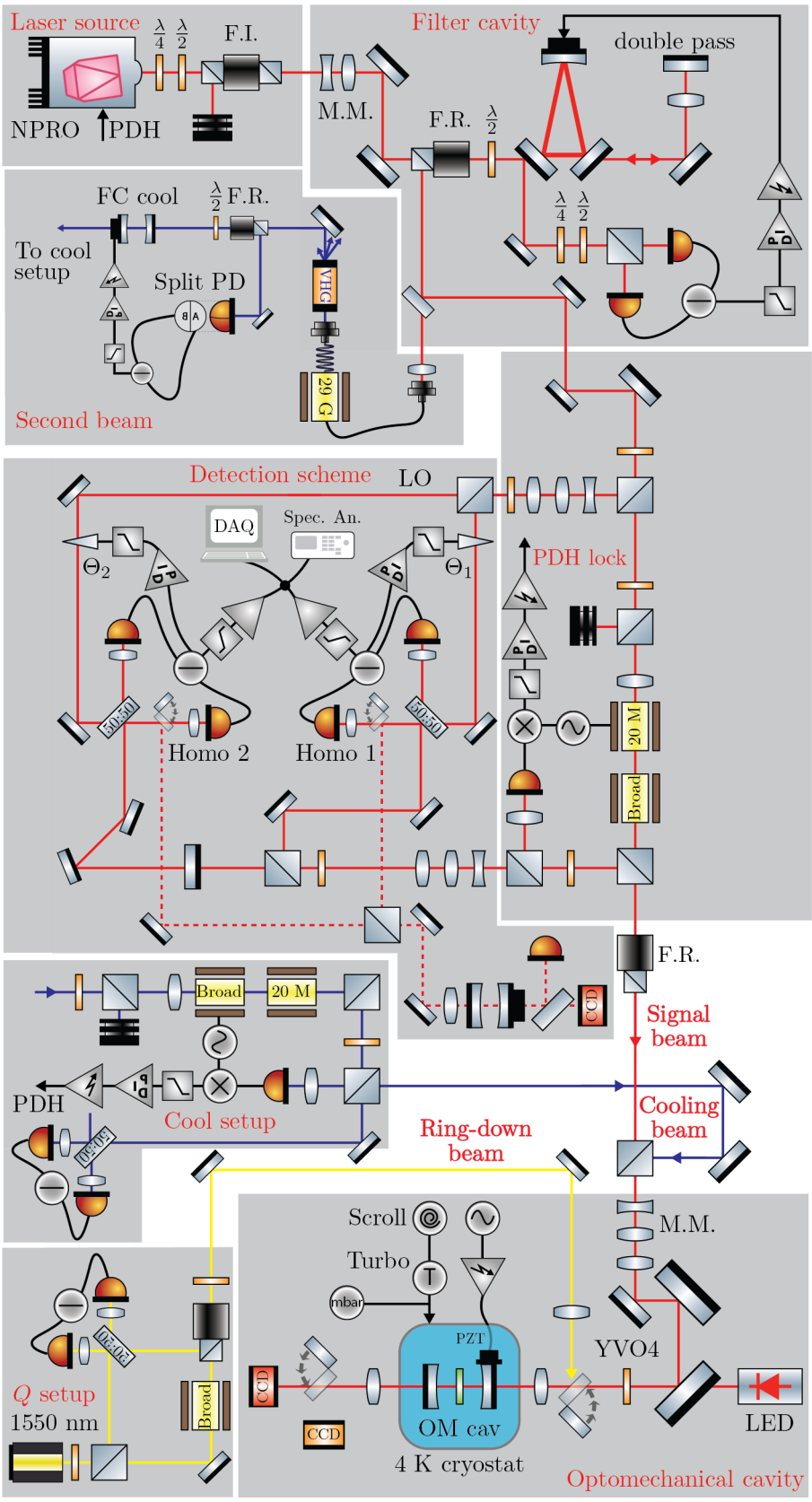

Figure 4.5: Full experimental scheme.

5 LASER LIGHT PREPARATION

5.1 LASER SOURCE AND CLASSICAL NOISE

The main laser source is a single-frequency continuous-wave (CW) solid-state laser from InnoLight GmbH [1], now Coherent Inc. [2]. The specific model (Prometheus, datasheet at [2]) is a Nd:YAG laser with a pump diode at 808 nm that emits roughly 1 W laser power at 1064 nm and up to 20 mW phase-coherent laser light at 532 nm via single-pass second harmonic generation. The Prometheus and the two output modes are illustrated in figure 5.1 b).

The laser features a monolithic resonator, consisting of a single Nd:YAG crystal [54, 55, 75]. The specific design is called nonplanar ring oscillator (NPRO, see figure 5.1 a)) and its biggest benefit is its unidirectional operation, which allows for long-term high-power applications. In contrast, linear resonators are either limited in output power or in lifetime due to spatial hole burning at the nodes of the standing wave. A ring-resonator features two counter propagating travelling waves and unidirectional operation is achieved by applying losses to one of the two waves. Due to the nonplanarity of the design (two of the corner sides that give rise to total internal reflection are slightly tilted relative to the plane of incidence), the NPRO slightly rotates the polarisation during each round trip. Applying a magnetic field along the longer dimension of the crystal counteracts the rotation via the Faraday effect of the Nd:YAG and due to the nonplanar design for one circulation direction. Therefore, it effectively leads to lower optical losses at the polarization dependent reflection coating of the front face of the crystal, while the polarization rotation is further increased for the counter-circulating wave.

It is crucial for the presented experiment to be able to slowly vary the laser frequency by more than a FSR of the optomechanical cavity, allowing to find the TEM_{00} mode and to maximize the mode matching to it. Our Prometheus system can tune the laser frequency by about 40 GHz by means of changing the laser crystal temperature and stabilizing it with ≈ 1 Hz bandwidth, which fulfills our requirements. The frequency stability of 2 MHz/min agrees with the $1-2$ MHz/min frequency shifts observed in our laboratories.

At the same time, a fast actuator is needed to be able to account for relative frequency jitter between the laser resonator and the optomechanical cavity up to audio frequencies. Our Prometheus laser has a built-in piezoelectric transducer (piezo) pushing on the laser crystal and therefore changing the resonator length and frequency. The max-

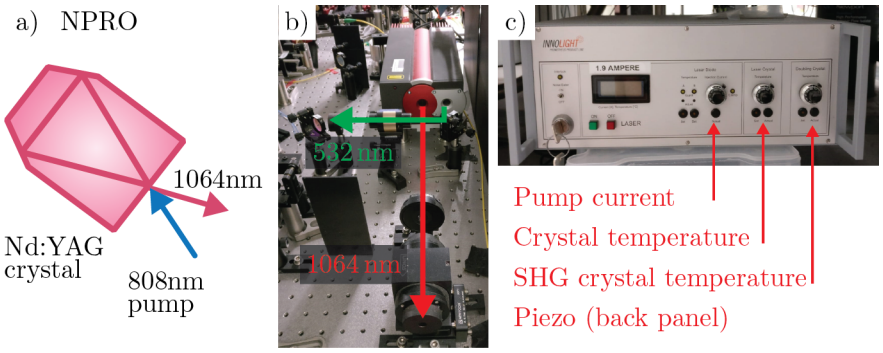

Figure 5.1: NPRO design and Prometheus laser. a) Schematics of the monolithic NPRO crystal design. The 808 nm pump field enters the crystal and the active medium resonates at 1064 nm. b) Photo of the Prometheus laser with drawn lines in red and green depicting the output of the main 1064 nm laser mode as well as the frequency doubled light at 532 nm. c) Photographs of the front panel of the controller featuring the input for laser temperature and laser piezo, as well as the diode current of the NPRO and the phase matching temperature of the second harmonic generation.

imum bandwidth of the piezo is about 100 kHz, the stroke per volt is 2 MHz, while the maximum tuning range is ±65 MHz, which is sufficient for our purposes. We mainly scan over the optomechanical cavity resonance and sidebands to create feedback signals, see chapter 7. Figure 5.1 c) shows the front panel of the controller unit with the inputs for laser crystal temperature and piezo, as well as the current of the pump diodes and the phase matching temperature for the second harmonic generation.

A stable cavity mode is guaranteed by a slightly convex output plane. The spectral line width is supposed to be ≈ 1 kHz integrated over 100 ms and the output mode is a single TEM_{00} mode.

5.2 LASER LIGHT MODULATION AND LASER NOISE

Quantum noise

Ultimately, even an ideal laser system is subject to laser noise due to the quantum nature of light (see section 2.2) i.e. the quantum fluctuations of the photon number of a given state (equation 2.43). Therefore the resulting quantum noise power spectral density for a laser beam with power $P_0 = \hbar\omega n$ and a measurement bandwidth of 1 Hz reads

$$S_{qq} = \frac{hcP_0}{\lambda} \tag{5.1}$$

where c denotes the speed of light and λ is the laser wavelength. This is the so called photon shot noise and it prominently couples into the experiment at two places. First, inside the optomechanical cavity, the fluctuating power interacts with the mechanical oscillator and imprints a random displacement noise onto the latter. Here, we usually

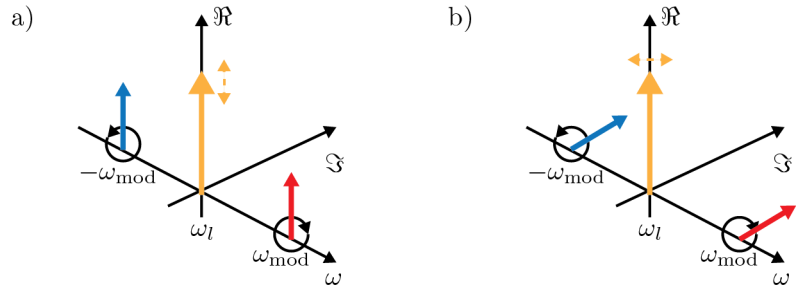

Figure 5.2: Laser modulation in the sideband picture. a) Laser amplitude modulation at frequencies $\pm\omega_{\mathrm{mod}}$. The sidebands rotate in opposite directions and the vectorial addition cancels out all contributions within the imaginary axis (phase), effectively yielding an amplitude modulation of the carrier within the real axis. b) Laser phase modulation at frequencies $\pm\omega_{\mathrm{mod}}$. The sidebands rotate in opposite directions and the vectorial addition cancels out all contributions within the real axis (amplitude), effectively yielding a phase modulation of the carrier within the imaginary axis. This figure is derived from [131].

use the term radiation pressure shot noise or quantum back-action noise. Second, at the detection of the cavity output fields the fluctuations of photons will yield fluctuations of the generated photocurrent of the detector [36]

$$S_{II} = \frac{\sqrt{\eta}e^2}{\hbar^2\omega^2} \times S_{qq}, \tag{5.2}$$

where e is the electron charge and η the detection efficiency. The shot noise has two important and notable characteristics: First its frequency independence (or whiteness) and second that fluctuations of the power are proportional to the square root of the power. Whereas for classical noise (next section) the fluctuations are directly proportional to the power. This means, that the ratio of quantum to classical laser noise

$$\frac{S_{qq}}{S_{cl}} \propto \frac{1}{\sqrt{P_0}} \tag{5.3}$$

will increase for lower laser power. Therefore, a quantum noise limited laser drive can be achieved by simply arbitrarily reducing the laser power, while the the real challenge lies in being shot noise limited at large powers that are needed to boost the optomechanical coupling strength $g = g_0\sqrt{\bar{n}_{\mathrm{cav}}}$.

Classical laser noise

In reality, all lasers are imperfect and perturbations due to e.g. fluctuations of pump power, vibrations of the laser resonator or thermal effects, might induce additional noise onto the laser field. We will refer to the excess noise as classical laser noise and distinguish between

amplitude (intensity) and phase (frequency) noise.

One approach to model amplitude and phase noise is by means of amplitude and phase modulation of the laser field at a given modulation frequency ω_{mod} and amplitude (am) and phase (pm) modulation depths $m_{\text{am}}, m_{\text{pm}} \ll 1$. The equations for the laser field would then have the form

$$a_{\text{am}} e^{i\omega_l t} = a_0 \left(1 + m_{\text{am}} \cos\left(\omega_{\text{mod}} t\right)\right) e^{i\omega_l t} \tag{5.4}$$

$$a_{\text{pm}} e^{i\omega_l t} = a_0 e^{i\left(\omega_l t + m_{\text{pm}} \cos(\omega_{\text{mod}} t)\right)} \tag{5.5}$$

which, using Bessel functions and the limit of small modulation depths (see [131] for the full derivation), yield the sideband description of the laser noise at a given modulation frequency

$$a_{\text{am}} e^{i\omega_l t} = a_0 \left(e^{i\omega_l t} + \frac{1}{2} m_{\text{am}} e^{i(\omega_l + \omega_{\text{mod}})t} + \frac{1}{2} m_{\text{am}} e^{i(\omega_l - \omega_{\text{mod}})t}\right), \tag{5.6}$$

$$a_{\text{pm}} e^{i\omega_l t} \approx a_0 \left(e^{i\omega_l t} + \frac{i}{2} m_{\text{am}} e^{i(\omega_l + \omega_{\text{mod}})t} + \frac{i}{2} m_{\text{am}} e^{i(\omega_l - \omega_{\text{mod}})t}\right). \tag{5.7}$$

Therefore, laser amplitude noise can be modeled as two correlated sidebands rotating in phase with the carrier light at $\pm\omega_{\text{mod}}$, while laser phase noise is modeled by two correlated sidebands rotating out of phase with the carrier at $\pm\omega_{\text{mod}}$. Altogether, the first pair of sidebands will only affect the amplitude (length of the carrier in figure 5.2 a)) and the second pair of sidebands will (in first order) only affect the phase (angle of the carrier with respect to the imaginary axis) of the laser field. This model is depicted in figure 5.2 b) which is inspired and reproduced from [131]. It not only serves as a good intuitive picture and model of noise, but is also useful when we come to use electro optical modulators (EOM) at various points of this thesis, e.g. for the generation of a secondary cooling beam or the generation of error signals for locking the various cavities in the experimental setup.

This intuitive picture can also be applied for classical laser noise, as correlated sidebands at each modulation frequency and even for quantum noise as uncorrelated sidebands at all frequencies, effectively leading to a cylindrical shaped noise around the frequency axis.

At the end of this section we discuss where these noise sources enter the presented setup and how they influence the experimental efforts. We emphasize that our entanglement protocol is based on a resonant laser drive with respect to the optomechanical cavity. Therefore, laser amplitude noise will yield fluctuations of the intra cavity

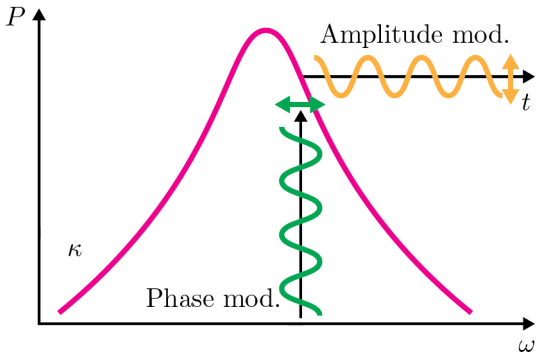

Figure 5.3: Frequency to amplitude noise conversion. Consider an optical cavity with line width κ. If the laser beam is stabilized with some detuning with respect to the resonance, laser frequency noise (green modulation) will modulate the detuning of the laser and produce amplitude noise fluctuations (yellow modulation) on the output light, determined by the slope (line width) of the cavity. Therefore, especially in case of a high finesse cavity, it is important to lock the laser very close to the resonance of the cavity to minimize the effect, as in first order there is no conversion (zero slope).

power, which is coupled to the mechanical oscillator. These fluctuations will drive the oscillator and produce noise. If the classical amplitude noise level is too high or the optical input power too large (see equation 5.3), it can mask the intrinsic thermal motion of the oscillator and/or overcome the coherent quantum noise drive of the mechanics.

Phase noise on the other hand can be also seen as frequency noise, as the frequency is the difference of phase over time, $f(t) = (2\pi)^{-1} d\phi/dt$. As the laser is locked to the resonance of the cavity, frequency noise should ideally not drive the mechanics in first order. Note, that whenever we are not ideally on cavity resonance, which is to some extent always the case, frequency noise will be converted to amplitude noise and, as described, affect the oscillator motion by laser amplitude noise. The frequency- to amplitude-noise conversion is illustrated in figure 5.3.

Both classical noise sources will also enter the detection of the cavity output modes, but this problem is moved to the discussion of our balanced homodyne detection schemes.

Summary

The monolithic design makes the laser highly frequency stable (and the slightly convex output plane yields a stable cavity) as relative fluctuations of the resonators length $\Delta l/l$ are very small, which

would usually be converted to relative frequency fluctuations Δf at frequency f, following the equation [36]

$$\Delta f = f \times \frac{\Delta l}{l}. \tag{5.8}$$

The laser intensity noise is specified as $< -135\,\mathrm{dB/Hz}$ for frequencies above 20 kHz. The Nd:YAG laser has a broad and large peak in its intensity noise spectrum at around 1 MHz due to the laser relaxation oscillations. This peak is completely removed (damped) by an active intensity noise stabilization, the so called noise eater. The amplitude and frequency noise properties of NPRO lasers are well studied within the scope of gravitational-wave detection (e.g. [36, 81–83]) and they have proven to be low-noise laser sources for quantum optomechanical experiments.

5.3 THE FILTER CAVITY

Nonplanar ring oscillators prove to be stable and low-noise laser sources used in a vast amount of optical and optomechanical experiments. However, the experiment presented here requires a shot noise limited input field for membrane frequencies above 500 kHz. At these sideband frequencies and for typical input powers used here, the Prometheus is still limited by classical laser noise, which needs to be filtered and reduced. One way to reduce classical noise is by means of an optical filter cavity (FC).

Note, that the filter cavity presented here is described in the PhD thesis of Hannes Böhm [33]. It has been further investigated and characterized by Jason Hölscher-Obermaier, who has conducted most of the filtered and unfiltered laser noise measurements [70].

Optical filter cavities (sometimes referred to as mode-cleaner cavities) are an important tool in many quantum optomechanical experiments and the backbone of the experimental setup presented here.

Our filter cavity serves several purposes. It is used as a beam position and beam size reference on the optical table for all optical components and cavities following the filter cavity, even if the laser source needs to be replaced or repaired.

Furthermore, the filter cavity serves as a spatial and temporal mode filter [142]. When the cavity TEM_{00} mode is stabilized to the laser (or vice versa), it will only transmit that mode and reflect higher-order modes, featuring different spatial shapes and frequencies, that might be partially existent in the incoming laser beam. Therefore, the transmission of the FC consists of a single Gaussian mode, which is very desirable for most experiments.

Optical low pass filter

The single most important purpose of the filter cavity is its characteristic to perform as a first-order optical low pass filter. Picture the laser carrier on resonance with the filter cavity. Due to its line width κ_{FC}, it will act as an optical low pass for frequencies outside of its bandwidth and therefore reduce laser noise at sideband frequencies above its line width according to its transfer function. The transfer functions [112] for single pass and double pass filtering are given by

$$\chi_{\mathrm{FC}}^{(1)}(\omega) = \left(\frac{1}{1 + \left(\frac{\omega}{\kappa_{\mathrm{FC}}} \right)} \right)^{1}, \tag{5.9}$$

$$\chi_{\mathrm{FC}}^{(2)}(\omega) = \left(\frac{1}{1 + \left(\frac{\omega}{\kappa_{\mathrm{FC}}} \right)} \right)^{2}, \tag{5.10}$$

where κ_{FC} is the line width of the filter cavity (optical low pass). Filter functions are usually visualized and quantified by means of Bode plots, a log-log plot of the filter transfer functions magnitude $|\chi_{\mathrm{FC}}|$ and a lin-log plot of the filters phase $\arg \chi_{\mathrm{FC}}$.

The line width κ_{FC} is in this context referred to as the corner frequency of the filter cavity, where

$$\chi_{\mathrm{FC}}^{(1)}(\omega = \kappa_{\mathrm{FC}})| = 1/2 = -3\,\mathrm{dB}, \text{ and} \tag{5.11}$$

$$\chi_{\mathrm{FC}}^{(2)}(\omega = \kappa_{\mathrm{FC}})| = 1/4 = -6\,\mathrm{dB}. \tag{5.12}$$

Above the corner frequency the first (second) order reduces amplitude noise by $1/100 = -20\,\mathrm{dB}$ ($1/100^2 = -40\,\mathrm{dB}$) per decade, which is depicted in figure 5.4 for the two configurations of our specific filter cavity in each, single and double pass.

To get strong suppression of classical laser noise at frequencies above 500 kHz, a high finesse filter cavity with small line width of $\approx 50\,\mathrm{kHz}$ is needed, ideally operated in double pass configuration.

Realization of the filter cavity

The filter cavity used in this experiment is a three-mirror cavity (see figure 5.5) consisting of two plane mirrors that are rotated by 45° with respect to the straight line defined by the incoming and outgoing light. These mirrors build up the short side of an isosceles triangle with the waist of the cavity being between them. The third (end) mirror is placed further away and is almost hit under normal incidence.

The plane mirrors are fixed to a spacer made of a single block of Invar, which is a nickel-iron alloy that features an exceptionally low

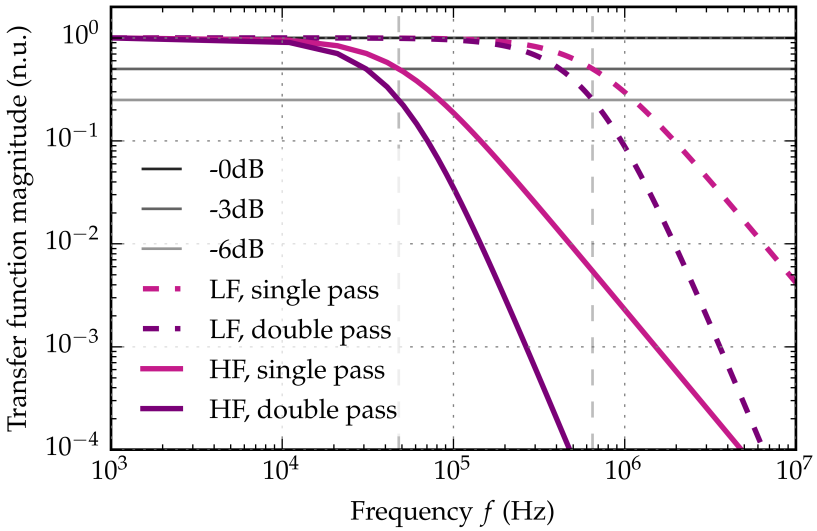

Figure 5.4: Filter cavity transfer functions. Performance of a single pass (first order) and double pass (second-order) filter cavity in low finesse and high finesse operation with corresponding line widths (corner frequencies) of $\kappa_{\mathrm{LF}} = 650\,\mathrm{kHz}$ and $\kappa_{\mathrm{HF}} = 48\,\mathrm{kHz}$ of our actual filter cavity, marked as dashed grey lines. The single pass traces (pink) yield $-3\,\mathrm{dB}$ noise reduction at the respective corner frequencies, while the double pass traces (purple) achieve $-6\,\mathrm{dB}$. We aim for high finesse double pass operation for correlation measurements, as we then hit the shot noise level at around 500 kHz (see figure 5.6), far below the membrane modes we are interested at ($\geq 1\,\mathrm{MHz}$).

thermal expansion coefficient $\alpha_{\mathrm{invar}} = 1 \times 10^{-6}\,\mathrm{m/K}$ around room temperature. This choice reduces the length noise due to thermal fluctuations and therefore the frequency noise significantly (see equation 5.8 from the discussion of phase noise). Additionally, the end mirror is held by an adjustable mount to properly align the cavity mode. In fact, the mirror is glued to a piezo which can be used as an actuator for fast length stabilization of the filter cavity with respect to the laser source. The cavity itself is stiff and relatively light, to be able to easily follow the input signal for length stabilization. The cavity foot is massive and placed on a vibration isolating rubber sheet, following a heavy and weak design rule to be more insensitive to incoming vibrations from the optical table and surroundings. Additionally, as there are many acoustic noise sources in the laboratory, a surrounding box out of acoustic isolating foam is built around the filter cavity.

The end mirror is highly reflective and curved for cavity stability (1 m radius of curvature), whereas the coatings of the plane mirrors are polarization dependent. Therefore by changing the input polarization with a $\lambda/2$ waveplate placed directly in front of the filtering

PARAMETER	SYMBOL	VALUE
Power reflectivities (nominal)	$R_{\mathrm{in/out}}$	99.97 % max.
	R_{end}	99.99 %
Radius of curvature	$\mathrm{RoC}_{\mathrm{end}}$	2 m
Cavity waist size	w_{FC}	500 µm
Round trip length	L_{FC}	60 cm
Free spectral range	$\omega_{\mathrm{FSR}}/2\pi$	500 MHz
PARAMETER AND SYMBOL	**LOW FINESSE**	**HIGH FINESSE**
HWHM, $\kappa_{\mathrm{FC}}/2\pi$	650 kHz	48 kHz
Finesse, $\mathcal{F}$	380	5200
Single pass transmission*	505 mW	306 mW
	63.6 %	38.2 %
Double pass transmission*	300 mW	105 mW
	37.7 %	13.1 %

Table 5.1: Filter cavity parameters. Measured and partly taken from [33, 70]. The asterisk marks power transmission measurements retaken at a later stage, after carefully cleaning the filter cavity mirrors in situ. Preceding was a continuous degradation of the power transmission with time, likely caused by outgassing of the glue used to fix the end mirror of the filter cavity and which subsequently laid down on the highly reflective coating causing additional internal losses. The transmissions are measured with respect to 800 mW incoming laser power.

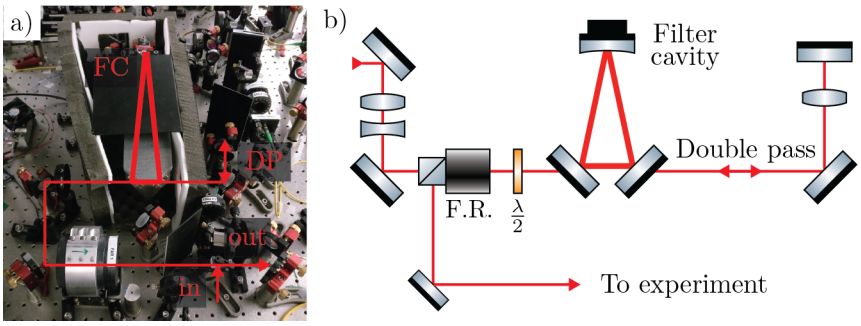

Figure 5.5: Illustration of the filter cavity. a) Photo of the filtering cavity (FC). The Invar spacer building the three mirror optical cavity is covered by acoustic noise absorbing foam, as noise sources from all over the laboratory can affect the performance of the FC. b) Schematic of the FC A set of lenses and mirrors is used to mode match the incoming laser light onto the cavity mode. A Faraday rotator is splits up the incoming light from the returning mode from the FC. A $\lambda/2$ waveplate can switch between high and low finesse operation. The light transmitted (single pass) through the FC is focused onto a mirror, which throws the mode back onto the FC, effectively turning the FC into a second order optical low pass filter.

cavity, one can switch between the high finesse (small line width) and low finesse (large line width) mode (see table 5.1 for all parameters).

Low finesse operation is useful for daily operation, alignment and characterization of most experimental parameters, since the stabilization of the cavity length is easier for larger line widths (see noise noise performance at low frequencies in figure 5.6) and more laser power is available in transmission, as shown in table 5.1.

The main feature of high finesse operation is the small band width of around 50 kHz, which we exploit to filter classical laser noise at sideband frequencies above its line width.

The laser output is first transmitted through a Faraday isolator to reduce possible back-reflections from the filter cavity, which could distort the laser functionalities or even damage the laser. Afterwards a set of lenses and mirrors are used to mode match the incoming laser light to the filter cavity. In single pass transmission of the cavity we use another adjustable mirror and lense to focus the transmission onto a plane mirror with high reflectivity. This highly reflective mirror, if placed in the focus of the lens, throws back the mode, which is still resonant with the cavity. This allows us to use the FC in double pass configuration, which effectively transforms the FC into a second order low pass filter for classical laser noise.

A careful characterization of the amplitude and frequency noise in transmission of the filtering cavity is given by Jason Hölscher [70]. In short, the filtering effect of the cavity in high finesse and double pass configuration is sufficient to push the classical laser amplitude noise well below the shot noise: Amplitude noise is shot noise limited at frequencies above 500 kHz and already deeply reduced by the $1/\omega^2$

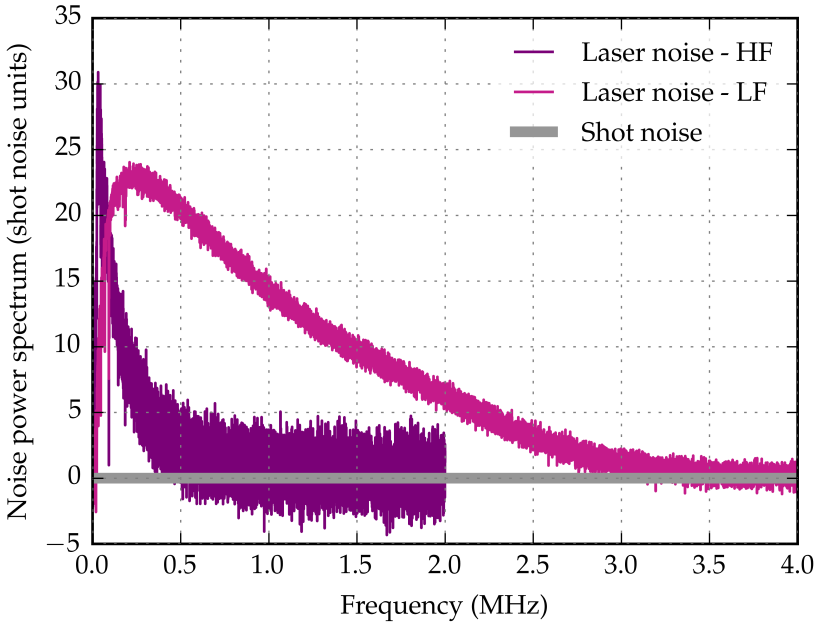

Figure 5.6: Filter cavity noise performance. Noise measurements in double pass configuration. A balanced detector scheme is used, where each photodetector detects 5 mW optical power. The subtracted signal yields the shot noise of the light (grey line) and the sum yields the classical amplitude noise, which is here given in units of shot noise. While low finesse operation yields a shot noise limited light mode at frequencies above ≥ 3 MHz, high finesse operation already hits the shot noise floor at ≥ 500 kHz in accordance with figure 5.4 and far below the membrane modes we are interested in, at frequencies above > 1 MHz. Note, however, that the high finesse operation does end up increasing low frequency noise at frequencies below ≤ 50 kHz, which is likely due to the imperfections of the cavity length stabilization.

behavior of the double pass filter at 1 MHz. Note, that the filtering cavity needs to be carefully locked on resonance, such that incoming frequency noise is not turned into amplitude noise in transmission of the cavity. The operation of the filter cavity ensures a shot noise limited laser drive of the optomechanical cavity at sideband frequencies of our mechanical oscillators and for typical input powers to reach the strong cooperativity regime.

5.4 CREATION OF A DETUNED SECONDARY LASER BEAM

To be able to characterize the parameters of the quantum cooperativity independently, we partly rely on radiation pressure sideband cooling of the membrane motion or on optomechanically induced transparency (OMIT) to determine the single photon coupling strength g_0. To perform such measurements, one ideally would need a second laser with independent frequency detuning relative to the main laser and a fixed phase relation. We chose to generate this second beam

(the so called cooling beam) from our initial laser system (with the first beam being called the signal beam) via the following approach.

Step 1: Sideband modulation. A fraction of the main laser light is split by a half waveplate and a polarizing beam splitter. The light is coupled into a single mode polarization maintaining fiber and then propagates through a GHz electro optical phase modulator (EOM), which is used to modulate the beam with roughly one free spectral range of the optomechanical cavity, e.g. $\omega_{\mathrm{cool}} \approx \omega_{\mathrm{FSR}} \approx 2\pi \times 30\,\mathrm{GHz}$.

Step 2: Sideband extraction. Fiber coupled EOM's have a large modulation depth and get a significant amount of the carrier into the sidebands, at the cost of higher order sidebands, such that sidebands at integer multiples of $\pm\omega_{\mathrm{cool}}$ are generated (compare with equation 5.7). We want to extract one of the first order sidebands. This is achieved by a free space broadband filter cavity. The requirements on the filtering cavity are relaxed due to prefiltering the light by a free space volume holographic grating and the large modulation frequency (free spectral range of the optomechanical cavity), such that $\kappa_{\mathrm{cool}} \ll \omega_{\mathrm{cool}}$ is easily achieved by a short cavity, consisting of two mirrors directly glued on a ring piezo, which is used to lock the cavity length to the laser frequency.

Step 3: Additional functionality. After the generation and extraction of the so called cooling beam, it is coupled into a second GHz modulator. This allows for the generation of new modulation sidebands, e.g. for producing an error signal for the optomechanical cavity, or MHz sweeps for mapping the cavity line width or optomechanical induced transparency. It is also possible to apply GHz sweeps for scanning a full free spectral range of the optomechanical cavity for mode matching and alignment purposes. The main purpose of the cooling beam is sideband cooling for determining the optomechanical coupling strength g_0, through carefully choosing the first modulator modulation frequency to be red detuned with the optomechanical cavity, e.g. $\omega_{\mathrm{cool}} = \omega_{\mathrm{FSR}} - \omega_m$.

Step 4: The cooling beam is being re-united with the signal beam on a polarizing beam splitter. It has a set of lenses and mirrors such that it can be matched to the signal beam and the optomechanical cavity. The separation of one free spectral range and the choice of perpendicular polarizations for the signal and cooling beam ensures that no parasitic effects between both beams occur.

The schematic of the generation of the secondary cooling beam that is phase coherent with the signal beam and its implementation is depicted in figure 5.7. Among other applications, we shall make use of this beam for sideband cooling and optomechanically induced transparency measurements for the characterization of the optomechanical cavity as described in chapter 9.

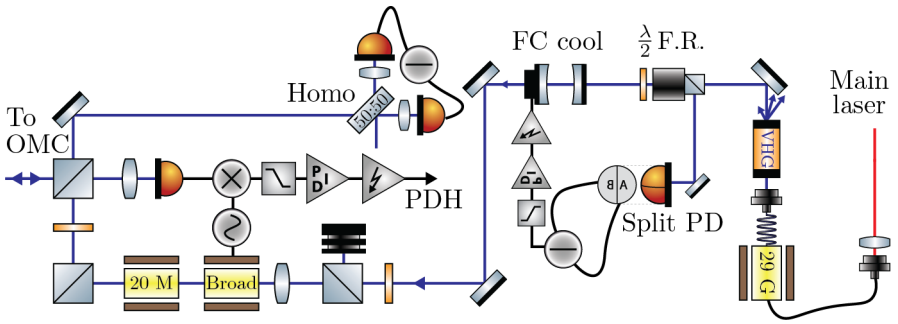

Figure 5.7: Generation of the cooling beam. Some part of the filtered light from the main laser source is being separated (red) and coupled into an in-fiber electro optical phase modulator (EOM), which is deeply modulating the light with approximately one free spectral range of the optomechanical cavity. The goal is to filter a single first order sideband that is phase coherent with the main laser and that can be used for several applications that need two-tone input, i.e. using one beam to lock the optomechanical cavity and use the second for characterizing the optomechanical coupling strength. The modulated light consists of the carrier and components of the first and higher order modes. By transmission through a volume holographic grating (VHG) a pre-filtering takes place due to displacement as a function of frequency. One first order sideband is then mode matched to a short linear cavity that is locked in transmission of the first order sideband, such that all other modes are reflected. This so called cooling beam can be used to lock the laser to the optomechanical cavity (20 MHz modulation for PDH lock), a broadband EOM can be used to sweep the beam for probing the cavity line width or for optomechanically induced transparency (OMIT) measurements and a homodyne detector for collecting data.

6 HOMODYNE DETECTORS

6.1 EXPERIMENTAL SETUP

Schematically, the core of homodyne detection lies in the interference at the beam splitter and the detection of its output ports by two detectors, see chapter 3.2 for reference. Experimentally, however, several additional components play a crucial role.

We will start with the preparations of the signals and local oscillators, continue with the alignment of the beams onto each detector and close with the processing of the DC and AC signals of the detectors.

The signal

The signal consists partly of the light directly reflected off the optomechanical cavity (OMC), that is, higher order modes due to the finite mode matching, the TEM_{00} mode partly reflected at the input coupler and the PDH locking sidebands at $\pm 20\,\mathrm{MHz}$ off-resonant with the OMC. The rest of the signal is generated within the OMC by the cavity field interacting with the membrane, starting at sideband frequencies of around 1 MHz.

A small fraction of the signal (usually $1 - 2\,\mu\mathrm{W}$) is split off and sent to the PDH detector to generate a locking signal. The rest of the signal beam ($< 50\,\mu\mathrm{W}$) is divided by a polarizing beam splitter (PBS) equally between the phase and amplitude detectors.

The local oscillator

For a proper homodyning signal, a strong and phase coherent beam is necessary. The local oscillator (LO) is taken from the same laser source after transmission through the filter cavity. The beam path is artificially extended to match the signal path length and is then reflected off a highly reflective mirror glued to a piezo. This piezo is used to adjust the relative phase between LO and signal. Typical LO powers are $> 5\,\mathrm{mW}$ per detector, therefore at least a factor of 100 larger than the signal.

Alignment cavity

Each homodyne detector needs to be aligned properly to maximize the interference between the two respective input beams. Therefore, the frequencies, spatial modes, polarization and propagation of the

signal and LO must match. The frequency is given by the common laser source and the polarization is cleaned by means of a PBS.

The alignment of the spatial modes and propagation is set by a three lens system in the returning signal and another lens system in the LO path. Additionally, each of the four inputs of the two detectors has a set of mirrors for mode matching purposes.

However, it is useful to not directly monitor the homodyne subtraction signal as there are too many independent degrees of freedom to be optimized. A reliable and easy way to align the detectors is by means of an alignment cavity. We incorporate a flip mirror after one of the beam splitter ports and send the light to a short linear cavity glued into a piezo. The piezo is scanned and all four beams are then aligned onto this alignment cavity while monitoring the mode matching of its fundamental resonance.

Beam splitter and detectors

To achieve an optimal subtraction of the individual detectors, it is crucial that the beam splitter is perfectly balanced. Note, that real beam splitter coatings aren't arbitrarily close to a 50/50 balancing. It is possible, however, to fine tune the balancing by incorporating the beam splitter onto a rotational mount, as the coating's reflectivity will be slightly dependent on the angle of incidence of the signals/local oscillators. This step has to be iterated with the step before.

After all beams and the beam splitter are aligned well, the positions of the detectors themselves should be optimized, as the beam could be chopped at the edges of the diodes. We use highly curved lenses to focus the beams onto the detectors, such that we can locate the beams well within the center of the diodes.

Diodes and electronic circuits

We use InGaAs diodes from Laser Components [3], optimized for high quantum efficiencies of $\geq$ 95 % and low dark noise levels, a large band width due to low capacities of $15 - 20\,\mathrm{pF}$ without a bias voltage and a diameter of 500 µm and an anti reflective coating with a power reflectivity smaller than 0.05 % for an angle of incidence around 20°.

The electronic circuit of the detectors has been designed and realized by Hannes Böhm within our group and details of the circuit boards can be found in his PhD thesis [33]. In short, the photocurrent is divided into a slow DC channel with roughly 30 kHz band width and a fast AC channel, where the low frequency component is blocked by a capacitor. The DC channels are used for locking and

will be discussed in chapter 7.6. The AC channel contains the small signals at sideband frequencies, which can be amplified by a transimpedance amplifier. Large gains are possible before saturating the electronics because of the absence of the large DC component. To achieve a decent subtraction by means of a large common mode rejection of classical laser noise, the detector characteristics such as gains and corner frequencies of filters has been matched as close to each other as possible.

Amplification and filtering

The subtracted signal is low pass filtered by two high order low pass filters with corner frequencies around 13 MHz to aggressively filter the Pound-Drever-Hall (PDH) modulation frequency at 20 MHz, without influencing the flat, shot noise dominated range containing the membrane signals. Otherwise, the PDH modulation can saturate the amplifier or limit the range and therefore the resolution of the data aquisition card (DAQ).

The filtered signal of each homodyne setup is being amplified by low noise variable gain high speed amplifiers from Femto [4] model DHPCA-100. A wide range of gain settings is important to take advantage of the full range of the DAQ for shot noise and dark noise measurements not featuring mechanical signals with a 40 dB signal to noise ratio.

The filtered homodyne signals can subsequently be fed into a spectrum analyzer to measure the noise power spectrum, or into the DAQ for the measurement of time traces.

6.2 DETECTOR CHARACTERIZATION

This section summarizes the results of optimally aligned detectors and the characteristics of the diodes.

The mode matchings of each signal and local oscillator onto the alignment can surpass 95 %. Then, the interference on the beam splitters needs to be characterized. This is done by closing one photodiode and choosing equal power for the incoming signal and local oscillator. By scanning the phase of the LO it is possible to measure the interference fringe (figure 6.1 a)) whose quality is describes by means of the visibility

$$vis. = \frac{V_{\max} - V_{\min}}{V_{\max} + V_{\min}}, \tag{6.1}$$

where $V_{\max}$ is the peak value of the fringe and $V_{\min}$ the voltage measured at the minimum. It is crucial to measure both values with respect to the actual zero of the closed detector, as a residual bias voltage would distort the visibility. Note, that for perfect interference and

equal power $V_{\text{min}} = 0$ and the visibility reaches 100 %. We regularly achieve visibilities of $> 92\,\%$, limited by the mode matching of the optomechanical cavity and the modulation depth of the PDH modulation, as the higher order modes and the modulation sidebands will be reflected directly at the optomechanical cavity and degrade the optimal interference at the beam splitters.

The subtraction of the individual photocurrents will strongly suppress classical amplitude noise as that noise is correlated in both outputs of the beam splitter and then subtracted. We quantify the common mode rejection by turning off the noise eater of the laser and measurements of the laser relaxation oscillation peak at frequencies of interest, namely around 1 MHz. Comparing the noise power spectra of the sum current (full classical laser noise) to the difference current (shot noise limited detection) yields the suppression of the relaxation oscillation peak, see figure 6.1 b). We achieve common mode rejections of at least 45 dB which is roughly a factor of $> 31\,000$.

Finally, figure 6.1 c) displays the frequency response of the detectors. Dark traces are shot noise measurements (no signal) and light traces are dark noise traces. The grey curve shows the spectrum analyzer dark noise as a reference. The spectrum is shot noise limited by one order of magnitude compared to dark noise starting at ≥ 500 kHz. The high pass at frequencies below 500 kHz is due to the splitting of AC and DC detector channels. Moreover, the spectrum is flat at membrane mechanical frequencies of above 1 MHz. Both detectors show the same characteristics, which is important to equally measure the phase and amplitude quadrature of the light.

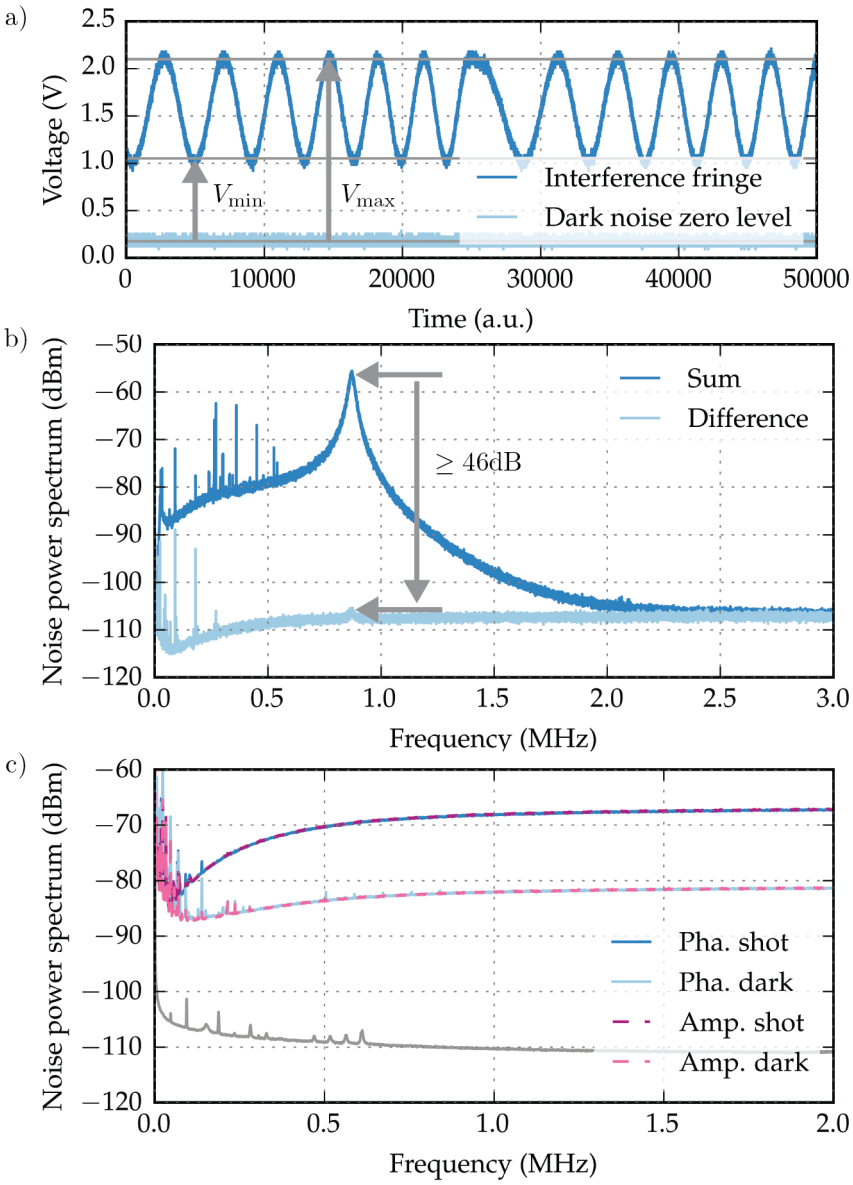

Figure 6.1: Homodyne detector characterizations. a) Homodyne visibility measurement. A visibility of only $\approx$ 42 % for visualization purposes. b) Common mode rejection. Measurement of the laser relaxation oscillation peak for the sum and difference measurement of the local oscillator (5 mW per detector). This equals the suppression of classical laser noise by the balanced detection scheme. c) Noise power spectrum for shot noise and dark noise measurements. Flat and equal shot noise limited detection for both detectors above membrane resonant frequencies of $\geq$ 500 kHz (see main text for details).

7 CAVITY LOCKING SCHEMES

From the beginning of the thesis, we assumed to have stable lasers and optical cavities, e.g. fixed cavity resonance frequencies. We also studied the behavior of the linearized optomechanical interaction for different and stable detunings of the laser with respect to the optomechanical cavity and even when speaking of our homodyne detection scheme, we assumed to be able to have a fixed relative phase between the signal and the local oscillator.

Real systems in the laboratory, however, are subject to a manifold of external noise sources from the vibrations of the ground floor, acoustics, electronic noise, thermal drifts and many more. Therefore it is highly nontrivial to have stable references or stable relative phases of different beams on the optical table.

In this chapter we will provide a short explanation on how feedback control systems are appropriate to measure the deviations from a chosen setpoint and how to adequately manipulate this signal to create a so called error signal, which can be fed back into an actuator to stabilize the system around its setpoint. Here, I use and recommend the books by Saulson [111] and Abramovici [17], since both are on point fast track guides for scientists, not familiar with feedback control theory and offer applications in optics.

The most important locking schemes used within this experiment are described, focusing on the lock of the filter cavity, the optomechanical cavity and the two homodyne detectors.

7.1 FEEDBACK CONTROL SYSTEMS

Feedback control systems are used to stabilize a parameter to a known and desired reference. This happens by means of a feedback control loop (FCL), as depicted in figure 7.1. A description of the main components of a FCL and its operation is following. We will make use of the notations used in [17].

- The plant is the system whose output parameter we want to control. Initially, the output is the sum of its free-running output and any disturbances coupling into the signal, e.g. drifts and fluctuations.
- The sensor is used to detect the plant's output, usually by generating some sort of voltage. Note, that it is desirable that the sensor produces a signal linear to the plant.

- The detected signal is inverted and compared to a known reference value. This produces the so called error signal, which is a measure of the deviations of the system that need to be corrected.
- The controller is used to manipulate the error signal by appropriately filtering and amplifying the error signal.
- The actuator is the component that can effectively act onto the plant and influence its output.

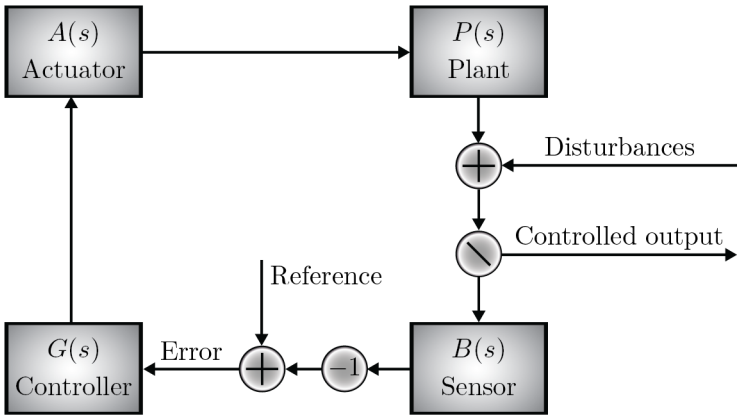

Figure 7.1: Feedback control systems. Basic schematic to control the output of the apparatus of interest, the plant, that is suffering from disturbances. A part of its output is detected by the sensor, which compares the inverted output with the desired reference, yielding the error signal. The controller is appropriately manipulating the error signal, such that it can be fed into an actuator that is able to correctly influence the plant's output. A typical plant is a cavity whose output is monitored by a photodetector. The error signal is shaped within a PID controller and fed into a piezo that can actuate the length and therefore the frequency of the cavity with respect to the input laser frequency.

If the signal of the sensor is very close to the reference, the error signal diminishes and the plant's output is close to the desired reference. However, if the plant's output is disturbed, an error signal proportional but inverted with respect to the disturbance is produced and used to bring the plants output closer to the reference. Note that we simplified the full system by leaving out additional noise sources that can enter at each of the other components. We also neglected the fact that the inputs and outputs of each component might have different unit, which needs to be taken into account when setting up a control loop.

The theory on feedback control systems is usually treated by means of Laplace transformations of the transfer functions of each component of the loop, whereby the involved equations are transformed to simple algebraic equations. We denote the transfer functions of the

components as $B(s), G(s), A(s), P(s)$, in accordance with figure 7.1, and the complex Laplace coordinate $s = \sigma + i\omega$, while $\omega = 2\pi\omega$ is the angular frequency. The transfer functions provide the output signal (voltage) for a given input signal and are therefore denoting the response of each component for a signal at a given frequency.

The function

$$L(s) = B(s)G(s)A(s)P(s) \tag{7.1}$$

is the so called open loop transfer function. It is the answer to the question, what the full loop will do to a given disturbance, and it needs to be shaped in a desirable way, e.g. amplified to increase the error signal within some bandwidth and low pass filtered to cut off high frequency contribution that would for instance excite resonances of the actuator and therefore introduce instabilities of the loop.

It can be shown [17] that the ratio of the sensors output voltage and the reference voltage, the so called closed loop transfer function, is given by

$$\frac{v_{\text{sensor}}(s)}{v_{\text{reference}}(s)} = \frac{L(s)}{1 + L(s)}. \tag{7.2}$$

In case of high open loop gains $L(s) \gg 1$, the closed loop transfer function becomes unity. The intuitive picture is that the controlled output of the plant is following the given reference or, in other words, the plant output is locked to a stable reference signal.

7.2 BASICS ON THE STABILIZATION OF OPTICAL EXPERIMENTS

In optical experiments, such as interferometers or high finesse resonators, we are mainly interested in controlling the length and therefore the resonance frequency with respect to the input laser frequency, or vice versa. These are our plants which are subject to external disturbances, such as thermal drifts in the laboratory, acoustic noise or vibrations of the surroundings. Photodiodes serve as our sensors and read out the light returning from the cavities and convert the signal into a voltage. The error signal is further shaped by means of an FPGA based PID box and its amplified output voltage is then sent to the actuator, usually divided into: a) Peltier elements on laser crystals or cavity spacers to account for slow but large drifts due to temperature drifts in the laboratory on the order of $\leq 5\,\text{Hz}$ b) Piezo-electric transducers on mirror mounts to change the path, cavity and/or laser crystal length with a large bandwidth $\approx 10\,\text{kHz}$.

The missing ingredient is the generation of an appropriate error signal, which should be linear to deviations from the reference, e.g. linear to an unintentional detuning between the light frequency and

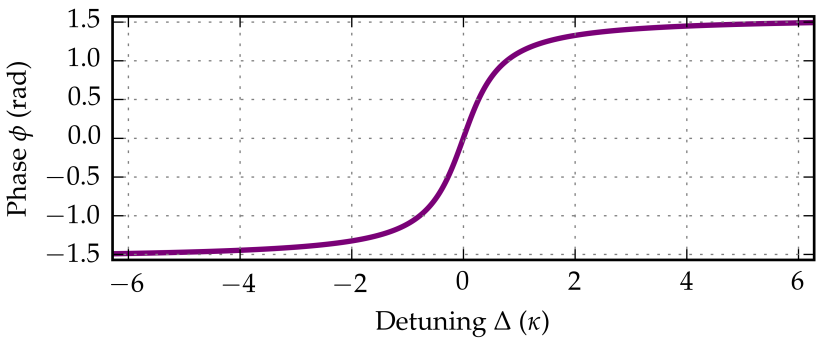

Figure 7.2: Phase in reflection of a cavity. Phase shift $\phi(\Delta)$ as function of detuning with respect to the cavity resonance, equation 7.3. The detuning Δ is given in units of cavity line widths κ. The phase has a zero-crossing and sign flip at the cavity resonance and produces a linear signal for small detuning. It fulfills all necessary features that are needed for an error signal. Note, that a second beam far off from resonance is needed as a stable reference. Stable means in this context, that it does not change its phase for a small detuning, such that it can be used to measure the phase of the resonant beam of interest.

the cavity resonance and also featuring a sign flip to discriminate between lower or higher frequencies (lengths). Note, that the resonance itself is symmetric and simply measuring the reflected power will not provide any information about a positive or negative detuning.

We want to consider the phase of the light reflected off an optical cavity, which is given by the argument of the optical transfer function (equation 2.51)

$$\phi(\Delta) = \arctan\left(\frac{\Re(\chi_{\text{opt}})}{\Im(\chi_{\text{opt}})}\right) \approx \arctan(2\Delta/\kappa) \approx 2\Delta/\kappa - \frac{1}{3}(2\Delta/\kappa)^3 + \cdots , \tag{7.3}$$

where we assumed only small losses within the cavity $\kappa_{\text{ex}} \approx \kappa$ and used the Taylor series of the arctan for small detunings.

Therefore, the phase of the light reflected off a cavity accumulates a phase linear to the detuning Δ and with a sign flip around the resonance $\Delta = 0$, which is fulfilling our requirements for an error signal.

Largely detuned light modes, e.g. light modes far off from the cavity resonance, are insensitive to small detunings, since the arctan flattens for large positive (negative) values at $+\pi/2$ ($-\pi/2$), see figure 7.2.

To be able to measure the phase $\phi(\Delta)$, a stable reference is needed. However, we just found that modes far off from resonance are insensitive and therefore appropriate to be used as such a reference.

The following sections describe the different locking schemes, mainly distinguishable by the source of the stable reference for the generation of the error signal.

7.3 POLARIZATION LOCK OF THE FILTER CAVITY

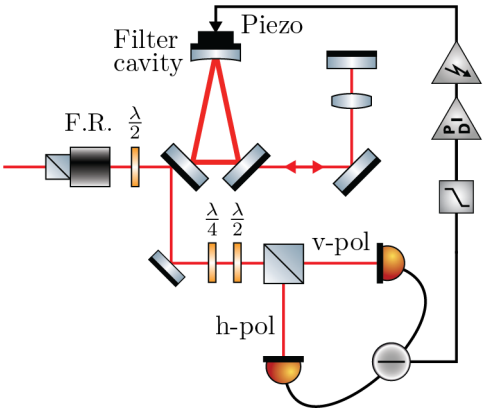

Figure 7.3: Polarization lock setup used to lock the filtering cavity. Consider operation of the filter cavity in h-polarization. The polarization of the incoming beam is slightly wrong, such that a residual amount of light in v-polarization (far from resonance) is reflected. The dispersion-shaped error signal (phase of the h-pol. light in reflection of the cavity) can be measured with respect to the light in h-polarization. This is done by splitting the polarizations at a polarizing beam splitter and taking the difference of the individual photocurrents. The error signal is filtered and amplified and then fed back onto the piezo which can move the end-mirror of the cavity and stabilize its resonance onto the frequency of the incoming laser light.

The filtering cavity has two modes of operation, the low and high finesse modes as described in section 5.3. The operation mode is chosen by the polarization of the incoming light, let's say horizontally polarized (h-pol). The cavity itself is highly birefringent, such that the vertically polarized (v-pol) light is off-resonant and can be used as a phase reference for the generation of an error signal as described by equation 7.3, to follow the laser frequency.

This method goes back to the work of Hänsch and Couillaud [65] who showed that by using this method a dispersion-shaped error signal can be generated with a zero-crossing and sign flip around the resonance.

Such an error signal can be retrieved by splitting the horizontally and vertically polarized contributions of the reflected light at a polarizing beam splitter and the detection of each polarization by means of a photodiode. The full setup is depicted in figure 7.3 and figure 7.4 shows a a measurement of the difference and sum currents for a scan of the cavity length by one free spectral range. While the sum current features the total power reflected off the cavity, the difference current

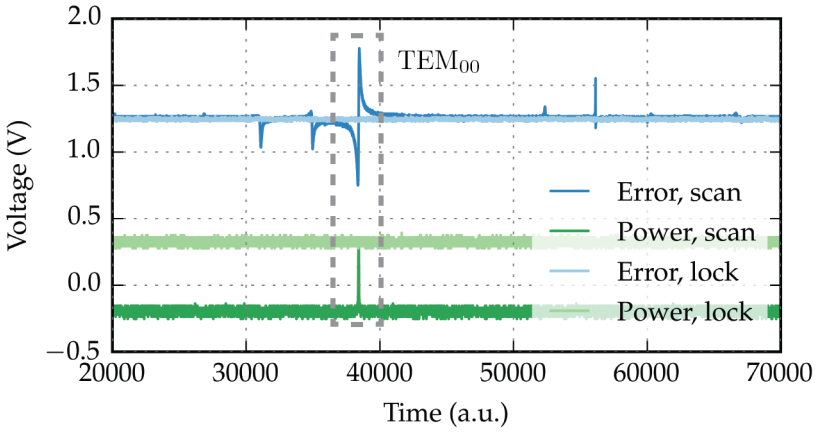

Figure 7.4: Polarization lock of the filter cavity. Opaque traces depict scanned data and light traces feature the running control loop. The error signal (blue) features a steep linear slope with a zero-crossing around the resonance (green). Turning the stabilization on will keep the error signal at zero and the power level on the maximum of the resonance (dashed grey box). Note, that our PID electronics working point has an offset of 1.25 V, which is our imaginary *zero* level.

features the dispersion-shaped error signal, which can be used to stabilize the filter cavity by means of a feedback control loop. The error signal is manipulated by a PID controller to appropriately shape the open loop transfer function and find suitable trigger conditions for the cavity mode we want to lock on. The output of the PID is amplified and then fed back into the piezo, which is controlling the length of the filter cavity, such that it follows the laser frequency.

Choosing the correct setpoint of the error signal and therefore matching the zero-crossing of the error signal with the cavity resonance is crucial, such that residual frequency noise is not converted into amplitude noise in transmission of the filtering cavity, as has been discussed in chapter 5.2. After successfully locking the filter cavity to the free-running laser, the filter cavity can passively filter classical laser noise of the laser due to its finite line width.

The major upsides of this locking scheme is that it does not rely on additional modulations of the light field and it is easy and cheap to design and build. However, the size and signal to noise ratio depends on the relative retardation (path length difference) between the different polarizations, which is given by the birefringence of the cavity and is not readily tunable. Also, the locking point itself is affected by low frequency classical laser noise, that is, the width of the error signal trace in 7.4.

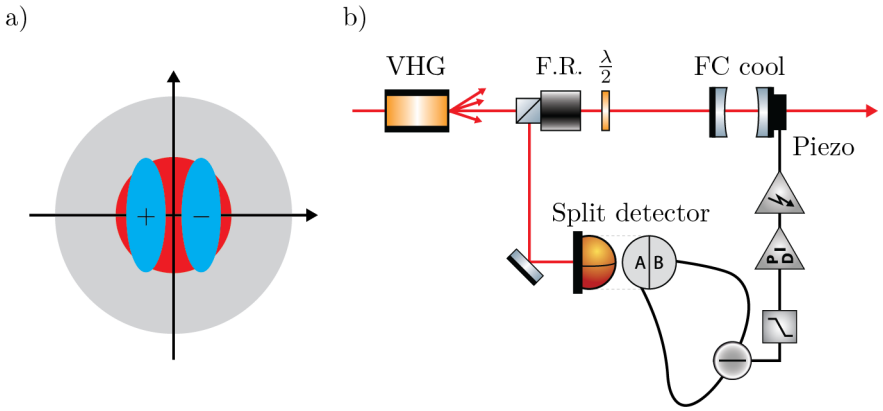

Figure 7.5: Polarization lock setup. b) Experimental scheme of the cooling beam filter cavity. The incoming light is strongly modulated with roughly one free spectral range of the optomechanical cavity ($\approx 29\,\mathrm{GHz}$) such that one of the first order sidebands need to be filtered from the carrier and several higher order sidebands, see chapter 5.4. A volume holographic grating (VHG) will do a pre-filtering by displacing the individual beams. The lock itself relies on a slight misalignment of the incoming beam, such that the TEM_{00} (red) and TEM_{10} (blue) modes hit a split diode (compare with a)). While the TEM_{00} is symmetric, the TEM_{10} features a zero-crossing and sign flip, such that taking the difference current will yield an appropriate error signal that can be fed into the piezo actuating the cavity length.

7.4 TILT LOCK OF THE COOLING BEAM FILTER CAVITY

A very similar error signal can be generated by using a higher order cavity mode as a stable phase reference [120]. This is possible because of the different Gouy phase of different Hermite–Gaussian modes.

We consider a resonant TEM_{00} mode and an off-resonant TEM_{10} mode due to a slightly misaligned incoming laser beam. Note, that the TEM_{00} has a symmetric electric field amplitude and a maximum at its center, while the amplitude of the TEM_{10} mode has a zero-crossing and a sign flip at the very same position. This is illustrated in figure 7.5 a) and the setup is depicted in figure 7.5 b).

The detection of the sum of both fields by means of a segmented photodiode yields the total reflected power of the light in case of the sum of the photocurrents, and a suitable error signal in case of the difference current. A measurement of these signals for the lock of the filter cavity used to filter and create the cooling beam for our experiment (see chapter 5.4) is depicted in figure 7.6. Note, that the abundance of modes comes from the fact that we strongly modulate the laser to create sidebands at roughly one free spectral range of the optomechanical cavity, but the strength of the modulation also creates higher order sidebands and the purpose of this filter cavity is to filter a single first order sideband by stabilizing the cavity to it and

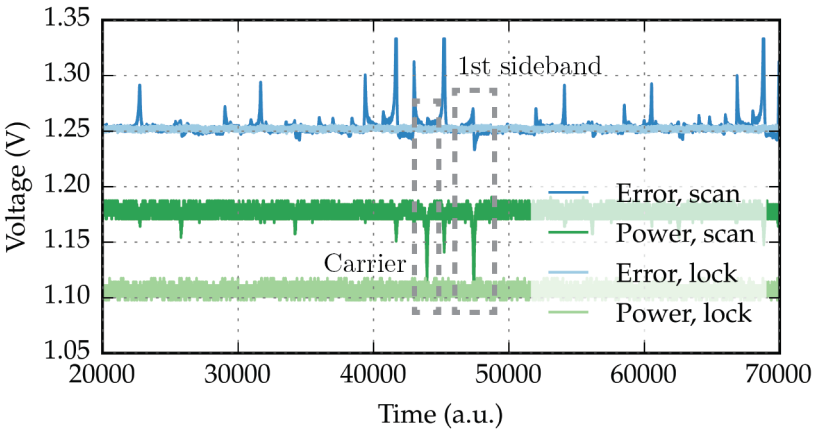

Figure 7.6: Tilt lock of the cooling beam filter cavity. The purpose of this filter cavity is to transmit the first sideband at the next free spectral range of the optomechanical cavity. The deep modulation of the carrier will create higher order sidebands, which explains the abundance of resonances and error signals. The carrier and the first sideband are marked by dashed grey boxes. Note, that the tilt lock alignment is optimized to feature a proper error signal for the sideband we are interested in. Opaque traces depict scanned data and light traces feature the running control loop. The error signal (blue) features a steep linear slope with a zero-crossing around the resonance (green). Turning the stabilization on will keep the error signal at zero and the power level on the maximum of the resonance. Note, that our PID electronics working point has an offset of 1.25 V, which is our imaginary *zero* level.

filtering all other (off-resonant) modes.

This so called tilt locking scheme is also easy to implement and does not rely on modulation sidebands as a reference. But it is strongly susceptible to changes of the alignment and beam pointing.

7.5 POUND-DREVER-HALL LOCK OF THE OPTOMECHANICAL CAVITY

The locking scheme used for locking the laser to our optomechanical cavity is the so called Pound-Drever-Hall lock [49], which is described in detail by E. Black in [31, 32]. The basic idea is to use a known phase modulation on the light field as phase reference.

An intuitive picture of the generation of the error signal is obtained by recalling the sideband picture of a phase modulation, figure 5.2 b) in chapter 5.2. After a quarter oscillation period of the modulation frequency, both sidebands will be collinear with the carrier along the real axis, but feature opposite signs. For a carrier ecaxtly on cavity resonance, bot sidebands will have the same magnitude and the interference of all beams will cancel out, providing a zero-crossing at

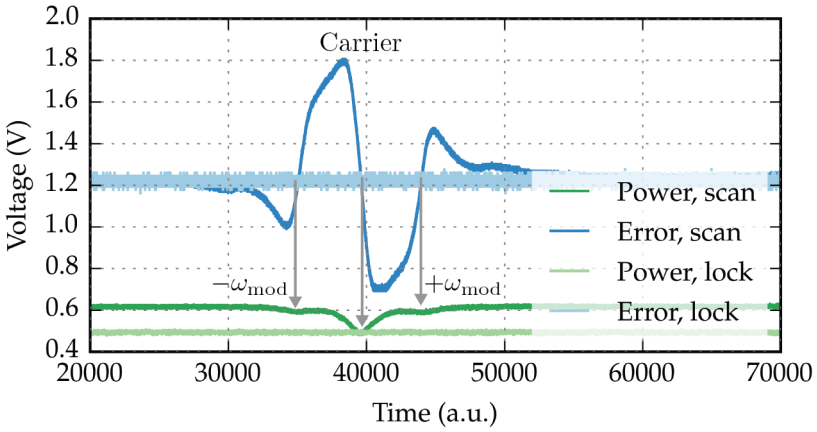

Figure 7.7: Pound-Drever-Hall lock of the optomechanical cavity. Opaque traces depict scanned data and light traces feature the running control loop. The modulation sideband frequencies in the error and power signals are depicted by grey arrows. The error signal (blue) features a steep linear slope with a zero-crossing around the resonance (green). Turning the stabilization on will keep the error signal at zero and the power level on the maximum of the resonance (note, that the signal of the PDH detector is inverted). Note, that our PID electronics working point has an offset of 1.25 V, which is our imaginary *zero* level.

resonance. A slight detuning in any direction will produce a signal linear in detuning, but with different signs and therefore a signal that is eligible for use as an error signal.

The technical setup is shown in figure 7.8 and consists of an electro optical phase modulator (EOM), a photodiode measuring the reflected carrier and both sidebands and generating a high frequency signal and a mixer, where the diode signal is mixed with the modulation frequency with a correct phase setting, basically filtering the frequency components around the modulation frequency and swapping it to low sideband frequencies around DC, which are appropriate to drive a piezo. This signal can be filtered by PID electronics and needs to be low pass filtered to remove high frequency components from the mixing process. Afterwards the signal can be fed back into the laser, forcing the laser beam to resonate with the optomechanical cavity. Note, that the very same signal can be used to stabilize the cavity length to the laser frequency. However, for stability reasons, we decided to remove all moving parts from the optomechanical cavity which needs to be placed within a cryostat that can introduce mechanical instabilities. Therefore, we use the laser piezo for a fast control of the laser frequency onto the optomechanical cavity.

Figure 7.7 features measured power and error signals for the Pound-Drever-Hall technique. This technique relies on modulation sidebands (in our case at $\pm\omega_{\mathrm{mod}}/2\pi = \pm 20\,\mathrm{MHz}$, which is one or-

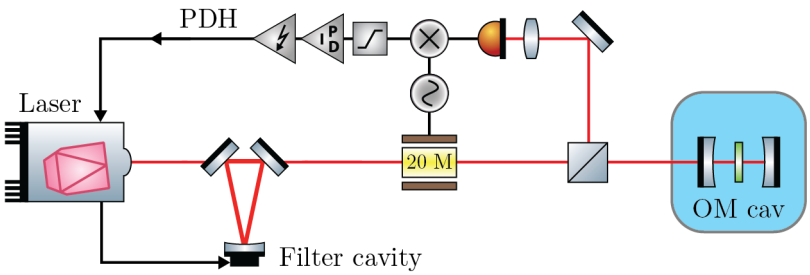

Figure 7.8: Pound-Drever-Hall locking scheme. The incoming light is modulated by the PDH modulation frequency (in our case 20 MHz), while the carrier enters the optomechanical cavity (OMC) on resonance, the modulation sidebands are far outside the cavity line width and reflected. A frequency jitter of the light or of the cavity length will detune the input mode from the cavity resonance or vice versa. Carrier light is reflected and the interference of it with the modulation sidebands produce the PDH error signal as described in the main text. After appropriately filtering the signal, it is used as a feedback signal onto the laser piezo, which then is stabilized to the optomechanical cavity length. The very same setup is also realized for the cooling beam, such that signal or cooing beam can be used to stabilize the laser, depending on the measurements one wants to take. Note, that the filter cavity is in between laser and the OMC and its length is stabilized to the laser frequency.

der of magnitude larger than the optomechanical cavity line width) and it gives us the possibility to adjust the demodulation phase and modulation depths to optimize the signal to noise ratio of the error signal. The error signal can also be used to determine the cavity line width, because the known modulation frequency can be used as a calibration for the x-axis of the traces shown in figure 7.7. Moreover, the generated signal can be very sensitive and indeed, oftentimes it is favorable to use the error signal for the optimization of the mode matching instead of the direct power of the reflected light. Ultimately, the PDH modulation is also used for the stabilization of the amplitude quadrature measurement, as we will be shown in the next section.

7.6 DC SUBTRACTION LOCK OF THE HOMODYNE DETECTORS

We conclude with the stabilization of the homodyne detectors. The homodyne detectors themselves rely on the interference of the signal and local oscillator fields. Scanning the phase of the local oscillator by means of a piezo leads to a sinusoidal swapping of the power between the two photodiodes. This interference fringe can be measured by splitting the photocurrent of the detectors by means of a slow DC channel and a fast AC channel. While the latter is used for the shot noise limited measurements of the mechanics, the DC channel (subtraction of the DC signals of the individual detectors) features the fringe. Note, that we intend to apply a dual-rail detection scheme

to simultaneously measure the phase and amplitude quadrature.

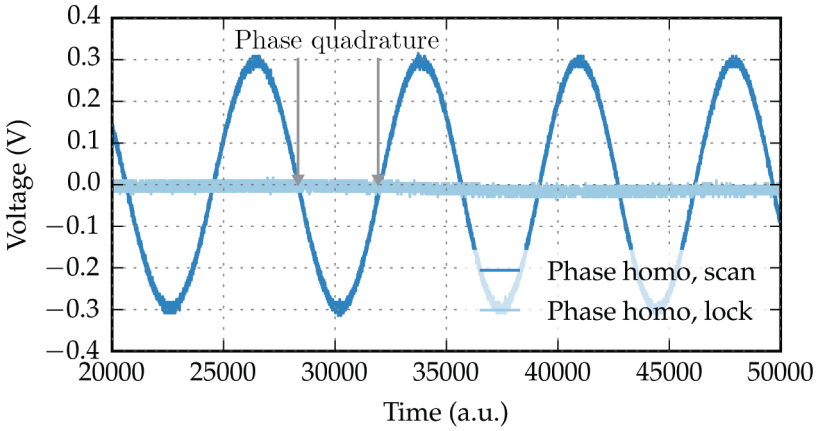

Figure 7.9: Phase homodyne stabilization. Depicted in opaque is the DC subtraction of the individual detectors. The zero-crossing of the fringe coincides with the phase quadrature (indicated by grey arrows), such that the signal can be readily fed back into the laser piezo setting the phase of the local oscillator. For comparison, the locked time signal of phase homodyne in light blue.

The phase quadrature is coincident with the zero-crossing of the interference fringe, see figure 7.9. Therefore, for small deviations around that position, the fringe singal can be approximated by a linear slope with sign flip around the phase quadrature which coincides with the zero-crossing. For that reason, this signal can be directly fed back to the piezo, thereby setting the phase of the local oscillator to stabilize the detector onto the phase quadrature.

The amplitude quadrature coincides with the maximum (or minimum) of the DC subtraction channels. To first order, there is no signal produced at all at these positions of the fringe. However, the signal beam also contains the Pound-Drever-Hall sideband, used for locking the optomechanical cavity in the first place. Therefore, the phase signal we are interested in is also contained around the sidebands at the modulation frequency, which are detected by the AC channels of the homodyne detectors. Hence, we split a part of the AC signal and demodulate it with the PDH frequency. This way, we can tune the modulation phase and generate an interference fringe that is appropriately shifted with respect to the DC subtracted fringe. Choosing the correct demodulation phase will create an interference signal with zero-crossing coinciding with the maximum (or minimum) of the DC subtracted light. This signal can be fed back to the piezo setting the local oscillator phase to hold the homodyne detector at the

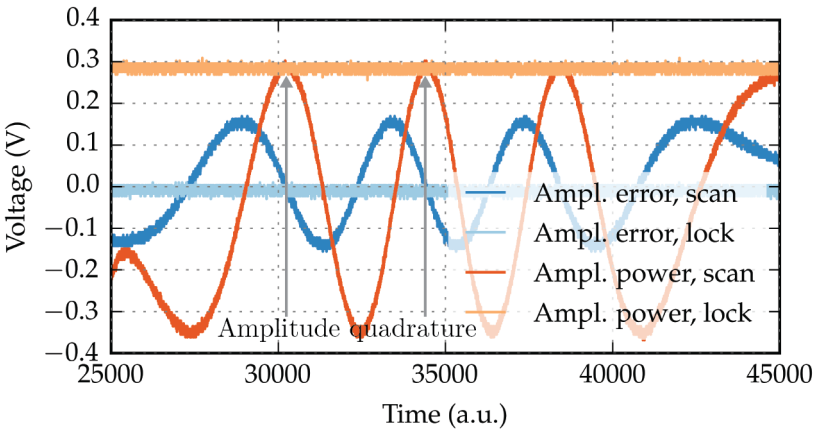

Figure 7.10: Amplitude homodyne stabilization. Dark orange features the direct subtraction of the individual detectors, while the amplitude quadrature coincides with the maxima of this trace (grey arrows). Mixing the AC subtraction of the detectors with the PDH modulation frequency and tuning the phase correctly, can yield the very same fringe shifted appropriately such that its zero-crossing coincides with the maxima of the DC subtraction (grey arrows). Using the error signal to lock around the zero-crossing (light blue trace) will keep the direct subtraction onto its amplitude quadrature (light orange curve).

amplitude quadrature at all times. Both signals are depicted in figure 7.10 to further illustrate the procedure.

Part IV

THE OPTOMECHANICAL SYSTEM

The field of cavity quantum optomechanics features a rich number of mechanical oscillators, spanning from kg mirrors at the advanced LIGO detectors [87], over µm-scale toroid microcavities on a chip [80, 123], to photonic crystal nano beams [41], photonic crystal "zipper" cavities [40], and cold atoms coupled to optical cavities [124].

In this work we focus on 100 kHz to several MHz micromechanical silicon nitride (SiN) membrane oscillators, which correspond to side lengths between 200 µm and 1.5 mm. Jack Harris discovered the exceptional mechanical and optical properties of commercially available[1] SiN membranes in 2008 [153] and moreover studied the optomechanical coupling of a membrane inside a Fabry-Pérot cavity [74].

This part contains the centerpiece of the experiment in this thesis: The micromechanical oscillator and the optomechanical cavity.

Chapter 8 starts by discussing the fabrication of SiN membranes and continues with their optical and mechanical properties. A description of the multimode nature of thin films follows, with special focus on the concept of effective mass. We continue with introducing the mechanical Q factor, which is the figure of merit for the mechanical performance of mechanical oscillators and enters the cooperativity via the mechanical dissipation rate γ. We continue with measurements of Q factors and discussions on the different loss channels limiting the mechanical performance. I present high Q factors of above 5×10^6 for a number of mechanical modes covering a broad frequency range by means of a phononic bandgap. The highest measured quality factor in our laboratories is as high as $Q = 34.2 \times 10^6$. Such Q factors are necessary to reach the strong cooperativity regime and these kind of phononic bandgap membranes are later used in correlation measurements presented in chapter 11

The chapter ends with a brief look at a more exotic material (within the field of optomechanics), which in principle offers the possibility for the fabrication of stacked membranes onto a Bragg mirror. Such a system can yield a dramatic increase of the effective optomechanical coupling strength.

Chapter 9 introduces the optomechanical system itself: A thin SiN membrane incorporated into a high finesse Fabry-Pérot cavity, i.e. the membrane in the middle cavity. The optomechanical coupling strength for that system is described for two different experimental realizations: First, the membrane being placed in the center the cavity. Second, the membrane being directly clamped on a flat end-mirror. The physical and experimental advantages of the latter configuration are discussed as well as its experimental realization. The cryogenic system is introduced, which is necessary to cool the thermal bath of the membrane as the average phonon number directly enters the cooperativity. A detailed presentation and discussion of all measurements for the characterization of the parameters that enter the cooperativity is given: The optomechanical coupling strength, the cavity line width, the mechanical decoherence as well as the mean number of photons. I show that the experiment is operating in the strong cooperative regime; the necessary condition for generating optomechanical entanglement in the presented setup.

1 Commercially available SiN membranes from Norcada Inc., www.norcada.com.

8 MICROMECHANICAL MEMBRANES

The goal of this chapter is to introduce silicon nitride micromechanical membranes and motivate why they are good candidates for the generation of multimode optomechanical entanglement.

I will first describe the material properties of silicon nitride and then combine these parameters with a model of a thin film to calculate the mechanical resonances of SiN membranes and compare them with experimental measurements. Afterwards, I continue with the optical properties of thin SiN membranes, which is the motivation to place them inside a Fabry-Pérot cavity instead of using them in an end-mirror configuration. The concept of effective mass follows, which describes the interaction of different mechanical modes with a Gaussian cavity mode. This concept is important as it replaces the physical mass in the optomechanical coupling strength.

The second part of this chapter is dedicated to the description of mechanical decoherence and losses, as well as the mechanical quality factor. The so called Q factor is the figure of merit to determine the mechanical performance of an oscillator. Q measurements for a large number of different membranes are presented and discussed, slowly converging to the optimal choice for the presented experiment: a trade-off between largest Q factors and reducing the number of mechanical modes that significantly interact with the cavity field. Phononic bandgap shields are introduced next, which provide large Q factors for a large amount of mechanical modes over a wide spectral range. The latter is necessary to bring the multimode optomechanical system into the strong cooperativity regime, a necessary condition for entanglement measurements as presented in chapters 10 and 11.

This chapter closes with a brief glance at InGaP membranes, which I had the chance to characterize and which in principle offer the possibility to fabricate a stack of membranes, thereby effectively increasing the coupling strength.

8.1 PROPERTIES AND FABRICATION OF HIGH STRESS SILICON NITRIDE FILMS

Over the course of this thesis the micromechanical oscillators of choice will be high stress silicon nitride (SiN) membranes, with varying thicknesses between 30 and 50 nm and side lengths from 250 to 500 µm. They are typically suspended in 200 µm thick and 5 to 10 mm wide silicon (Si) frames, as depicted in figure 8.1.

The technique to deposit thin SiN films on silicon wafers is called low pressure chemical vapour deposition (LPCVD) [77]. It is conducted at low pressures of approximately 375 mbar and high temperatures of around 820 °C, which features slow deposition rates and therefore uniform films. We are mainly interested in high stress (> 1 GPa) mechanical oscillators, which typically display high frequencies and low mechanical dissipation. High stress builds up when cooling the chip after deposition due to a mismatch of the thermal expansion coefficient of the Si frame and SiN in its stoichiometric composition (Si_3N_4).

Afterwards, a photoresist mask is applied to the backside of the chip and the desired shape of the membrane is etched through the resist via electron beam lithography (e-beam). Potassium hydroxide (KOH) is used to etch through the remaining Si layer to release the freestanding SiN window (compare with figure 8.1, bottom left).

The mechanical, optical and thermal parameters used over the course of this chapter are collected in table 8.1.

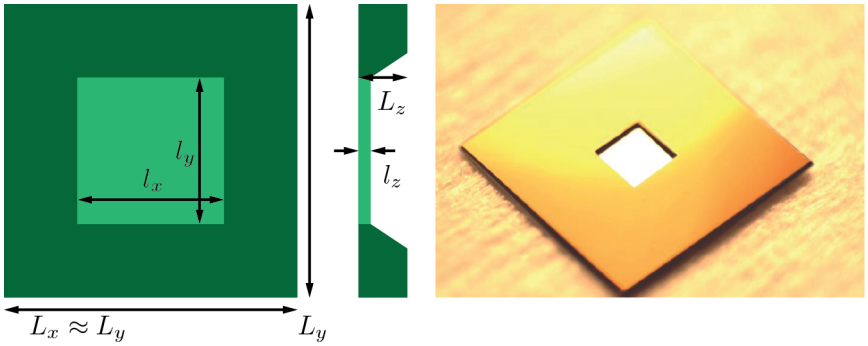

Figure 8.1: Schematic and photography of a SiN membrane. A top view and view through a cut at the middle of the membrane is depicted on the left side. Typical silicon frame dimensions $\{L_x, L_y, L_{th}\}$ are around $\{5\,\text{mm}, 5\,\text{mm}, 200\,\mu\text{m}\}$, while we focus on SiN windows with dimensions $\{l_x, l_y, l_{th}\}$ of up to $\{500\,\mu\text{m}, 500\,\mu\text{m}, 50\,\text{nm}\}$. The right side features a photography of a commercially available SiN membrane from Norcada Inc. [5].

8.2 OPTICAL PROPERTIES OF A THIN FILM

In addition to the fabrication process and mechanical properties of SiN membranes, we will now focus on the optical properties of thin SiN films to understand why they are suitable and how they can be incorporated into optomechanical experiments. Therefore, the goal of this section is to study the reflection, transmission, absorption and the refractive index of a thin SiN membrane.

We will make use of the transfer matrix approach [48] for a two dimensional thin film ($l_x, l_y \gg \lambda$, $l_z \ll \lambda$), which links the electromagnetic field amplitudes $E(0)$ and $H(0)$ at the front boundary of the membrane with the wavelength dependent refractive index $n(\lambda)$, to

MATERIAL PROPERTY	VALUE FOR SIN
Young's modulus, E (GPa)	$200 - 400$
Poisson ratio, ρ	0.27
Tensile stress, T (MPa)	$800 - 1200$
Densitiy, ρ ($10^3\,\mathrm{kg/m^3}$)	2.7
Index of refraction, n	2.011 at 1064 nm
	1.996 at 1550 nm
Absorption coefficient, k	1.5×10^{-4}
Thermal expansion coefficient, α ($10^{-6}\,\mathrm{m/K}$)	2.3
Heat capacity per unit volume, C_v ($\mathrm{J/m^3K}$)	710
Coeff. of thermal diffusion, D ($10^{-3}\,\mathrm{Wm^2/J}$)	9.29

Table 8.1: Material properties of SiN. Values extracted from [5, 56, 77, 90, 108, 125, 133, 141].

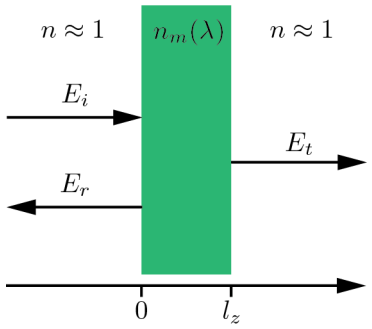

Figure 8.2: Reflection and transmission at a thin film. Side view of the membrane with thickness l_z and index of refraction $n(\lambda)$ surrounded by air/vacuum. The transfer matrix M links the incident (E_i) and reflected (E_r) field amplitudes at position 0 to the transmitted (E_t) field amplitude after passing the membrane via equation 8.1.

the transmitted fields $E(l_z)$ and $H(l_z)$ at position l_z, the rear boundary, via

$$\begin{pmatrix} E(l_z) \\ H(l_z) \end{pmatrix} = M \begin{pmatrix} E(0) \\ H(0) \end{pmatrix}, \tag{8.1}$$

with the transfer matrix

$$M = \begin{pmatrix} \cos\Delta\phi & \sin\Delta\phi/k \\ -k\sin\Delta\phi & \cos\Delta\phi \end{pmatrix}. \tag{8.2}$$

Here, $\Delta\phi = knl_z$ denotes the phase difference due to the SiN film and $k = 2\pi/\lambda$ is the wave vector of the laser light. The refractive index for wavelengths used in this work is $n \approx 2$, see references [90, 108] and table 8.1.

From equation 8.1 one can calculate the fraction of the incident amplitude field that is reflected off (transmitted through) the membrane, defined by the equation $r = E_r/E_i$ ($t = E_t/E_i$) to be [119]

$$r = \frac{(1/n - n)\sin\Delta\phi}{(n + 1/n)\sin\Delta\phi - 2i\cos\Delta\phi}, \tag{8.3}$$

$$t = \frac{-2in}{(n + 1/n)\sin\Delta\phi - 2i\cos\Delta\phi}. \tag{8.4}$$

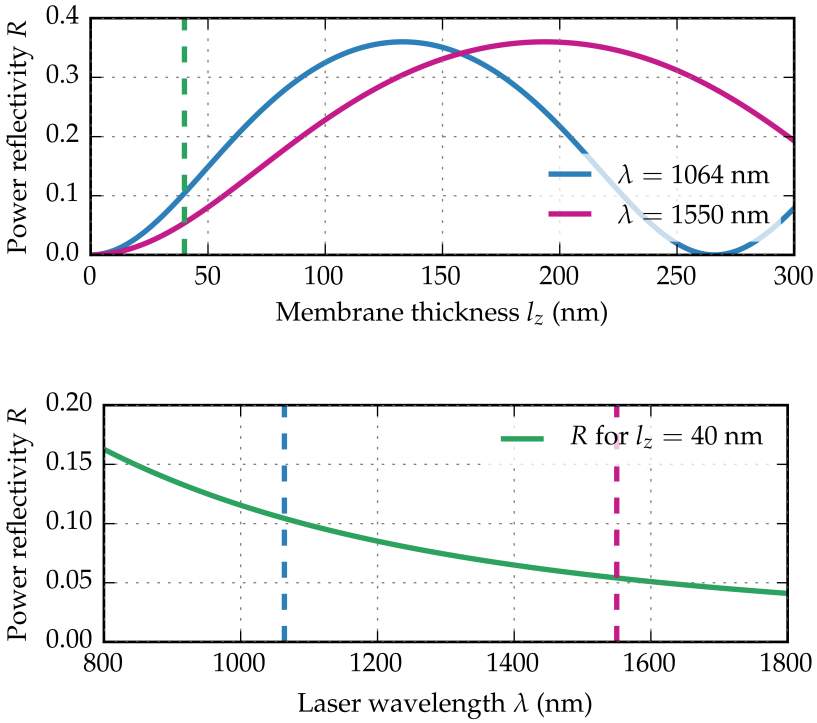

Figure 8.3: (Top) Power reflectivity as a function of membrane thickness for 1064 nm (Blue) and 1550 nm (Magenta). The maximum for each wavelength is located at $\lambda/8$ and reaches $\approx 0.37 = 37\,\%$. Typical membranes used in this work are typically 40 nm thick (Green dotted line) with power reflectivities $R_{1064} = 10\,\%$ and $R_{1550} = 5\,\%$. (Bottom) R in dependence of laser wavelength for a 40 nm membrane.

In the absence of absorption, the power reflection $R = |r|^2$ and transmission $T = |t|^2$ coefficients fulfill the relation $R + T = 1$. The power reflectivity R is depicted in figure 8.3 as a function of membrane thickness l_z (Top) and laser wavelength λ (Bottom). For typically used SiN membranes of thickness $l_z \approx 40$ nm the resulting power reflectivity at 1064 nm wavelength is only around $R_{1064} = 10\,\%$.

Because of their low reflectivities, SiN membranes are not suitable for use as an end mirror in a two-mirror optomechanical cavity. As we will see when we study the membrane in the middle configuration, strong coupling can be achieved when placing the membrane

inside a high finesse Fabry-Pérot cavity. This is indeed possible without spoiling the cavity finesse because of the low absorption rates [74, 144].

However, real membranes are never perfectly reflective or transmissive, i.e. some part of the light traveling through the substrate will be absorbed. An elegant way to consider absorption in the model is via the concept of a complex index of refraction $n \to n + i \cdot k$, in which n still indicates the phase velocity, and k, the absorption coefficient, indicates the amount of attenuation while traveling through the medium. The absorption of SiN is found to be very small, calculations in [56] indicate $k = 1.5 \times 10^{-4}$ and the absorption has been measured to be $6.9\,\mathrm{cm}^{-1}$ at 1064 nm in [125].

8.3 TRANSVERSAL MECHANICAL MODES OF A 2D MEMBRANE

In this section we will consider a thin membrane in the x-y plane and the aim is to study its transversal motion $u(x, y, t)$. This motion is described by an elastic wave equation [84]

$$\rho \frac{\partial^2 u}{\partial t^2} + \frac{E l_z^2}{12(1-\sigma^2)} \Delta^2 u = 0. \tag{8.5}$$

Here, Δ denotes the (two dimensional) Laplace operator, E, the Young's modulus, l_z is the thickness of the membrane and ρ is the Poisson ratio of the membrane. Considering the support of the membrane within its frame as the boundary condition (the frame is fixed), a set of solutions for a rectangular membrane can be found [84] as

$$u_{m,n}(x, y, t) = a_{m,n} \cos(\omega_{m,n} t) \sin(m\pi x / l_x) \sin(m\pi y / l_y), \tag{8.6}$$

$$\omega_{m,n} = \pi \sqrt{\frac{T}{\rho} \left(\frac{m^2}{l_x^2} + \frac{n^2}{l_y^2} \right)}, \tag{8.7}$$

with T as the tensile stress of the membrane, n and m as the so called mode numbers, the solutions $u_{m,n}(x, y, t)$ are the mode shape functions that are normalized to the maximum displacement and $\omega_{m,n}$ are the resonant (characteristic) frequencies of the membrane and the first mechanical resonances are depicted in figure 8.5. Note that in case of a square membrane $\omega_{i,j} = \omega_{j,i}$ are degenerate. Real membranes, however, are not perfectly symmetric thus these modes become quasi-degenerate. A comparison of a measured spectrum of a membrane and a fit to the theoretical model to this measurement is depicted in figure 8.4.

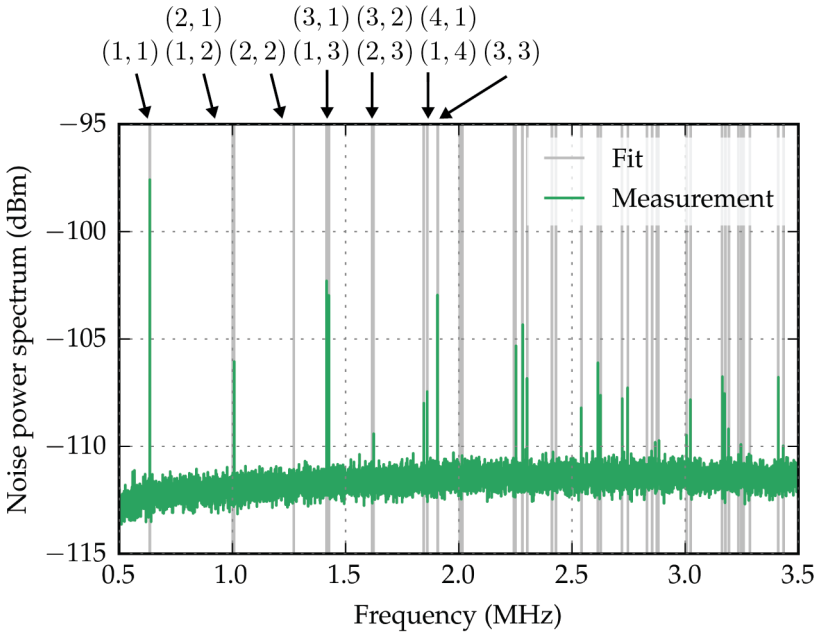

Figure 8.4: Comparison of a measured spectrum with the theoretical model of a square membrane. The noise power spectrum (NPS) of a Norcada Inc. membrane is measured by homodyne detection and is shown in green. Vertical grey lines show the resonance frequencies of the membrane fitted to the spectrum, as predicted by equation 8.7. The measured fundamental frequency is $\omega_{1,1} = 2\pi \times 635.7\,\text{kHz}$, the fitted fundamental resonance is $= 2\pi \times 635.6\,\text{kHz}$ and obtained by fitting the tensile stress $T = 540\,\text{MPa}$. The dimension mismatch between $l_x = 495\,\mu\text{m}$ and $l_y = 499\,\mu\text{m}$ is fitted to match the observed non-degeneracy of the $(1,2)$ and $(2,1)$ mode and the material parameters are as in table 8.1. All modes visible in the measurement, including the quasi degenerate modes, are well predicted by theory. The first eleven modes are marked by arrows. Note that some membrane peaks are not visible in the spectrum, which will be explained in the next section, when we investigate the effective mass of the membrane.

8.4 CONCEPT OF MODAL AND EFFECTIVE MASS

In the next chapter we want to study more deeply the equation of motion of a SiN membrane, therefore we will describe the membrane as a harmonic oscillator. Before doing that we need to carefully study the different concepts of mass.

Let us assume, for the moment, that the membrane moves uniformly in the perpendicular direction of its surface. In that case the mode function would simplify to $u(x,y) = 1$ and the mass of the membrane could be determined by integrating the mass density ρ over the volume of the membrane; this is the so called physical mass:

$$m_{\text{phy}} = \rho \int_0^{l_x} \int_0^{l_y} \int_0^{l_z} dx\, dy\, dz\, (1)^2 = \rho \times l_x l_y l_z. \tag{8.8}$$

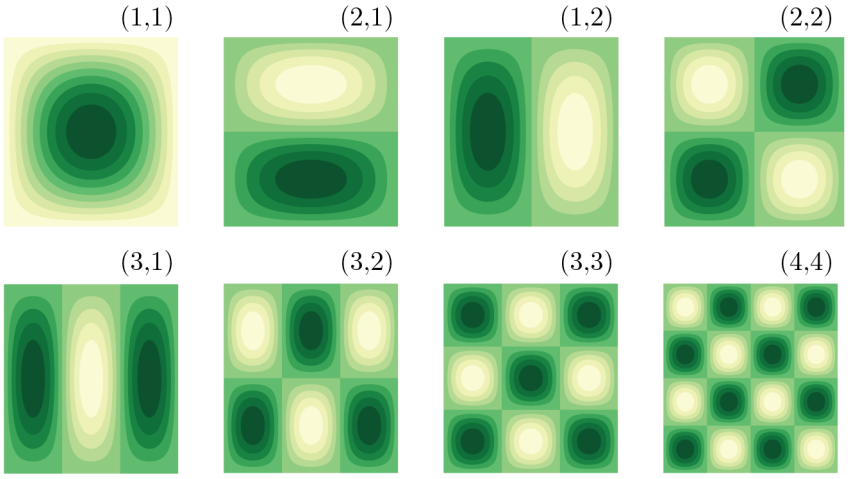

Figure 8.5: Contour plots of the mode shape functions $u_{m,n}(x,y)$ (Equation 8.6) of a rectangular membrane, omitting their time dependencies. The $(1,1)$ mode is the so called fundamental (drum head) mode of the membrane and features the lowest frequency as determined by equation 8.7. Higher order modes with equal mode numbers $m = n$ have frequencies $\omega_{m,m} = m \times \omega_{1,1}$. Also, modes with equal odd mode numbers (E.g. $(1,1)$ and $(3,3)$) have antinodes in the center of the membrane, whereas modes with equal and even mode numbers (E.g. $(2,2)$ and $(4,4)$)

However, as has been shown in the last section, the membrane has numerous different modes $u_{m,n}(x,y)$ and for each of those, one has to calculate what part of the membrane is actually moving. This leads to the modal mass

$$m_{m,n} = \rho \int_0^{l_x} \int_0^{l_y} \int_0^{l_z} dx\, dy\, dz\, (u_{m,n}(x,y))^2, \tag{8.9}$$

for each respective mode (m,n), in which the information of the moving parts of the membrane is encoded into $u_{m,n}(x,y)$. Note that the mass density ρ and the integral over the thickness l_z of the membrane remain constant.

Furthermore, we have no direct access to measure the displacement of the membrane directly. In fact, we solely rely on the optical read out of the motion with laser light and detect the light on photodiodes for further analysis. However, the light mode itself has a certain shape, usually a Gaussian TEM_{00} mode, such that the optically probed displacement [132]

$$D = \int_0^{l_x} \int_0^{l_y} \int_0^{l_z} dx\, dy\, dz\, (u_{m,n}(x,y) \times w(x,y)) \tag{8.10}$$

is determined by the mechanical mode $u(x,y)$ and the normalized optical intensity distribution $w(x,y)$. The displacement D is oftentimes referred to as the overlap of the mechanical and the optical modes. Besides the read-out of the membrane motion, the overlap also modifies the optomechanical interaction between the membrane motion

and the cavity mode, see chapter 9.3.2. This modification is usually built in as a modification of the modal mass of the membrane and is called the effective mass [105]

$$m_{\text{eff}} = \frac{m_{m,n}}{D^2}. \tag{8.11}$$

As can be seen from this equation, a probing beam exactly matching the mechanical mode shape will lead to $D = 1$ and minimum effective mass $m_{\text{eff}} = m_{m,n}$ of the (m, n) mode. In the remainder of this thesis the index *effective* will be dropped most of the time and context will ensure what definition needs to be considered at a given moment.

Any mode mismatch will lead to $D < 1$ and therefore the respective mode will appear to be heavier $m_{\text{eff}} > m_{m,n}$. In the extreme case of the optical beam averaging over the mechanical mode shape yielding zero overlap $D \to 0$ (e.g. figure 8.6, plot b) and d)), the respective mode will appear to have an infinite effective mass $m_{\text{eff}} \to \infty$. This effectively means that the optomechanical coupling is weak (i.e. vanishes), as the light is not sensitive to the motion of the oscillator. Several examples for mechanical mode functions and a Gaussian optical mode are given in figure 8.6.

8.5 EQUATION OF MOTION OF A DRIVEN OSCILLATOR

At this point we want to look at the equation of motion of a driven oscillator. This will lead to the mechanical susceptibility or transfer function of a mechanical oscillator, which is standard approach to clearly study the features of a resonator. It is also the foundation of the following sections and chapters dealing with dissipation, thermal noise and mechanical quality factors.

Each degree of freedom, e.g. each mechanical mode of the membrane, can be modeled by a harmonic oscillator driven by some external force F_{ext} via [47]

$$m\ddot{x}(t) + m\omega_m^2 x(t) = F_{\text{ext}}(t), \tag{8.12}$$

where $\omega_m = 2\pi f_m$ is the angular resonance frequency and m is the effective mass of a given mechanical mode of the membrane. At this point, we will consider a single mechanical mode. The extension of the following discussion to a multimode system is trivial. In reality, however, every oscillator experiences some sort of damping. Therefore we will expand equation 8.12 by two damping mechanisms. The first is the velocity dependent viscous damping at a rate γ, which describes the damping due to residual gas. It will be briefly introduced in section 2.1. The second is the so called structural damping term, which can be seen as an expansion of Hooke's law. It generalizes the spring constant $k = m\omega_m^2$ by adding an imaginary phase lag

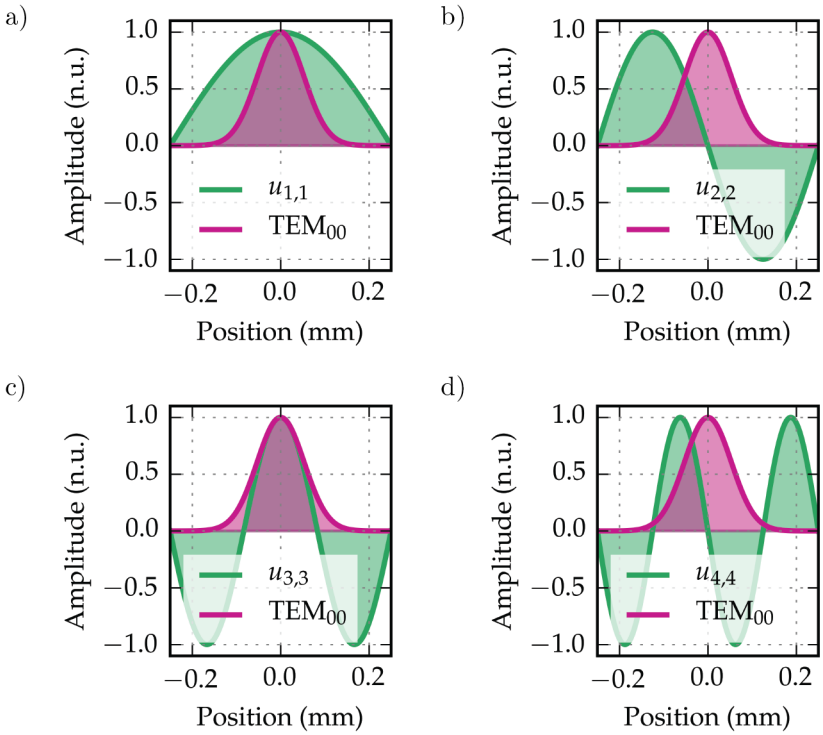

Figure 8.6: Depiction of mechanical mode shape functions (green) and optical read-out (purple) to illustrate the concept of overlap functions and the effective mass of a mechanical mode. The optical read-out is the TEM$_{00}$ cavity mode with a beam waist radius of 75 µm. Additionally, each subplot features one of the first four mechanical modes with equal mode numbers $m = n$ for a 500 µm SiN membrane. Here we look at cuts along the x-axis of the membrane. All functions are depicted in normalized units (normalized with respect to its respective maximum). If the optical and mechanical modes overlap perfectly, there is no modification of the modal mass of the specific mechanical mode. Subplots a) and c) show an overlap of roughly 30 %. Calculating the overlap integral (equation 8.10) for b) and d) lead to zero overlap and therefore infinite effective mass. In the experiment, however, the alignment of the optical beam with respect to the membrane is not perfect, such that there is a residual overlap.

ϕ to $k(1 + i\phi)$. The full equation of motion of a damped harmonic oscillator under the influence of an external force would then be

$$m\ddot{x}(t) + \gamma\dot{x}(t) + k(1 + i\phi)x(t) = F_{\text{ext}}(t). \tag{8.13}$$

This equation can be solved in the Fourier space by means of the Fourier transformations

$$\tilde{x}(\omega) = \int_{-\infty}^{\infty} dt\, x(t)e^{-i\omega t}, \tag{8.14}$$

$$\tilde{F}_{\text{ext}}(\omega) = \int_{-\infty}^{\infty} dt\, F_{\text{ext}}(t)e^{-i\omega t}, \tag{8.15}$$

of the position $x(t)$ and external force $F_{\text{ext}}(t)$, while $\omega = 2\pi f$ is the angular frequency. Replacing all time dependent variables in the sec-

ond order differential equation 8.13, leads to an algebraic equation that is easily solvable. The solution is defined as the mechanical susceptibility, oftentimes referred to as transfer function:

$$\chi(\omega) = \frac{\tilde{x}(\omega)}{\tilde{F}_{\text{ext}}(\omega)} = \frac{1}{m\left[(\omega_m^2 - \omega^2) + i(\gamma\omega/m + \phi\omega_m^2)\right]}. \tag{8.16}$$

The transfer function provides the frequency response of a mechanical oscillator under the influence of an external force F_{ext}. Whereas the absolute value

$$|\chi(\omega)| = \frac{1}{m\sqrt{(\omega_m^2 - \omega^2)^2 + (\gamma\omega/m + \phi\omega_m^2)^2}} \tag{8.17}$$

describes the actual displacement and the argument

$$\arg\chi(\omega) = \arctan\frac{\omega_m^2 - \omega^2}{\gamma\omega/m + \phi\omega_m^2} \tag{8.18}$$

specifies the phase lag between the applied force and the response of the oscillator. The transfer function is depicted in figure 8.7. While the external force is white, which is to say that it has a flat frequency response, the transfer function ensures that the displacement shows the typical behavior of a harmonic oscillator. That is, a sharp peak at its resonance, a constant tracking at low frequencies and the $1/m\omega^2$ behavior at higher frequencies.

Transfer functions are useful for several reasons. Among other features, they plainly picture the response of an oscillator below, around and above its resonant frequency. Moreover, we will face transfer functions at various points of the experimental setup. For instance the transfer functions of optical filters such as the filter cavity (chapter 5.3), detector responses (chapters 6 and 10.4), electronic low and high pass filters, etc. These are all either useful tools to achieve certain goals, or they are experimental features that need to be carefully taken into account to correctly characterize the setup.

8.6 FLUCTUATIONS AND DISSIPATION

As a starting point to introduce important quantities such as thermal noise spectral densities and mechanical quality factors, I like to introduce the fluctuation-dissipation theorem (FDT). Many parts of this section are derived from Peter Saulson's textbook [111]. The FDT, in its general form formulated by H. B. Callen [37], states that any dissipation (loss) channel will generate fluctuations (noise) and vice versa. It can be applied to any linear system in thermal equilibrium with its environment. We will make use of the theorem to link mechanical loss to thermal force and position noise. Quantitatively, the FDT states that the single-sided thermal force noise spectral density S_F^{th}

of the thermal force power spectrum $4k_bT\Re(Z(f))$ and the thermal position noise spectral density S_x^{th} fulfill the following equations

$$S_F^{\text{th}} = 4k_BT\Re(Z(f)), \tag{8.19}$$

$$S_x^{\text{th}} = \frac{k_BT}{\pi^2 f^2}\Re(Y(f)), \tag{8.20}$$

while T is the bath temperature, k_B denotes Boltzmann's constant, $Y(f)$ the admittance and

$$Z(f) = \frac{F(f)}{\dot{x}(f)} = \frac{F(f)}{2\pi i f x(f)} \tag{8.21}$$

is the impedance of the system. At this point we followed the notation from [111] and replaced the angular frequency with the frequency $f = \omega/2\pi$ in units of Hz: The quantity that is being measured in the laboratory.

Note, that the less intuitive quantities admittance and impedance can be expressed through the intuitive and accessible transfer function χ, see equation 8.16. Inserting χ in equation 8.20 allows us to study the thermal noise power spectrum for different damping mechanisms. To investigate both damping mechanisms separately, we successively set either γ or ϕ to zero, yielding

$$S_x^{\text{vis}}(f) = \frac{4k_BT\gamma}{m\pi^2\left[(f_m^2 - f^2)^2 + f^2\gamma^2\right]}, \qquad \phi = 0, \tag{8.22}$$

$$S_x^{\text{str}}(f) = \frac{4k_BTf_m^2\phi}{m2\pi f\left[(f_m^2 - f^2)^2 + 4\pi^2 f_m^4\phi^2\right]}, \qquad \gamma = 0. \tag{8.23}$$

The thermal noise due to viscous damping is, for instance, the correct model for the oscillator damped by air or residual gas in a vacuum chamber. On the other side, the structural damping model is applied when investigating the losses within the oscillator due to internal friction. The off-resonant behavior for the two loss channels is different due to the additional f dependency in the denominator of structural damping power spectrum. However, both models behave similarly around the mechanical resonance. Note, increasing and decreasing the losses will only affect the shape of the respective noise spectrum, e.g. broadening and narrowing of the resonance peak (see inset of figure 8.7). That is, a redistribution of the amount of energy stored in the resonance compared to the noise level at all other frequencies. The thermal energy, which is proportional to the area below the function $S_x(f)$, is only affected by the temperature T of the bath.

8.7 THE QUALITY FACTOR Q

A very useful approach to characterize and compare losses of resonators, is by means of the quality factor Q. There are several definitions that become approximately identical in the limit of large Q's.

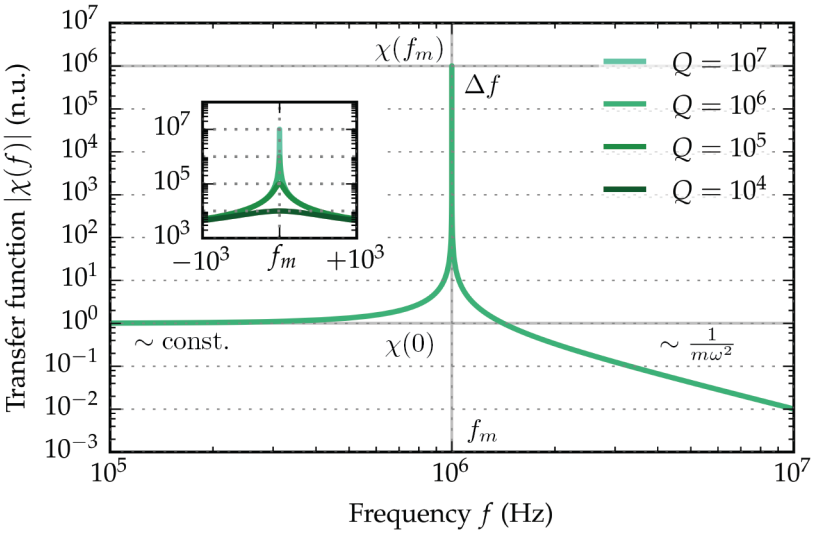

Figure 8.7: Mechanical transfer function and the definition of the mechanical quality factor. Depicted is the transfer function $|\chi(f)|$ of the fundamental mode of a SiN membrane with 10 pg effective mass, 1 MHz resonant frequency and a quality factor of $Q = 10^6$. For frequencies far below the resonance, the response becomes unity and the mechanics will follow the external force. For frequencies far above the resonance, it features the typical $\sim 1/m\omega^2$ behavior. The resonance for high Q oscillators becomes a sharp peak with an full width at half maximum that can become sub Hz. The two definitions of the quality factor in frequency space can be easily illustrated in this figure. The first is the ratio of the transfer function at the resonance divided by its DC response, $Q = |\chi(f_m)|/|\chi(0)|$. And the second is the ratio of the resonant frequency and the full width at half maximum, $Q = f_m/\Delta f$. The inset pictures a frequency range of ± 1 kHz around the resonance f_m for varying quality factors from $Q = 10^4 \ldots 10^7$. It can be seen that the width of the resonance peak becomes narrower and therefore the amount of energy stored withing the resonance scales with the quality factor of the membrane.

We will begin in the frequency domain, where the quality factor is defined by

$$Q = \frac{f_m}{\Delta f} = \frac{|\chi(f_m)|}{|\chi(0)|}, \tag{8.24}$$

with f_m being the resonant frequency, Δf being the full width half maximum (FWHM) of the resonance and χ being the transfer function. This definition is depicted in 8.7. The ratio essentially indicates how much energy the oscillator can store in its resonance f_m.

Since Δf can become sub Hz for high Q resonators like SiN membranes (compare with inset in figure 8.7), it can be hard to measure experimentally. We follow [111] and give an equivalent (for $Q \gg 1$) definition in the time domain

$$Q = 2\pi \frac{E}{\Delta E}, \tag{8.25}$$

in which, E is the energy stored in the resonator and ΔE is the energy loss per cycle.

Let's say that we apply some external force to the oscillator and thereby drive it at its resonance f_m. If we quickly turn off the external force, the overall motion of the resonator can be described by

$$x(t) = x_0 \times \cos(2\pi f_m t) \times \exp(-t/\tau), \tag{8.26}$$

which is a composition of the amplitude x_0 at the moment when the external drive is turned off, the oscillation of the resonator at its resonant frequency and an overall envelope function with a characteristic decay time τ, that is linked to the quality factor by the relation

$$Q = \pi f_m \tau. \tag{8.27}$$

We will make use of this approach to measure the quality factor of our mechanical devices in the remainder of this chapter.

In reality there can be many different loss mechanisms contributing to the overall quality factor of the devices. As the losses can be added (equation 8.13) and are inversely proportional to the quality factor, the overall Q is the inverse sum of Q factors attributed to each loss channel

$$\frac{1}{Q} = \frac{1}{Q_{\text{vis}}} + \frac{1}{Q_{\text{str}}} + \frac{1}{Q_{\text{clamping}}} + \dots, \tag{8.28}$$

while $Q_{\text{vis}} = \omega_m/\gamma$ and $Q_{\text{str}} = 1/\phi$ are the quality factors attributed to viscous and structural damping and Q_{clamping} is attributed to mechanical loss due to clamping, gluing or any other mount of the membrane into the optomechanical cavity. Clamping will be discussed further when I describe the optomechanical system in the next chapter. An elegant way to bypass clamping losses is by means of a phononic shield for the membrane as have been done within the presented work, see section 8.10.

8.8 Q MEASUREMENT APPARATUS

The quality factor of the membrane has been introduced and at this point it will be explained how it is measured experimentally by means of ring-down measurements. Throughout the duration of this thesis, ring-down measurements have been performed in different setups and with varying schemes. At this point I will describe a test setup and results of ring-down measurements performed on a large number of different membranes. The main parts of the test setup are a fiber optic interferometer and a cryostat containing the membrane. The setup is illustrated in figure 8.8.

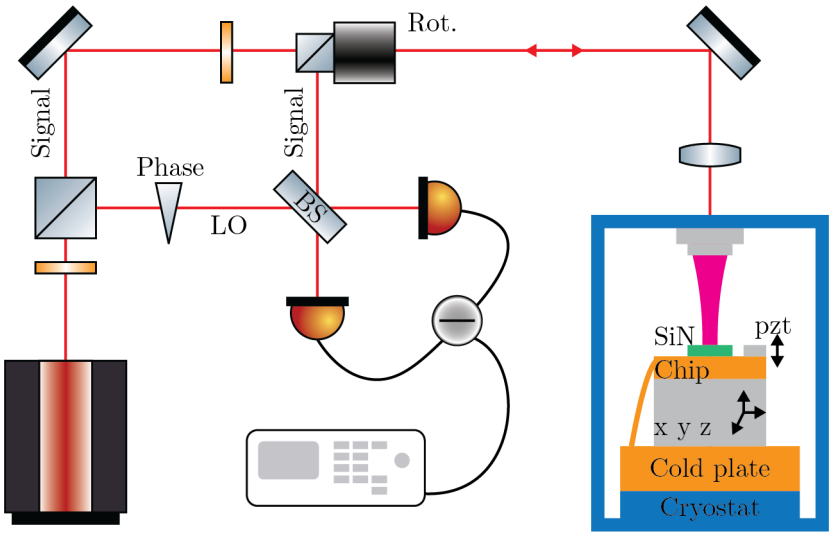

Figure 8.8: Illustration of fiber optical Q measurement test setup. A fiber laser is split into signal and local oscillator. The latter is coupled through a fiber stretcher that can actuate on the phase, which is used to lock the homodyne detectors. The signal is transmitted through a Faraday rotator. The fiber is fed into the cryostat and after being coupled out of the fiber, the light is being focused onto the membrane. The membrane is clamped (see main text) onto a chip holder that is thermalized through copper braids. The membrane can be brought into the focus of the light by means of a stack of positioners. A piezo is attached to the chip and can be driven with white noise to excite the membrane motion for ring-down measurements. The light reflected off the membrane is being coupled back into the fiber and into the signal port of the fiber beam splitter. The beam splitter outputs are again coupled into free-space and focused onto two photodetectors. The difference current is plugged into the spectrum analyzer to perform zero-span measurements to resolve the ring-down. Pictures of the cryostat, the positioner stack and a clamped membrane can be found in figure 8.9.

We use a liquid helium flow cryostat from Janis Research [7] to cool a small vacuum chamber down to roughly 5 K. The vacuum is provided by a turbomolecular pump model HiPace 80 from Pfeiffer Vacuum [8], which quickly reaches pressures on the order of 10^{-6} mbar.

The chamber contains a stack of x, y and z positioners from attocube systems [6] that holds a small sample holder made out of copper for thermalization. The membrane under test can be clamped, glued or simply laid down onto the copper sample holder. Additionally to the membrane, a small piezo is attached to the chip. This piezo can be driven by white noise or specific frequencies to excite the mechanical modes of the membrane. The positioners are cryogenically compatible and allow lateral and longitudinal alignment of the membrane with respect to the beam of a measurement laser.

The measurement laser enters the chamber through a fiber collimator attached to the optical viewport of the cryostat. The light reflected off the membrane, i.e. the light that recorded the phase information

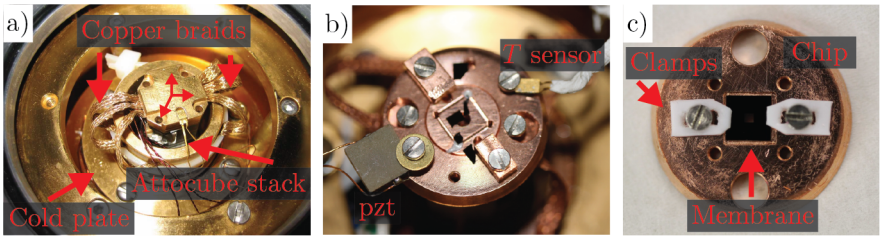

Figure 8.9: Interior of the cryostat amd clamped membrane. Picture a) features the interior of the cryostat, with the cold plate, Attocube positioner stack [6] and copper braids for thermalization. b) is a close up of the chip (membrane holder) with attached temperature sensor and piezo and c) features the chip with a clamped SiN membrane by means of Teflon clamps.

of the membrane motion, gets fetched by the same collimator if the membrane is aligned well with respect to the waist of the light mode.

The light from the laser source is split into a signal beam interacting with the membrane and a local oscillator (LO). The local oscillator is traveling through a fiber stretcher which acts as a phase shifter and which is used as an actuator to stabilize the relative phase of LO and signal. Both signal (after interacting with the membrane) and LO are combined at a balanced (50/50) fiber BS. The two outputs of the BS exit fiber collimators and are focused down onto two photodetectors and are therefore performing a balanced homodyne detection. The difference of the slow (DC) channels yields the interference fringe when the LO is being scanned by the fiber stretcher. This signal provides the error signal to lock the interferometer. The difference of the fast (AC) channels of the detectors ultimately yields the spectrum of the membrane motion measured with a spectrum analyzer.

Mechanical modes can be identified by our model (equation 8.7) and then selectively excited by a function generator and the piezo clamped next to the membrane. We get a time-resolved measurement of the ring-down by measuring the band power at a high rate with a large resolution bandwidth (usually around 2 kHz) compared to the width of the mechanical resonance at exactly the resonant frequency. The band power is measured in units of dB m, which is a logarithmic scale, turning the exponential decay in equation 8.26 into a linear decay. The decay time τ can be extracted via a linear fit to the data and the quality factor of the membrane is then derived by $Q = \pi f_m \tau$. Figure 8.10 shows the ring-down of the $(3,3)$ mode of a 500 µm by 500 µm Norcada [5] membrane at room temperature and at around 5 K, yielding quality factors of $Q_{\mathrm{RT}} = 0.57 \times 10^6$ at room temperature and $Q_{\mathrm{LT}} = 22.4 \times 10^6$ at low temperature for a resonant frequency of $f_m = 1.22$ MHz. The highest measured quality factor in our laboratories were measured for a similar device reaching a low temperature quality factor of $Q_{\mathrm{LT}} = 34.2 \times 10^6$ at 865 kHz.

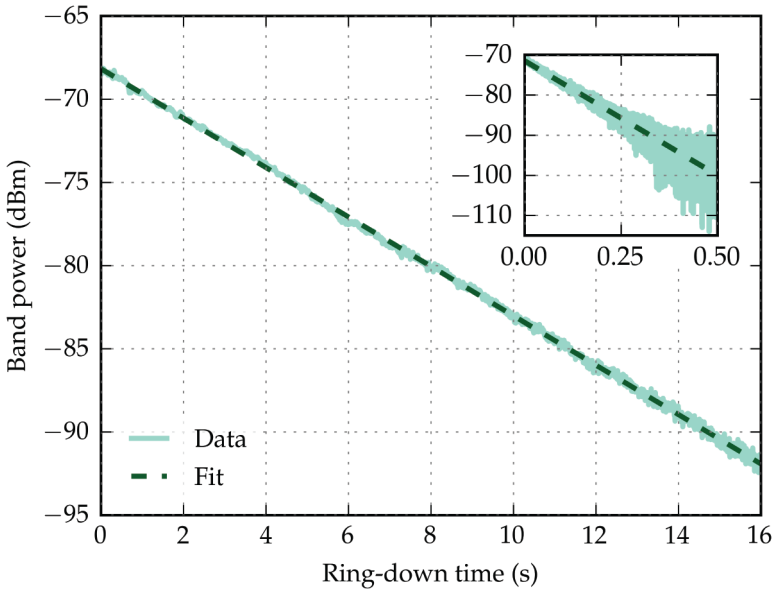

Figure 8.10: Ring-down measurement performed on the $(3,3)$ mode of a $500 \times 500\,\mu m$ Norcada membrane inside our fiber setup. Depicted is the band power over time, measured with a spectrum analyzer in zero-span mode. Therefore measuring the band power at a single frequency, e.g. $f_m = 1.22\,\mathrm{MHz}$, with a band width of $2\,\mathrm{kHz}$. Light green traces are measured data while dark green depicts the fitted exponential, which yields the time constant τ according to equation 8.26. The resulting low temperature quality factor is then $Q_{\mathrm{LT}} = \pi f_m \tau = 22.4 \times 10^6$. The inset shows a similar measurement of the same membrane and mode at room temperature, yielding $Q_{\mathrm{RT}} = 0.57 \times 10^6$.

8.9 Q MEASUREMENTS AND DISCUSSIONS ON DAMPING MECHANISMS IN SIN MEMBRANES

This section is dedicated to discussions of a broad spectrum of Q measurements that I have performed on commercially available SiN membranes as well as custom made membranes by collaborators at TU Delft. These discussions will mostly deal with what is currently known about SiN membranes in general and how I empirically improved their performance within our optomechanical system.

Measurements on commercially available membranes from Norcada [5] have been performed on devices with side lengths ranging from 0.5 mm up to 1.5 mm. We solely chose a thickness of 50 nm since thicker membranes would increase the effective mass and yield larger absorptions in the material, as has been shown earlier in this chapter.

Figure 8.11 shows room temperature and low temperature measurements at around 5 K taken inside a Helium flow cryostat. Depicted are data points of three different devices with side lengths of

0.5 mm. The data illustrates several important facts that I will address in the following paragraphs.

Clamping techniques and overcoming scattering results

It is plainly visible that the results scatter by several orders of magnitude (see Nor. 1 and Nor. 2 in figure 8.11 for reference). The reason for this is that the devices are always connected to the outside world, usually by a metal holder, a positioner or a mirror. In any case, it can be a low Q environment and the contact between a low Q holder and a high Q membrane will yield some momentum transfer of membrane oscillations to the holder at some characteristic timescale $\tau_{\text{clamping}} \sim Q_{\text{clamping}}$. This effect is also called radiation damping and it can be reduced through a mismatch between membrane and silicon chip (frame) size, as explained and observed by [22].

Oftentimes, the fundamental mode suffers the most from losses. This is because, as one can see in figure 8.5, the fundamental mode has the largest extent over the surface of the membrane and one common loss channel is the friction of bending parts of the membrane where it is suspended within the silicon chip. Higher order modes suffer less from this effect as they are more confined to the membrane center.

When membranes are incorporated into optomechanical systems, the chip needs to be somehow clamped. Clamping, however, is a delicate business. On the one hand the chip needs to be fixed to, let's say, a mirror and the chip must stay fixed when cooling down to Helium temperatures (which involves different contractions of optics, metals, screws and the membrane itself) and additionally one has to guarantee thermalization of the membrane with its environment. The two main approaches to fix membrane chips onto a sample holder, e.g. the optomechanical cavity, are by means of rigidly clamping them via PTFE (Teflon) or metal clamps, or by gluing them with a thermally conductive epoxy, e.g. Stycast [9].

Over the course of hundreds of measurements on several dozen devices, I empirically converged my experience into the following procedure that produced reliably good Q factors exceeding 10^7 (see Nor. 3 in figure 8.11):

- Avoid any clamping mechanism. Therefore, a vertically oriented setup where the membrane only experiences conservative (loss-free) gravitational forces is preferable.
- If that is not possible: Minimize the contact area between the membrane chip and its holder.

- Use preferably copper or other materials with good thermal conductivity as chip holders. Ensure thermalization by polishing the membrane holder with µm roughness polishing sheets.
- Additionally, Apiezon - a low temperature and high-vacuum compatible grease with good thermal conductivity - can be applied to the chip holder. Remove the bulk of the grease with acetone, such that only a thin layer remains on the holder. In addition to improved thermalization, the membrane adheres to the grease and stays fixed during a cool-down.
- To ensure that the membrane does not slip from the chip when initially pumping down the vacuum chamber, the silicon chip should be clamped from the sides with PTFE (Teflon) clamps. Because of the large mismatch of the thermal expansion coefficients, $\alpha_{\mathrm{PTFE}} = 112 \times 10^{-6}\,\mathrm{m/K} \gg 16.7 \times 10^{-6}\,\mathrm{m/K} = \alpha_{\mathrm{copper}}$ [10], the Teflon clamps will contract and therefore release the silicon chip at low temperatures.

This procedure yields quite consistently quality factors of above 1×10^7, as for Nor. 3 in figure 8.11. Which is comparable to the best results reached for commercially available membranes without any special designs.

Increasing Q at low temepratures

The second important result is the increase of the quality factor with cooling down the membrane to cryogenic temperatures. Here, several effects take place at the same time. We know from equation 8.28 that, for instance, large losses due to clamping can limit the quality factor of a device and therefore mask other loss contributions like internal friction of the suspended membrane, or gas damping at a given pressure in the vacuum chamber. Yet, several isolated statements can be made. Some are more of a technical nature and others demonstrating physical effects. If possible, use the procedure presented earlier in this section to avoid clamping losses due to rigid clamping or joints from gluing.

Residual gas damping due to momentum transfer to air molecules will exhibit another dissipation channel and limit the overall quality factor. This effect is depending on the velocity of the motion and therefore a viscous damping mechanism (section 8.6). Quick measurements in our test setup were usually conducted at pressures of around $10^{-5}\,\mathrm{mbar}$. Sometimes I would wait until reaching $10^{-6}\,\mathrm{mbar}$. Low temperature measurements always reached the range of $10^{-7}\,\mathrm{mbar}$ due to additional cryogenic pumping, i.e. the effect of trapping particles at cold surfaces. Figure 8.12 shows the Q factor as

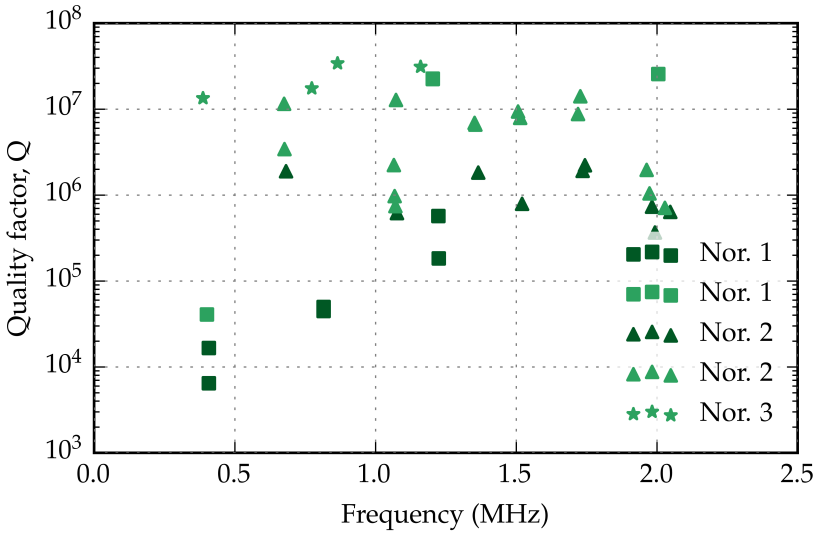

Figure 8.11: Q measurements on high stress Norcada membranes. This plot focuses on measurements performed after using the clamping procedure described in the main text. It allows for more predictable and repeatable Q factors. Note, that dark markers correspond to room temperature and light markers to measurements at cryogenic temperatures. The most important features are the following. First, lowest frequency modes, especially the fundamental mode, show larger discrepancies between room temperature and cryogenic temperatures. Second, for higher order modes, room temperature Q's seem to saturate at 10^6, while the mechanical quality increases by roughly one order of magnitude to 10^7 at low temperatures. And third, even though this clamping technique gives quite consistently good Q values at low temperatures, there is still some scattering for specific modes, which can spoil experiments relying on a multimode system in the strong cooperativity, e.g. the entanglement protocol presented in chapter 10. These points will be addressed in the following sections to improve the performance of our membranes.

a function of residual gas damping in the vacuum chamber using the relation [29, 57]

$$Q_{\text{air}} = (\pi/2)^{3/2} \frac{\sqrt{R_0 T / M_m}}{p} l_z \rho f_m, \tag{8.29}$$

which is further described in the caption. It shows that the maximum Q factor that can be reached at low temperatures and corresponding pressures of below 10^{-6} mbar (dashed gray line) is approximately 4×10^8, which is larger than any of my measurements. Our quality factors are therefore not limited by residual air damping.

Thermoelastic loss is the dissipation of energy due to stretching or compression of the resonators material. This increases or decreases the temperature of the material locally, which leads to temperature gradients and a heat flow that dissipates a fraction of the oscillation

energy in the material [61, 141] and vice versa. The fluctuation dissipation theorem states that a fluctuation in the temperature yields a displacement noise. This is a structural damping mechanism as described in section 8.6 and its loss angle (phase lag) is given by the relation [62]

$$\phi_{\text{thermoel.}} = \frac{E\alpha^2 T}{C_v} \frac{\omega_m \tau_d}{1 + \omega_m^2 \tau_d^2}, \tag{8.30}$$

in which E is the Young's modulus, α the thermal expansion coefficient, C_v the heat capacity per unit volume and $\tau_d / l_z^2 / \pi^2 D$ a material and geometry dependent time constant and D is the thermal diffusivity. Computing this equation, with the numerical value of the parameters taken from table 8.1, for a membrane mode with frequency $\omega_m = 2\pi \times 1.2\,\text{MHz}$ and thickness $l_z = 40\,\text{nm}$ at room temperature, yields $\phi_{\text{thermoel.}} = 1.17 \times 10^{-7}$ and ultimately $Q_{\text{thermoel.}} = 8.5 \times 10^6$. This value is just a guide value since several parameters do vary or are not exactly known. Thermoelastic damping can be limiting for smaller membranes with higher resonances or for higher modes of a given membrane. The same calculation for the very same membrane at liquid Helium temperatures yields a quality factor of 5.1×10^8, which, on the one hand can explain the increase of the Q factor with temperature and on the other hand means that we are not limited by thermoelastic losses at low temperatures.

Membrane dimensions and stress

The final point I want to address is the interdependence between Q factors, membrane dimensions and stress. We decided to go with smaller membranes to, first of all, push the fundamental frequency of the membrane further away from low frequency classical laser noise and to create a more sparse mechanical mode spectrum. It was already known from earlier work [145] that the quality factor scales with side length and stress, but scales inversely with membrane thickness. It was indicated that $Q \sim (l_x/l_z)^2$ for $l_x/l_z < 10^5$ [38], which we can deeply fulfill.

We chose to use membranes with side lengths of around 300 µm and keep small thicknesses of around 40 nm. Additionally we aimed for even higher tensile stress to achieve higher mechanical mode frequencies. These membranes got fabricated by our group member and microfabrication expert Claus Gärtner at the facilities of TU Delft, Netherlands, and under supervision of our collaborator Prof. Simon Gröblacher. The results are depicted and discussed in figure 8.13. Using the average Q factor of the fundamental mode of the Nor. 1 device from figure 8.11 and using the $(l_x/l_z)^2$ dependency introduced

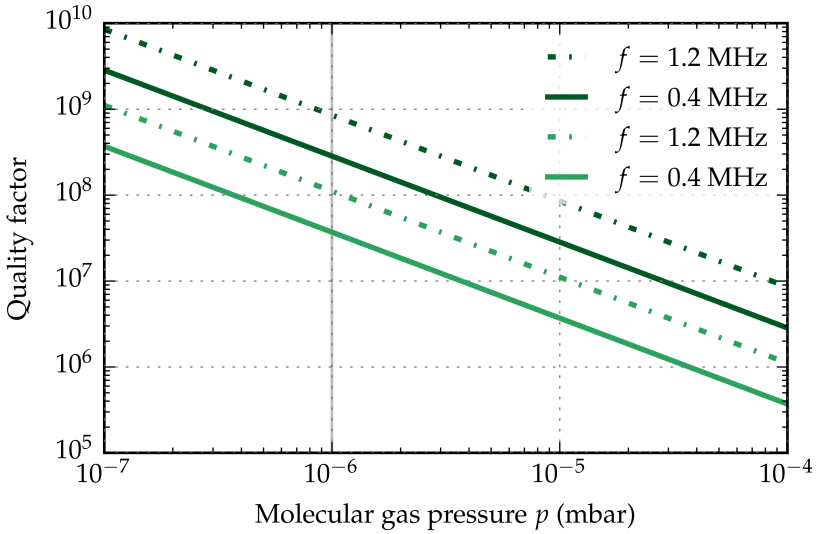

Figure 8.12: Molecular gas damping as a limit of the mechanical quality factor. Solid lines are depicting resonant frequencies at 400 kHz, the lowest frequencies we deal with in this work presented, and dashed lines denote resonances at 1.2 MHz, frequencies where entanglement measurements have been conducted. Dark green lines apply to room temperature (RT) and light green lines to 5 K (LT). We see that, while Q measurements at room temperature at rather high pressures of above 10^{-4} mbar can limit the quality factor, low and room temperature Q measurements at pressures below 10^{-6} mbar (grey line) are never limited by residual gas damping. This curves are generated via the molecular damping relation [29, 57] $Q_{\text{air}} = (\pi/2)^{3/2} \frac{\sqrt{R_0 T/M_m}}{p} l_z \rho f_m$, in which $R_0 = 8.31\,\text{J/molK}$ is the gas constant, $M_m = 29\,\text{g/mol}$ is the molar mass of the surrounding air, $\rho = 2700\,\text{kg/m}^3$ the mass density, $l_z = 40\,\text{nm}$ the thickness, f_m the mechanical resonance of the membrane, T the temperature and p the pressure of the environment.

in the last paragraph, we can calculate expected quality factor of the membranes fabricated in Delft. For a membrane with a side length of 284 µm, the expected Q factor would be $13.4 \times 10^6 \times (284/500)^2 \approx 4.3 \times 10^6$. The actual measured value is 5.6×10^6, which is reasonably close. The discrepancy can be explained by the enhanced tensile stress of approximately 20 % compared to Norcada membranes. High tensile stress membranes show in general higher quality factors than low stress membranes. More careful studies of low and high stress membranes and the impact of cooling SiN resonators to liquid Helium temperatures, show that the dissipation decreases with temperature and the ultimate quality factors are determined by the tensile stress. High stress membranes show a better performance by means of smaller mechanical dissipation of around two orders of magnitude compared to low stress resonators [122].

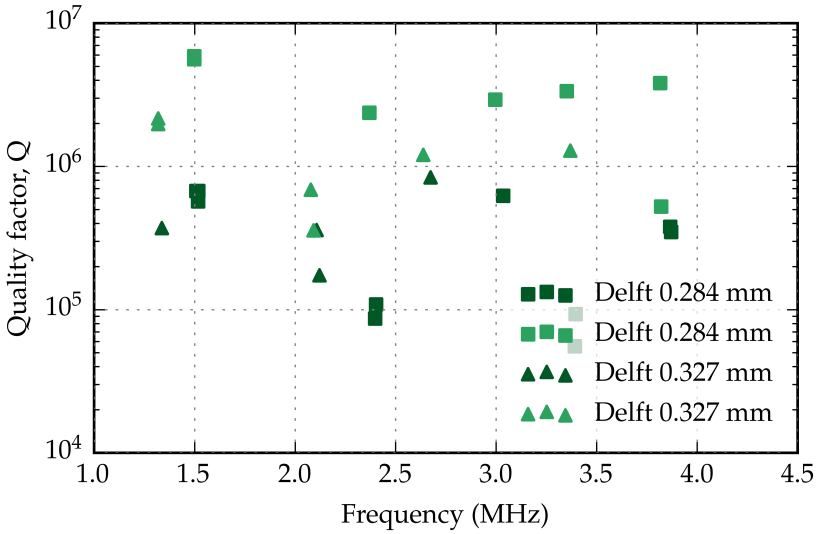

Figure 8.13: Q measurements on custom made SiN membranes, designed by us and fabricated by Claus Gärtner at the facilities of TU Delft, Netherlands. The main motivations were the fabrication of smaller membranes with higher stress, to decrease the mass, increase the resonance frequency and decrease the number of modes within the line width of our optomechanical cavity. While the tensile stress is approximately 20 % higher than for Norcada membranes and the fundamental frequency has been shifted from roughly 400 kHz to 1.2 MHz, significantly lowering the number of mechanical modes in the frequency bandwidth of the optomechanical cavity and also pushing the frequencies of interest to a region with much lower laser noise, according to equation 5.10. Dark markers, again, correspond to RT and light markers to LT. Note, that the absolute Q's are lower than for the larger Norcada membranes. The effect is in accordance to the size ratio of the membranes, see main text. On the other side, the problem of lower order modes suffering disproportionately from mechanical losses has been solved by the frame (chip) to window ratio, as the relative difference between RT and LT is similar across all modes. Yet, the absolute performance of individual modes still varies by one order of magnitude and potentially spoiling the performance of other mechanical modes.

Summary

I presented an empirically developed approach that reliably decouples a membrane from losses that appear when mechanically clamping or gluing a membrane onto a holder. It can be stated that residual gas damping is negligible in our systems and the scaling of Q factors with membrane dimensions and the effect of higher tensile stress were in accordance with other studies. At least at low temperatures and for smaller membranes we are not yet (solely) limited by intrinsic losses, but also by radiation dissipation. That is the coupling of a high Q membrane to its low Q environment, to which it is connected. This effect is also varying from mechanical mode to me-

chanical mode, since it depends on matching eigenfrequencies of the membrane with phonons from its environment. This limiting factor for our type of membranes is in agreement with careful studies presented in [135]. We will follow their approach in the next section to introduce a higher frequency/size mismatch of the membrane to its frame and environment, not only by further increasing the mismatch of membrane to frame size ratio, but also by means of carefully shaping the membrane frame in a way to decouple the membrane modes at frequencies we are interested in from phonons of the environment.

8.10 A PHONONIC SHIELD FOR SIN MEMBRANES

In this section we will study a method to fully decouple the high Q membrane from its low Q environment and thereby minimizing the membrane losses due to mechanical coupling to the environment. This decoupling is achieved by means of a phononic crystal structure [128, 150], which yields an energy bandgap for phonons, thus reducing the radiation damping of the membrane modes within a certain frequency range. Our structures have been designed with finite element modeling (FEM) using COMSOL. The calculations have been made by Laurin Steidle under supervision and instructions of Witlef Wieczorek in Vienna. Further improvements have been added by Richard Norte and the fabrication was done by Claus Gärtner, both within Simon Gröblacher's group at TU Delft, Netherlands.

The isolation comes from a repetitive sequence of unit cells, which need be designed in a way to not show eigenmodes in the phonon dispersion and therefore to form an energy bandgap. The procedure begins by starting with an arbitrarily shaped unit cell, e.g. a rectangle, and then calculating the range of wave vectors for this design by applying a periodic boundary condition on the solutions. The design is then iteratively modified and re-evaluated until it features a desired frequency region without eigenmodes, i.e. the phononic bandgap. The suppression comes from destructive interference at the periodic structure. This procedure is done most efficiently by FEM modeling (COMSOL) and an optimization algorithm. The final design is then used as a mask to release the periodic structure by removing the excess silicon from the frame material. The cell in the middle of the structure, the so called defect cell, contains the SiN membrane.

Figure 8.14 a) shows one implementation of a unit cell with chamfers and embedded bridges and b) a plain rectangular design with bridges at the border of the cell. In c) the simulated noise power spectrum from FEM simulations of the design from figure a) is depicted, as well as a simulation of the membrane NPS without the lattice. This design yields a broad bandgap from 1 to $\sim$ 3.1 MHz and a second

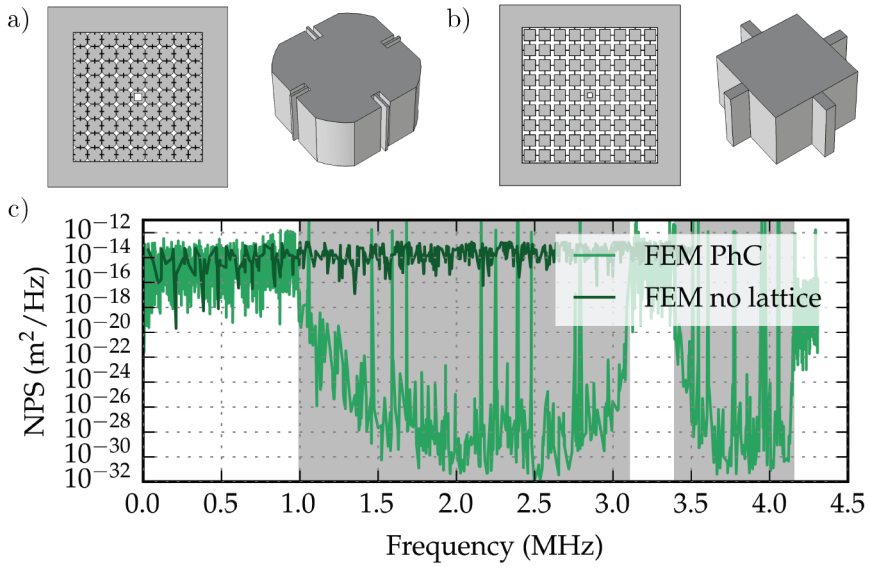

Figure 8.14: Phononic bandgap membrane design. Figure a) features a bandgap design with chamfered edges of a rectangular cell with embedded bridges. This design shows a broader spectral bandgap compared to design b) with rectangular cells and attached bridges. The simulated displacement noise spectrum of design a) is shown in plot c) in light green. Dark green shows the NPS of the same but non-patterned chip (and no membrane). The grey region depicts the frequency ranges of the phononic shield showing several orders of magnitude less motion at the region of the membrane and its resonances. These simulations are provided by courtesy of Laurin Steidle.

bandgap from 3.4 to $\sim$ 4.2 MHz.

The actual realization of a phononic shield membrane and its performance are depicted in figure 8.15. Figures a) and b) feature a photograph and a drawing of the defect cell containing the SiN membrane. Figure c) shows the measured noise power spectra on the defect cell and directly on the membrane, while the full chip is excited by white noise applied to a piezo close to the chip. The measurement on the defect cell features several orders of magnitude less noise power for resonances within the bandgap region. This is the case, because incoming phonons from the environment destructively interfere as the periodic structure and are reflected. Therefore, the high Q membrane resonances within the bandgap do not couple to the low Q environment, minimizing radiation losses of the membrane modes.

Measurements of the quality factor of two phononic bandgap membranes are shown in Figure 8.16, while the device PS3.1 is the one, where entanglement measurements have been performed on, see chapter 11. The excitation of mechanical modes within the bandgap of such shielded membranes is highly non-trivial, since the membranes where specifically designed to not transmit vibrations through the

chip to the membrane. The measurements were conducted in-situ within the optomechanical cavity and the excitation was performed via blue-detuned drive of the cavity. A detailed description of the procedure will follow in the next chapter (in section 9.3.3), where I will present and characterize the full optomechanical system. At this point we will restrict ourselves to the results of the measurements, which feature low temperature Q factors above 4×10^6 for all relevant modes modes within the half width at half maximum (HWHM) of the optomechanical cavity of $\leq 2.7\,\mathrm{MHz}$ and therefore paving the way towards bringing the multimode optomechanical system into the strong cooperativity regime.

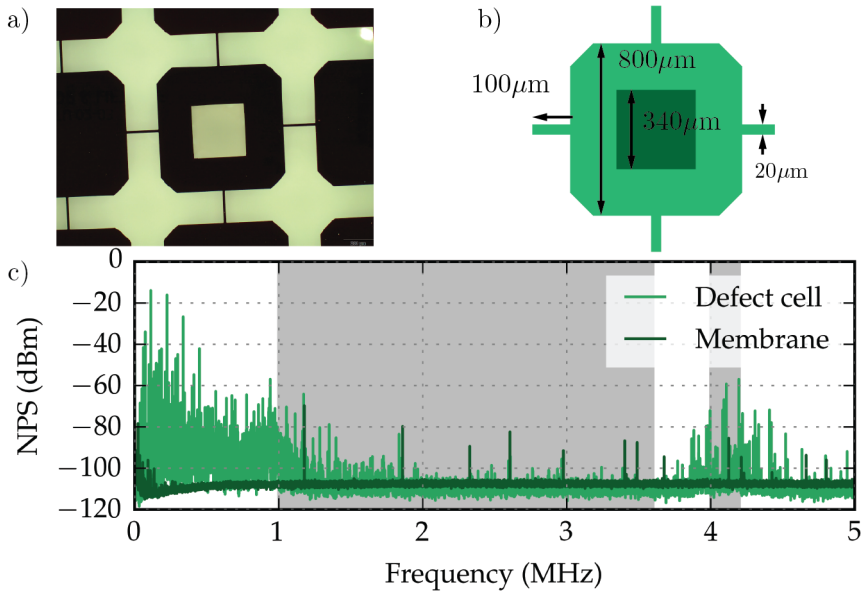

Figure 8.15: Phononic bandgap membranes and noise power measurements. Figure a) shows a photograph of the phononic bandgap membrane later used for entanglement measurements. Photo and fabrication were both by Claus Gärtner. Figure b) shows a schematic and the dimensions of our defect cell (light green) with the SiN membrane (dark green). The size of the membrane and the tensile stress achieved during the fabrication together with our model for the membrane yield a fundamental frequency of around 1.2 MHz. Due to fabrication constraints we combined the chamfered design with attached bridges in between the unit cells, that is basically a combination of the designs a) and b) in 8.14. Figure c) shows the noise power spectrum measured on the membrane (dark green) and on the defect cell (light green), while white noise is applied to the holder of the chip, therefore exciting many modes in the full chip. The measurement on the defect cell shows that its modes can only be excited outside of the bandgap. Excitations of modes within the bandgap (gray shaded area) are strongly suppressed ($\approx -110\,\mathrm{dB\,m}$ compared to -80 up to $-20\,\mathrm{dB\,m}$). Therefore, external phonons at frequencies outside of the bandgap do not transmit through the shield and do not reach the membrane. Therefore, membrane modes which lie within the bandgap are not excited by the applied white noise.

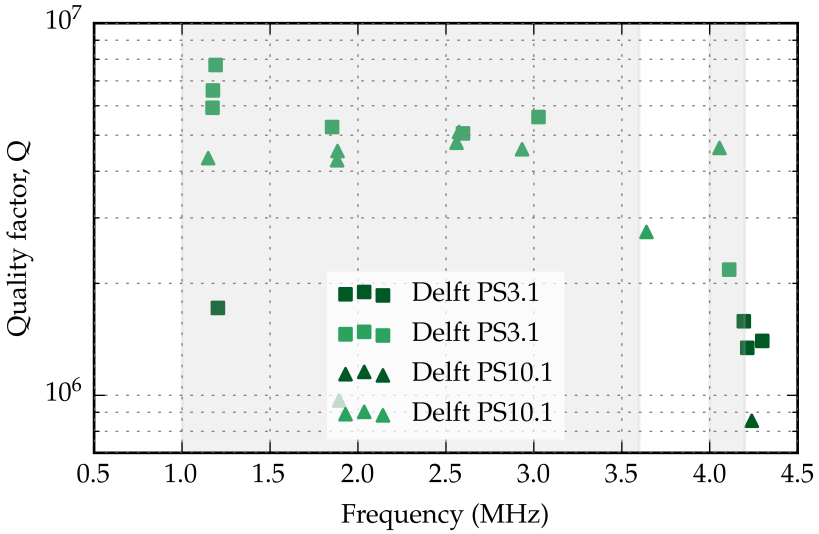

Figure 8.16: Q measurements on phononic bandgap membranes. One membrane each from two different batches of phononic bandgap membranes produced at TU Delft. All measurements yield Q factors above a million, except of the highest measured mode of the PS10.1 device, which lies outside of the designed bandgap area (grey shaded region). All low temperature (light green markers) quality factors within the phononic bandgap and withing the HWHM of the optomechanical cavity yield Q's larger than 4×10^6, bringing the full multimode system, consisting of the membrane and the Fabry-Pérot cavity (see chapter 9) in which it is placed, into the strong cooperativity regime.

8.11 A FIRST GLANCE AT INDIUM GALLIUM PHOSPHIDE MEMBRANES

Before moving to the realization of the optomechanical cavity, I want to briefly present Q measurements on InGaP membranes. InGaP membranes combine the benefits of realizing high stress thin films with the possibility to fabricate a stack of membranes, which eventually can lead to an enhancement of the optomechanical coupling strength.

Within the last years a series of publications discussed the possibility to resonantly enhance the optomechanical coupling strength by using a number of membranes placed within a Fabry-Pérot interferometer. The stack of membranes can form a series of (sub-)cavities resonantly enhancing the interaction and yielding a large effective optomechanical coupling strength between the cavity mode and the membrane stack. The initial proposal was by Xuereb *et al.* in [147, 148]. An analysis for two membranes has been given by J. Li *et al.* [86] and the topology has been recently realized by Piergentili *et al.* [104] for

a pair of low and high stress membranes, reaching a factor of ≈ 2.5 larger coupling strengths compared to the single membrane case.

However, it is inconvenient to clamp a stack of membranes onto each other, as the stack will quickly limit the length of the cavity, especially because piezos need to be incorporated to set the exact distances between each membrane to fulfill a resonance condition. Additionally, the system will become mechanically unstable and hard to control when the number of elements increases.

A different approach would be by means of microfabrication of a stack of membranes with the correct thickness and spacing, preferably onto a highly reflective Bragg mirror. A promising material to fabricate a stack of membrane stacks is $In_xGa_{1-x}P$. At the same time, thin InGaP films can feature high stress, one of the main reasons that SiN membranes exhibit high quality factors.

Garrett Cole designed and fabricated a batch of $\approx$ 30 nm thick $In_xGa_{1-x}P$ (InGaP) membranes grown on GaAs. The optical characterization has been conducted within the group of Cindy A. Regal at JILA in Boulder Colorado, while the measurements of the mechanical quality factors were conducted by me within our laboratories in Vienna. The results have been jointly published by G. D. Cole *et al.* in [44].

Measurements of the quality factor on four different InGaP membranes have been made in our fiber setup at room temperature and at low temperature (17 K). The results are plotted in figure 8.17. Note that the room temperature values scatter widely and especially low order modes exhibit low quality factors. Also, almost all measurements at low temperature yield Q factors of $1 - 2 \times 10^6$, similar to the high stress SiN membranes in figure 8.11. In fact, the InGaP membranes tested here feature a tensile stress of about 200 MPa. Further reduction of the In content should increase the stress to values around 1 GPa [44] and hence comparable Q's as the high stress SiN membranes.

Measurements of the optical losses by incorporating the membranes into high finesse cavities yields optical losses of 40 ppm due to scatter and absorption, proving that InGaP membranes are eligible mechanical oscillators for optomechanical experiments and promising candidates towards the fabrication of vertically stacked membranes with large effective coupling strengths, theoretically feasible to reach the single photon strong coupling regime.

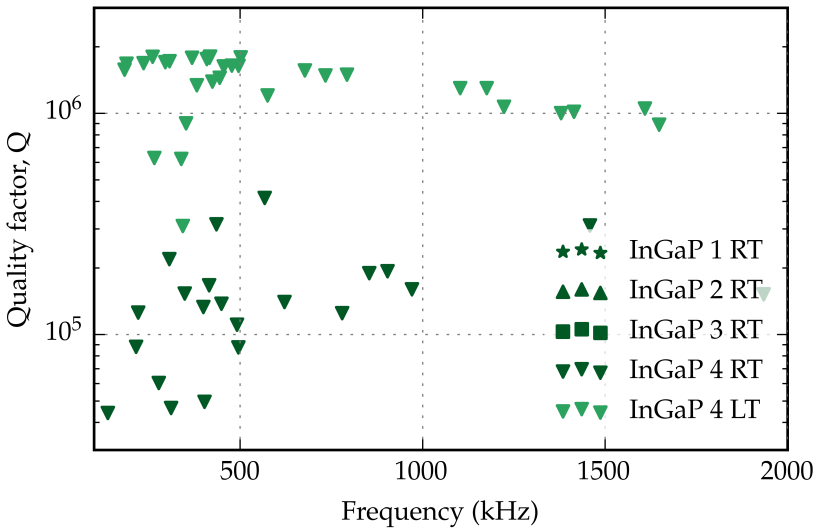

Figure 8.17: Q measurements on InGaP membranes. Q measurements at room temperature (dark) show a similar behavior as SiN membranes: Low order modes are more susceptible to mechanical losses due to coupling to the environment. Low temperature measurements at 17 K (light) show almost without exceptions values above 1×10^6. Note that the InGaP membranes tested here have rather low tensile stress. It can be assumed that high stress versions would yield fundamental resonant frequencies of 1 MHz and above, just like thin SiN membranes.

9 OPTOMECHANICAL CAVITY

This chapter introduces the optomechanical cavity (OMC), which consists of a silicon nitride membrane (see chapter 8) placed inside a high finesse Fabry-Pérot cavity. This system is known as the membrane-in-the-middle (MIM) cavity.

I will first describe the optomechanical interaction of a membrane placed inside an optical cavity and distinguish two cases: First, the membrane placed at the center of the cavity. And second, the membrane placed directly at the end of the cavity. It will be shown that the latter approach has several experimental benefits. The membrane-at-the-end optomechanical cavity is designed and realized, including the thermalization of the membrane within the cryogenic system and at high vacuum. This will minimize the coupling to the environment and therefore $\bar{n}\gamma$, which directly improves the quantum cooperativity.

Next, the experimental setup around the optomechanical cavity and the cryostat is presented and discussed, as these elements are the main tool to characterize the quantum cooperativity. The remainder of the chapter deals with a step by step characterization of the optical parameters, the single photon coupling strength and in-situ measurements of the quality factor of the membrane. The chapter closes with a summary and discussion of the achieved quantum cooperativity, showing that the system is operating in the strong cooperativity regime and that it should therefore exhibit the generation of optomechanical entanglement.

9.1 THE MEMBRANE-IN-THE-MIDDLE CAVITY

The goal of this section is to introduce the description of the full optomechanical experimental system, which is a thin dielectric silicon nitride membrane placed into a high finesse Fabry-Pérot cavity. The reflectivity of the membrane is too small for the standard end-mirror configuration in optomechanics, but we will see that placing the membrane inside a cavity leads to similar optomechanical coupling strengths as a high reflectivity membrane in the end-mirror configuration.

Figure 9.1 depicts the basic topology of the MIM system. We consider a thin membrane with amplitude reflectivity r and transmission t, as described in chapter 8, and a single-sided high finesse Fabry-Pérot cavity. The cavity consists of an input coupler with $r_1^2 + t_1^2 = 1, \delta_1 = 0$ and an end-mirror with $r_2^2 + t_2^2 = 1, \delta_2 = 0$, separated by

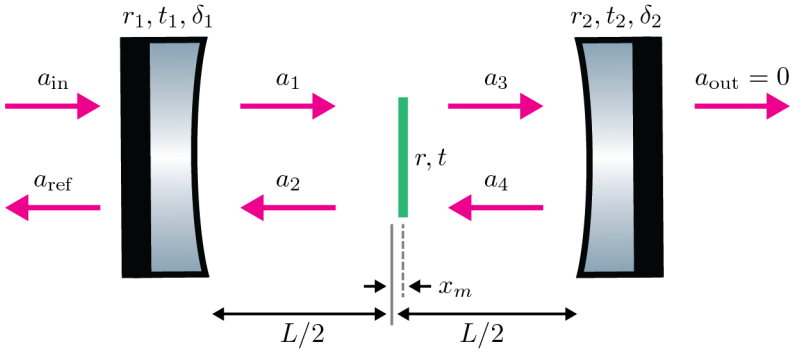

Figure 9.1: Schematic of the membrane-in-the-middle cavity. The bare Fabry-Pérot cavity is formed by two curved mirrors with amplitude reflectivities $r_{1,2}$, transmissions $t_{1,2}$ and absorptions $\delta_{1,2}$. The outer fields consist of the incoming laser beam a_{in} and the reflected and transmitted beams a_{ref} and $a_{\text{out}} = 0$ as we consider a single-sided cavity. While the intra-cavity fields are split by the thin membrane placed within the resonator and forming two coupled sub-cavities. The illustration helps to write down the set of coupled equations for all fields, see main text. The membrane position x_m is defined relative to the cavity center at $L/2$.

a distance L, while $r_{1,2}, t_{1,2}, \delta_{1,2}$ are the amplitude reflectivities, transmissions and losses. The membrane is placed somewhere between the mirrors and its position is described by x_m, which is measured with respect to the center $L/2$ of the cavity.

By using the boundary conditions at each mirror and the membrane, one can derive the following set of coupled equations for the classical electric field amplitudes

$$a_1 = it_1 a_{\text{in}} + r a_2 e^{ikL_1}, \tag{9.1}$$
$$a_2 = r a_1 e^{ikL_1} + it a_4 e^{ikL_2}, \tag{9.2}$$
$$a_3 = it a_1 e^{ikL_1} + r a_4 e^{ikL_2}, \tag{9.3}$$
$$a_4 = r_2 a_3 e^{ikL_2}, \tag{9.4}$$
$$a_{\text{ref}} = it_1 a_2 e^{ikL_1} + r_1 a_{\text{in}}, \tag{9.5}$$
$$a_{\text{out}} = it_2 a_3 e^{ikL_3}, \tag{9.6}$$

in which $k = 2\pi/\lambda$ is the wave vector of the light and ikL_1 and ikL_2 the accumulated phase in the left sub-cavity and right sub-cavity, respectively, given by $L_1 = L/2 + x_m$ and $L_2 = L - L_1$. For a derivation of the solutions for the cavity resonance frequency f_{cav} and the optomechanical coupling strength $g_m \equiv 2\pi d \times f_{\text{cav}}/dx_m$, I refer to the work of [74, 145] and only present the results and discuss the solutions with regard to the setup presented in this work.

The cavity resonance in units of the free spectral range is given by

$$\omega_{\text{cav}}/\omega_{\text{FSR}} = 2\pi \times f_{\text{cav}}/\omega_{\text{FSR}} = \cos^{-1}(|r|\cos(2kx_m)) + \arg(r), \tag{9.7}$$

in which r is the membrane reflectivity as in equation 8.3. The complex argument (or phase) of r is giving an offset to the resonance, while the resonant condition is mainly given by the laser wavelength $\lambda = 2\pi/k$ and the membrane position x_m and reflectivity r. Figure 9.2 shows several consecutive free spectral ranges of the membrane-in-the-middle cavity as a function of the membrane position x_m. Depending on its position and reflectivity, the membrane does alter the effective free spectral range (FSR) with respect to the bare cavity FSR.

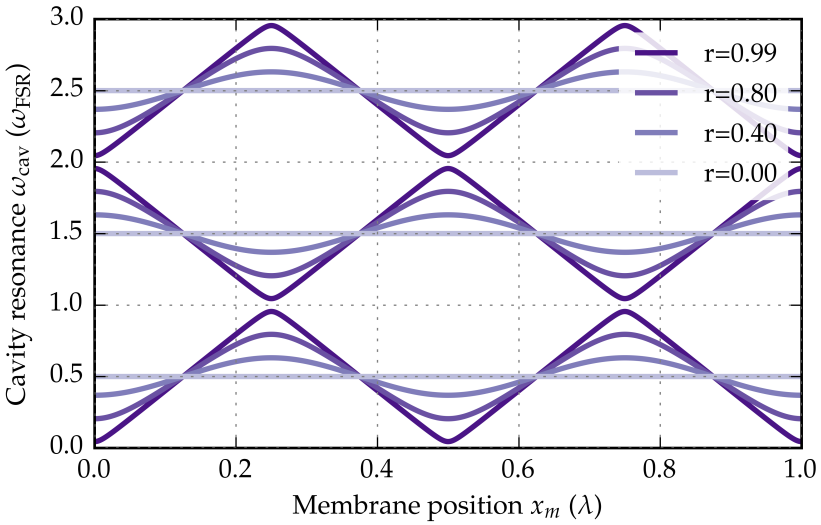

Figure 9.2: Resonant frequency of the membrane-in-the-middle cavity in units of bare free spectral range for different membrane reflectivities ($r = 0.00 - 0.99$ from lighter to darker traces), as a function of the microscopic position of the membrane in units of the laser wavelength. Note, the offset due to the argument of r is ignored here. Depending on its position within the standing wave of the optomechanical cavity, the membrane does alter the frequency of consecutive resonances. For high reflective membranes ($r \approx 1$) placed at nodes or anti-nodes of the cavity, the system effectively acts as a resonator with half the length and therefore twice the free spectral range. This effect is seen in the darkest trace with $r = 0.99$ at the position $x_m = 0.5 \times \lambda$). Note, that this plot assumes the membrane is macroscopically placed close to the center of the cavity, i.e. $x_m \ll 1$.

The solution for the optomechanical coupling for the membrane-in-the-middle system as a function of membrane position for $x_m \approx 0$, i.e. membrane placed closely to the center of the cavity, is given by the derivative of the resonance frequency

$$g_m(x_m) \equiv \frac{d\omega_{cav}}{dx_m} = -g_0 \frac{2|r| \sin(2kx_m)}{(1 - |r|^2 \cos^2(2kx_m))^{1/2}}. \tag{9.8}$$

This function is plotted in figure 9.3 in units of a hypothetical and equivalent end-mirror coupling strength $g_0 = \omega_{cav}/L$ and as a function of the membrane position. The main feature here is that the membrane coupling is a periodic function of membrane position. At nodes

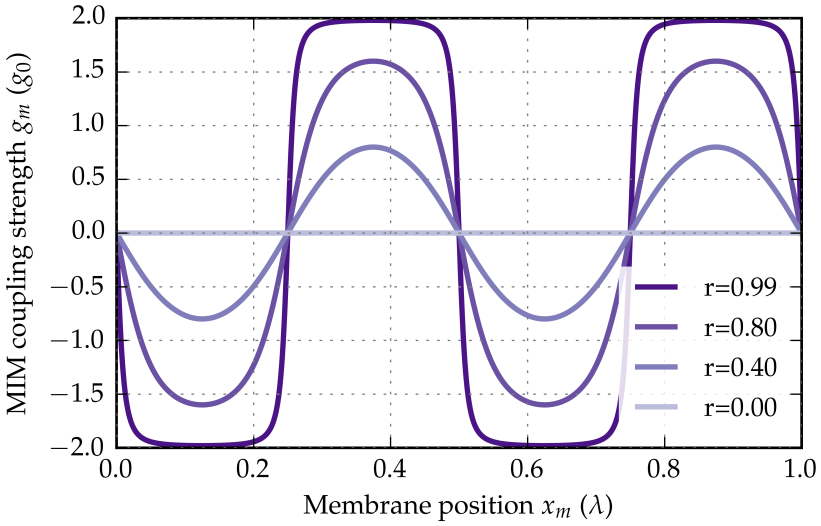

Figure 9.3: Membrane-in-the-middle (MIM) coupling strength. Depicted are several realizations of equation 9.8 in units of g_0 as a function of the membrane position in units of the laser wavelength for the membrane being placed close to the center of the cavity, $x_m \ll 1$. Nodes and anti-nodes of the cavity standing wave correspond to the zero-crossings of the traces. In between are maxima of the coupling strength, which in case of a perfectly reflecting membrane ($r = 1$) reach $g_m = 2g_0$. Essentially splitting the system into a cavity of length $L/2$ for a photon on either side of the membrane and therefore twice the single photon coupling strength as $g_0 \propto 1/L$.

of the intra-cavity field, e.g. $2kx_m = m \times \pi$ (the numerator becomes zero) and at anti-nodes, e.g. $2kx_m = (2m + 1) \times \pi$ (the denominator becomes infinite) the coupling strength becomes zero. The maximum coupling strength in between those points and for a perfectly reflecting membrane ($r = 1$) is twice the end-mirror coupling, i.e. $g_m = 2g_0$. Figure 9.3 depicts several traces for different membrane reflectivities.

The takeaway is that placing a thin membrane with moderate reflectivity inside a Fabry-Pérot resonator leads to similar coupling strengths as the standard end-mirror configuration. Therefore, combining the advantageous mechanical and optical properties of silicon nitride membranes with the simplicity of the well studied Fabry-Pérot cavity is a valid combination to pursue. Note, that the solutions for the resonances and coupling strengths are derived for the case of the membrane placed (macroscopically) close to the center of the cavity.

9.2 EXPERIMENTAL DESIGN: MEMBRANE AT THE END

Over the course of assembling and operating the presented experiment, several iterations of membrane-in-the-middle cavities have been designed, realized and characterized. While the very first designs leaned towards the initial proposed system, i.e. membrane

placed close to the center of the cavity, newer designs featured a topology where the membrane is placed very close to a high reflective flat end-mirror. This approach was motivated by ease of alignment and mechanical stability, but it has physical advantages also. The membrane in the center design and its disadvantages are shown and discussed in figure 9.4. Here, we will directly continue with the membrane at the end design.

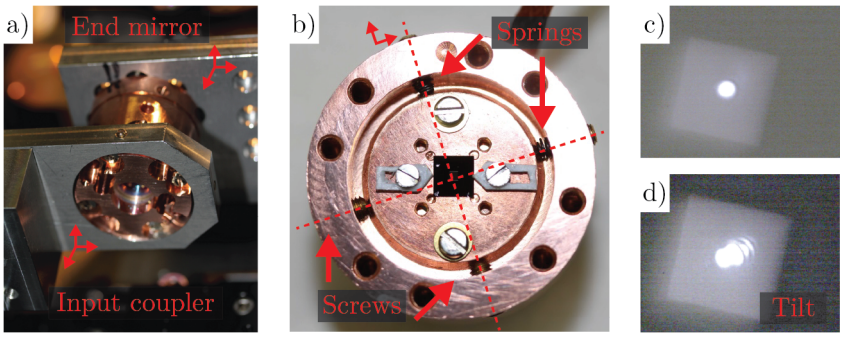

Figure 9.4: Old membrane-in-the-middle design. a) Picture of the membrane-in-the-middle cavity spacer, consisting of two spacers holding the input coupler and end mirror respectively, while the membrane is clamped onto a separate chip fixed onto the end-mirror spacer, see b). Each spacer is connected via adapter plates to a 3d µm-precision positioning stage for alignment purposes. b) The membrane chip is embedded within the end-mirror spacer and can be aligned within the $x-y$ plane by means of two screws pressing the chip against two springs. The whole procedure is time consuming and the outcome is very susceptible to external forces, e.g. when mounting the cavity back into the cryostat, or when cooling the system, which cause the membrane to tilt with respect to the cavity mode. A well aligned cavity mode (picture c) can be distorted by membrane tilt and produce images like in d). Tilt strongly increases losses within the system and therefore we moved to the more mechanically stable and easier to align membrane at the end configuration.

Wilson [145] derives a modification of equation 9.8, which features an envelope function transforming the peak coupling values as the membrane is moved towards either of the cavity mirrors. The coupling strength reads

$$\tilde{g}_m(x_m) \approx \frac{g_m(x_m)}{g_0 - g_m(x_m) \times (x_m/L)}, \tag{9.9}$$

and allows a comparison of the coupling strength for different membrane positions. These two cases, as well as the full envelope across the full length of the cavity is depicted in figure 9.5. The main message is that the periodic behavior is maintained at all positions and that the end-mirror configuration is slightly advantageous in terms of optomechanical coupling strength.

The main experimental advantages are a strongly simplified alignment procedure, since the number of degrees of freedom is reduced

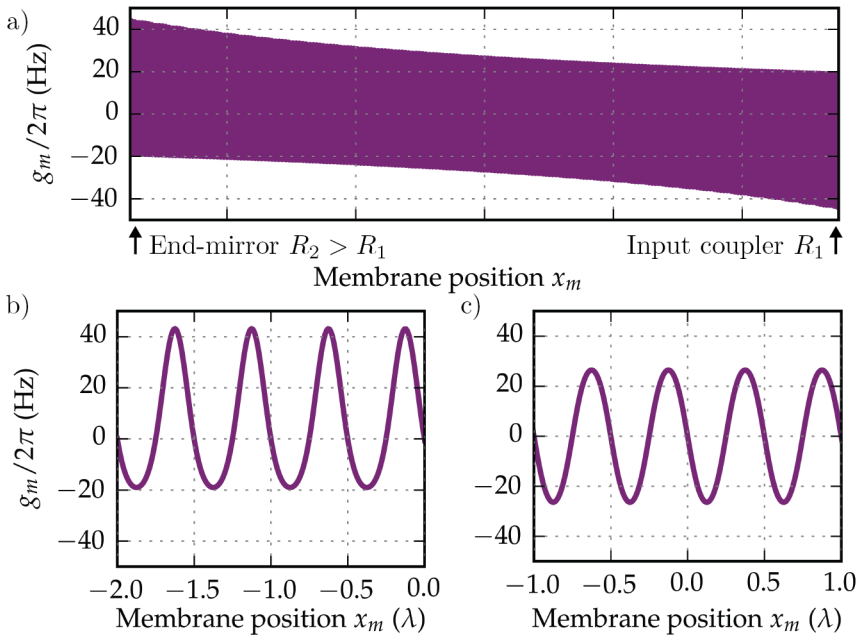

Figure 9.5: Optomechanical coupling for a membrane-in-the-middle (MIM) cavity. a) Shows the coupling strength g_m across the full lengths of a 5 mm long cavity, for a mechanical oscillator with a frequency of 1 MHz and an amplitude reflectivity of 35 % and 40 nm thickness. The left side marks the end-mirror configuration and features a slightly larger optomechanical coupling strength compared to the center of the cavity. b) and c) depict a zoom into a position at the end-mirror and the middle of the cavity respectively, with the membrane at the end topology providing a larger g_m. The reason for the asymmetry is that the end-mirror reflectivity is higher than the input coupler reflectivity ($R_2 > R_1$) and the sub-cavity with the end-mirror has a higher finesse and therefore a larger power build-up and effectively more light interacting with the membrane (compared to the lower finesse sub-cavity, if the membrane is placed closer to the input coupler).

and a more rigid and compact design that allows for a shorter cavity that is less susceptible towards external vibrations and features almost no membrane tilt during cool downs in the cryostat.

Our specific design currently in use is depicted in figure 9.6. The cavity consists of a spacer holding a flat end-mirror (1.0 inch diameter) and the SiN membrane (A). Spacer A is connected to the cold plate of the cryostat via an adapter plate (C). The flat end-mirror is embedded in a drill-hole and fixed by a thin ring that pushes the mirror uniformly against the spacer and keeps it there. Between each mirror-to-metal connection, a thin layer of Teflon is used to prevent the substrates from being scratched. Only the outer parts of the mirror are resting on a hole in the spacer, such that most of the mirror coatings are bare, providing enough space to carefully place a glued chip (SiN membrane chip on empty Si chip, see chapter 8.9) and clamp it to the spacer with metal or Teflon clamps, see figure 9.6 c). These clamps can be fixed via screws onto four indentations, which are four

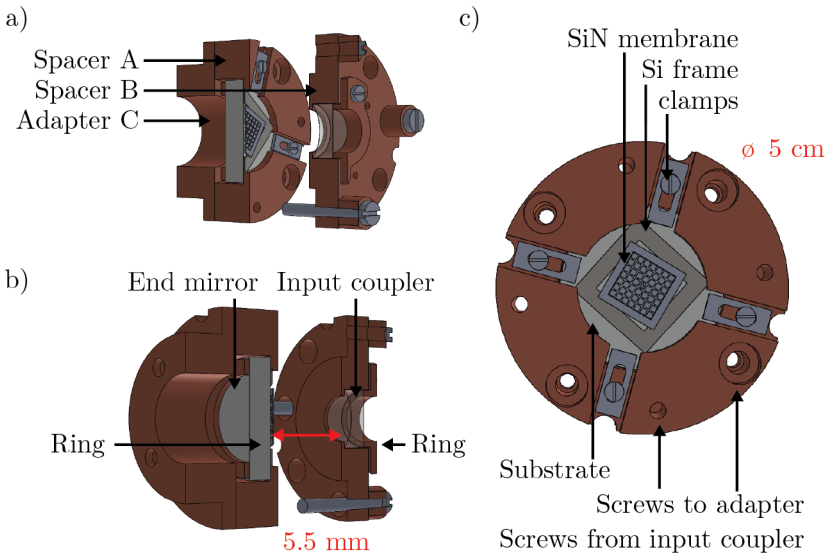

Figure 9.6: CAD drawings of the optomechanical cavity. a) and b) show a sectional view from the front and back of the cavity. The length of the cavity (mirror to mirror) is 5.5 mm and the diameter of the full spacer is 5 cm. The mirrors are clamped uniformly onto the spacers by means of a ring. c) The Si chip to which the SiN phononic bandgap membrane is glued, is fixed onto the flat end-mirror by clamps. Four long screws running through a hollow cylinder and a spring are used to fix the spacers to each other during the alignment procedure. The springs are short-circuited by the cylinders when the spacers are finally bolted together.

small areas on the outer part of the spacer A, each shifted by 90° with respect to each other. These areas also offer space for small sized silicon diode based temperature sensors from Lake Shore Cryotronics [9] for thermalization measurements close to the membrane.

The second spacer (B) contains the input coupler, which is a 0.5 inch (diameter) mirror with 10 cm radius of curvature. The input coupler is also fixed to its spacer via a ring clamping it to an indented part of the coupler. Additionally, the outer side of the spacer contains several threaded holes to fix temperature sensors or piezos for shaking the spacer and exciting the membrane motion for ring-down measurements. The two mirrors form a 5.5 mm long, hemispherical optical cavity. The cavity waist (radius) is positioned on the flat mirror, close to the membrane and has a nominal size of $w_0 = 88\,\mu\text{m}$.

Most of the metal parts, like spacer A and B, are made of copper to achieve fast and good thermalization at cryogenic temperatures below 10 K. This is assured by the choice of material, since copper has roughly a thermal conductivity of about 400 W/mK, which is larger than that of most other materials. Additionally, each connection of different parts features a boundary resistance R_{bd} that determines the temperature drop across an interface of two metals. It is a function

of the microscopical contact area and the pressure applied to bolt the two surfaces [113]. We carefully polish all areas such that heat will be transferred across and tightly bolt them together. For polishing, we start off with sandpaper and then apply fiber polishing paper to reach µm-level roughness.

We use nickel plated screws out of brass, since brass has a good thermal conductivity and a larger coefficient of thermal expansion compared to copper, such that screw-joints will remain tight while cooling down and not loosen during thermalization.

The optical properties are mainly given by the reflectivities of the mirrors and are summarized in table 9.1. The end-mirror has a nominal transmission of $T_2 \leq 2\,\text{ppm}$ and the input coupler transmission is $T_1 \approx 950\,\text{ppm}$. These parameters are chosen to ensure a single-sided cavity, even in the presence of additional losses due to scatter, absorption, tilt or diffraction of the membrane and due to the fact that the membrane is slightly off the cavity waist position due to the finite thickness of the chip. The nominal (calculated from the data sheets of the mirrors) empty cavity Finesse is $\mathcal{F}_{\text{empty}} \approx 6600$. The empty free spectral range of $\omega_{\text{FSR}}/2\pi = 27.3\,\text{GHz}$ is given by the nominal cavity length of $L = 5.5\,\text{mm}$. The deduced cavity line width is $\kappa/2\pi = 2.1\,\text{MHz}$, keeping us in the so called bad cavity limit ($\omega_m < \kappa$) and ensuring efficient scattering into the Stokes and anti Stokes sidebands for a resonant laser drive. The cavity parameters are listed and compared to experimentally obtained values in table 9.1.

In summary, we chose a quasi monolithic cavity design to ensure optimal mechanical stability, a short resonator length to increase the single photon coupling strength and to minimize the heat-load onto the Helium flow cryostat and achieve good thermalization.

9.2.1 *The alignment procedure*

The costs of leaving out any positioners and piezos are plain, e.g. in situ re-alignment of the cavity or the membrane during a cool-down is not possible. Furthermore, the microscopical placement of the membrane with respect to the standing wave is random for each cool-down.

Fortunately, the design proves to be very stable such that all the downsides do not impose serious problems. Once correctly aligned, membrane tilt does not occur, even after several cool-downs, which can be necessary to reach the maximum coupling strength as every cool-down is random. No increase of optical (finesse) or mechanical losses have been observed over the course of weeks and over 10 cool-downs.

As mentioned earlier, placing the membrane in the center of the Fabry-Pérot cavity proved to be difficult to align in the first place and it regularly suffered from membrane tilt during cool-downs. The two mirrors need to form a stable cavity mode and, in addition to that, the membrane needs to be aligned properly in several ways: The membrane needs to be placed into the cavity waist laterally (which is defined by the position of the flat end-mirror) as it behaves like a partially reflective flat mirror and will introduce losses the further it is away from the end-mirror. Then, the membrane must properly overlap with the cavity waist transversally (effective mass) to optimize the coupling. On top of that, the membrane must not exhibit any tip and tilt with respect to the cavity axis as that would significantly distort the cavity mode and decrease the finesse of the optomechanical cavity. These challenges are partly illustrated in figure 9.4 a) to d).

In contrast, when placing the membrane directly onto the flat end-mirror, significant tilt was only observed once out of two dozen installments (if following the membrane gluing procedure from chapter 8.9). In terms of internal alignment, only the input coupler needs to be aligned correctly to build up a cavity mode and to hit the membrane in its center. The membrane then automatically sits within a couple of µm close to the cavity waist (transversally) and all other alignments remain to be externally. Also, small misalignments during a cool-down can be addressed by external re-alignments that are accessible at all times.

The common alignment procedure is outlined in the following and diagrammed in figures 9.6 and 9.8, which help understanding the procedure:

- Align the laser beam externally by a set of mirrors and a lens system, i.e. mode matching. Guide the beam straight through the center of the cryostat windows in a plane parallel to the optical table. Use the lens system to focus the beam at the lateral position of the end-mirror by using a laser viewing card or a camera.

- In transmission of the cryostat's rear window, collect the light from the laser and from an LED and produce a sharp image at the position of the CCD camera (see figure 9.8). Align the camera by means of tip and tilt (perpendicular to the light) and transversal translation to hit the center.

- Mount the end-mirror with membrane chip (spacer A) onto the adapter plate into the cryostat. Fix the spacer at a position, where the incoming beam is reflected back into itself and the residual transmission through the end-mirror and the LED light produce a clear image in the CCD.

- Align the reflected light onto the Pound-Drever-Hall locking detector by the mirror set and lens system.
- Add spacer B and the input coupler (IC). It is helpful to use the cooling beam (see chapter 5.4) at this stage, because it can be swept by a 40 GHz $> \omega_{\mathrm{FSR}}$ modulation to scan over a full free spectral range of the cavity.
- The screws used to fix spacer B to A are not directly pressing the two spacers onto each other, but are running through a hollow cylinder and a spring. The dimensions are chosen in a way, that when tightening the screws, the springs will kick in first and hold the full spacer together, while offering the opportunity to align the input coupler in the plane perpendicular to the beam direction.
- A good starting point for achieving a cavity power build-up is to initially place the IC in a way that the direct reflection of it hits the PDH detector. Move the IC around until the TEM_{00} cavity mode is found on the CCD.
- Next, the cavity mode needs to hit the center of the membrane by transversally shifting the IC. This can be done manually by hand or by means of a set of µm precision positioners attached to the IC by an additional adapter plate.
- The four screws can be slowly tightened, up to the point where the hollow cylinders bypass the springs and rigidly fix all parts together to form a quasi monolithic block.
- External mode matching can be optimized by means of maximizing the coupling into the TEM_{00}. Eventually, it is necessary to slightly optimize the PDH detector and the CCD camera positions after mode matching.

This procedure leads repeatedly to a well aligned and stable membrane at the end cavity. The whole procedure may take as little as several minutes overall, including opening and closing the cryostat and pumping the chamber. Therefore, this system is also convenient for testing purposes (e.g. Q measurements of several membranes) on a daily basis.

9.2.2 *The cryogenic system and thermalization*

The optomechanical cavity needs to be placed in high vacuum, to reach Q factors as large as 1×10^7 and above (see the discussion of air damping in figure 8.12), and it needs to be thermalized to temperatures as low as $\approx 10\,\mathrm{K}$ to reduce the average number of phonons

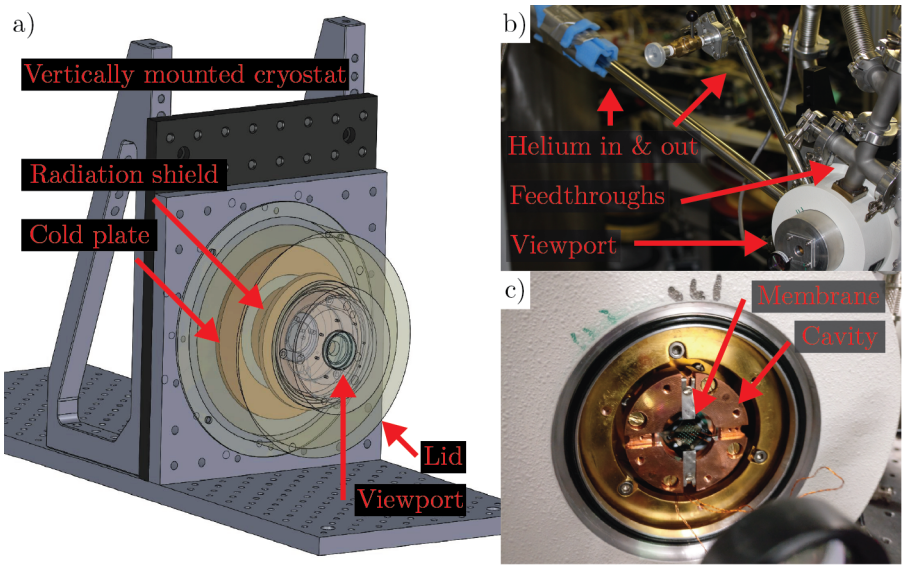

Figure 9.7: The cryogenic setup. a) A CAD drawing of the vertically mounted cryostat, which is partly transparent for better visualization. The optomechanical cavity (OMC) is mounted on the gold plated cold plate. A copper thermal shield covers the membrane and is also thermalized at the base temperature to serve as an 4 K environment for the OMC and limits room temperature radiation heating up the membrane. The final temperatures at which the membrane typically thermalizes are between 8 and 10 K. The lid contains a viewport for optical access and is tightened by turning on the vacuum pump and compressing a Viton o-ring seal. b) Picture of the cryostat with mounted Helium supply and return pipelines. The feedthroughs feature wires for vacuum and thermal sensors as well as a piezo. c) Close-up of the open cryostat without thermal shield and lid. The OMC (without input coupler) is shown and the membrane (with its bandgap structure) is placed at its center.

in the membrane. The cryostat serves that purpose and basically reduces $\bar{n}\gamma$ in the quantum cooperativity.

In the experiment presented, we use a liquid Helium continuous flow cryostat from Janis Research Company [7] with the sample placed in vacuum. The full system is illustrated in figure 9.7 and consists of a cold finger (plate), radiation shield, sample holder, feedthroughs and a cryogenic transfer line for the liquid Helium supply. The incorporation of the cryogenic system into the remainder of the experiment can be seen in figure 9.8.

The transfer line can be connected to a liquid Helium dewar to supply the cryostat with Helium and cool it down to temperatures as low as 4.2 K. During the cool-down the low temperature liquid will boil and the gas will leave the system via the return line. During this process, the boiling will cause large vibrations that can be seen as a jitter in the error signal of the OMC. After thermalization of the cold plate the system becomes vibrationally quite as it does not include any

moving metal parts, i.e. compared to a pulse-tube system. Together with the quasi monolithic design of the optomechanical cavity, the laser stabilization onto the cavity yields long-term stability enabling long measurement runs without interruptions.

The feedthroughs enable us to lay wires into the sample chamber. These include wires for temperature sensors for measurements at the cold plate and directly at the OMC and a voltage supply for a piezo used for ring-down measurements. Additionally, a vacuum sensor is connected to determine the vacuum level reached inside the chamber as well as a vacuum hose connected to the pump-station. The hose is cemented to damp mechanical vibrations of the pump-station and limit their impact on the cryogenic system. We use a pump-station from Pfeiffer Vacuum Technology AG [8] consisting of a scroll pump to provide the necessary pre-vacuum for the turbomolecular pump, which reaches levels as low as 1×10^{-5} mbar at room temperature. After cooling down the system, cryogenic pumping will kick in and the final vacuum reached is below $< 1 \times 10^{-6}$ mbar. The vacuum is limited by residual outgassing of components and the vacuum seals in use.

The final temperature of the membrane is usually between 8 to 10 K. Apart from the low vibrations, another upside of this cryostat is a quick cool-down time of around 30 min. The membrane finally thermalizes after roughly 60 min, which can be monitored by the shift of the resonant frequency due to the contractions while cooling. A heater is included to rapidly heat-up the system overnight, such that cool-downs on a daily basis are possible. The only downside compared to a closed cycle pulse tube cryostat or a dilution refrigerator is that it cannot be run indefinitely as the cool-down is limited to the amount of liquid Helium in the dewar, e.g. typically one day.

9.3 CHARACTERIZATION OF THE SYSTEM

After introducing the optomechanical system, it is time to characterize it and bring it into the strong cooperativity regime. A simplified schematic of the different tools present to characterize and operate the optomechanical system are illustrated in figure 9.8.

9.3.1 *The optical parameters*

Mode matching

After following the alignment procedure from the last section, we start with the mode matching of the optomechanical cavity. The mode matching is defined as the ratio between the amount of power coupled into the TEM_{00} mode of the OMC and the sum of all modes. A straightforward way to do this is by locking the laser to the cavity and

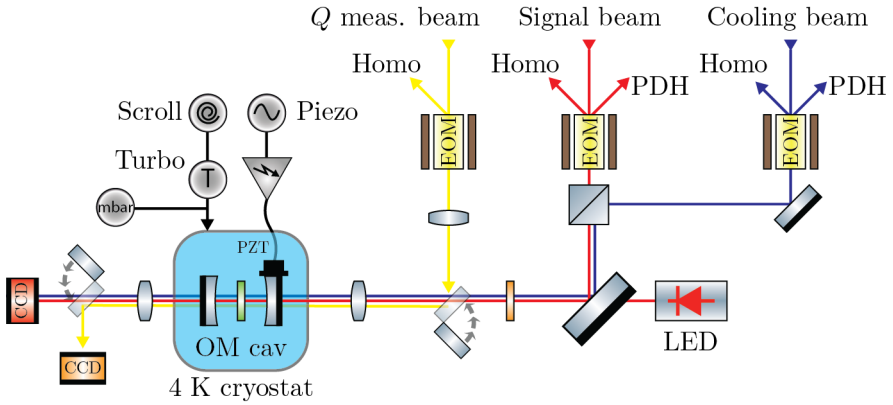

Figure 9.8: Simplified schematic of the optomechanical cavity setup. The optomechanical cavity is placed within the Helium flow cryostat. A scroll pump and a turbomolecular pump reach high vacuum before the cryostat can be cooled. A piezo, temperature sensors and a vacuum sensor are connected inside of the cryostat via feedthroughs. The cavity can be pumped by the main signal beam at 1064 nm and by the cooling beam shifted by one free spectral range of the cavity (see chapter 5.4). Both beams can generate a Pound-Drever-Hall locking signal and therefore be used for stabilizing the laser to the cavity. A third beam, the Q measurement beam from a different laser source at 1550 nm can be used to probe the membrane displacement without imposing cavity optomechanical effects such as cooling and heating. Each beam features a spare electro optical phase modulator (EOM) for the generation of single frequency sidebands or sweeping sidebands for probing purposes. All three beams have a respective homodyne detector for detecting the phase quadrature, while the signal beam also has a detector for the amplitude quadrature to reconstruct the state of the system or correlation measurements described in part five of this thesis. A red LED is used to illuminate the membrane. Two CCD's in transmission of the cryostat can be used for imaging of the membrane and cavity mode: with one CCD sensitive at 1064 nm and the other at 1550 nm.

monitoring the DC channel of the PDH detector on an oscilloscope. Since the laser piezo is only able to scan over a small fraction of the full free spectral range (FSR), it is necessary to slowly tune the laser temperature over one FSR while rapidly scanning the laser simultaneously. A specific cavity mode can be identified by looking at the image of it on the CCD (see figure 9.8 in transmission of the OMC). The voltage of the PDH resonance is proportional to the power of the light mode, such that the measurement of all voltages $V_{m,n}$ for all resonances (m,n) seen on the PDH detector can be used to calculate the mode matching of the $(0,0)$ mode via the relation

$$MM_{(0,0)} = \sum_{m=0} \sum_{n=0} \frac{V_{0,0}}{V_{m,n}}, \tag{9.10}$$

while n and m are the mode numbers and run from zero to the highest mode visible on the detector. It is useful to look at the height of the error signal (see chapter 7) instead of the resonance (cavity dip),

as the noise on the error signal is filtered and the signal is amplified, yielding a better signal to noise ratio and more accurate measurements. For symmetry reasons, the $(1,0)$ and $(0,1)$ modes need to vanish, when the $(0,0)$ mode is aligned perfectly. Once the mode matching reaches values above 90 %, we found best performance by minimizing the $(1,0)$ and $(0,1)$ modes.

If membrane tilt (compare figure 9.4 c) and d)) is minimal, it is possible to reach mode matching values of $mm_{(0,0)} \geq 95\,\%$, which is limited by a combination of residual membrane tilt, residual diffraction at the membrane window and small mode distortions by the curved (10 cm) input coupler.

A good mode matching is important for two reasons. Any light not coupled into the fundamental mode of the cavity does not interact with the membrane. Also, it is reflected back to the PDH detector and decreases the signal to noise ratio of the locking detector and therefore also the feedback and the stability of the optomechanical system.

Note, that during a cool-down, all spacers and screws will slightly contract and move relatively to each other. Therefore, it is ideal to measure and optimize the mode matching after cooling down and before continuing with further measurements.

Free spectral range and cavity length

Considering the relatively short (nominal) cavity length of just 5.5 mm, errors in the manufacturing of the spacers, polishing of all parts and contraction while cooling, can lead to a significantly different cavity length and FSR.

One straightforward method to determine the FSR is by sending two independent beams onto the same resonance of the optomechanical cavity, and then shifting the frequency of one beam until it enters the cavity at the next resonance. Then, the FSR is equal to the frequency difference of the beams.

We do exactly this by sending the signal beam in and tuning the temperature of the laser until it resonates. Then the cooling beam is sent to the OMC and its modulation frequency is swept until the adjacent resonance is found.

Both modes can be monitored on the oscilloscope by measuring the DC channel of the PDH detector. This measurement method is slightly corrupted by the small birefringence between the different polarizations of the two beams. This effect can be accounted for, by intentionally changing the signal beam's polarization and measuring the frequency difference between its vertically and horizontally polarized parts. However, the measured effect is on the order of several MHz and negligible, since it is smaller than one percent of the nominal FSR.

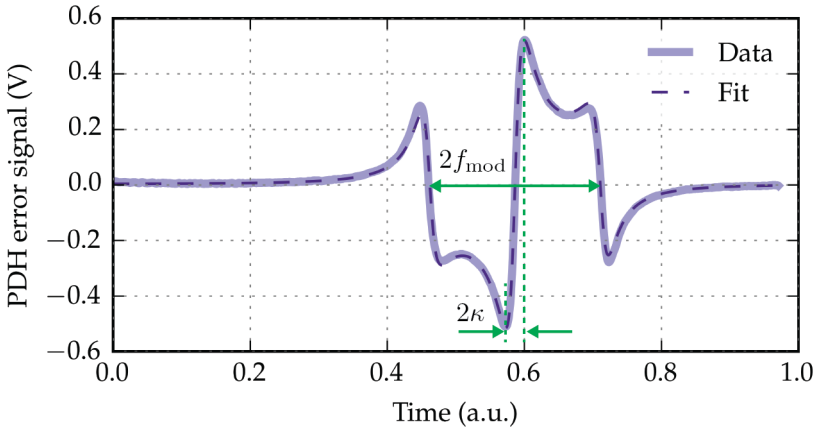

Figure 9.9: Cavity line width from error signal fit. The main signal beam with PDH sidebands at $\pm f_{\mathrm{mod}}$ is scanned over the cavity resonance. A measurement of the error signal taken with an oscilloscope is depicted in light purple and a fit of the PDH error signal is plotted in dashed dark purple lines. The distance of the outer zero-crossings correspond to twice the modulation frequency and can be used to calibrate the time-axis into absolute frequency units. The difference of the turning points of the centered zero-crossing is equal to the full width at half maximum (2κ) of the carrier light. These two distances are depicted in green and can be compared to each other to determine the cavity line width κ.

The measured empty cavity free spectral range is $\omega_{\mathrm{FSR}}/2\pi = 28.947\,\mathrm{GHz}$, which corresponds to a cavity length of $L = 5.18\,\mathrm{mm}$. This value is needed together with the cavity line width to determine the cavity finesse and optical losses of the system as will be shown in the following section.

The cavity line width and optical losses

The second important optical parameter is the optical cavity line width. It enters the quantum cooperativity directly and can be, together with the FSR, used to calculate the finesse of the cavity and therefore the additional internal cavity losses.

We present two methods to determine the line width. The first is by using the PDH modulation frequency as a frequency-ruler and the second is by sweeping a weak probing sideband over the resonance.

The first method, takes advantage of the fact, that we exactly know what the PDH modulation frequency is, in our case $\omega_{\mathrm{mod}} = 2\pi \times 20\,\mathrm{MHz}$. This method is useful to quickly measure the line width and determine the losses of the system after alignment or after thermalization during a cool-down. On the other hand, it is susceptible to the exact phase relation between the modulation and demodulation signals of the error signal, and is also affected by the nonlinearity of the piezo while scanning over the full range.

The PDH method is based on the fact that the Pound-Drever-Hall error signal features three zero crossings when the laser frequency is swept over the cavity resonance. One at the carrier frequency and two at $f_{\mathrm{mod}} = \pm 20\,\mathrm{MHz}$ with respect to the carrier. The frequency difference between these sidebands is precisely known as we set it with a function generator. This information can be used to calibrate the x-axis of the oscilloscope traces (time). The turning points of the zero-crossing of the carrier beam is equal to the full width at half maximum ($2 \times \kappa$) of the cavity resonance. The latter can be compared to the known frequency difference of the sidebands to calculate the cavity line width κ. It is important to carefully choose the relative phase of the modulation and demodulation signals of the detector and fit the error signal to retrieve the distance of the sideband zero-crossings ($= 2f_{\mathrm{mod}} = 40\,\mathrm{MHz}$) and the distance of the turning points around the centered zero-crossing of the carrier. Comparing these distances yields the cavity line width κ. Figure 9.9 gives an example of measurement data and its fit. Since we determined the free spectral range independently, we can now calculate the cavity finesse.

The second method to determine the cavity line width makes use of a probing sideband that is swept over the cavity resonance. This scheme is equivalent to a measurement of optomechanically induced transparency (OMIT), which is the radiation pressure based optomechanical analog of electromagnetically induced transparency (EIT) in atomic physics. It is the effect of the reflection of a weak probing beam on cavity resonance due to destructive interference with the anti-Stokes scattered photons of the red-detuned pump beam [76, 140].

The optomechanical cavity is locked on resonance by a weak signal beam. The cooling beam (chapter 5.4) is placed red-detuned with respect to the cavity resonance. Another electro optical phase modulator (EOM) is used to create sidebands on the cooling beam that are continuously sweeping from the carrier towards higher and lower frequencies. The upper sideband probes the cavity resonance. The cooling beam and its upper probing sideband are measured by homodyne detection in reflection of the cavity. The signal is then measured by a network analyzer, which compares the homodyne signal to the sweep that is used to generate the sideband. Figure 9.10 illustrates a measurement of the magnitude and phase of the signal. These measurements are divided by a measurement far off resonance, such that spectral features (transfer functions) of the detector, the EOM and other electronics are accounted for. Fitting a Lorentzian to the cavity dip in magnitude and the turning points of the phase yields the line width κ. The resulting finesse is 6499 ± 316, which matches very well with the nominal value of 6500.

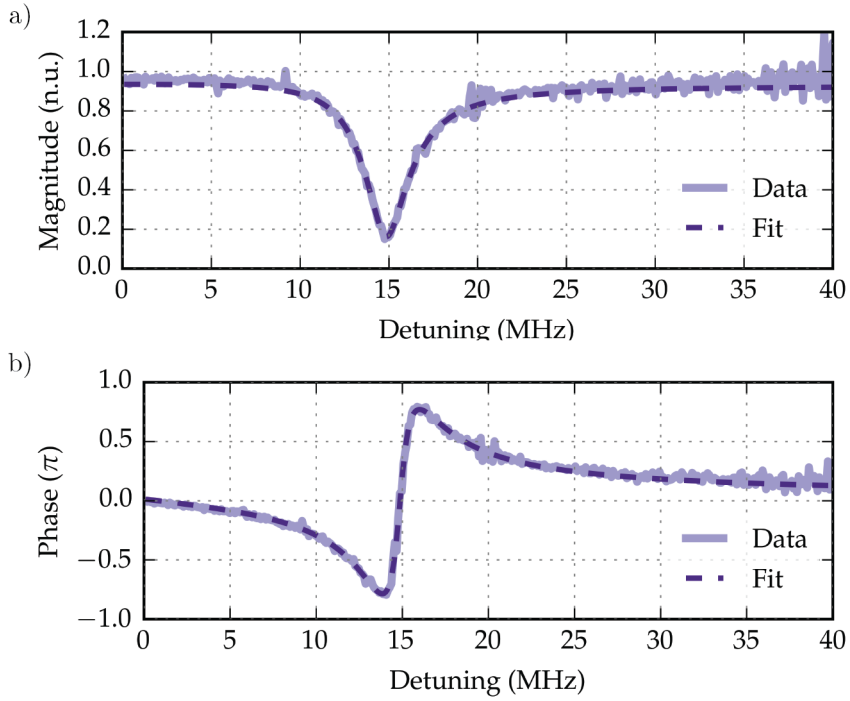

Figure 9.10: Sideband probing of cavity resonance. Measured magnitude a) and phase b) of the light reflected off the optomechanical (light purple) cavity. The cooling beam is red-detuned and at DC frequency. The probing sideband sweeps over the cavity resonance and maps the line width in its amplitude response in a) and in its dispersion shaped phase response in b). A fit of both functions is plotted in dashed dark purple lines: The distance to cavity resonance (i.e. minimum in magnitude and zero-crossing in phase) is 14.67 ± 0.149 MHz and the finesse is 6499 ± 316, which matches very well with the nominal value of 6500.

The DC trace of the same PDH detector, together with power meter measurements of the incoming, reflected and transmitted light, which are proportional to the squares of the amplitudes a_{in}, a_{ref} and a_{out} (see figure 9.1 for reference), and their relations, equations 9.5 and 9.6, can be used to determine the power transmission of each mirror and the total losses of the system. A third independent equation for our three unknown variables is given by the finesse $\mathcal{F} \approx \pi/(1 - r_1 r_2)$ of the cavity [16].

The results for κ, $\mathcal{F}$, t_1^2, t_2^2 and the losses δ for the optomechanical cavity (with and without a SiN membrane incorporated) can vary a lot. The empty cavity is, for instance, heavily dependent on how clean the mirrors are. We use a polymer called First Contact [11] to remove dust and other large particles from the mirror coatings that otherwise could scratch it while cleaning it. After using the polymer solution, one can use lense paper and acetone to clean the surface. A good way to dry the coating without leaving residuals and produce stains on it is by blowing off the acetone with a clean source of Helium/Nitrogen until the whole surface is dry. With the membrane incorporated

on the other side, any misalignments, i.e. membrane tilt, can yield a significant decrease of the finesse (increase of κ) due to additional losses.

Average results for the empty cavity finesse are around $\mathcal{F}_{\text{empty}} \approx 6500$ and around $\mathcal{F} \approx 6200$ for the full optomechanical cavity. We believe this is mainly limited by diffraction at the membrane window, the membrane being slightly off the cavity waist and residual tilt, scattering and absorption. A full set of measurements and fits can be found in table 9.1.

Two methods to measure the cavity line width and determine the cavity finesse have been presented. The PDH locking signal method, which is a quick method after re-assembling the optomechanical cavity. And the probing sideband method that yields more accurate results and that is less susceptible to error sources. Next, I showed how to obtain the mirror transmissions and internal cavity losses. The results are summarized in table 9.1 and are in good agreement with the designed values and data sheets of the mirror coatings.

The cavity line width is $\kappa/2\pi \approx 2.34\,\text{MHz} > 1.2\,\text{MHz} = \omega_m$, such that the optomechanical system is operated in the bad cavity regime, which is a necessary condition for the efficient application of the entanglement protocol discussed in chapter 10. In addition, the cavity length has been successively reduced until reaching the current value of 5.18 mm. A short cavity length increases the single photon coupling strength that is discussed in the following section.

PARAMETER, SYMBOL	EMPTY	MEMBRANE
Cavity length, L	5.18 mm	-
	(5.5 mm)	
Free spectral range, $\omega_{\mathrm{FSR}}/2\pi$	28.95 GHz	-
	(27.3 GHz)	
Cavity line width, $\kappa/2\pi$	2.25 MHz	2.34 MHz
	(2.1 MHz)	
Finesse, $\mathcal{F}$ (PDH method)	6438	
(sideband probe)	6499	6179
	(6500)	
Input mirror transmission, T_1	936 ppm	960 ppm
	(950 ppm)	
Output mirror transmission, T_2	0.7 ppm	0.4 ppm
	(<2 ppm)	
Additional losses, δ	38 ppm	56 ppm

Table 9.1: Nominal and measured optical cavity parameters extracted from the error signal and sideband probing. Results of the PDH error signal method for determining the optical line width (see figure 9.9) and cavity finesse. Power meter measurements of the input, transmitted and reflected light yield the power transmissions of the mirrors and the additional losses. The power transmission of the mirrors are in good agreement with the nominal values given in parentheses.

9.3.2 *Single photon coupling and cooling*

The goal of this section is to determine the single photon coupling strength g_0 as it determines how strongly a single photon interacts with the membrane. The presented approach utilizes the effects of optomechanical radiation pressure cooling on the mechanical resonant frequency ω_m and mechanical damping γ. I will first provide a short description of the physics, explain the experimental procedure and then discuss measurements.

The starting point is the classical version of the set of linearized optomechanical equations of motion, given by taking the average of their quantum counterparts from chapter 4.2.1. These equations can be solved in frequency space (Fourier transformation) and in the presence of the optomechanical interaction leads to a modified version of the interaction free mechanical susceptibility $\chi(\omega)$, which has been already derived in chapter 8 equation 8.16. The real and imaginary part of the modified susceptibility lead to modifications of the resonant frequency $\delta\omega_m(\omega)$ and impose an additional damping rate $\gamma_{\mathrm{opt}}(\omega)$ onto the mechanical oscillator [27], reading

$$\delta\omega_m(\Delta) = \bar{n}_{\mathrm{cav}} g_0^2 \frac{2\Delta}{\kappa^2/4 + \Delta^2}, \tag{9.11}$$

$$\gamma_{\mathrm{opt}}(\Delta) = \bar{n}_{\mathrm{cav}} g_0^2 \left(\frac{\kappa}{\kappa^2/4 + (\Delta + \omega_m)^2} - \frac{\kappa}{\kappa^2/4 + (\Delta - \omega_m)^2} \right), \tag{9.12}$$

which assume a high Q oscillator ($Q \gg 1$), the so called bad cavity limit ($\kappa \gg \omega_m$) and a weak laser drive ($\kappa \gg g$), which are all given in the system presented here.

The modification of the resonance frequency

$$\omega_{m,\mathrm{eff}} = \omega_m + \delta\omega_m(\Delta) \tag{9.13}$$

is the so called optical spring effect [72, 98], and the additional optical damping term leads to an effective mechanical damping

$$\gamma_{\mathrm{eff}} = \gamma_m + \gamma_{\mathrm{opt}}(\Delta). \tag{9.14}$$

Depending on the laser detuning Δ, the optomechanically added damping rate can flip its sign and either increase the effective damping and cool the oscillator motion (red-detuning) or cause anti-damping and heat the oscillator motion (blue-detuning), compare with chapter 4.2. In the sideband resolved regime $\kappa \ll \omega_m$, the ratio of cooling (anti-Stokes) to heating (Stokes) photons can be improved and efficient cooling as well as ground state cooling can be achieved [117, 126].

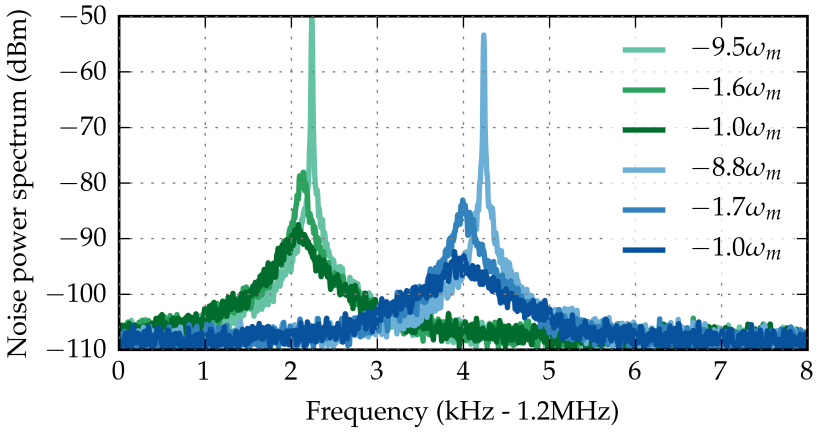

Figure 9.11: Noise power spectra for a sideband cooled mechanical mode. Cooling power of 2 mW in green and 4 mW in blue. Note, that the x-axis is shifted by 1.2 MHz and the blue curves by another 2 kHz for a clearer illustration. Measurements starts far off red-detuned ($\approx -10\,\omega_m$) with almost no cooling effect and with strongest interaction at $-\omega_m$ (darkest traces). The shift of the resonant frequency as well as the broadening mechanical line width are clearly visible and used to determine the single photon coupling strength in figure 9.12.

Experimentally, the cooling beam is used to lock the laser to the optomechanical cavity (OMC) and the signal beam is used for cooling. Note that for this measurement cooling and signal beam change their roles, because here we want to characterize the coupling strength of the signal beam, as the coupling comes from the cooling effect, which can be slightly different for the two beams due to different polarizations and mode matchings.

The goal is to measure $\delta\omega_m(\Delta)$ and $\gamma_{\text{opt}}(\Delta)$ as a function of detuning and fit equations 9.11 and 9.12. The cavity line width κ has been measured independently (see section 9.3.1) and the number of cavity photons $\bar{n}_{\text{cav}}$ can be retrieved by power meter measurements of the incoming light. Therefore, the single photon coupling strength g_0 is the only free parameter to be fitted.

Noise power spectra of the fundamental mechanical mode are measured for a set of different detunings Δ (see figure 9.11). These spectra are fitted to obtain the full mechanical line width γ_{eff} of the mechanical peak and the modified resonant frequency $\omega_{m,\text{eff}}$. These, in turn, are plotted and fitted in figure 9.12 a) and b). A fit of this data set yields a single photon coupling strength of $g_0 = 2\pi \times 46.2\,\text{Hz}$. This is the single photon coupling strength obtained by a 2 µW cooling beam coupled to the fundamental resonance of a membrane with resonant frequency $2\pi \times 1.2\,\text{MHz}$. This value is very close to the maximum theoretical value of 47 Hz calculated via equation 9.8 for 5.18 mm cavity and $2\pi \times 1.2\,\text{MHz}$ membrane sitting in the center of

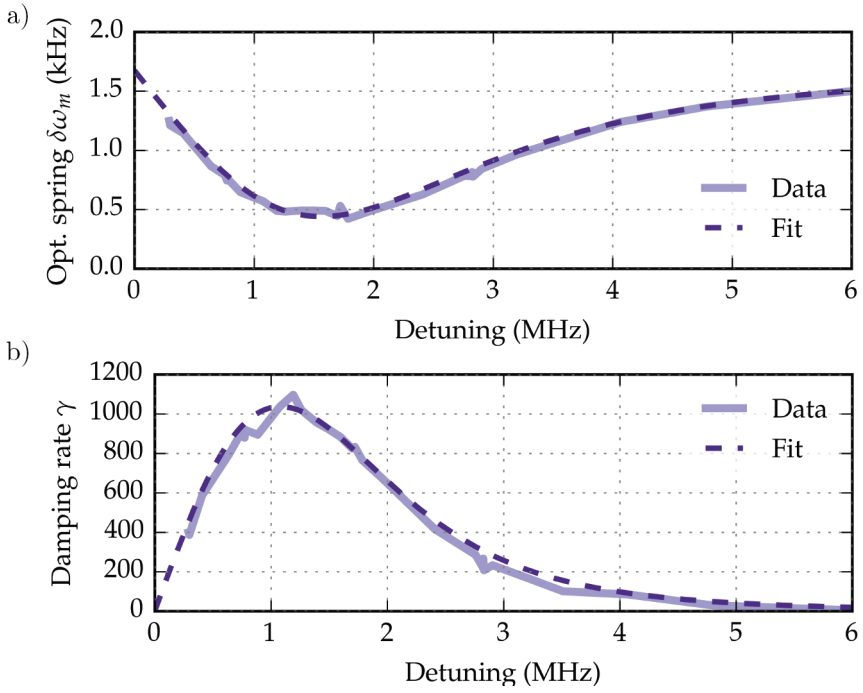

Figure 9.12: Radiation pressure sideband cooling to determine the single photon optomechanical coupling strength. Optical spring effect, that is the shift of the mechanical resonance frequency, in a) and the full mechanical damping rate in b). The data is taken from fits of noise power spectra measured for different detunings Δ, a subset of these spectra is plotted in figure 9.11. Data is depicted in light purple and a fit of equations 9.11 and 9.12 is plotted in dashed dark purple lines. The resulting single photon optomechanical coupling strength is $g_0 = 2\pi \times 46.2\,\mathrm{Hz}$.

the optical intra-cavity mode.

At this point, I want to take a brief detour and discuss the amount of cooling and the final phonon occupation number for the presented noise power measurements in figure 9.11. Naively, one would assume the ratio of phonon numbers to be inversely proportional to the ratio of mechanical damping rates, i.e. $\bar{n}_{\mathrm{fin}}/\bar{n}_{\mathrm{th}} = \gamma_m/(\gamma_m + \gamma_{\mathrm{opt}})$. However, the quantum back-action noise onto the membrane will produce a fluctuating force onto the mechanical motion and therefore drive the membrane, which is a heating mechanism. This effect leads to a minimal number of phonons that reads $\bar{n}_{\mathrm{min}} = (\kappa/4\omega_m)^2$ [27], which limits ground state cooling to systems operated in the sideband resolved regime [117], as $(\kappa/4\omega_m)^2 \ll 1$ for $\kappa \ll \omega_m$.

Our system is not sideband resolved and operates in the bad cavity limit. Strongest cooling is reached in the dark blue trace of figure 9.12. The red-detuning during this measurement was $\Delta \approx -\omega_m$ and the final occupation number is

$$\bar{n}_{\mathrm{fin}} = \frac{\gamma_m \bar{n}_{\mathrm{th}} + \gamma_{\mathrm{opt}} \bar{n}_{\mathrm{min}}}{\gamma_m + \gamma_{\mathrm{opt}}} = 13.1, \tag{9.15}$$

with $\gamma_m = 1\,\mathrm{Hz}$, $\gamma_{\mathrm{opt}} = 2346\,\mathrm{Hz}$, $\bar{n}_{\mathrm{min}} = 1.27$ and $\bar{n}_{\mathrm{th}} = 27635$ at a bath temperature $T_{\mathrm{bath}} \approx 10\,\mathrm{K}$.

Next, we address the fact that each mechanical mode has a different mode shape and will therefore couple differently to the TEM_{00} cavity mode. We dealt with this fact by introducing the concept of the effective mass in chapter 8.4, which replaces the physical mass within the single photon coupling strength.

There are two approaches to determine the g_0 for each mechanical mode. One can either measure it in the way just presented for the fundamental resonance, which can be automated but yet still time consuming. Or, one can determine the displacement of the cavity mode with respect to the membrane center and calculate the effective mass of each mode, giving a correction factor to the coupling strength of the first mechanical resonance [96]

$$g_{0,(n,m)} = \eta_{(n,m)}(x,y)\, g_0, \tag{9.16}$$

while (x,y) is the lateral displacement of the cavity mode with respect to the membrane center and $\eta_{(n,m)}$ is a variation of the overlap integral now applied to g_0 instead of the mass as in equation 8.10. The displacement can be retrieved by imaging of the membrane and the cavity mode as shown in figure 9.4 c) and figure 9.13 b) and c). The image is produced by red LED light shining through the optomechanical cavity and producing an image on a CCD camera in transmission of the cryostat. The overlap function can be calculated by

$$\eta_{(n,m)}(x,y) = e^{-\frac{w_m^2}{8}(n^2k^2+m^2k^2)} \sin(nkx)\sin(mky), \tag{9.17}$$

while k is the wave vector and $w_m \approx w_0$ the beam waist at the membrane position.

A list of single photon coupling strengths for a number of mechanical modes is given in table 9.2. The calculations assume a coupling strength of $g_0/2\pi = 40\,\mathrm{Hz}$ for the fundamental mechanical mode, i.e. the $(1,1)$ mode. Moreover, the lateral shift (imperfect alignment) of the membrane with respect of the cavity mode is $5\,\mu\mathrm{m}$ in one direction and $10\,\mu\mathrm{m}$ in the perpendicular direction. We use this method during the evaluation of multimode entanglement measurements in chapter 11.

#	(n,m)	FREQUENCY f_m (MHz)	COUPLING $g_0/2\pi$ (Hz)
01	$(1,1)$	1.183	40.0
02	$(2,1)$	1.869	13.5
03	$(1,2)$	1.872	7.08
04	$(2,2)$	2.366	2.67
05	$(3,1)$	2.643	18.0
06	$(1,3)$	2.649	21.3
07	$(3,2)$	3.015	3.75
08	$(2,3)$	3.018	8.49
09	$(4,1)$	3.445	13.9
10	$(1,4)$	3.454	7.86
11	$(3,3)$	3.550	12.4

Table 9.2: Single photon coupling strength for the first 11 membrane modes. A g_0 of $2\pi \times 40\,\mathrm{Hz}$ is assumed for the fundamental mode. Moreover, the membrane is considered to be shifted off the center of the cavity mode by 5 µm in one direction and 10 µm in the perpendicular direction. The modes, frequencies and coupling strengths are for a real membrane used for entanglement measurements in chapter 11 and the g_0 of higher order modes are calculated by equations 9.16 and 9.17.

9.3.3 *In situ Q measurements*

Measurements of the mechanical quality factor have been discussed in detail in chapter 8. However, for a full characterization of the experiment during entanglement measurements, it is necessary to measure the Q factor in situ: That is for a membrane incorporated within the optomechanical cavity, inside the cryostat and at low temperatures.

While in principle it is possible to use the same approach as in chapter 8, which is to excite the membrane by applying a modulation signal onto a piezo clamped onto the cavity spacer at a position close to the membrane, there are several additional points to consider.

First, the read-out must be done at a wavelength that does not experience the optical cavity when impinging onto the input coupler. The slightest detuning from the cavity resonance would end up in significant cooling and alter the ring-down time ($\gamma_m \to \gamma_{\mathrm{opt}}$). Therefore, we use a second laser source at a different wavelength where the reflectivities of the cavity mirrors are too low to yield to a cavity build-up and therefore too low for optomechanical radiation pressure effects. The laser model is a Cobrite fiber laser from ID Photonics GmbH [12] at 1550 nm, which is amplified by a fiber amplifier to roughly $\approx$ 100 mW. A homodyne detection scheme for this beam has been implemented, see figure 9.8.

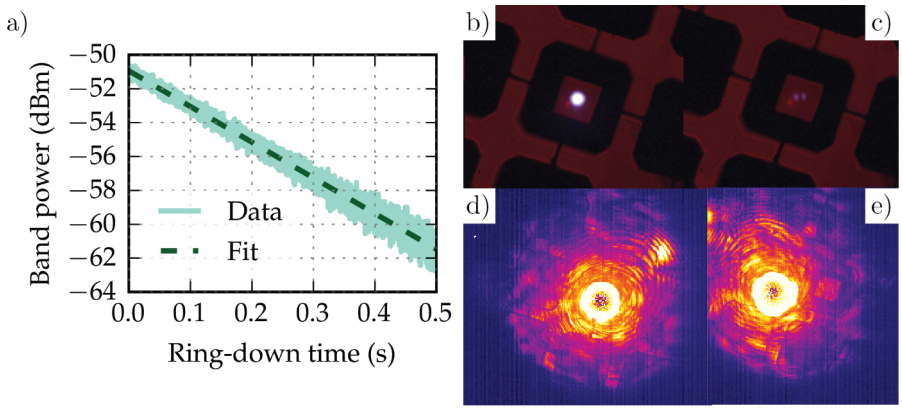

Figure 9.13: In situ Q measurements and imaging. a) A ring-down Q measurement for a phononic bandgap membrane excited by blue-detuned drive of the optomechanical cavity. This measurement yields 7.68×10^6. Imaging of the phononic bandgap structure and the TEM_{00} mode in b) and TEM_{01} mode in c). The structured Si frame is visible in black, while the removed parts are transparent (red). The center of each picture features the defect cell with the mainly transparent membrane in its center (also in red). These images can be used to determine the displacement between cavity mode and membrane for calculating the coupling strength of higher order mechanical modes (or the effective mass). Subfigures d) and e) show the imaging of the 1550 nm light. In d) the light is hitting the membrane directly, while the beam is misaligned in e) to image the membrane position by scattered light. Imaging is very important for Q measurements as the 1550 nm light does not resonate and no other tools can be applied to hit the membrane directly.

Second, the phononic bandgap structure decouples the membrane window in the defect cell from its environment. Therefore excitations from a piezo are strongly suppressed until they reach the membrane, compare with figure 8.14 c). Here, we used two alternative methods. The first method relies on an intensity modulator in the 1550 nm beam path that can strongly modulate the intensity of the light field with the resonant frequency of the mechanics, effectively driving the membrane by a modulated force on it. The second method uses the signal beam, which can be slowly scanned over the cavity resonance and drive the system once it is blue-detuned. Rapidly turning off the signal beam by a shutter and continuously measuring the membrane motion via the 1550 nm light allows for an easy and reliable way to excite phononic bandgap membranes.

Figure 9.13 a) shows a ring-down of the fundamental mode of a phononic bandgap membrane measured with the blue-detuned signal beam method. The remaining figures show signal beam (b) and c)) as well as the 1550 nm light in d) and e). Details are given in the caption. The Q factor in this measurement is 7.68×10^6. This value is, after following the discussions from chapter 8, at the higher end for a 340 µm sized membrane. It is also large enough to push the op-

tomechanical system into the strong cooperativity regime as will be discussed in the next section.

9.4 SUMMARY AND THE STRONG COOPERATIVITY REGIME

The mechanical oscillators have been introduced and discussed in chapter 8, with focus on understanding the different mechanical loss mechanisms and the improvement of the mechanical quality factor for a multitude of mechanical modes. The results were consistently large quality factors ranging between 4×10^6 and 7.3×10^6 for mechanical modes in a large frequency range from 1 to 4 MHz.

This chapter introduced the optomechanical cavity and studied the optomechanical interaction of a thin SiN membrane placed inside a high finesse Fabry-Pérot resonator. The realization of this system has been presented as well as an extensive characterization of the full optomechanical system and all parameters entering the quantum cooperativity

$$C = \frac{4g^2}{\kappa\gamma\bar{n}} = \frac{32\hbar}{\pi} \times \frac{\mathcal{F}^2 P_{\text{in}}}{\lambda c} \times \frac{Q}{m\omega_m k_B T}. \tag{9.18}$$

Here, the cavity line width κ and the average photon number that enters the optomechanical coupling strength $g = \sqrt{n_{\text{cav}}} g_0$ are replaced by the easily measurable input power P_{in} and cavity finesse $\mathcal{F}$. The mechanical line width γ is replaced by the resonant frequency ω_m and the quality factor Q, which are retrieved from the noise power spectrum and ring-down measurements. And the average phonon number is replaced by the bath temperature T.

For the measured and presented parameters in this chapter, an input power of $P_{\text{in}} = 10\,\mu\text{W}$ leads to a quantum cooperativity of $C = 1.0$ and therefore $P_{\text{in}} > 10\,\mu\text{W}$ leads to operation in the strong cooperativity regime. This is the main experimental achievement on the generation of entanglement in this thesis and it paves the way for entanglement measurements that are following in the next part of the thesis.

Part V

TOWARDS OPTOMECHANICAL ENTANGLEMENT

The last part of this thesis is dedicated to the verification of optomechanical entanglement by the membrane-in-the-middle optomechanical system.

In chapter 10, we will briefly look at the history of proposals for optomechanical entanglement protocols. Ultimately, the pulsed-continuous entanglement protocol is introduced, which is a variant of the pulsed protocol by Hofer and Hammerer [69]. Whereas the pulsed protocol has been successfully applied to LC circuits in the microwave regime [99], the pulsed-continuous protocol is here applied to a continuous variable multimechanical mode system in the optical regime. At the end of the chapter, we will discuss the data acquisition and the most important details of the calibration of the measured data.

Chapter 11 starts with showing several sets of evaluations on simulated data including a model of classical laser noise of the free-running laser as well as the detector characteristics (frequency response). We will see that simulations of a genuinely single mode system will yield entanglement when operated in the strong cooperativity regime. This statement, however, is not true for a multimode system. It will be shown that flattening the detector characteristics as well as multimode evaluations are crucial for the verification of entanglement with our multimode micromechanical membranes. Evaluations of measurements are presented while operating the system in the strong cooperativity regime. We will see that multimode evaluations show promising results towards the verification of optomechanical entanglement, yielding an entanglement witness as close as 3 % to the entanglement bound that needs to be crossed.

The future prospects of the presented experiment are discussed in chapter 12. We will discuss low frequency laser noise as an effect that corrupts the performance of the experiment, as well as a larger cooperativity to improve the generated entanglement. An elegant solution for the low frequency laser noise problem is presented, as well as feasible ways to increase the quantum cooperativity to a level where we, with our current results and understanding, assume to witness entanglement.

We will close the thesis with a summary of the main achievements and results in chapter 13.

10 ENTANGLEMENT PROTOCOL

This chapter provides a theoretical understanding of the generation and verification of steady-state continuous variable entanglement in optomechanical systems. For a general reading on quantum entanglement I want to refer to Horodecki *et al.* [71]. An overview of continuous variable entanglement with Gaussian states as being used in this thesis is given by Adesso and Illuminati in [19].

The basic formalism on optomechanics is given in chapter 4, and further reading on optomechanics can be found in the review article by Aspelmeyer *et al.* [27]. The starting point for the protocol used within the presented experiment is the work by Vitali *et al.* [136] and Genes *et al.* [58].

The general idea for the so called pulsed-continuous entanglement protocol that is used in this thesis goes back to the work on pulsed entanglement by Hofer and Hammerer [69]. That work has been extended to time-continuous systems in [66–68]. The code applied to the experimental data has been developed by several individuals, mainly Jason Hölscher-Obermaier, who has described it in detail within his thesis [70], Sebastian Hofer, Corentin Gut and Witlef Wieczorek. Many of the presented plots in the following sections are based on evaluations and simulations conducted by Corentin Gut.

We will see that this protocol, when applied to an inherently multimode mechanical system such as the membrane in the middle optomechanical topology, can generate and verify entanglement if operated in the strong cooperativity regime. The main advantages of this protocol are that it relies neither on ground state cooling of the mechanics nor an (unstable) blue-detuned drive. It works in the presence of sufficiently low classical laser noise and the verification can be performed in post-processing.

The remainder of this chapter is mainly based on the linearized optomechanical Hamiltonian (equation 4.11), the derived interactions between light and mechanics for a red-detuned and blue-detuned laser drive and the dynamics given by the quantum Langevin equations, section 4.2.1.

At the end of this chapter, the focus is put on the acquisition and the post-processing of the experimental data. The goal is to prepare the data obtained by dual-rail homodyne measurements which is subject to dark noise, detector efficiencies and homodyne visibilities, sufficient to apply the covariance matrix formalism.

10.1 GENERATION OF OPTOMECHANICAL ENTANGLEMENT

The generic optomechanical system is a cavity, consisting of an optical cavity mode coupled to an end-mirror featuring a harmonic degree of freedom. The interaction between these modes in the linearized regime is given by the linearized optomechanical Hamiltonian (4.11).

For a blue-detuned drive, $\Delta = +\omega_m$, we expect enhanced Stokes scattering onto the cavity resonance. This two-mode squeezing interaction generates correlated pairs of photons and phonons. Which, in the right parameter regime, can generate measurable entanglement between optical and mechanical quadratures.

Vitali *et al.* [136] consider the linearized Langevin equations for the amplitude and phase quadratures of the light and mechanics and derive the steady-state (4×4) covariance matrix σ_{ij} (3.17) in the presence of input quantum noise and thermal noise. Since we consider Gaussian states and are restricted to linear operations, the covariance matrix is sufficient to fully characterize the generated state. A frequently used measure for bipartite entanglement with Gaussian states is the so called logarithmic negativity $E_{\mathcal{N}}$, which verifies entanglement for $E_{\mathcal{N}}(\sigma_{ij}) > 0$ [18, 20, 21]. By assuming stability conditions by applying the Routh-Hurwitz criterion [46], robust optomechanical entanglement for a sufficiently strong coupling can be obtained for realistic experimental parameters.

However, we have seen that a blue-detuned drive can heat the mechanics and generate instabilities, even for the smallest input powers and detuning, and this heating can prevent the system from developing a steady-state. For strong coupling, the rotating-wave approximation (RWA) breaks down and Stokes terms mix in, which heat the system and cause instabilities. Additionally, Vitali *et al.* [136] assume that the internal cavity and mechanical modes are experimentally accessible, which is not the case. These issues have been addressed by Genes *et al.* [58] and Paternostro *et al.* [102]. The detection of entanglement is realized by analyzing the mediated entanglement on the experimentally accessible output light modes after exiting the optomechanical cavity, effectively transferring the light-mechanics entanglement onto light-light entanglement.

A red-detuned drive cools the mechanics and allows for stronger pumping of the cavity. For properly designed experimental parameters [58], a red-detuned pump can indeed generate steady-state optomechanical entanglement, that is, by means of a strong pump very close to the instability region. A discussion of the right parameters is given by Hofer in [66–68]. Most importantly, he shows that generally, operation in the strong cooperativity regime is a necessary condition for entanglement.

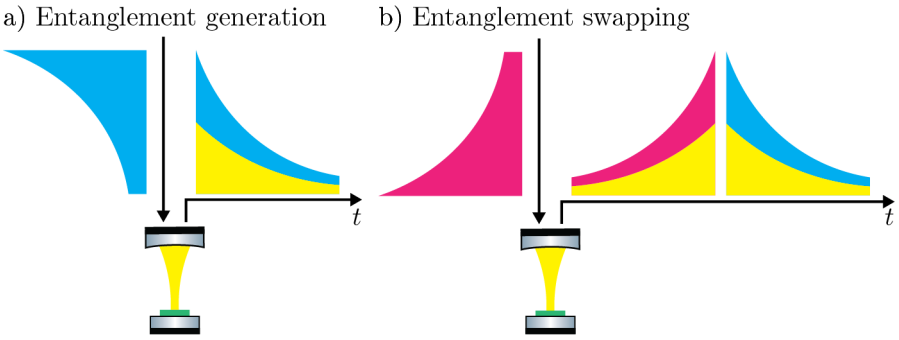

Figure 10.1: Pulsed protocol schematic. Two step pump-probe protocol. a) Entanglement generation. A blue-detuned pulse is sent into the cavity. The two-mode squeezing interaction is enhanced and will scatter photons onto cavity resonance and create entangled photon-phonon pairs. The light coupled out of the cavity will now contain photons on cavity resonance (yellow). b) Entanglement swapping. A red-detuned pulse is sent into the cavity. This time the beam splitter interaction is favored and scatters photons upwards in frequency onto cavity resonance, effectively swapping the mechanical state onto the the light field. Therefore, the light-mechanics entanglement is mediated to light-light entanglement. This entanglement can be verified by measuring both pulses which are time-wise separated and analyze them for correlations, see main text.

10.2 PULSED ENTANGLEMENT GENERATION AND VERIFICATION

A different approach by means of a pulsed pump-probe protocol, originally presented in [69] and pictured in figure 10.1, avoids continuous heating that causes instabilities and prevents establishing a steady-state. We do not apply this protocol experimentally, but it will help to develop and understand the following pulsed-continuous protocol that we use.

First, a blue-detuned pulse ($\Delta = +\omega_m$) is sent into the optomechanical cavity (see figure 10.1 a)). The cavity will favor Stokes scattering and the interaction is dominated by two-mode squeezing equivalent to parametric down-conversion. A blue-detuned photon at $\omega_{\text{cav}} + \omega_m$ will be annihilated and an entangled pair of a photon at ω_{cav} and a phonon at ω_m will be created, effectively entangling motional quanta of the oscillator with single photons in the intra-cavity mode.

The pulse will then exit the optomechanical cavity and contain the entangled photon at the cavity resonant frequency, which is entangled with the mechanics.

Second, a red-detuned pulse ($\Delta = +\omega_m$) is sent into the optomechanical cavity (see figure 10.1 b)). Now, the cavity will favour anti-Stokes scattering and the and the interaction is dominated by the beam splitter interaction. A red-detuned photon at $\omega_{\text{cav}} - \omega_m$ will be annihilated and a resonant photon at ω_{cav} is created by absorbing

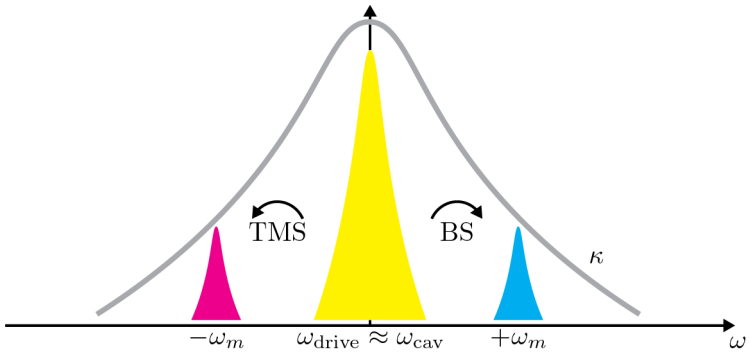

Figure 10.2: Continuous entanglement generation. The optomechanical cavity with line width κ isdriven by a single beam close to the cavity resonance. Since the cavity is operated in the bad cavity regime ($\kappa > \omega_m$) both, two-mode squeezing (TMS) as well as beam splitter (BS) interaction will appear simultaneously and continuously. The full signal reflected off the cavity can be detected and appropriate filter functions can be applied to separate the TMS (entangling) mode in time and frequency from the BS (read-out) mode. These modes can be further analyzed in a similar way as in the pulsed protocol.

the energy of a photon at ω_m and therefore effectively swapping the mechanical state onto a photon in the intra-cavity mode.

The pulse will then exit the optomechanical cavity and contain a photon that inherits the entanglement from the mechanics, which has been entangled with the first blue-detuned pulse.

The entangled output modes can be detected by means of homodyne detection and the entanglement can be verified by calculating the correlations and an entanglement measure or witness. Discussion of the full dynamics and the right parameter regime can be found in [66, 67]. This pulsed protocol does not rely on the formation of a steady-state such that it is stable by pumping with a blue-detuned pulse. Moreover, the entanglement is unambiguous since the pulses are separated in time and not overlapping.

This scheme has been successfully applied to a membrane capacitively coupled to an LC circuit in the microwave regime [99].

10.3 PULSED-CONTINUOUS ENTANGLEMENT PROTOCOL

We combine the previous ideas by generating entanglement with a single, slightly red-detuned drive and a system operated in the strong cooperativity regime. Verification is performed by applying the pulsed protocol in post-processing.

Consider an optomechanical system in the bad cavity regime, $\omega_m \leq \kappa$, driven close to the cavity resonance $\omega_{\text{drive}} \approx \omega_{\text{cav}}$ as depicted in figure 10.2. The intra-cavity light mode is interacting with the oscillating

membrane, which will lead to modulation sidebands at $\pm\omega_m$. This is analogue to the Stokes and anti-Stokes scattering picture discussed earlier. Light scattered downwards in frequency results in two-mode squeezing by generating a red-detuned photon at $\omega_{\mathrm{cav}} - \omega_m$ and a phonon at ω_m that are entangled. Simultaneously, upwards scattered light will absorb a phonon and results in swapping of the mechanical state onto a photon at frequency $\omega_{\mathrm{cav}} + \omega_m$. Therefore, the generation of light-mechanics entanglement and its mediation to detectable light-light entanglement occur in parallel. It is important to stress that there is no inherent time-wise separation, but rather two spectrally separated components.

The carrier light and the sidebands exit the optomechanical cavity and are detected by the dual-rail homodyne setup. Time traces of the amplitude and phase quadratures of the light are recorded for post-processing. The main idea is to cut this data into blocks of a given time period and analyze two consecutive blocks for quantum correlations. This is done by correctly applying mode functions to the signal in these two blocks.

A profound derivation and explanation of this method applied to our system has been given by Jason Hölscher-Obermaier in [70] chapter 5.3. I will solely render the most important details to provide an understanding of the following results of simulations and measurements of correlation data.

Consider the signal beam returning from the optomechanical cavity and containing the red-shifted sideband (entanglement mode) and the blue-shifted sideband (read-out mode) denoted by its annihilation operator $\hat{a}_{\mathrm{sig}}$. We introduce the following mode functions to extract the correct sidebands

$$\alpha(t) = \mathcal{N}_\alpha \times \exp(+i\omega_m t) \times \exp(+\Gamma t),\ t \leq 0, \tag{10.1}$$

$$\beta(t) = \mathcal{N}_\beta \times \exp(-i\omega_m t) \times \exp(-\Gamma t),\ t \geq 0, \tag{10.2}$$

in which $\mathcal{N}_{\alpha,\beta}$ are normalization factors. $\alpha(t)$ is applied to the signal $\hat{a}_{\mathrm{sig}}$ within the first block, whereas $\beta(t)$ is applied to the second block. The envelopes $\exp(\pm\Gamma t)$ make sure to emphasize the end and beginning of the first and second light mode respectively. Since at first the correlations will be large and then get diminished over time, Γ is closely connected to the mechanical decoherence rate. The rotating terms $\pm\exp(i\omega_m t)$ make sure to select the correct sideband, which is the red-shifted entanglement mode rotating at $-\omega_m$ and the blue-shifted read-out mode rotating at $+\omega_m$. The envelopes as well as the rotating contributions are plotted in figure 10.3.

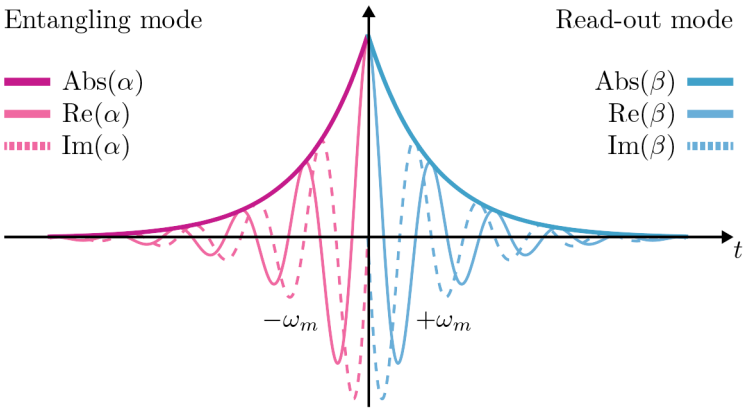

Figure 10.3: Filtering effect of mode functions in time and frequency. A plot of the mode function from equation 10.1 and 10.2 which are applied to the signal $\hat{a}_{\text{sig}}$. For negative times, the mode function $\alpha(t)$ is applied to retrieve the entangling mode, which is the light scattered into the red sideband (red traces) by the TMS itneraction. For positive times, the mode function $\beta(t)$ is applied to retrieve the read-out mode, which is the light scattered into the blue sideband (blue traces) by the BS interaction. Red and blue sidebands are rotating with $-\omega_m$ and $+\omega_m$ respectively. Solid dark lines feature the envelope of the mode function (absolute part). Light lines are used for the oscillating real (solid) and imaginary (dashed) part, which are used to yield the amplitude and phase quadrature of the resulting modes. Reproduced from [70] (figure 5.1 in chapter 5.3).

By applying the mode functions onto the signal, new operators can be defined that are separated in time and localized in frequency. Their annihilation operators read

$$\hat{a}(t) = \int_{-\infty}^{0} \alpha(\tau - t)\hat{a}_{\text{sig}}(\tau)d\tau, \tag{10.3}$$

$$\hat{b}(t) = \int_{0}^{+\infty} \beta(\tau - t)\hat{a}_{\text{sig}}(\tau)d\tau. \tag{10.4}$$

We will refer these modes as the entanglement and read-out modes, as their confinement in time and frequency makes them treatable in a similar way as pulses in the pulsed protocol.

The amplitude and phase quadratures are derived by taking the real and imaginary parts of the annihilation operators and read

$$\hat{Q} = \Re(\hat{a}), \qquad \hat{P} = \Im(\hat{a}), \tag{10.5}$$

$$\hat{X} = \Re(\hat{b}), \qquad \hat{Y} = \Im(\hat{b}), \tag{10.6}$$

in which we dropped the time dependence in the notations and use $\hat{Q}, \hat{P}$ for the entangling mode and $\hat{X}, \hat{Y}$ for the read-out mode, respectively, such that numeral indices remain free for denoting the various mechanical modes that will create sidebands at numerous frequencies in our multimode system.

As in chapter 3 we can define the vector

$$\mathbf{R} = \left(\hat{Q}, \hat{P}, \hat{X}, \hat{Y}\right)^\top \tag{10.7}$$

and the covariance matrix

$$\sigma = \begin{pmatrix} \langle Q^2 \rangle & \langle QP \rangle & \langle QX \rangle & \langle QY \rangle \\ \langle QP \rangle & \langle P^2 \rangle & \langle PX \rangle & \langle PY \rangle \\ \langle QX \rangle & \langle PX \rangle & \langle X^2 \rangle & \langle XY \rangle \\ \langle QY \rangle & \langle PY \rangle & \langle XY \rangle & \langle Y^2 \rangle \end{pmatrix} - \begin{pmatrix} \langle Q \rangle^2 & \langle Q \rangle \langle Q \rangle & \langle Q \rangle \langle X \rangle & \langle Q \rangle \langle Y \rangle \\ \langle Q \rangle \langle P \rangle & \langle P \rangle^2 & \langle P \rangle \langle X \rangle & \langle P \rangle \langle Y \rangle \\ \langle Q \rangle \langle X \rangle & \langle P \rangle \langle X \rangle & \langle X \rangle^2 & \langle X \rangle \langle Y \rangle \\ \langle Q \rangle \langle Y \rangle & \langle P \rangle \langle Y \rangle & \langle X \rangle \langle Y \rangle & \langle Y \rangle^2 \end{pmatrix}, \tag{10.8}$$

in which the top-left quarter corresponds to the entangling mode and the bottom-right quarter to the read-out mode. Note that we drive the cavity by a shot noise limited laser beam, i.e. a coherent state, while the membrane is initially in a thermal state. Coherent and thermal states are both Gaussian and we only apply linear operation on them, such that the resulting modes are also Gaussian. Thus, the covariance matrix is sufficient to fully characterize the produced state and we can apply an entanglement witness like the logarithmic negativity to quantify the correlations, i.e. optomechanical entanglement occurs if $E_\mathcal{N}(\sigma) > 0$ [18, 20, 21]. In any case, a statement about entanglement is connected to quantum correlations between a linear combination of the measured quadratures. Moreover, entanglement is connected to correlations that squeeze some quadrature of the above state below the quantum shot noise level.

The presented approach can be readily expanded for a multimode system. Appropriate entangling and read-out mode functions can be defined similarly to equations 10.1 and 10.2, by adjusting the frequency ω_{m_i} and envelope Γ_i for the i-th mechanical mode. These mode functions can be applied to the signal $\hat{a}_{\mathrm{sig}}$ which contains sidebands at each mechanical resonance that is interacting with the intracavity mode. This procedure yields a pair of pulse modes $\hat{a}_i(t)$ and $\hat{b}_i(t)$ for each interacting mechanical mode. Their quadratures $\hat{Q}_i, \hat{P}_i$ for the entangling pulse and $\hat{X}_i, \hat{Y}_i$ for the read-out pulse enter a generalized vector

$$\mathbf{R} = \left(\hat{Q}_1, \hat{P}_1, \hat{X}_1, \hat{Y}_1, \cdots, \hat{Q}_n, \hat{P}_n, \hat{X}_n, \hat{Y}_n\right)^\top, \tag{10.9}$$

in which n is the total number of considered mechanical modes. The covariance matrix is then defined as

$$\sigma_{ij} = \frac{1}{2}\left\langle R_i R_j + R_j R_i \right\rangle - \left\langle R_i \right\rangle \left\langle R_j \right\rangle, \tag{10.10}$$

as introduced earlier in equation 3.17.

The remainder of this thesis will show correlation measurements and attempts to verify bipartite entanglement between light-light pulses as defined during this section. To apply this protocol we will need to plug the frequencies ω_{m_i} and envelopes Γ_i into an evaluation code. The frequencies can be easily obtained by calculating the noise power spectrum of the time traces, whereas the entanglement witness (e.g. logarithmic negativity) can be evaluated and plotted for different Γ, i.e. the spectral width of the pulses. The continuous variable entanglement comes from the fact that we obtain a steady-state and that independent of at what point in time we apply our analysis, it should yield the same entangled quantum state.

10.4 DATA ACQUISITION AND POST-PROCESSING

The dual-rail homodyne detection scheme provides us with the phase and amplitude quadratures of the light modes. However, measurements are not ideal and subject to unwanted noise sources and signals as well as frequency dependent transfer functions of the devices that are used to measure and process the signals we are interested at. We need to account for these effects and correctly calibrate the voltages measured with the detectors. A measurement consists of three different time traces: Signal traces of the light that is reflected off the optomechanical cavity. Shot noise traces of the local oscillator. Dark noise traces of the homodyne detectors.

I will discuss the main steps between the filtering, amplification and acquisition of the homodyne signals and the post-processing and calibration of the measured time traces.

Acquisition

The detection scheme and its characterization have been discussed in chapter 6. The homodyne traces are measured with a NI PXI-5122 DAQ card from National Instruments [13]. The card has two input channels and uses 14-bit resolution analog-to-digital converters. We typically use an input impedance of $50\,\Omega$ to impedance match our detectors, an input range of 200 mV and set a sampling frequency of 100 MHz with an external clock (function generator).

One has to consider the following points to appropriately and effectively use our data collection system:

- Avoid saturation that can damage the DAQ card: The mechanical signals we are interested at are weak modulation sidebands around a strong carrier field at DC frequency. The unfiltered DC component will dominate the input of the card and therefore limit the voltage range and resolution of the small MHz sidebands we are interested in, or even saturate and damage the DAQ. We filter the DC component of the signal with a high

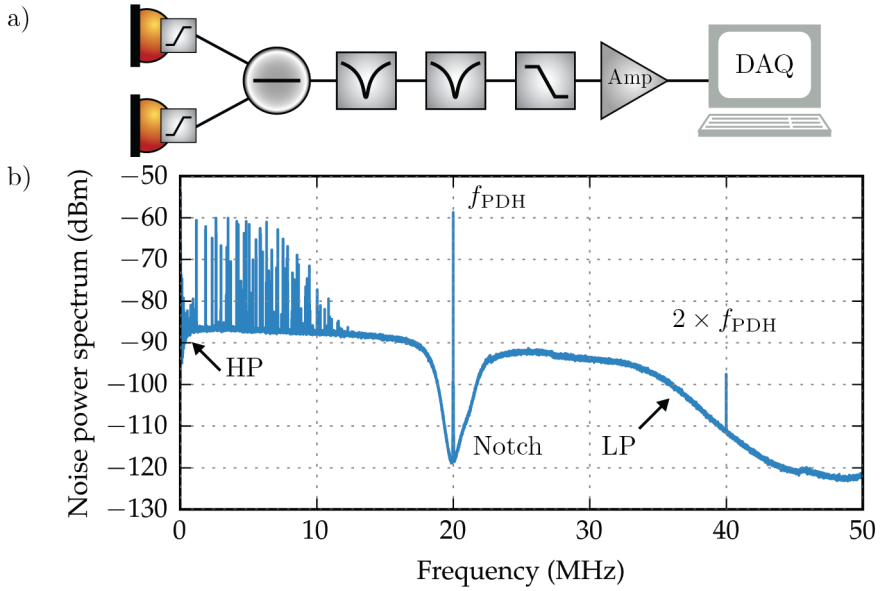

Figure 10.4: Detector characteristics: Schematics and noise power spectrum. a) Filtering scheme. Each detector signal is high pass filtered on the detectors circuit board to prevent the following components from saturations. After taking the difference of the photocurrents, the PDH modulation is filtered by two notch filters. A high order low pass filter makes sure to filter all signals before the Nyquist frequency to avoid aliasing effects. A voltage amplifier makes sure to use the full input range of the DAQ where the homodyne signal is measured. b) The resulting detector characteristics as a noise power spectrum (phase detector). The high pass sits at a frequency below $\approx$ 300 kHz and followed by the mechanical spectrum from roughly $1 - 15$ MHz. Two notch filters at 20 MHz filter the PDH modulation and a high order anti-alias filter is placed at frequencies $\geq$ 30 MHz to hit the dark noise level of the DAQ just below the Nyquist frequency of $f_{\mathrm{Nyquist}} =$ 50 MHz. The filtering scheme as well as the resulting detector characteristics are matched for both homodyne detectors.

pass filter on each individual photodetector. The high pass aggressively filters the strong DC component as well as low frequency laser noise with large amplitudes.

- Prevent aliasing effects: Aliasing is an effect that causes different signals to become indistinguishable from each other when sampled. This effect is observed if the sampling rate is smaller than twice the largest frequency component on the measured signal, the so called Nyquist frequency $f_{\mathrm{Nyquist}} = 0.5 \times f_{\mathrm{sampling}}$. We avoid aliasing effects by low pass filtering all frequency components of our time series below the Nyquist frequency $f_{\mathrm{Nyquist}} = 50$ MHz according to a typical sampling rate of $f_{\mathrm{sampling}} = 100$ MHz. We do this by low pass filtering the homodyne signals with a high order filter model BLP-30+ from [14], which passes signals from DC to its corner frequency at

approximately 30 MHz and then aggressively filters the signal down to the dark noise level at the Nyquist frequency.

- Avoid saturations of the DAQ due to the Pound-Drever-Hall modulation frequency: The generation of the PDH error signal relies on a moderate modulation of the signal beam that is sent onto the optomechanical cavity. This modulation at $f_{\mathrm{PDH}} = 20\,\mathrm{MHz}$ is approximately 30 dB stronger than the mechanical sidebands and would saturate the DAQ. We filter the PDH modulation by two narrow notch filters around 20 MHz, each with an attenuation of $\geq 15\,\mathrm{dB}$.
- Make use of the full input range and resolution of the DAQ: As mentioned at the beginning of this section, we will need to measure signal, shot noise and dark noise time series. Each will feature a different noise power level and needs to be amplified by a different gain to make use of the full range of the DAQ card. We use a low-noise variable-gain high-speed amplifier from Femto [4] model DHPCA-100. Typical amplifications are 30 dB, 40 dB and 50 dB for signal, shot noise and dark noise time series and an input voltage range of 200 mV of the DAQ card.

The full filtering scheme between the detection by the photodiodes and the acquisition by the DAQ system is illustrated in figure 10.4 a) and the resulting detector characteristics in form of a noise power spectrum is shown in figure 10.4 b).

Detector and electronics inversion

As discussed in section 10.3, a statement about entanglement is connected to squeezing of some linear combination of quadratures measured in the experiment. Therefore, optomechanical signal measurements need to be compared to shot noise measurements to calibrate the measured signal traces in volt to units of shot noise, whereas the variance of shot noise quadratures are typically set to 1/2.

We found that our analysis of time series data suffers from the detector and subsequent electronic characteristics (see figure 10.4 b)) as the measured shot noise is not perfectly flat. The physical intuition as to why a non-flat detector response disturbs the calibration is the following: Shot noise is a perfectly uncorrelated white noise source, and phase and amplitude quadrature measurements will yield a covariance matrix with 1/2 on its diagonal, and zeros elsewhere. A non-flat detector and electronics response will shape the shot noise noise power spectrum and this will introduce spurious correlations that alter the shot noise and its covariance matrix. Therefore, a non-flat shot noise measurement is not appropriate to calibrate signal time traces to shot noise units.

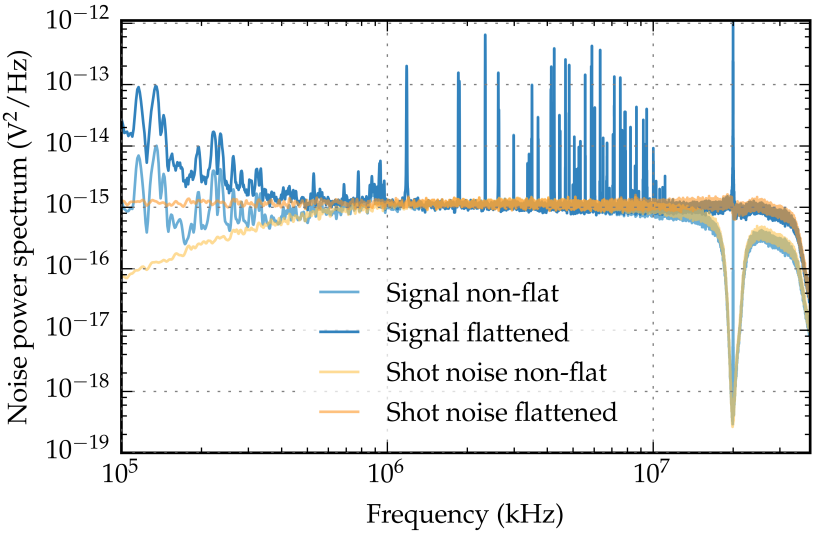

Figure 10.5: Non-flat vs. flattened noise power spectra. Direct NPS of raw signal and shot noise data in light blue (signal) and light yellow (shot noise). NPS of the flattened, i.e. inversed filters applied to the raw data, NPS in blue and yellow. The detector inversion is applied to the low frequency high pass filter, the notch filters at the PDH modulation and the slightly descending low pass behavior visible from approximately 10 MHz onwards. Note, that the inversion applied to the signal trace does artificially increase the low frequency laser noise.

An appropriate way to account for the non-flat detector and electronics response is by means of measuring and characterizing all filters that shape the recorded time trace characteristics, calculate the inverted filters and apply them to the measured time series. Tobias Westphal, a postdoctoral researcher in our group, suggested a procedure for modeling filters based on poles and zeros. From a data set of all electronics' transfer functions and noise power spectra of shot noise measurements, one can provide an inverse filter to flatten the detector characteristics in post-processing. I provided the data and Tobias Westphal modeled an inverse filter which can be applied to our time series. The model included the high pass filter below 300 kHz, the notch filters at 20 MHz and the slightly descending low pass behavior starting at approximately 1 MHz to 30 MHz before the aliasing filter kicks in (see figure 10.4 b)).

The noise power spectra (NPS) for non-flat and flattened signal and shot noise traces calculated from time series are depicted in figure 10.5. The resulting shot noise NPS is flat up to approximately 30 MHz with a small residual feature of the notch filters at 20 MHz. This method greatly improved the performance of the shot noise calibration of our data sets. The effect on the expected entanglement will be shown and more deeply discussed in simulations in chapter 11.1.

Calibration and post-processing

After the acquisition of experimental data and the inversion of the detector characteristics, the signal traces that can contain entanglement, need to be calibrated from units of volts to units of shot noise. Therefore, the shot noise time series itself needs to be calibrated, including the effects of dark noise, detector efficiencies as well as homodyne visibilities.

The step-by-step procedure is given by the following list:

1. Shot noise conversion factor: The integrated shot noise limited noise power spectrum (NPS) should lead to quadrature values of $1/2$. We calculate the NPS of the measured shot noise time trace and determine the bandpower in a frequency region where the measurement is shot noise limited (see figure 10.5). This bandpower density is then extrapolated over the full frequency range from DC to the Nyquist frequency. A conversion factor for the shot noise time series is obtained by multiplying the full bandpower by the Nyquist frequency and forcing it to be $1/2$. The same calibration factor is used for the dark noise time series.

2. Signal conversion factor: The signal time series might have a different conversion factor, as all measurements need to be conducted successively and the additional power in the signal as well as small laser power drifts might change the shot noise floor. The calibration factor is obtained in the same way as for the shot noise with one important exception: The signal NPS features mechanical resonances such that we restrict the shot noise limited band power to be extrapolated to the widest shot noise limited region, i.e. between the first and second mechanical resonance.

3. Computation of the covariance matrices (CM): The CM's of the signal, σ, shot noise, σ_{shot}, and dark noise, σ_{dark}, time series are computed in units of shot noise. Note, the shot noise CM should be a diagonal matrix with entries of $1/2$.

4. Dark noise correction: The dark noise is uncorrelated at the level of CM's. Therefore, the dark noise CM can be subtracted from the signal CM, $\sigma \to \sigma - \sigma_{\text{dark}}$, and the shot noise CM, $\sigma_{\text{shot}} \to \sigma_{\text{shot}} - \sigma_{\text{dark}}$.

5. Detector quantum efficiencies η and homodyne visibilities ν have been both discussed in chapter 6. The quantum efficiency of our detectors is $\eta \approx 95\,\%$. Non-ideal quantum efficiencies can be treated as an attenuation of the optical power. The homodyne visibility, $\nu \approx 90 - 95\,\%$, is a measure of interference between the signal and the local oscillator at the homodyne

beam splitter. Therefore, the homodyne visibility only enters signal measurements and does not affect shot noise measurements, which is only a measurement of the local oscillator, in which no interference takes place.

The transformations of the covariance matrices of the signal and shot noise are given by the following equations [70]:

$$\sigma \to \frac{\sigma - (1 - \eta\nu^2)\sigma_{\text{shot}}}{\eta^2\nu^2}, \tag{10.11}$$

$$\sigma_{\text{shot}} \to \frac{\sigma_{\text{shot}}}{\eta}, \tag{10.12}$$

in which the shot noise CM on the right hand side of both equations is the uncorrected CM.

6. Shot noise correction of the signal: The dual-rail homodyne detection scheme (see chapter 3.3) relies on adding a 50 : 50 beam splitter to equally split the signal between the phase and amplitude homodyne detector. The open port of this beam splitter adds one additional shot noise unit on the signal time series. On the level of covariance matrices, the corrected signal CM is obtained by subtraction of one unit of shot noise CM: $\sigma \to \sigma - \sigma_{\text{shot}}$. This is valid as the additional shot noise in that open beam splitter port is uncorrelated to the signal coming from the optomechanical cavity.

Summary

This chapter introduced the pulsed-continuous entanglement protocol that is applied to the presented optomechanical experiment. It is based on a continuous wave interaction between the cavity light mode and the multimode mechanical membrane placed inside the cavity. The verification is applied to the light modes exiting the optomechanical cavity, which are detected by a dual-rail homodyne detection scheme. Mode functions are applied to the time series to spectrally and time wise defined pulses that are then analyzed at the level of covariance matrices. We concluded by explaining the data acquisition, post-processing and calibration of the detected light modes.

The following chapter will provide results on simulations and experimentally obtained data, by applying the pulsed-continuous entanglement protocol and the calibration procedure presented in this chapter.

11 CORRELATION MEASUREMENTS

Our multimode optomechanical system has been introduced in chapter 8 and brought into the strong cooperativity regime in chapter 9. Operating the experiment in the strong cooperativity regime should enable the generation of continuous wave optomechanical entanglement with the presented experiment. In chapter 10 a pulsed-continuous entanglement protocol has been presented, which offered a way to generate and verify such entanglement. Moreover, the data acquisition as well as the required post-processing and calibration steps, have been discussed in section 10.4.

This chapter presents the results of measurements taken in the strong cooperativity regime. I will briefly summarize the experimental parameters in table 11.1, which are obtained by the methods presented in chapters 8 and 9. Then, several single mode and multimode simulations are presented, emphasizing the necessity of evaluating the multimode system to successfully verify the generated entanglement. The simulations are followed by experimental results of measurements taken in the strong cooperativity regime. We finish with discussions on the result of the experiment.

The resulting plots will feature an entanglement witness [52, 73], that verifies entanglement when its experimental value is lower than one shot noise unit (0.5), i.e. displaying squeezing of some linear combination of the measured and post-processed phase and amplitude quadratures. To prove that the system is performing accurately, we will also evaluate shot noise time series, which should lie directly at a witness value of 0.5.

All analysis, including the entanglement witness, is a function of the spectral width, Γ, of the mode functions used to define the entangling and read-out modes in the entanglement protocol (see chapter 10.3). We expect the optimal Γ to be in between the mechanical decoherence rate $\bar{n}\gamma$ and the optomechanical interaction rate g^2/κ. Whereas this condition is straightforward for the evaluation of a single mechanical mode, this is non-trivial for multimode evaluations, as each mode features its own interaction and decoherence rate. Therefore, the witness is evaluated and plotted as a function of different Γ, where wide Γ correspond to short pulses in time (susceptible to too short interaction times) and narrow Γ correspond to long pulses (susceptible to mechanical decoherence).

Note, that the code for the data evaluation as well as the simulations have been written and used by Witlef Wieczorek, Sebastian

Hofer and Jason Hölscher-Obermaier. Currently the code is maintained, improved and expanded by Corentin Gut, who ran the code for the presented simulations and evaluations of experimental data. I contributed with the experimental data presented in this chapter, which were measured together with the aid of Joshua Slater.

11.1 ENTANGLEMENT SIMULATIONS

This section is dedicated to the evaluation of simulated signal and shot noise data using the experimental parameters in table 11.1. Two important parameters that are not included in table 11.1 is the classical laser amplitude and phase phoise. These were included in the simulations in accordance to measurements of the free-running laser performance in transmission of the high finesse filter cavity, see chapter 5 and the thesis of Jason Hoelscher Obermaier for details on the measurements [70]. We will also compare a flat detector response to simulations with a detector response that includes all the experimental filters.

The title of each figure will include information about whether a single mode or multimode system is simulated. Furthermore, the title includes the type of the detector characteristics, which is either non-flat, i.e. the realistic detector response in the experiment, or flat, i.e. flattened as described in chapter 10.4. If all traces feature the same optical power, that value will be included in the title, otherwise the input power is contained in the legend.

Evaluation of simulated signal time series will be plotted in different shades of purple, shot noise traces are depicted in gray and a light gray line at a witness value of 0.5 separates non-entangled data points (≥ 0.5) from entangled data points (< 0.5).

The legend contains information about which mechanical modes are included in the evaluation of the respective trace: 'Sig #1 20 µW' indicates a single mode evaluation of the first mechanical mode and a signal input power of 20 µW. Whereas 'Sig #1#2#3 100 µW' indicates a multimode evaluation of the first three mechanical modes (ordered by frequency) and a signal input power of 100 µW.

We will start with the single mode case and a non-flat detector response as encountered in the experiment. Single mode simulations for different input powers are shown in 11.1 a) and feature entanglement for an input power of 20 µW and a quantum cooperativity as low as $C_{20\,\mu W} = 2$. Two additional features are displayed and important in this figure: First, larger input powers not only lead to smaller witness values, but also feature larger optimal pulse widths Γ (shorter pulses). This is because the interaction rate g^2/κ increases and the quantum correlations build up over a shorter timescale. Second, the evaluation of simulated shot noise data yields a witness value of 0.5 in

PARAMETER, SYMBOL	UNITS	VALUE
Fundamental mode, ω_m	rad Hz	$2\pi \times 1.18 \times 10^6$
Quality factor, Q	1	7.3×10^6
Mechanical line width, $\gamma = \omega_m / Q$	rad Hz	1.02
Bath temperature, T_b	K	10
Thermal occupation, $\bar{n} = k_b T / \hbar \omega_m$	1	1.76×10^5
Laser wavelength, λ	nm	1064
Laser frequency, $\omega_{\text{laser}} = 2\pi c_0 / \lambda$	rad Hz	$2\pi \times 2.82 \times 10^{14}$
Detuning, $\Delta = \omega_{\text{laser}} - \omega_{\text{cavity}}$	rad Hz	$-2\pi \times 200 \times 10^3$
Cavity line width (HWHM), κ	rad Hz	$2\pi \times 2.46 \times 10^6$
Mode matching	1	0.93
Homodyne visibility, ν	1	0.95
Homodyne efficiency, η	1	0.95
Max. input power, P_{in},	µW	12
Single photon coupling strength, g_0	rad Hz	$2\pi \times 40$
Optomechanical coupling strength, g	rad Hz	$2\pi \times 205 \times 10^3$
Mechanical decoherence rate, $\bar{n}\gamma$,	Hz	28.5×10^3
Interaction rate, g^2/κ,	Hz	8.57×10^3
Quantum cooperativity, $C = 4g^2/\kappa\gamma\bar{n}$	1	1.2

Table 11.1: Experimental parameters for the following entanglement evaluations. All parameters were determined during one measurement run using the methods presented in chapter 8 and 9. These parameter set is also used for the following entanglement simulations in section 11.1. Note, that the derived values for the optomechanical coupling strength, the interaction rate, the mechanical decoherence rate and the quantum cooperativity are given for the maximum experimental input power of 12 µW and for the fundamental mechanical mode ω_m.

accordance to theory. However, for large pulse widths the shot noise curve falls below 0.5 and becomes correlated. The reason for that is that if the pulses become too broad they start to probe frequencies of the laser's noise power spectrum where the shot noise is no longer white, see light yellow shot noise trace in figure 10.4. This effect is not problematic as long as the optimal pulse width lies in a region with the correct shot noise behavior. If that is not the case anymore, the detector characteristics need to be inverted to improve the results of the evaluations by maintaining a flat noise power spectrum over a wider range probed by broader pulses.

Experimental data, however, will not be single mode due to the multimode nature of the SiN membrane, which can not be ignored. Figure 11.1 b) presents simulations of a multimode membrane and single mode evaluations of the first five (ordered by frequency) mechanical modes for 20 µW input power. A comparison of the fundamental mechanical mode (#1) in the single mode simulation, which was entangled, to the multimode simulation, shows that a simple single mode evaluation does not anymore demonstrate the quantum correlations. In fact, all sufficiently strong interacting modes become correlated and we lose the quantum correlations by partially tracing over all modes but the one we are interested at.

We will now attempt to demonstrate the quantum correlations by taking into account the multimode nature of the mechanics by multimode evaluations of the same simulated data. Figure 11.1 c) shows simulated data for 20 µW input power (as in figure b) as well as for 50 µW and 100 µW. The displayed traces show multimode evaluations including the first three mechanical modes for each input power. There are two notable results in these evaluations: First, by only considering the first three mechanical modes, the signal traces show genuine multimode entanglement in the sense that their witness value falls below the threshold of 0.5, i.e. the three mode evaluation for 100 µW yields a witness of approximately $0.46 - 0.47$, which is very close to the single mode system for the same power (approximately 0.45). Second, as the mode functions that define the pulse modes grow in number or become broader, a broader frequency range is covered by them. The broader the frequency span, the less flat the total covered shot noise range probed by the modes becomes. Therefore, the shot noise evaluation starts to show wrong behaviors at smaller pulse widths and stronger than in case of a single mode evaluation. Therefore, the entangled signal traces are not trustworthy. To investigate this problem further, an inverse detector model was applied to the simulated date in figure 11.1 c). The results of evaluations on the flattened simulations are shown in figure 11.2. The figure shows that by flattening the detector response, a flat shot noise trace is obtained and the signal traces show the expected behavior, i.e. featuring an optimal pulse width that yields to entanglement.

Therefore, the detector response needs to be fixed when we evaluate experimental data by the same inversion procedure. Figure 11.2 also shows single mode evaluations of the multimode system, which are obtained by tracing out the second and third mode. The entanglement vanishes as a result of this procedure. This means that multimode evaluations are necessary for the verification of optomechanical entanglement in our multimode system.

In summary, we compared single mode and multimode evaluations of simulated data for single mode and multimode mechanical systems, while making sure to use experimentally feasible parameters, the frequency response of our homodyne detectors as well as including classical laser noise. The single mode evaluations showed that while for a single mode system entanglement is generated and verified, that is not the case if only one mechanical mode is evaluated in a multimode simulation. However, multimode evaluations can retrieve quantum entanglement. This happens at the cost of a higher number of mode functions. In this case, the evaluation of shot noise, which acts like a benchmark for our evaluation protocol, artificially shows entanglement because of the non-flat detector response (see figure 11.1 c)).

In terms of the evaluation of experimental data however, we expect to generate entanglement when operating in the strong cooperativity regime. Moreover, the simulations indicate that the multimode nature of the membrane needs to be considered by applying multimode evaluations containing more than the fundamental mode of the membrane. And finally, to produce trustworthy results, the non-flat detector characteristics need to be fixed by the presented methods in chapter 10.4.

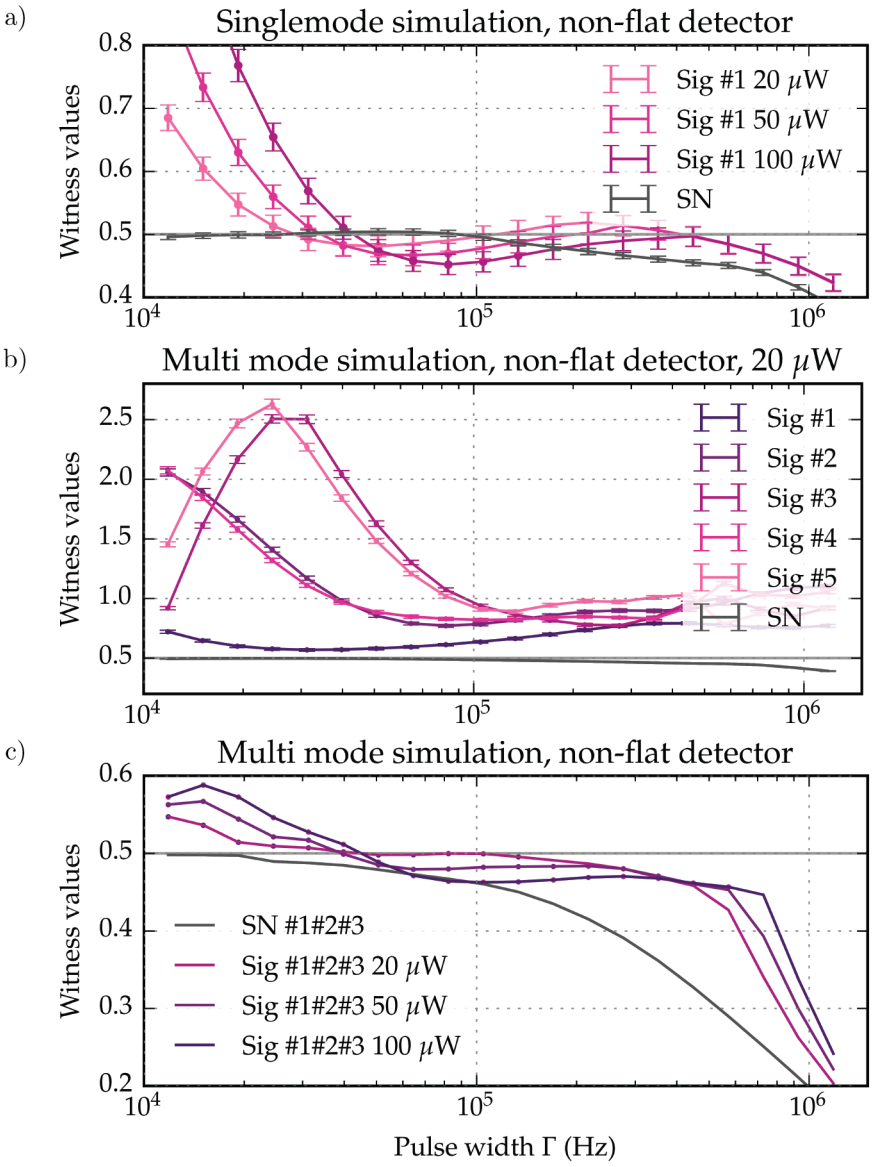

Figure 11.1: Comparison of single mode and multimode entanglement simulations. The entanglement witness is plotted as a function of pulse widths Γ. The shot noise threshold separates entanglement data points (< 0.5) from non-entangled points. Figure a) shows evaluations of a single mode system for different input powers. Entanglement is clearly witnessed for input powers as low as 20 µW. Figure b) shows single mode evaluations of the first five modes of a multi mode simulation. The fundamental mode, and also the next four following modes, if individually analyzed get fairly close to the entanglement threshold set by the show noise. However, single mode analysis of a multimode system does not yield entanglement, regardless regardless of which mode one analyses. Figure c) shows that by considering several mechanical modes in the evaluation, most of the entanglement is retrieved, but at the cost of non-flat shot noise behavior. The results are discussed in detail in the main text.

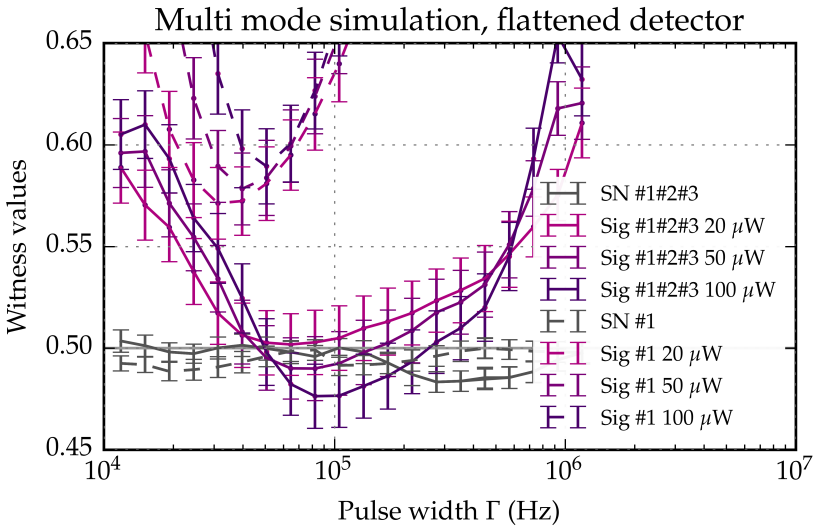

Figure 11.2: Multimode simulations of flattened detector response. This figure shows the same multimode simulations as presented in figure 11.1 c). The only difference is that before analysis the entanglement witness, we first apply an inverse filter model to flatten the detector response. The result is a flat shot noise behavior, that does not dive below the entanglement threshold of 0.5. Moreover, the signal behaves normal, i.e. it shows an optimal pulse width that yields entanglement. Single mode evaluations of the multimode simulations are displayed with dashed lines for all powers. The single mode evaluations are obtained by tracing out the second and third mechanical modes, which has the consequence that the entanglement vanishes. The conclusion for further evaluations of experimental data is that both detector inversion and multimode evaluations are necessary to obtain optomechanical entanglement in our multimode system.

11.2 EVALUATION OF EXPERIMENTAL DATA

In this section, results of three different experiments will be presented and discussed. The measurement runs were taken at input powers of 6, 9 and 12 µW, with corresponding quantum cooperativities C of 0.6, 0.9 and 1.2. The experimental parameters are summarized in table 11.1.

The results are presented as entanglement witnesses as a function of pulse widths, i.e. the same way as for the simulations in section 11.1. As the simulations suggested, we will only evaluate data with flattened detector response (see figure 11.1 c)).

Each plot will include a horizontal light gray line at a witness value of 0.5, dividing data points that demonstrate entanglement (below 0.5) from data points that do not (above 0.5). Shot noise evaluations are depicted in dark gray and signal measurements occur in three different color schemes: Single mode evaluations are plotted in green traces, two mode evaluations are plotted in purple and multimode (three or more modes) evaluations are depicted in blue.

A complete visualization of all measurements and combinations of different mechanical modes are given at the end of this chapter in figures 11.7 (6 µW), 11.8 (9 µW) and 11.9 (12 µW).

The main text will show figures of a subset of all data points, to discuss specific aspects of the evaluations more precisely.

First, we want to look at the power scaling of the entanglement witness as a function of input power. Figure 11.3 contains the single mode evaluation of the fundamental mechanical mode for each input power, as well as a simulated trace for 20 µW. The 6 and 9 µW curves together with the simulation, show an expected trend towards smaller witness values and closer to the entanglement threshold of 0.5.

However, the 12 µW measurement is pulled off and does not fit into the trend. We do not understand this behavior but the best estimate is that because this data has been measured with the highest possible optical input power, the system was nearly unstable and the stabilization of the optomechanical cavity was also unstable. From experience, we know that operation close to instability generated excess noise that severely affected the performance of the experiment. The influence of excess low frequency laser noise is discussed in greater detail in the next chapter 12.1.

Figure 11.3 contains several vertical lines: A black dashed line indicates the mechanical decoherence rate $\bar{n}\gamma = 28\,\mathrm{kHz}$ at a bath temperature of $T_b = 10\,\mathrm{K}$. The dashed green lines depict the interaction rate g^2/κ for each measurement (matching colors), which are 4.3 kHz, 6.45 kHz and 8.6 kHz from lower to larger optical powers. Since, decreasing Γ leads to very long pulses that are computationally too demanding to evaluate, the evaluation of experimental data

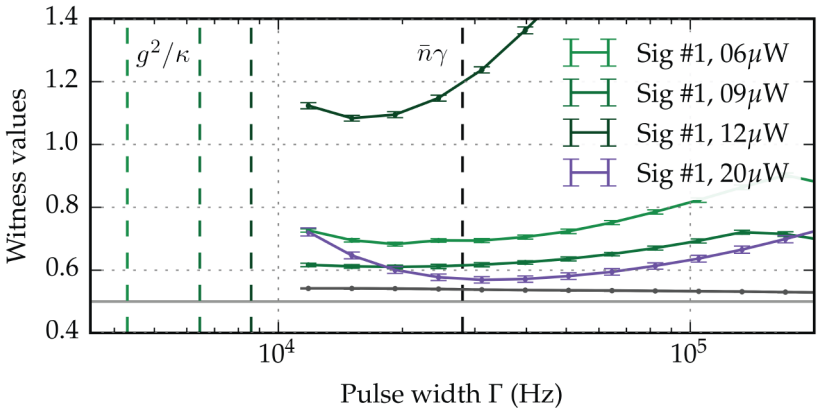

Figure 11.3: Single mode entanglement witness as a function of input power. Green traces depict single mode evaluations of the fundamental membrane mode as a function of the pulse width. Vertical dashed green (matching colors) lines indicate the corresponding interaction rates, g^2/κ, and the black dashed line depicts the mechanical decoherence rate, $\bar{n}\gamma$. The purple trace shows a simulated trace for comparison. The results are discussed in the main text.

ends earlier. At any rate, we expect the optimal pulse width that minimizes each witness curve to be below the decoherence rate and above the interaction rate, which is the case for all three measurements. Note that the interaction rate is smaller than the decorence rate. This means that by the time significant interaction has taken place, non-negligible mechanical decoherence has already leveraged. The interaction rate needs to be increased by a factor of four to match and surpass the mechanical decoherence rate. This corresponds to a quantum cooperativity of $C \approx 4$ for which single mode entanglement for a genuine single mode system is expected.

We will now study the behavior of the entanglement evaluation when expanding the evaluation by including more mechanical modes. Figure 11.4 a) shows different combinations of single mode and multimode evaluations. The shot noise evaluations for each combination are plotted on top of each other in gray.

The fundamental, the fifth and the sixth mechanical mode are the modes with the largest single photon coupling strengths: $g_0^{\#1} = 40\,\mathrm{Hz}$, $g_0^{\#5} = 18\,\mathrm{Hz}$ and $g_0^{\#6} = 23.3\,\mathrm{Hz}$, compare with table 9.2. The quantum cooperativities are approximately $C_5, C_6 \approx 0.4 < 1.2 = C_1$. These values are calculated by equation 4.19 with parameters obtained by the methods in chapter 9 and for this experiment summarized in table 11.1. Therefore, we do not expect entanglement from single mode evaluations of the fifth and sixth mode (as we just have seen, we would expect single mode entanglement for $C \approx 4$), but the cooperativity is on the order of one and therefore large enough to expect some contribution to a multimode evaluation. The purple traces in figure

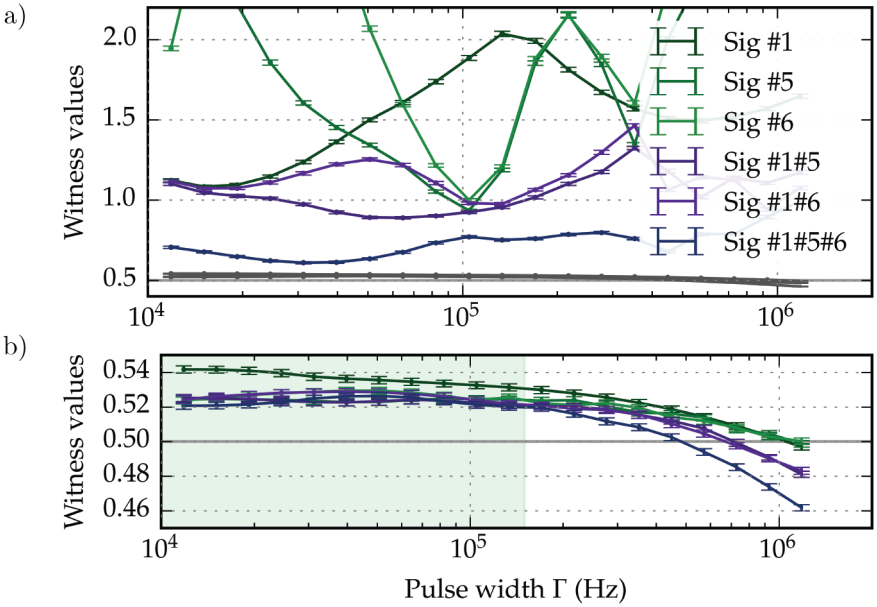

Figure 11.4: Multimode entanglement witness curves. a) Singe mode (green), two mode (purple) and three mode (blue) evaluation of the measurement taken with 12 µW input power. Shot noise traces plotted on top of each other in gray. b) Zoom around the entanglement threshold at 0.5. Plotted are the shot noise traces with matching colors to their corresponding signal traces from figure a). The frequency span where the shot noise curves are flat are shaded in light green. The results are discussed in the main text.

11.4, which illustrate two-mode evaluations, show that the combination of the first and fifth/sixth mode lead to an improved entanglement witness. This can be enhanced further by evaluating the witness for the three modes all together in figure 11.4 (blue trace). The take away is that the performance of the entanglement verification is improved significantly by explicitly taking into account the multimode nature of the membranes.

Figure 11.4 b) shows a zoom-in around the witness threshold. Depicted are the shot noise evaluations of the same single mode and multimode evaluations as in a). Note that in this figure all shot noise traces feature the same trace color as the signals, such that each curve can be assigned and more importantly, distinguished from each other. There are two main issues with the shot noise evaluations: First, there is an offset of around 4 % in contrast to the ideal shot noise level of 0.5. This indicates that there is some residual bias in the calibration of the shot noise band power. This problem is currently under investigations. Second, the shot noise evaluation dives below 0.5 at broad pulse widths. However, the slope of the shot noise diving is successfully reduced in contrast to non-flat detector responses and is flat up to pulse widths of approximately 160 kHz (light green shaded area), which spans the region where we expect to find entanglement and

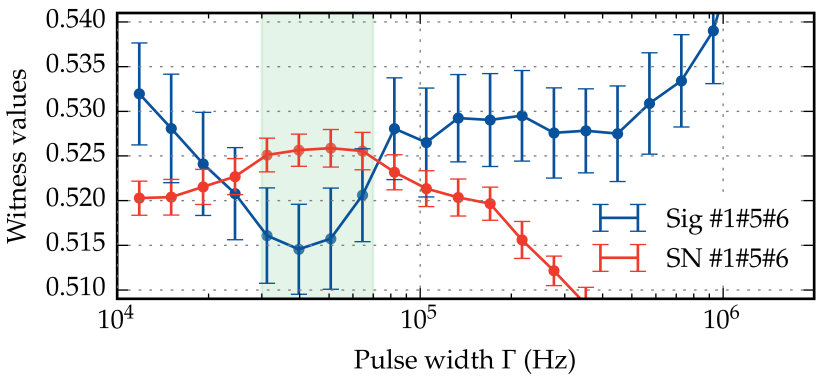

Figure 11.5: Best witness for the current calibration method. Multimode evaluation of the first, fifth and sixth modes, i.e. the three modes with the strongest coupling strengths. Signal evaluation in blue and shot noise evaluation in red. However, the signal curve dives below the shot noise for pulse widths that exhibit an expected flat shot noise behavior (green shaded area). Sub shot noise witness values for the signal trace are an indication for squeezing and hence, for entanglement. While all data points correspond to physical covariance matrices, they all have witness values larger than 0.5. Since we are shot noise limited at the sideband frequencies we are interested at, we assume that the shot noise offset comes from an imperfect calibration of the experimental data. The optimization of the calibration procedure is work in progress.

thus we can ignore it (see figure 11.1 a) and c) and figure 11.8 b)).

The best entanglement witness results have been obtained with multimode evaluations of the 9 µW data set. Figure 11.5 shows multimode evaluations of the #1#5#6 mode combination. The signal trace is depicted in blue and the corresponding shot noise trace in red. The signal evaluation dives below shot noise for pulse widths from approximately 20 kHz up to 80 kHz, which is in line with the interaction and mechanical decoherence rates of modes constituting this combination of modes. The smallest witness value is 0.515 for a pulse width of 40 kHz, where the shot noise trace behaves well, i.e. is flat (green shaded area). This value is only 3 % or 0.13 dB above the entanglement witness threshold at 0.5. The sub shot noise witness of this mode combination is an indicator for squeezing and therefore, for genuine multimode optomechanical entanglement. However, this evaluation appears to be subject to an error in the calibration as the shot noise traces are not around the witness value 0.5. Since we are shot noise limited in the frequency range of interest (500 kHz to 5 MHz), we expect that the current calibration method can be optimized to remove the offset in the witness curves of the experimental data.

A recently updated version of the calibration is acknowledging the fact that both detectors are slightly different (level of measured noise power spectra and homodyne detector visibilities). Results of a four-

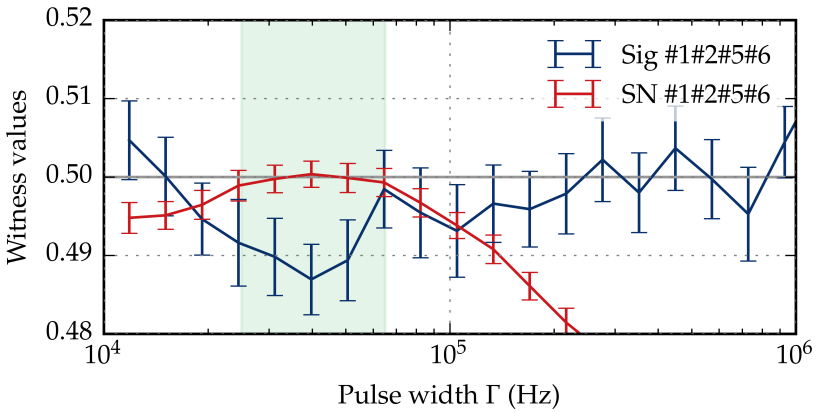

Figure 11.6: Best witness for an updated calibration method. Same data set as in figure 11.5 but with a new calibration method and a four mode evaluation. This plot features the same qualitative behavior except that the modified calibration successfully removes the shot noise witness offset in the interesting pulse width band, i.e. flat shot noise (green shaded area). The signal trace reaches an entanglement witness of 0.487 which is 2.6 % or 0.11 dB below the shot noise and the entanglement witness bound. Note that in contrast to figure 11.5, all data points are unphysical, i.e. the corresponding covariance matrix does not resemble a physical state. Therefore, this calibration is work in progress.

mode evaluation (#1#2#5#6) of the same 9 µW data set used in figure 11.5 yields to a well behaving shot noise curve, i.e. flat and offset-free (green shaded area). The entanglement witness of the signal (blue) dives below the entanglement witness by 2.6 % or 0.11 dB. This result indicates that entanglement is present for this four-mode evaluation. In contrast to figure 11.5, all data points are unphysical, which means that the variances of phase and amplitude quadratures violate the Heisenberg uncertainty relation. We assume that this issue still rises from imperfect calibration of the data. A second possible explanation is noise of the system, as the shot noise curve should ideally be at 0.5. Up to now, this ambiguity could not be resolved and the calibration procedure is still under investigation.

Before summarizing the thesis, the next chapter discusses low frequency laser noise in the detection as a an experimental issue that decreases the performance of the optomechanical system. Furthermore, several possible improvements to the experimental setup are discussed, which could increase the cooperativity to a a regime where the current protocol would clearly witness entanglement.

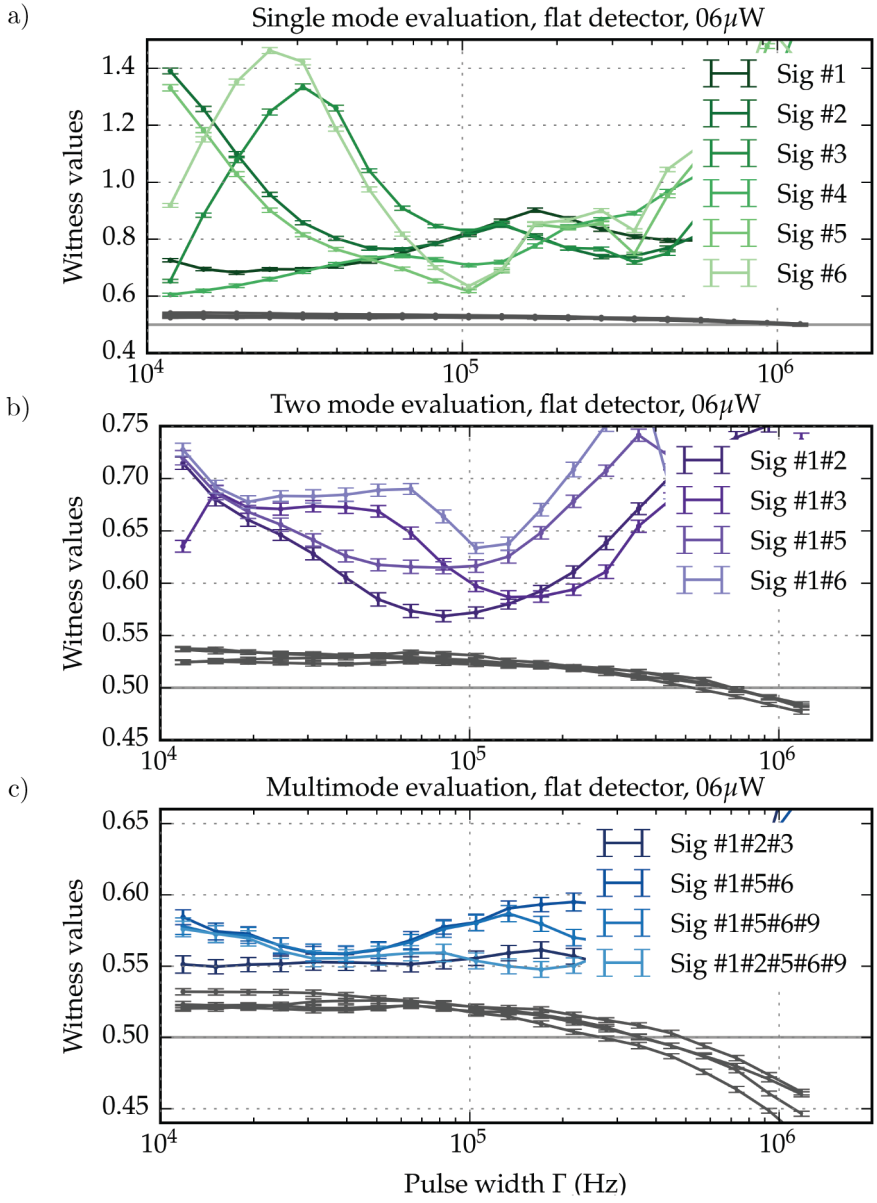

Figure 11.7: Entanglement witness evaluations for 6 µW input power.

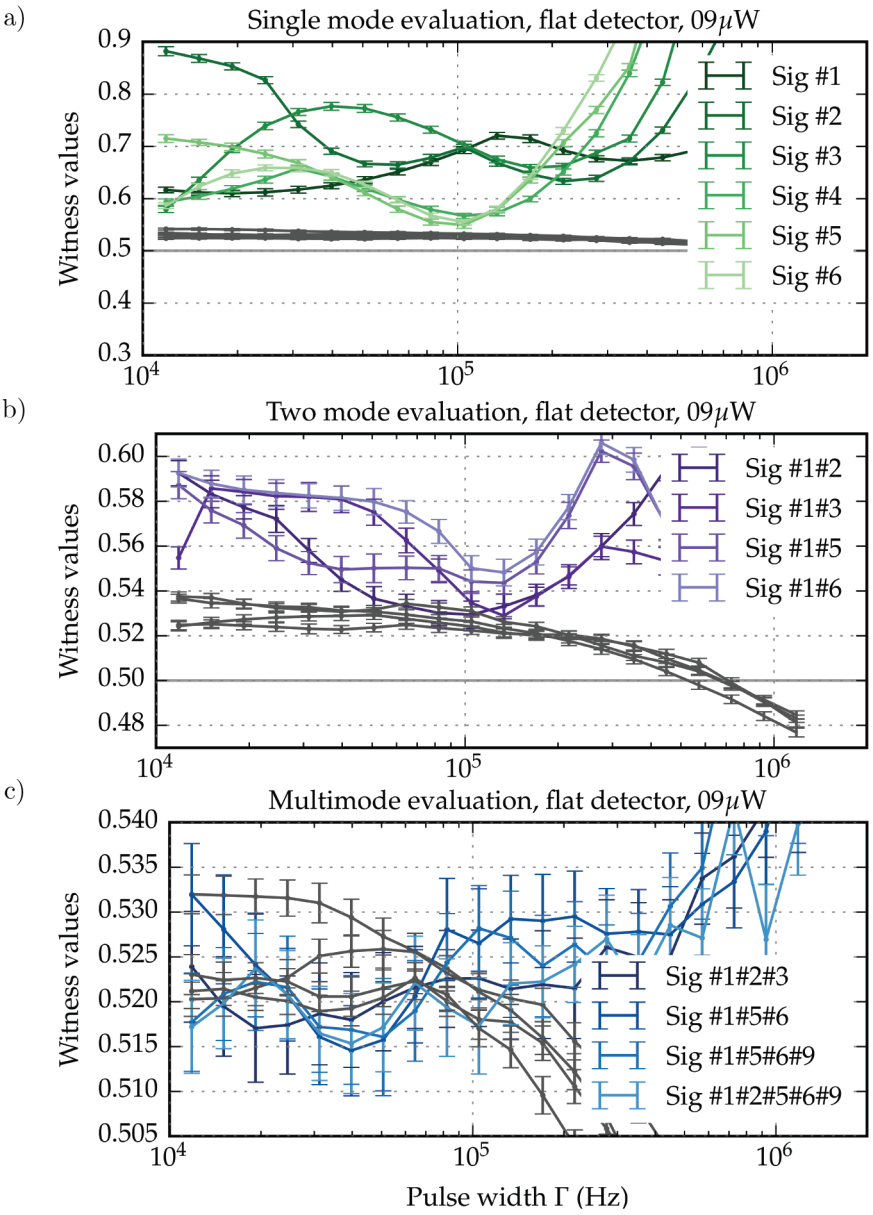

Figure 11.8: Entanglement witness evaluations for 9 µW input power. Note that figure c) is zoomed-in and discussed in detail in figure 11.5 earlier.

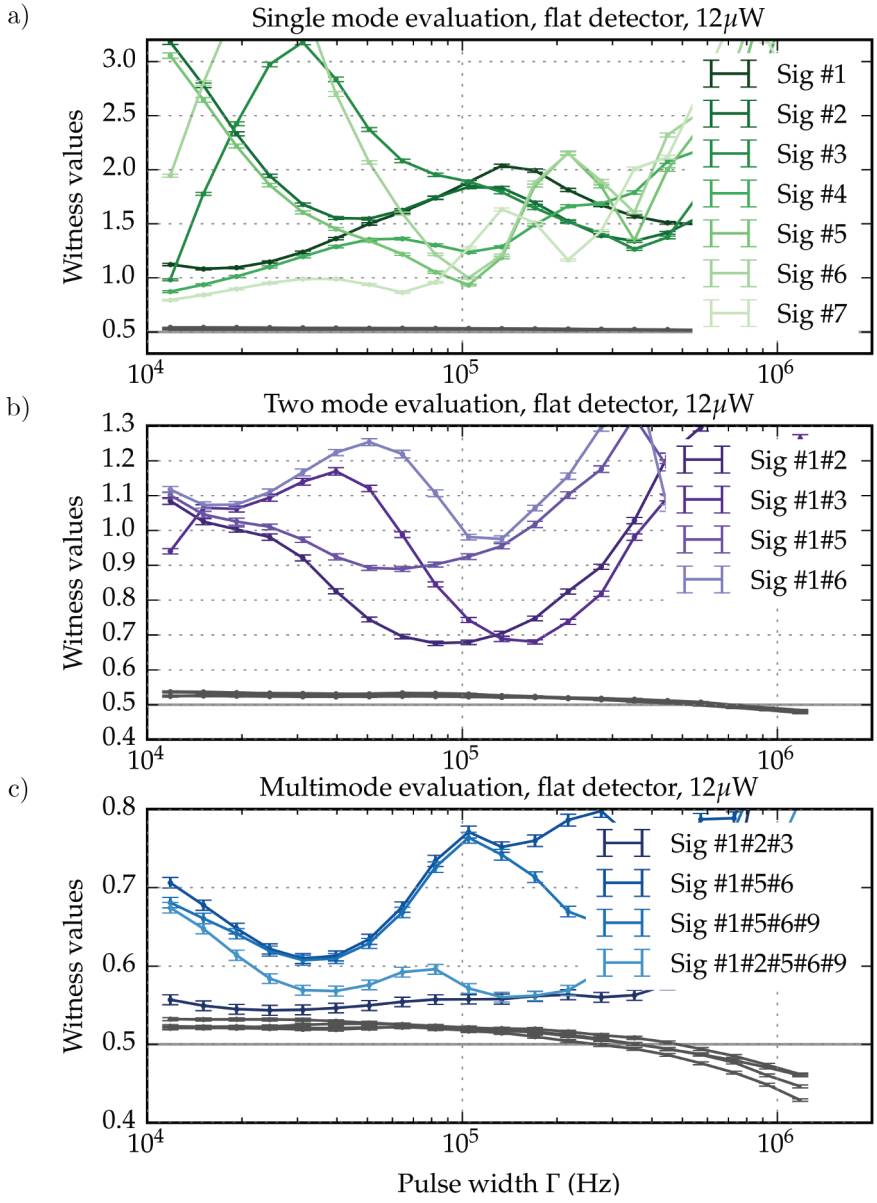

Figure 11.9: Entanglement witness evaluations for 12 µW input power.

12

FUTURE PROSPECTS

This chapter discusses two potential bottlenecks that limit the current performance of the experiment and the measurements presented in chapter 11. We will discuss both issues and provide promising solutions to overcome these hurdles. At the end of this chapter,

The first problem that we could track down is excess low frequency classical laser noise. The laser noise model used in the simulations was based on measurements made in transmission of the filter cavity, but for a free-running laser. We found additional low frequency laser noise on the laser light when the laser was further locked to the optomechanical cavity. Second, the inversion of the detector characteristics, especially the flattening of the high pass filter, not only flattens the shot noise noise power spectrum, but it also increases the low frequency noise contributions for signal measurements. This effect can be seen in figure 10.5. The mode functions that define the pulses used in the pulsed-continuous protocol are then also subject to this excess classical noise.

To further explore these issues, extensive simulations have been performed to evaluate the expected entanglement as a function of improved quantum cooperativities and increased low frequency laser noise. These simulations are shown in figure 12.1 and will be discussed in the following sections.

The presented data made thorough troubleshooting necessary. Ultimately, classical laser noise has been found to be the main reason for the difference between simulations and experimental data. The noise model used for simulations is based on a free-running laser, while during measurements the laser is locked to the optomechanical cavity (OMC). Laser noise measurements, while locked to the OMC, revealed excess laser noise at frequencies below 100 kHz. Though being far off from mechanical resonances, the spectrally broad mode functions ($\approx$ 100 kHz) still collected low frequency laser noise. This has been confirmed by simulations in which the classical noise in the model has been scaled up.

On the other hand, increasing the quantum cooperativity further would not only increase the generated entanglement in the first place, but it would also allow for increased pulse length and therefore decreased spectral width of the mode functions.

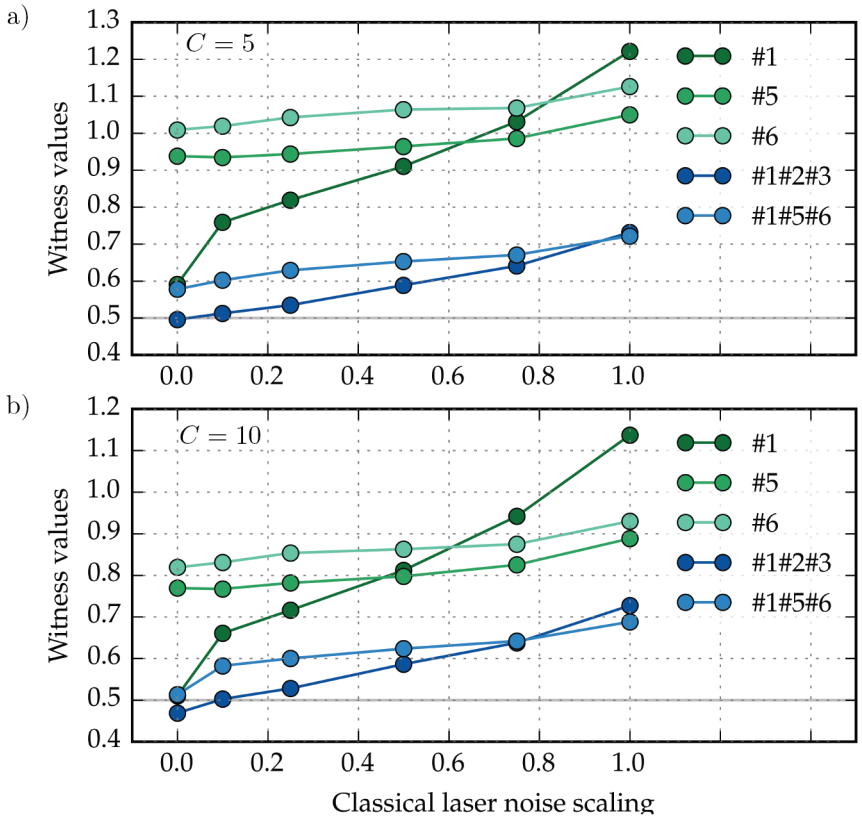

Figure 12.1: Entanglement witness as a function of improved quantum cooperativities and increased low frequency laser noise. Simulations for a quantum cooperativity of 5 in figure a) and 10 in figure b). The entanglement witness is plotted increasing excess low frequency laser noise, while $x = 0$ corresponds to our laser noise model of the free-running laser and $x = 1$ features a increased laser phase noise and amplitude noise according to measurements from figure 12.2. Each data point corresponds to the optical pulse width that minimizes the entanglement witness. The results are discussed in the main text.

Figure 12.1 contains entanglement simulations for moderately increased cooperativities (5 and 10) and an artificially increased laser noise from the current model (free-running laser) linearly increased to values measured while the laser is locked to the OMC. Note that the presented simulations are a worst case scenario, as the excess laser noise is conservatively modeled by a linearly falling function to match the observed low frequency noise. Therefore, these simulations will overestimate classical noise at larger frequencies, i.e. around the mechanical membrane modes, and therefore are more pessimistic than the real system. In fact, it can be assumed that the real system will perform better than the curves in figure 12.1 imply.

These graphs show that it is necessary to significantly reduce low frequency laser noise, or to remove it completely, i.e. $x = 0$ in figure 12.1, where laser noise is not increased by the OMC lock. This state-

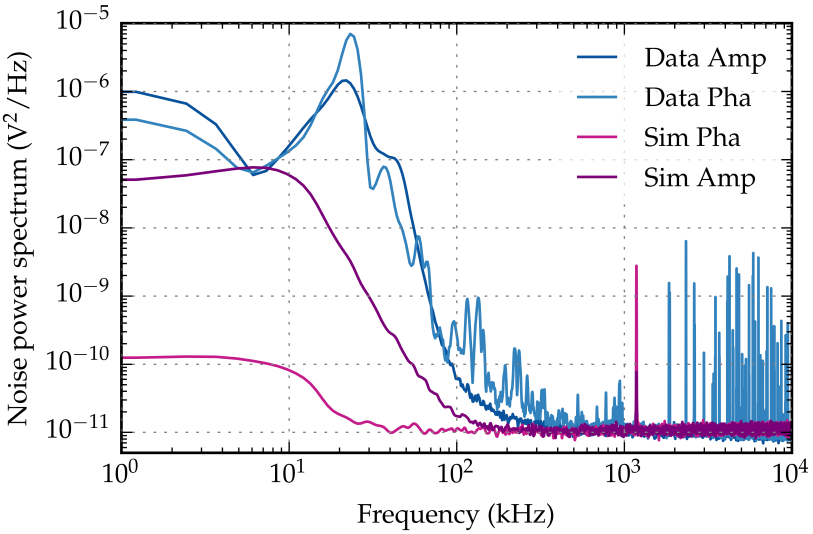

Figure 12.2: Low frequency laser noise characterization. NPS of simulated (single mode) data based on the free-running laser noise model are depicted in purple traces. NPS of the phase and amplitude homodyne detectors of the entanglement measurements from chapter 11 are plotted in blue curves. A difference of one order of magnitude for the amplitude detector and a difference of four orders of magnitude for the phase detectors are visible in a low frequency span from DC to approximately 300 kHz.

ment is at least true for moderate and realistic improvements of the quantum cooperativity.

The remainder of this chapter discusses ways to remove the classical low frequency laser noise and to simultaneously improve the cooperativity. This should allow one to enter a regime where optomechanical entanglement can be significantly inferred by our protocol.

12.1 LOW FREQUENCY LASER NOISE

We start the discussion of excess low frequency laser noise by first determining the difference between the actual noise power spectra (NPS) of the flattened data from chapter 11 and of the simulations based on the noise model for the free-running laser. The resulting NPS are shown in figure 12.2. While the low frequency (DC to 300 kHz) laser noise on the amplitude quadrature is only moderately underestimated in the simulations, the phase quadrature is underestimated by almost four orders of magnitude.

The discrepancy has been traced back to the fact that the laser noise model has been measured in transmission of the filter cavity, but with a free-running laser, while for correlation measurements, the laser needs to be stabilized to the optomechanical cavity. The source of this excess noise is assumed to be the full locking scheme of the main components: Laser, filter cavity and optomechanical cavity. The laser

is stabilized to the OMC through the FC, while the latter is following the laser frequency, see chapter 5. This is indicated by some measurements of the laser noise for different lock settings of the filter cavity. While a significant reduction of the noise is possible, it is questionable wheter we can remove the excess noise entirely. For this reason we aimed for a better and more elegant solution to this problem.

A different approach to remove the low frequency noise is based on optimization of the homodyne balancing of each detector, as for an ideal beam splitter all classical noise should be canceled. As shown in chapter 6, strong common mode rejection is already obtained, which couldn't be improved by optimizing the alignment. On the other hand, the slightest misalignment does significantly increase the remaining noise. We decided to try to measure the individual AC signals of each detectors of the phase homodyne setup and to apply the subtraction in post-processing. The results of the difference of detector A and B are shown in figure 12.3, for different weightings according to the equation $i_A - b \cdot i_B$. The results are compared to the noise power spectrum of the direct analog subtraction of each detectors and show that the full excess noise could be subtracted that way. Note that for these measurements, the OMC was not locked. This remains to be tested.

This approach seems to be promising for improving the performance of the experiment, as it gives us more flexibility and control, can remove the excess low frequency laser noise, as well as grant us a detector response that is easier to model and therefore to flatten. More tests need to be performed and additional components are going to be needed to fully implement this on all photodiodes of both homodyne detectors.

12.2 IMPROVEMENTS ON THE QUANTUM COOPERATIVITY

The quantum cooperativity can be increased by either raising the single photon coupling strength g_0, or by raising the optical input power and thereby the intra-cavity photon number $\bar{n}_{\mathrm{cav}}$, or by decreasing the crucial decoherence rates for the given system. These are the mechanical line width γ, the optical line width κ and the thermal occupation number $\bar{n}$.

An improvement of the mechanical line width can go along with increasing the size of the membrane for lower resonant frequencies and larger mechanical quality factors, see chapter 8. However, we chose the current size to shift the first mechanical resonance as far as possible towards larger frequencies to maximize the distance to low frequency laser noise, as well as to increase the spectral distance to higher order modes and thereby limit the maximum number of modes that efficiently interact with the light field.

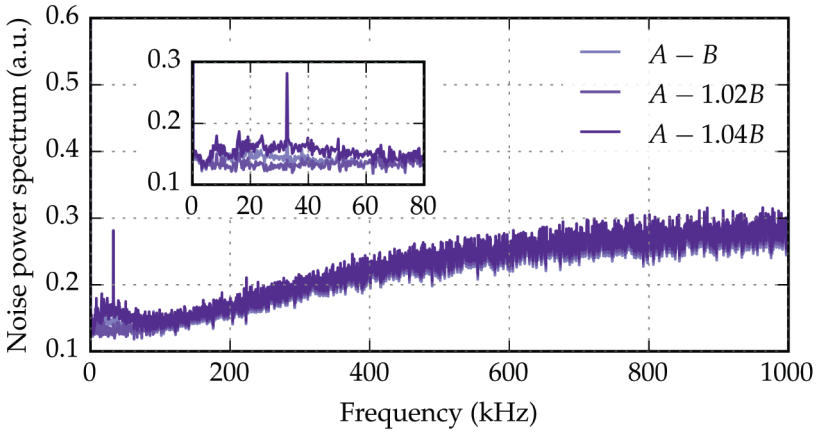

Figure 12.3: Single detector measurements and subtraction. Calculated noise power spectra from time series of individually measured detectors, but with subtraction in post-processing of the phase homodyne setup. Here, each AC channel is treated as described in section 10.4, with the only exception being that the subtraction is skipped and done in post-processing. By adding a parameter b and calculating the difference, $i_A - b \cdot i_B$, of the individually acquired time series, an optimal value for b can be found that optimized the difference and the low frequency laser noise. Three different combinations are shown in this figure and the inset zooms into the residual classical laser noise below 80 kHz. For $b = 1.02$, all classical noise if removed (broad features as well as sharp spikes).

Soft clamped membranes with room temperature quality factors as high as $Q = 2.1 \times 10^8$ have been fabricated [127], and very recently membranes with $Q = 1 \times 10^9$ have reached a cooperativity of $C = 119$ in an optomechanical cavity [115]. These ultra-coherent mechanical resonators feature only a narrow spectral bandwidth of around 200 kHz within which exist half a dozen high-Q mechanical modes. Around the bandgap, a vast amount of mechanical modes exist. From our current understanding, and the results showed in chapter 11, it cannot be assumed that the increased cooperativity will make up for the large number of mechanical modes and other spectral features outside the bandgap of soft clamped membranes. Therefore, we still believe that the current membranes used in our system are the best choice for a trade-off between mechanical quality factor, resonant frequencies and effective mass.

The average phonon number is determined by the bath temperature. The membrane thermalizes at approximately 10 K as Helium flow cryostats typically feature a large temperature gradient between the cold finger and the membrane placed in the optomechanical cavity. We have other cryostats available, that cool the membrane down to lower temperatures. These include pulse tube coolers, which offer advantages like long term operations and thermalization at 4 K. We have shown that our optomechanical cavity can be locked in such a pulse tube cryostat, despite the large amount of vibrational noise.

We have also low noise dilution refrigerators such as a model from Bluefors [15], that could yield even lower temperatures. Membranes in similar systems have been thermalized at bath temperatures of 360 mK [103]. A more conservative value of 1 K would improve the quantum cooperativity by a factor $\times 10$. The necessary modifications to place the optomechanical system into the dilution refrigerator are challenging, partially because proper thermalization requires careful engineering and is not guaranteed. Thus, this solution is more suitable as a back-up plan and short term solutions with similar impact should be prioritized.

The design of the optomechanical cavity sets the optomechanical coupling g as well as the cavity decay rate κ. Since we want to operate in the bad cavity regime it is not desirable to drastically change the design of the cavity. However, it is possible to significantly increase the input power that is impinging on the optomechanical cavity. For the current system, as characterized in chapter 9, the maximum input power realized during the measurements presented in chapter 11 was 12 µW. This is one order of magnitude below the Routh-Hurwitz stability criterion [46] and also one order of magnitude below the limit set by optical bistability due to the DC component of the radiation pressure force (equation 4.9).

We attributed issues of stabilizing and locking the system at larger input powers solely to technical reasons, e.g. residual heating of the membrane while scanning over the cavity resonance to find the locking position. One idea to circumvent this problem is based on a two-tone scheme. We could use the cooling beam (see chapter 5.4) to lock the cavity very close it its resonance. The optical power of the cooling beam could be chosen to be very small ($2 - 3$ µW) to ensure stable locking and avoid instabilities from being too close to the blue-detuned heating side of the resonance. Then the signal beam that is used to pump the optomechanical cavity and generate the entanglement, is sent off-resonantly to the cavity. By setting its modulation frequency, which determins the frequency difference between cooling beam and signal beam, it is possible to bring the signal beam to a specific red-detuning in a controlled way. Afterwards, the optical power could be increased by an electronically controlled waveplate and polarizing beam splitter. First attempts of this method made it possible to reproducibly lock the cavity with approximately 80 µW. However, this method needs to be characterized more carefully, e.g. check if the gain in input power is also possible for the optimal single photon coupling strength.

In conclusion, two methods have been presented that would increase the quantum cooperativity. The first is the reduction of $\bar{n}$ by moving the optomechanical cavity into a different cryostat. The second is by increasing the input power in a reliable and controlled way.

Conservatively estimated, each approach can presumably increase the quantum cooperativity by at least a factor of five. Based on our current results presented in chapter 11, either improvement will push the system into a realm where we expect to generate and verify strong optomechanical entanglement.

13

SUMMARY

Quantum entanglement is one of the most intriguing features of quantum physics and a rich resource for fundamental tests of physics as well as for future applications in quantum communication, computation and information. Optomechanical experiments are especially exciting systems, as they inherently constitute a light-mechanics interface interesting for quantum information networks.

In this thesis we presented a membrane-in-the-middle optomechanical system to pursue the generation and verification of multimode optomechanical entanglement with continuous variables.

The main experimental achievement was the operation of the optomechanical cavity in the strong cooperativity regime. As a consequence, the system operates in a regime where the generation of optomechanical entanglement is expected.

Furthermore, the so called pulsed-continuous entanglement protocol has been applied to time series measurements while operating in the strong cooperativity regime. Simulations have been presented that show that genuine multimode entanglement can occur naturally via a multimode oscillator like our SiN membranes, while single mode entanglement is consequently almost absent. Experimental results featured a three-mode entanglement witness which dives below the shot noise evaluation, which is an indication for squeezing and hence entanglement. Both traces show an offset above the entanglement bound at 0.5, whereby the smallest signal witness is as low as 0.515. This value is only 3 % or 0.13 dB above the entanglement threshold at 0.5.

An updated calibration method succeeds at removing the shot noise offset and yields to a signal witness that is 2.6 % or 0.11 dB below the entanglement threshold. Whereas these results are unphysical, they are indicating moderate genuine multimode entanglement. The calibration procedure is subject to current work.

Two different possible improvements have been presented, which in principle could improve the system sufficiently such that optomechanical entanglement can be significantly inferred. First, the acquisition of single photodiode time traces and the subtraction in post-processing is a promising way to reduce low frequency classical laser noise, which we believe limits the performance of the current data evaluation. The second improvement involves increasing the quantum cooperativity by reducing the average number of phonons via improved cryogenic cooling or by increasing the optical input power in a controlled way. Both directions are in principle sufficient to increase the quantum cooperativity to a level where we, with our cur-

rent understanding, expect to witness strong genuine multimode optomechanical entanglement.

BIBLIOGRAPHY

[1] https://www.engineeringtoolbox.com/: InnoLight GmbH.

[2] https://www.coherent.com/: Coherent, Inc.

[3] www.lasercomponents.com: LASER COMPONENTS GmbH.

[4] FEMTO Messtechnik GmbH: www.femto.de.

[5] Norcada Inc.: www.norcada.com.

[6] attocube systems AG: http://www.attocube.com/.

[7] Janis Research Company: www.janis.com.

[8] Pfeiffer Vacuum Technology AG: pfeiffer-vacuum.com.

[9] www.lakeshore.com/products/cryogenic-accessories/epoxy: Lakeshore Cryogenics.

[10] https://www.engineeringtoolbox.com/: engineeringtoolbox.

[11] http://www.photoniccleaning.com/: Photonic Cleaning Technologies, LLC.

[12] www.id-photonics.com: ID Photonics GmbH.

[13] http://www.ni.com: National Instruments.

[14] www.minicircuits.com: Mini Circuits.

[15] www.bluefors.com/: BlueFors Cryogenics Oy.

[16] K. Strain A. Freise. "Interferometer Techniques for Gravitational Wave Detection." In: *Living Rev. Relativity*, 13.1 (2010).

[17] A. Abramovici and J. Chapsky. *Feedback Control Systems: A Fast-Track Guide for Scientists and Engineers*. Springer US, 2012.

[18] Gerardo Adesso and Fabrizio Illuminati. "Entanglement in continuous-variable systems: Recent advances and current perspectives." In: *Journal of Physics A: Mathematical and Theoretical* 40.28 (2007), pp. 7821–7880. arXiv: 0701221 [quant-ph].

[19] Gerardo Adesso and Fabrizio Illuminati. "Entanglement in continuous-variable systems: recent advances and current perspectives." In: *Journal of Physics A: Mathematical and Theoretical* 40.28 (July 2007), pp. 7821–7880.

[20] Gerardo Adesso, Alessio Serafini, and Fabrizio Illuminati. "Determination of Continuous Variable Entanglement by Purity Measurements." In: *Physical Review Letters* 92.8 (2004), pp. 1–4. arXiv: 0310150 [quant-ph].

[21] Gerardo Adesso, Alessio Serafini, and Fabrizio Illuminati. "Extremal entanglement and mixedness in continuous variable systems." In: *Physical Review A - Atomic, Molecular, and Optical Physics* 70.2 (2004). arXiv: 0402124 [quant-ph].

[22] V. P. Adiga, B. Ilic, R. A. Barton, I. Wilson-Rae, H. G. Craighead, and J. M. Parpia. "Approaching intrinsic performance in ultra-thin silicon nitride drum resonators." In: *Journal of Applied Physics* 112.6 (2012).

[23] Alain Aspect, Jean Dalibard, and Gérard Roger. "Experimental Test of Bell's Inequalities Using Time-Varying Analyzers." In: *Phys. Rev. Lett.* 49 (25 Dec. 1982), pp. 1804–1807.

[24] Alain Aspect, Philippe Grangier, and Gérard Roger. "Experimental Tests of Realistic Local Theories via Bell's Theorem." In: *Phys. Rev. Lett.* 47 (7 Aug. 1981), pp. 460–463.

[25] Markus Aspelmeyer, Simon Groeblacher, Klemens Hammerer, and Nikolai Kiesel. "Quantum Optomechanics - throwing a glance." In: *Journal of the Optical Society of America B* 27.6 (2010), A189. arXiv: 1005.5518.

[26] Markus Aspelmeyer, Tobias J. Kippenberg, and Florian Marquardt. "Cavity Optomechanics." In: 321 (2013). arXiv: 1303.0733.

[27] Markus Aspelmeyer, Tobias J. Kippenberg, and Florian Marquardt. "Cavity optomechanics." In: *Reviews of Modern Physics* 86.4 (2014), pp. 1391–1452. arXiv: 0712.1618.

[28] Hans-a Bachor and Timothy C Ralph. *A Guide to Experiments*.

[29] Minhang Bao, Heng Yang, Hao Yin, and Yuancheng Sun. "Energy transfer model for squeeze-film air damping in low vacuum." In: *Journal of Micromechanics and Microengineering* 12.3 (2002), pp. 341–346.

[30] J. S. Bell. "On the Einstein Podolsky Rosen Paradox." In: *Physics Publishing Co.* 1.3 (1964), pp. 195–290.

[31] Eric Black. *Notes on the Pound-Drever-Hall technique*. Tech. rep. Technical Note LIGO-T980045- 00- D. CALIFORNIA INSTITUTE OF TECHNOLOGY and MASSACHUSETTS INSTITUTE OF TECHNOLOGY: LASER INTERFEROMETER GRAVITATIONAL WAVE OBSERVATORY (LIGO), Apr. 1998.

[32] Eric D. Black. "An introduction to Pound–Drever–Hall laser frequency stabilization." In: *American Journal of Physics* 69.1 (2001), pp. 79–87.

[33] Hannes Böhm. "Radiation-Pressure Cooling of a Mechanical Oscillator." In: (2007).

[34] V. B. Braginsky and A. B. Manukin. "Ponderomotive effects of electromagnetic radiation." In: *Soviet Physics JETP* 25.4 (1967), pp. 653–655.

[35] Daniel W C Brooks, Thierry Botter, Sydney Schreppler, Thomas P. Purdy, Nathan Brahms, and Dan M. Stamper-Kurn. "Non-classical light generated by quantum-noise-driven cavity optomechanics." In: *Nature* 488.7412 (2012), pp. 476–480. arXiv: 1107.5609.

[36] Oliver Sascha Brozek. "Frequenzstabilisierung eines Nd:YAG-Hochleistungs-Laser-Systems für den Gravitationswellendetektor GEO 600." PhD thesis. Hannover, Deutschland: Universität Hannover, 1999.

[37] Herbert B. Callen and Richard F. Greene. "On a theorem of irreversible thermodynamics." In: *Physical Review* 86.5 (1952), pp. 702–710. arXiv: 1707.04192.

[38] S. Chakram, Y. S. Patil, L. Chang, and M. Vengalattore. "Dissipation in ultrahigh quality factor SiN membrane resonators." In: *Physical Review Letters* 112.12 (2013), pp. 1–5. arXiv: 1311.1234.

[39] Jasper Chan, T. P.Mayer Alegre, Amir H. Safavi-Naeini, Jeff T. Hill, Alex Krause, Simon Gröblacher, Markus Aspelmeyer, and Oskar Painter. "Laser cooling of a nanomechanical oscillator into its quantum ground state." In: *Nature* 478.7367 (2011), pp. 89–92. arXiv: 1106.3614.

[40] Jasper Chan, Matt Eichenfield, Ryan Camacho, and Oskar Painter. "Optical and mechanical design of a "zipper" photonic crystal optomechanical cavity." In: 17.5 (2008), pp. 555–560. arXiv: 0812.4683.

[41] Jasper Chan, Amir H. Safavi-Naeini, Jeff T. Hill, Seán Meenehan, and Oskar Painter. "Optimized optomechanical crystal cavity with acoustic radiation shield." In: *Applied Physics Letters* 101.8 (2012). arXiv: 1206.2099.

[42] Yanbei Chen. "Macroscopic quantum mechanics: theory and experimental concepts of optomechanics." In: *Journal of Physics B: Atomic, Molecular and Optical Physics* 46.10 (May 2013), p. 104001.

[43] Jeremy B. Clark, Florent Lecocq, Raymond W. Simmonds, José Aumentado, and John D. Teufel. "Observation of strong radiation pressure forces from squeezed light on a mechanical oscillator." In: *Nature Physics* 12.7 (2016), pp. 683–687. arXiv: 1601.02689.

[44] Garrett D. Cole, Pen Li Yu, Karoline Siquans, Ramon Moghadas Nia, Jonas Schmöle, Jason Hoelscher-Obermaier, Thomas P. Purdy, Witlef Wieczorek, Cindy A. Regal, and Markus Aspelmeyer. "Tensile-strained InxGa1-xP membranes for cavity optomechanics." In: *Applied Physics Letters* 104.20 (2014). arXiv: 1404.0029.

[45] Jonathan Cripe, Nancy Aggarwal, Robert Lanza, Adam Libson, Robinjeet Singh, Paula Heu, David Follman, Garrett D. Cole, Nergis Mavalvala, and Thomas Corbitt. "Observation of a room-temperature oscillator's motion dominated by quantum fluctuations over a broad audio-frequency band." In: (2018), pp. 3–8. arXiv: 1802.10069.

[46] Edmund X. Dejesus and Charles Kaufman. "Routh-Hurwitz criterion in the examination of eigenvalues of a system of nonlinear ordinary differential equations." In: *Physical Review A* 35.12 (1987), pp. 5288–5290.

[47] W. Demtröder. *Experimentalphysik 1*. Experimentalphysik / Wolfgang Demtröder. Springer Berlin Heidelberg, 2008.

[48] W. Demtroeder. *Experimentalphysik 2*. Experimentalphysik / Wolfgang Demtroeder. Springer Berlin Heidelberg, 2008.

[49] R W P Drever, J. L. Hall, F. V. Kowalski, J. Hough, G. M. Ford, A. J. Munley, and H. Ward. "Laser phase and frequency stabilization using an optical resonator." In: *Applied Physics B* 31.2 (1983), pp. 97–105. arXiv: 1602.03504.

[50] A. Einstein, B. Podolsky, and N. Rosen. "Can quantum-mechanical description of physical reality be considered correct?" In: *Physical Review* 47.10 (1935), pp. 777–780. arXiv: 0701001 [quant-ph].

[51] Albert Einstein. "Entwicklung unserer Anschauungen über das Wesen und die Konstitution der Strahlung." In: *Physikalische Zeitschrift* 10 (1909).

[52] J Eisert, F G S L Brandão, and K M R Audenaert. "Quantitative entanglement witnesses." In: *New Journal of Physics* 9.3 (2007), p. 46.

[53] Stuart J. Freedman and John F. Clauser. "Experimental Test of Local Hidden-Variable Theories." In: *Phys. Rev. Lett.* 28 (14 Apr. 1972), pp. 938–941.

[54] I. Freitag, I. Kröpke, A. Tünnerman, and H. Welling. "Electrooptically fast tunable miniature diode-pumped Nd:YAG ring laser." In: *Optics Communications* 101.5-6 (1993), pp. 371–376.

[55] I. Freitag, A. Tünnermann, and H. Welling. "Power scaling of diode-pumped monolithic Nd:YAG lasers to output powers of several watts." In: *Optics Communications* 115.5-6 (1995), pp. 511–515.

[56] D. Friedrich, H. Kaufer, T. Westphal, K. Yamamoto, A. Sawadsky, F. Ya Khalili, S. L. Danilishin, S. Goßler, K. Danzmann, and R. Schnabel. "Laser interferometry with translucent and absorbing mechanical oscillators." In: *New Journal of Physics* 13 (2011). arXiv: 1104.3251.

[57] Khashayar Babaei Gavan, Joost Van der Heijden, Emile W.J.M. Van der Drift, and Herre S.J. Van der Zant. "Effect of pressure on the Q factor and the resonance frequency of SiN microcantilevers." In: *4th IEEE International Conference on Nano/Micro Engineered and Molecular Systems, NEMS 2009* 31.0 (2009), pp. 380–384.

[58] C. Genes, A. Mari, P. Tombesi, and D. Vitali. "Robust entanglement of a micromechanical resonator with output optical fields." In: *Physical Review A - Atomic, Molecular, and Optical Physics* 78.3 (2008), pp. 1–14. arXiv: 0806.2045.

[59] C. Gerry and P. Knight. *Introductory Quantum Optics*. Cambridge University Press, 2005.

[60] Marissa Giustina et al. "Significant-Loophole-Free Test of Bell's Theorem with Entangled Photons." In: *Phys. Rev. Lett.* 115 (25 Dec. 2015), p. 250401.

[61] Stefan Gossler. "The suspension systems of the interferometric gravitational-wave detector GEO 600." In: (2004).

[62] Andri M. Gretarsson, Gregory M. Harry, Steven D. Penn, Peter R. Saulson, William J. Startin, Sheila Rowan, Gianpietro Cagnoli, and Jim Hough. "Pendulum mode thermal noise in advanced interferometers: A comparison of fused silica fibers and ribbons in the presence of surface loss." In: *Physics Letters, Section A: General, Atomic and Solid State Physics* 270.3-4 (2000), pp. 108–114. arXiv: 9912057 [gr-qc].

[63] Simon Gröblacher, Klemens Hammerer, Michael R. Vanner, and Markus Aspelmeyer. "Observation of strong coupling between a micromechanical resonator and an optical cavity field." In: *Nature* 460.7256 (2009), pp. 724–727. arXiv: 0903.5293.

[64] The Aspelmeyer Group, Markus Aspelmeyer, Pierre Meystre, and Keith Schwab. "Quantum optomechanics." In: *Physics Today* 65.7 (2012), p. 29. arXiv: 1005.5518v1.

[65] T W Hänsch and B Couillaud. "Laser frequency stabilization by polarization spectroscopy of a reference cavity." In: *Optics Communications* 35.3 (1980), pp. 441–444.

[66] Sebastian Hofer. "Quantum control of optomechanical systems." PhD thesis. Vienna, Austria: Universität Wien, 2015.

[67] Sebastian G. Hofer and Klemens Hammerer. "Entanglement-enhanced time-continuous quantum control in optomechanics." In: *Physical Review A - Atomic, Molecular, and Optical Physics* 91.3 (2015), pp. 1–19. arXiv: 1411.1337.

[68] Sebastian G. Hofer and Klemens Hammerer. "Chapter Five - Quantum Control of Optomechanical Systems." In: ed. by Ennio Arimondo, Chun C. Lin, and Susanne F. Yelin. Vol. 66. Advances In Atomic, Molecular, and Optical Physics. Academic Press, 2017, pp. 263–374.

[69] Sebastian G. Hofer, Witlef Wieczorek, Markus Aspelmeyer, and Klemens Hammerer. "Quantum entanglement and teleportation in pulsed cavity optomechanics." In: *Physical Review A - Atomic, Molecular, and Optical Physics* 84.5 (2011), pp. 1–10. arXiv: 1108.2586.

[70] Jason Hölscher-Obermaier. "Generation and Detection of Quantum Entanglement in Optomechanical Systems." PhD thesis. Vienna, Austria: Universität Wien, 2017.

[71] Ryszard Horodecki, Paweł Horodecki, Michał Horodecki, and Karol Horodecki. "Quantum entanglement." In: *Reviews of Modern Physics* 81.2 (2009), pp. 865–942. arXiv: 0702225 [quant-ph].

[72] Mani Hossein-zadeh and Kerry J Vahala. "Observation of optical spring effect in a microtoroidal optomechanical resonator." In: 32.12 (2007), pp. 1611–1613.

[73] P Hyllus and J Eisert. "Optimal entanglement witnesses for continuous-variable systems." In: *New Journal of Physics* 8.4 (2006), p. 51.

[74] A. M. Jayich, J. C. Sankey, B. M. Zwickl, C. Yang, J. D. Thompson, S. M. Girvin, A. A. Clerk, F. Marquardt, and J. G.E. Harris. "Dispersive optomechanics: A membrane inside a cavity." In: *New Journal of Physics* 10 (2008), pp. 1–28. arXiv: 0805.3723.

[75] T Kane and R Byer. "Monolithic, unidirectional single-mode Nd:YAG ring laser." In: *Optics Letters* 10.2 (1985), pp. 65–67.

[76] M. Karuza, C. Biancofiore, P. Zucconi Galli Fonseca, M. Galassi, R. Natali, P. Tombesi, G. Di Giuseppe, and D. Vitali. "Optomechanically induced transparency in a membrane-in-the-middle setup at room temperature." In: *2013 Conference on Lasers and Electro-Optics Europe and International Quantum Electronics Conference, CLEO/Europe-IQEC 2013* 013804 (2013), pp. 1–5. arXiv: 1209.1352.

[77] a Kaushik, H Kahn, and a H Heuer. "Wafer-level mechanical characterization of silicon nitride MEMS." In: *Journal Of Microelectromechanical Systems* 14.2 (2005), pp. 359–367.

[78] Farid Ya Khalili, Sergey P. Tarabrin, Klemens Hammerer, and Roman Schnabel. "Generalized analysis of quantum noise and dynamic backaction in signal-recycled Michelson-type laser interferometers." In: *Physical Review A* 94.1 (2016), pp. 1–9. arXiv: 1604.01309.

[79] H. J. Kimble. "The quantum internet." In: *Nature* 453.7198 (2008), pp. 1023–1030. arXiv: 0806.4195.

[80] T. J. Kippenberg, S. M. Spillane, and K. J. Vahala. "Demonstration of ultra-high- Q small mode volume toroid microcavities on a chip." In: *Applied Physics Letters* 85.25 (2004), pp. 6113–6115. arXiv: 0412042 [physics].

[81] Patrick Kwee. "Charakterisierung von Lasersystemen fuer Gravitationswellendetektoren." In: September (2005).

[82] Patrick Kwee. "Laser Characterization and Stabilization for Precision Interferometry." In: *PhD Thesis* (2010).

[83] Patrick Kwee and Benno Willke. "Automatic laser beam characterization of monolithic Nd:YAG nonplanar ring lasers." In: *Applied optics* 47 (2008), pp. 6022–6032.

[84] Lev D Landau, E M Lifshitz, J B Sykes, W H Reid, and Ellis H Dill. *Theory of Elasticity: Vol. 7 of Course of Theoretical Physics*. 1960.

[85] C. K. Law. "Interaction between a moving mirror and radiation pressure: A Hamiltonian formulation." In: *Physical Review A* 51.3 (1995), pp. 2537–2541.

[86] Jie Li, André Xuereb, Nicola Malossi, and David Vitali. "Cavity mode frequencies and strong optomechanical coupling in two-membrane cavity optomechanics." In: *Journal of Optics (United Kingdom)* 18.8 (2016), pp. 1–6. arXiv: 1512.07536.

[87] LIGO Scientific Collaboration. "Observation of a kilogram-scale oscillator near its quantum ground state." In: *New Journal of Physics* 11 (2009), p. 073032.

[88] R. Loudon. *The quantum theory of light*. Oxford science publications. Clarendon Press, 1983.

[89] The LIGO Scientific Collaboration LSC. "A gravitational wave observatory operating beyond the quantum shot-noise limit." In: *Nature Physics* 7.12 (2011), pp. 962–965. arXiv: 1109.2295.

[90] Kevin Luke, Yoshitomo Okawachi, Michael R. E. Lamont, Alexander L. Gaeta, and Michal Lipson. "Broadband mid-infrared frequency comb generation in a Si_3N_4 microresonator." In: *Optics Letters* 40.21 (2015), p. 4823.

[91] Stefano Mancini, David Vitali, and Paolo Tombesi. "Scheme for Teleportation of Quantum States onto a Mechanical Resonator." In: *Phys. Rev. Lett.* 90 (13 Apr. 2003), p. 137901.

[92] Florian Marquardt, A. A. Clerk, and S. M. Girvin. "Quantum theory of optomechanical cooling." In: *Journal of Modern Optics* 55.19-20 (2008), pp. 3329–3338. arXiv: 0803.1164.

[93] Florian Marquardt and S. M. Girvin. "Optomechanics (a brief review)." In: 40 (2009). arXiv: 0905.0566.

[94] Moritz Mehmet. "Squeezed light at 1064nm and 1550nm with a nonclassical noise suppression beyond 10dB." In: September 1978 (2012).

[95] E. F. Nichols and G. F. Hull. "A preliminary communication on the pressure of heat and light radiation." In: *Physical Review* 13.5 (1901), pp. 307–320.

[96] William H. P. Nielsen, Yeghishe Tsaturyan, Christoffer B. Møller, Eugene S. Polzik, and Albert Schliesser. "Multimode optomechanical system in the quantum regime." In: (2016). arXiv: 1605.06541.

[97] a D O'Connell et al. "Quantum ground state and single-phonon control of a mechanical resonator." In: *Nature* 464.7289 (Apr. 2010), pp. 697–703.

[98] David Ottaway, Henning Rehbein, Thomas Corbitt, Yanbei Chen, Edith Innerhofer, Helge Mu, Daniel Sigg, Stanley Whitcomb, Christopher Wipf, and Nergis Mavalvala. "An All-Optical Trap for a Gram-Scale Mirror." In: 150802.April (2007), pp. 11–14.

[99] T A Palomaki, J D Teufel, R W Simmonds, and K W Lehnert. "Entangling Mechanical Motion with Microwave Fields." In: *Science* 342.6159 (2013), pp. 710–713.

[100] T. A. Palomaki, J. W. Harlow, J. D. Teufel, R. W. Simmonds, and K. W. Lehnert. "Coherent state transfer between itinerant microwave fields and a mechanical oscillator." In: *Nature* 495.7440 (2013), pp. 210–214. arXiv: arXiv:1206.5562v1.

[101] T. A. Palomaki, J. D. Teufel, R. W. Simmonds, and K. W. Lehnert. "Entangling mechanical motion with microwave fields." In: *Science* 342.6159 (2013), pp. 710–713. arXiv: arXiv:1011.1669v3.

[102] M. Paternostro, D. Vitali, S. Gigan, M. S. Kim, C. Brukner, J. Eisert, and M. Aspelmeyer. "Creating and Probing Multipartite Macroscopic Entanglement with Light." In: *Phys. Rev. Lett.* 99 (25 Dec. 2007), p. 250401.

[103] R. W. Peterson, T. P. Purdy, N. S. Kampel, R. W. Andrews, P. L. Yu, K. W. Lehnert, and C. A. Regal. "Laser Cooling of a Micromechanical Membrane to the Quantum Backaction Limit." In: *Physical Review Letters* 116.6 (2016), pp. 1–6. arXiv: 1510.03911.

[104] Paolo Piergentili, Letizia Catalini, Mateusz Bawaj, Stefano Zippilli, Nicola Malossi, Riccardo Natali, David Vitali, and Giovanni Di Giuseppe. "Two-membrane cavity optomechanics." In: (2018). arXiv: 1805.09699.

[105] M Pinard, Y Hadjar, and Antoine Heidmann. "Effective mass in quantum effects of radiation pressure." In: *Eur. Phys. J. D* 7 (1999), pp. 107–116. arXiv: 9901057 [quant-ph].

[106] Stefano Pirandola, Stefano Mancini, David Vitali, and Paolo Tombesi. "Continuous-variable entanglement and quantum-state teleportation between optical and macroscopic vibrational modes through radiation pressure." In: *Phys. Rev. A* 68 (6 Dec. 2003), p. 062317.

[107] Stefano Pirandola, David Vitali, Paolo Tombesi, and Seth Lloyd. "Macroscopic Entanglement by Entanglement Swapping." In: *Phys. Rev. Lett.* 97 (15 Oct. 2006), p. 150403.

[108] D P Poenar and R F Wolffenbuttel. "Optical properties of thin-film silicon-compatible materials." In: *Applied optics* 36.21 (1997), pp. 5122–8.

[109] T P Purdy et al. "Supplementary Materials for Observation of Radiation Pressure Shot Noise on a Macroscopic Object." In: 801.February (2013), pp. 801–805.

[110] T. P. Purdy, P.-L. Yu, R. W. Peterson, N. S. Kampel, and C. a. Regal. "Strong Optomechanical Squeezing of Light." In: *Physical Review X* 3.3 (Sept. 2013), p. 031012.

[111] S P R. *Fundamentals Of Interferometric Gravitational Wave Detectors (Second Edition)*. World Scientific Publishing Company, 2017.

[112] M. Rakhmanov, R. L. Savage, D. H. Reitze, and D. B. Tanner. "Dynamic resonance of light in Fabry-Perot cavities." In: *Physics Letters, Section A: General, Atomic and Solid State Physics* 305.5 (2002), pp. 239–244. arXiv: 0110061v1 [arXiv:physics].

[113] R.C. Richardson and E.N. Smith. *Experimental techniques in condensed matter physics at low temperatures*. Frontiers in physics. Addison-Wesley Pub. Co., 1988.

[114] Wenjamin Rosenfeld, Daniel Burchardt, Robert Garthoff, Kai Redeker, Norbert Ortegel, Markus Rau, and Harald Weinfurter. "Event-Ready Bell Test Using Entangled Atoms Simultaneously Closing Detection and Locality Loopholes." In: *Phys. Rev. Lett.* 119 (1 July 2017), p. 010402.

[115] Massimiliano Rossi, David Mason, Junxin Chen, Yeghishe Tsaturyan, and Albert Schliesser. "Measurement-based quantum control of mechanical motion." In: (2018). arXiv: 1805.05087.

[116] Amir H. Safavi-Naeini, Simon Gröblacher, Jeff T. Hill, Jasper Chan, Markus Aspelmeyer, and Oskar Painter. "Squeezed light from a silicon micromechanical resonator." In: *Nature* 500.7461 (2013), pp. 185–189. arXiv: 1302.6179.

[117] A. Schliesser, R. Rivière, G. Anetsberger, O. Arcizet, and T. J. Kippenberg. "Resolved-sideband cooling of a micromechanical oscillator." In: *Nature Physics* 4.5 (2008), pp. 415–419. arXiv: 0709.4036.

[118] E Schrodinger. "Probability Relations Between Separated Systems." In: 31.1935 (2017), pp. 446–452.

[119] E. Serra et al. "Microfabrication of large-area circular high-stress silicon nitride membranes for optomechanical applications." In: *AIP Advances* 6.6 (2016). arXiv: 1601.02669.

[120] D. A. Shaddock, M. B. Gray, and D. E. McClelland. "Frequency locking a laser to an optical cavity by use of spatial mode interference." In: *Optics Letters* 24.21 (1999), p. 1499. arXiv: 0809.0545.

[121] Lynden K. Shalm et al. "Strong Loophole-Free Test of Local Realism." In: *Phys. Rev. Lett.* 115 (25 Dec. 2015), p. 250402.

[122] D. R. Southworth, R. A. Barton, S. S. Verbridge, B. Ilic, A. D. Fefferman, H. G. Craighead, and J. M. Parpia. "Stress and silicon nitride: A crack in the universal dissipation of glasses." In: *Physical Review Letters* 102.22 (2009), pp. 1–4.

[123] S. M. Spillane, T. J. Kippenberg, K. J. Vahala, K. W. Goh, E. Wilcut, and H. J. Kimble. "Ultrahigh-Q toroidal microresonators for cavity quantum electrodynamics." In: *Physical Review A - Atomic, Molecular, and Optical Physics* 71.1 (2005), pp. 1–10. arXiv: 0410218 [quant-ph].

[124] Dan M. Stamper-Kurn. "Cavity optomechanics with cold atoms." In: (2012). arXiv: 1204.4351.

[125] Jessica Steinlechner, Christoph Krüger, Iain W. Martin, Angus Bell, Jim Hough, Henning Kaufer, Sheila Rowan, Roman Schnabel, and Sebastian Steinlechner. "Optical absorption of silicon nitride membranes at 1064 nm and at 1550 nm." In: *Physical Review D* 96.2 (2017).

[126] J. D. Teufel, T. Donner, Dale Li, J. W. Harlow, M. S. Allman, K. Cicak, A. J. Sirois, J. D. Whittaker, K. W. Lehnert, and R. W. Simmonds. "Sideband cooling of micromechanical motion to the quantum ground state." In: *Nature* 475.7356 (2011), pp. 359–363. arXiv: 1103.2144.

[127] Y. Tsaturyan, A. Barg, E. S. Polzik, and A. Schliesser. "Ultracoherent nanomechanical resonators via soft clamping and dissipation dilution." In: *Nature Nanotechnology* 12.8 (2017), pp. 776–783. arXiv: 1608.00937.

[128] Yeghishe Tsaturyan, Andreas Barg, Anders Simonsen, Luis Guillermo Villanueva, Silvan Schmid, Albert Schliesser, and Eugene S. Polzik. "Demonstration of suppressed phonon tunneling losses in phononic bandgap shielded membrane resonators for high-Q optomechanics." In: 22.6 (2013), pp. 6810–6821. arXiv: 1312.7776.

[129] M. Yu. Tikhonov V.B. Braginskii A.B. Manukin. "Investigation of Dissipative Ponderomotive Effects of Electromagnetic Radiation." In: *ZhETF* 58.5 (1901), p. 1549.

[130] Henning Vahlbruch. "Squeezed Light for Gravitational Wave Detectors." In: *Quantum Information with Continuous Variables of Atoms and Light* (2007), pp. 345–366.

[131] Henning Vahlbruch. "Squeezed Light for Gravitational Wave Astronomy." In: *PhD Thesis* (2008), p. 176.

[132] M. R. Vanner, J. Hofer, G. D. Cole, and M. Aspelmeyer. "Cooling-by-measurement and mechanical state tomography via pulsed optomechanics." In: *Nature Communications* 4.May (2013), pp. 1–8. arXiv: 1211.7036.

[133] Scott S. Verbridge, Harold G. Craighead, and Jeevak M. Parpia. "A megahertz nanomechanical resonator with room temperature quality factor over a million." In: *Applied Physics Letters* 92.1 (2008), pp. 4–6.

[134] E. Verhagen, S. Deléglise, S. Weis, A. Schliesser, and T. J. Kippenberg. "Quantum-coherent coupling of a mechanical oscillator to an optical cavity mode." In: *Nature* 482.7383 (2012), pp. 63–67. arXiv: 1107.3761.

[135] L. G. Villanueva and S. Schmid. "Evidence of surface loss as ubiquitous limiting damping mechanism in SiN micro- and nanomechanical resonators." In: *Physical Review Letters* 113.22 (2014), pp. 1–6. arXiv: arXiv:1405.6115v1.

[136] D. Vitali, S. Gigan, A. Ferreira, H. R. Böhm, P. Tombesi, A. Guerreiro, V. Vedral, A. Zeilinger, and M. Aspelmeyer. "Optomechanical entanglement between a movable mirror and a cavity field." In: *Physical Review Letters* 98.3 (2007), pp. 1–4. arXiv: 0609197 [quant-ph].

[137] N. G. Walker. "Quantum theory of multiport optical homodyning." In: *Journal of modern optics* 34.1 (1987).

[138] D.F. Walls and G.J. Milburn. *Quantum Optics*. SpringerLink: Springer e-Books. Springer Berlin Heidelberg, 2008.

[139] Gregor Weihs, Thomas Jennewein, Christoph Simon, Harald Weinfurter, and Anton Zeilinger. "Violation of Bell's Inequality under Strict Einstein Locality Conditions." In: *Phys. Rev. Lett.* 81 (23 Dec. 1998), pp. 5039–5043.

[140] S. Weis, R. Riviere, S. Deleglise, E. Gavartin, O Arcizet, A. Schliesser, and T. J. Kippenberg. "Optomechanically Induced Transparency som." In: *Science* 330.6010 (2010), pp. 1520–1523. arXiv: 1007.0565.

[141] T. Westphal. "Optomechanische Kopplung in einem Michaelson Sagnag Interferometer." MA thesis. Leibniz Universität eover, 2009.

[142] B. Willke, N. Uehara, E. K. Gustafson, R. L. Byer, P. J. King, S. U. Seel, and R. L. Savage. "Spatial and temporal filtering of a 10-W Nd:YAG laser with a Fabry–Perot ring-cavity premode cleaner." In: *Optics Letters* 23.21 (1998), p. 1704.

[143] D. J. Wilson, V. Sudhir, N. Piro, R. Schilling, A. Ghadimi, and T. J. Kippenberg. "Measurement-based control of a mechanical oscillator at its thermal decoherence rate." In: *Nature* 524.7565 (2015), pp. 325–329. arXiv: 1410.6191.

[144] D. Wilson, C. Regal, S. Papp, and H. Kimble. "Cavity Optomechanics with Stoichiometric SiN Films." In: *Physical Review Letters* 103.20 (Nov. 2009), p. 207204.

[145] Dalziel Joseph Wilson. "Cavity Optomechanics with High-Stress Silicon Nitride Films Thesis by." PhD thesis. 2012.

[146] E E Wollman, C U Lei, A J Weinstein, J Suh, A Kronwald, F Marquardt, A A Clerk, and K C Schwab. "Quantum squeezing of motion in a." In: ().

[147] André Xuereb, Claudiu Genes, and Aurélien Dantan. "Strong coupling and long-range collective interactions in optomechanical arrays." In: *Physical Review Letters* 109.22 (2012), pp. 1–5. arXiv: 1202.6210.

[148] André Xuereb, Claudiu Genes, and Aurélien Dantan. "Collectively enhanced optomechanical coupling in periodic arrays of scatterers." In: *Physical Review A - Atomic, Molecular, and Optical Physics* 88.5 (2013), pp. 1–13. arXiv: 1304.4574.

[149] André Xuereb, Roman Schnabel, and Klemens Hammerer. "Dissipative optomechanics in a Michelson-Sagnac interferometer." In: *Physical Review Letters* 107.21 (2011), pp. 1–5. arXiv: 1107.4908.

[150] P. L. Yu, K. Cicak, N. S. Kampel, Y. Tsaturyan, T. P. Purdy, R. W. Simmonds, and C. A. Regal. "A phononic bandgap shield for high-Q membrane microresonators." In: *Applied Physics Letters* 104.2 (2014), pp. 2–6. arXiv: 1312.0962.

[151] Horace P. Yuen and Jeffrey H. Shapiro. "Optical Communication with Two-Photon Coherent States — Part III: Quantum Measurements Realizable with Photoemissive Detectors." In: *IEEE Transactions on Information Theory* 26.1 (1980), pp. 78–92.

[152] A. Zeilinger. "General properties of lossless beam splitters in interferometry." In: *American Journal of Physics* 49.9 (1981), pp. 882–883.

[153] B. M. Zwickl, W. E. Shanks, A. M. Jayich, C. Yang, A. C.Bleszynski Jayich, J. D. Thompson, and J. G.E. Harris. "High quality mechanical and optical properties of commercial silicon nitride membranes." In: *Applied Physics Letters* 92.10 (2008), pp. 1–4. arXiv: 0711.2263.

COLOPHON

This document was typeset using the typographical look-and-feel `classicthesis` developed by André Miede and Ivo Pletikosić. The style was inspired by Robert Bringhurst's seminal book on typography "*The Elements of Typographic Style*". `classicthesis` is available for both LaTeX and LyX:

https://bitbucket.org/amiede/classicthesis/

Final Version as of August 28, 2018 (`classicthesis` Version 1.0).